Rapid Change of the Arctic Climate System and its Global Influences

—Synthesis Report of GRENE Arctic Climate Change Research Project (2011–2016)—

Takashi Yamanouchi, Kumiko Takata

GRENE-Arctic

Rapid Change of the Arctic Climate System and its Global Influences

—Synthesis Report of GRENE Arctic Climate Change Research Project (2011–2016)—

Takashi Yamanouchi[1], Kumiko Takata[2]

1) National Institute of Polar Research and Graduate University for Advanced Studies
2) National Institute of Polar Research, present affiliation: National Institute for Environmental Studies

Synthesis Report of GRENE Arctic Climate Change Research Project (2011–2016) “Rapid Change of the Arctic Climate System and its Global Influences” by Takashi Yamanouchi and Kumiko Takata

Published by Research Organization of Information and Systems,
National Institute of Polar Research
10–3 Midori-cho
Tachikawa-shi
Tokyo 190–8518
Japan

20 March 2020

Cover photo. Melt water stream over a glacier surface darkened by glacier microorganisms (cryoconite) in Greenland (photo by Shin Sugiyama, Hokkaido Univ.)

Preface

What is happening in the Arctic, under global warming? In warming due to anthropogenic increases in atmospheric carbon dioxide concentration, the surface temperature in the Arctic is increasing with a speed that is more than double the global average. We call this “Arctic warming amplification,” and an understanding of its mechanism is urgently needed.

To grasp these changes in the Arctic, to understand the mechanism, and to contribute to future climate projection, we conducted the Green Network of Excellence Program (GRENE) Arctic Climate Change Research Project “Rapid Change of the Arctic Climate System and its Global Influences” for five years between 2011 and 2016. Thirty-nine institutions all over Japan participated in the Project, and more than 360 scientists tackled all aspects of the Arctic climate system. Comprehensive Arctic research incorporating multidisciplinary work and collaborations between observation and modeling was realized.

Here, we have compiled more than 100 papers originated from GRENE Arctic Project and published in the international journals. During the Project, already more than 350 original articles were published; however, after the project term, still many distinguished papers came out. Although it is nearly four years since the Project successfully ended, we intended to synthesize the primary outcomes of the Project, since there was no collection of the papers in the English language (Japanese final report was published on HP in 2016). We hope you could enjoy and notice the significant products of the GRENE Arctic Project.

March 2020
Takashi Yamanouchi, Project Manager
Kumiko Takata, Project Coordinater

Contents

1. Introduction

Scientific background

What is happening now in the Arctic, under global warming? In warming due to anthropogenic increases in carbon dioxide concentration, the surface temperature in the Arctic is increasing with a speed that is more than double the global average (e.g., Serrreze and Barry, 2011; Fig. 1.1a). We call this "Arctic warming amplification," and an understanding of its mechanism is urgently needed.

Reduction of sea ice extent in the Arctic Ocean is continuing, and an abrupt decrease since the 2000s is especially noticeable (e.g., Stroeve et al., 2007; Fig. 1.1b). Owing to this change, potential for regular ship navigation through the Arctic Ocean has increased, and they have become broadly known as "Arctic sea routes." The reduction of the sea ice extent and the warming of the ocean are expected to lead to changes not only in the physical and chemical ocean environment, but also to changes of marine ecosystems.

Looking at the land area, many glaciers distributed around the Arctic are retreating. The Greenland ice sheet, the largest ice mass in the northern hemisphere, is also melting markedly, and the flow- out or collapse from its terminal glacier is serious (Zwally et al., 2002). This will be a concern in terms of the world sea level rise (IPCC, 2013). Moreover, the snow cover area or duration of the snow season is decreasing (Robinson et al., 1993). In such ways, snow and ice have been showing great changes, and thus great impacts on atmospheric circulation and terrestrial biology are foreseen. Changes in terrestrial biological activity will alter the amount of atmospheric carbon dioxide absorption by vegetation, and will affect global warming as feedback (IPCC, 2013). Although it is far away from Japan, we cannot turn a blind eye to Arctic climate change, since we are affected by it, too (e.g., Honda et al., 2009).

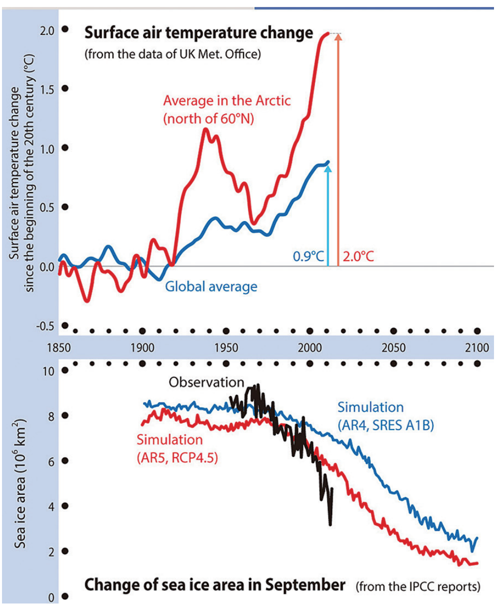

Fig. 1. 1 (top) Surface air temperature change (by T. Nozawa from the data of UK Met. Office). The mean surface air temperature in the Arctic has clearly increased twice as rapidly as that of the global mean, both in the last 100 years and in the last 40 years. (bottom) Change of sea ice area in September (from IPCC reports; Stroeve et al., 2012). The Arctic sea ice area in September has decreased faster than what has been simulated by climate models. Moreover, the decrease is projected to continue through the 21st century.

In order to grasp these abrupt changes in the Arctic, to understand the mechanism, and to contribute to future climate change projection, we conducted the Green Network of Excellence Program (GRENE) Arctic Climate Change Research Project "Rapid Change of the Arctic Climate System and its Global Influences" for five years between 2011 and 2016 (Fig. 1.2). 39 institutions from all over Japan participated in the project, and more than 360 Japanese scientists tackled all aspects of the Arctic climate system. Comprehensive Arctic research incorporating multidisciplinary work and collaborations between observation and modeling had been realized.

Here we will report the scientific results achieved. In the project, four strategic research targets were presented and the outcomes for each target are described on the following pages. Finally, the mutual relationships between each target and synthesis of "Rapid Change of the Arctic Climate System and its Global Influences" are shown in the flow diagram.

Historical back ground

We have a long history of Arctic research in Japan. The first scientific activity in the Arctic was made by Professor Nakaya of Hokkaido University famous for his studies on ice crystals in the falling snow, who visited Greenland Site 2 to study glacier ice crystal under the support of US expedition conducted in IGY 1957 (Higashi, 1962). Then he continued to join the Arctic, at T-3 observatory drifting in the Beaufort Sea, from 1959 to 1961, to conduct ice and oceanographic observation. He sent three young scientists from Hokkaido University to cover wintering observations at T-3.

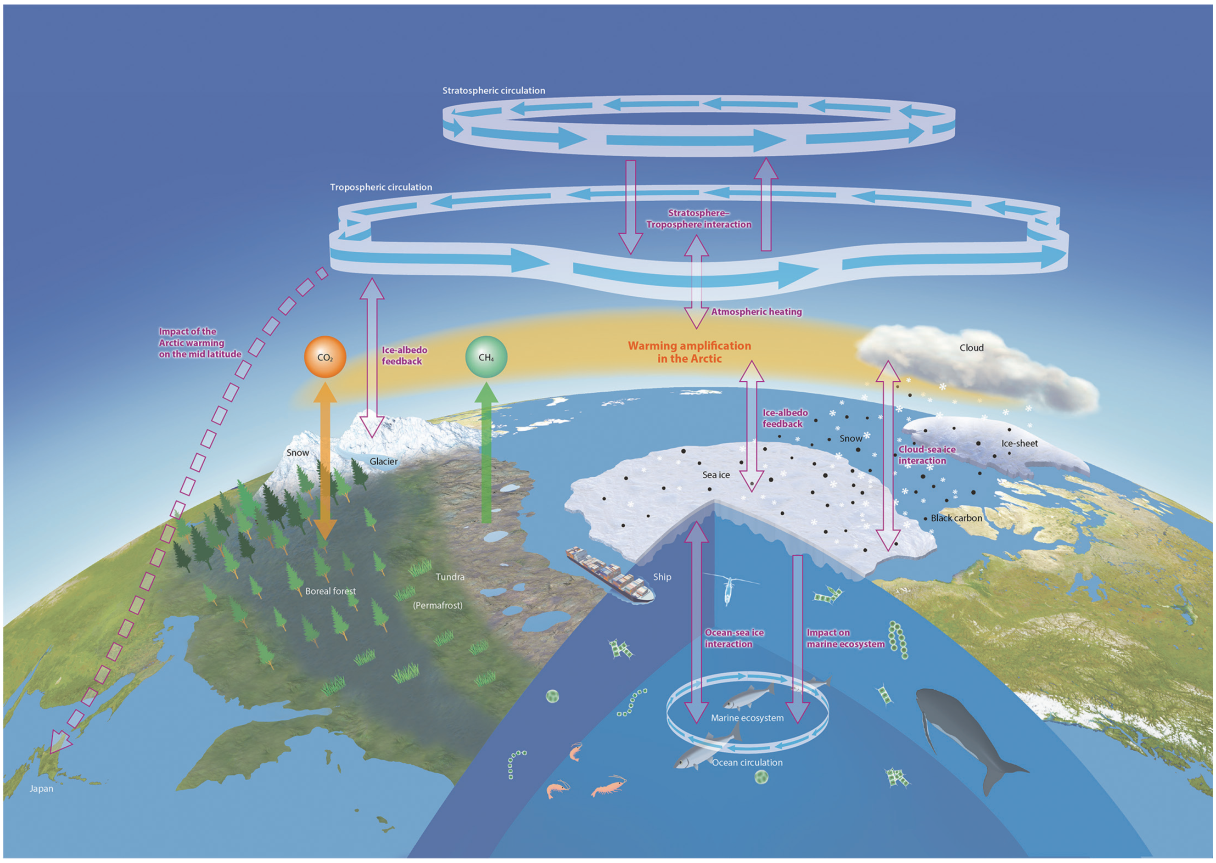

Fig. 1. 2 Schematic diagram of climate systems dealt in the GRENE Arctic Climate Change Research Project.

Before these activities by Nakaya, there was a pioneering expedition to the Arctic Ocean made by Captain Eiichi Taketomi, not well known to the public yet, who was a captain at Bureau of Fisheries, Ministry of Agriculture and Commerce. He passed through the Bearing strait, sailed into the Arctic Ocean to 66° 30' N first in 1923 by "Hakuho-maru" and then sailed up to the northern most of 71° N, 176° W and to the west end at 70° N, 164° W near the mouth of Kolima river in the eastern Siberia by the cruise with "Kaiho-maru", a kind of ice strengthen ship about 1000 ton, in 1937. Finally, he started on the trans world cruise in June 1941, planned to pass through the Arctic sea route, reach Germany, then head south to the Antarctic and back to Japan; however, unfortunately due to the start of World War II (attack/ intrusion of German troupe to the Soviet Union), the expedition was canceled on the way to the Bearing strait (Takahashi and Naganobu, 2016).

Since the Nakaya's expeditions, several small activities were continued by Japanese scientists during 1960s, 70s and 80s, before the Arctic research became so active even in Japan, following the termination of cold-war at the end of 1980s. In 1990s, National Institute of Polar Research (NIPR) established "Arctic Environment Research Center" and started research activities at Ny-Ålesund, Svalbard. Japan Agency for Marine Science and Technology (JAMSTEC) also started the marine observations in the Arctic Ocean in 1992. Including these two institutions, Arctic research activities became active by the Japanese scientists from many universities and institutes; however, their activities were rather small in the scale and limited to the single discipline, not so well known to the international communities. Noticing these situations, efforts were carried out to joint those Japanese diverse activities in the Arctic to concentrate in collaborated project. Finally, a new initiative of all-Japan activities have been started as a "GRENE Arctic Climate Change Research Project", drawn in detail from the next chapters.

References

Higashi, A., 1962. Obituary: Ukichiro Nakaya, 1900–1962. J. Glaciol., 4 (33), 378–380, https://doi.org/10.3189/S0022143000027763.

Honda, M., Inoue, J., Yamane, S., 2009. Influence of low Arctic sea-ice minima on anomalously cold Eurasian winters. Geophys. Res. Lett., 36, L08707, doi: 10.1029/2008GL0307079.

IPCC, 2013: Climate Change 2013: The Physical Science Basis. Contribution of Working Group I to the Fifth Assessment Report of the IPCC [Stocker, T.F., D. Qin, G.-K. Plattner, M. Tignor, S.K. Allen, J. Boschung, A. Nauels, Y. Xia, V. Bex and P.M. Midgley (eds.)]. Cambridge Univ. Press, Cambridge, United Kingdom and New York, NY, USA, 1535p. doi:10.1017/CBO9781107415324.

Robinson, D. A., Dewey, K. F., Heim Jr., R. R., 1993. Global snow cover monitoring: an update. Bull. Am. Meteorol. Soc. 74, 1689–1696.

Serreze, M., Barry, R. G., 2011. Processes and impacts of Arctic amplification: A research sysnthesis. Global and Planetary Change, 77, 85–96, doi.org/10.1016/j.gloplacha.2011.03.004.

Stroeve, J., Holland, M. M., Meier, W., Scambos, T., Serreze, M. C., 2007. Arctic sea ice decline: faster than forecast. Geophys. Res. Lett. 34, L09501. doi:10.1029/2007GL029703.

Stroeve, J. C., Kattsov, V., Barrett, A., Serreze, M., Pavlova, T., Holland, M., Meier, W. N., 2012. Trends in Arctic sea ice extent from CMIP5, CMIP3 and observations *Geophys. Res. Lett.* 39 L16502, doi:10.1029/2012GL052676.

Takahashi, S., Naganobu, M., 2016. Uncompleted voyage across the Arctic Ocean –Challenge of Arctic Ocearn crossing by Kaihou-maru in 1941–. Proceedings, The 31st International Symposium on Okhotsk Sea & Sea Ice, February 2016, Mombetsu, Hokkaido, Japan, S-2.

Zwally, H. J., Abdalati, W., Herring, T., Larson, K., Saba, J., Steffen, K., 2002. Surface melt-induced acceleration of Greenland icesheet flow. Science, 297(5579), 218–222, doi: 10.1126/science.1072708.

2. Development and practice of the project

Composition of the project

A new Arctic research project was assigned by Ministry of Education, Culture, Sports, Science and Technology, Japan (MEXT) in June 2011 under the Green Network of Excellence Program (GRENE) to NIPR to conduct cooperative research on Arctic climate change as a core institution among universities and research institutes. **4 Strategic Research Targets** were presented as follows:

1) Understanding the mechanism of warming amplification in the Arctic,
2) Understanding the Arctic system for global climate and future change,
3) Evaluation of the impacts of Arctic change on weather and climate in Japan and on marine ecosystem and fisheries,
4) Projection of sea ice distribution and Arctic sea routes,

under the Terms of Reference: to a) conduct cooperative research projects (themes) with applications, b) improve infrastructures and c) support research community such as Japan Consortium for Arctic Environmental Research (JCAR) and that cooperation among different research fields and especially cooperation between observation and modeling were desired.

NIPR started the GRENE Arctic Climate Change Research Project with the title, "Rapid Change of the Arctic Climate System and its Global Influences" (Project Manager: Takashi YAMANOUCHI, NIPR; Deputy Project Manager: Masao FUKASAWA, JAMSTEC), and issued Research Announcements to research community. Among 22 applications, **7 Research Themes** were selected as follows:

1) Improvement of coupled general circulation models based on validations of Arctic climate reproducibility and on mechanism analysis of Arctic climate change and variability (PI: Toru NOZAWA, National Institute for Environmental Studies (NIES) and now Okayama University).
2) Change in the terrestrial ecosystems of the pan-Arctic and effects on climate (PI: Atsuko SUGIMOTO, Hokkaido University),
3) Atmospheric studies on Arctic change and its global impacts (PI: Jinro UKITA, Niigata University),
4) The role of Arctic cryosphere in global change (PI: Hiroyuki ENOMOTO, NIPR),
5) Studies on greenhouse gas cycle in the Arctic and their response to climate change (PI: Shuji AOKI, Tohoku University),
6) Ecosystem studies on the Arctic Ocean declining sea ice (PI: Takashi KIKUCHI, JAMSTEC),
7) Projection of sea ice distribution and Arctic sea routes (PI: Koji SHIMADA, Tokyo University of Marine Science and Technology; Sub PIs: HASUMI and Hajime YAMAGUCHI, University of Tokyo),

and 5 year project had been started for FY2011~2015. 39 institutions from all over Japan participated in the project, and more than 360 Japanese scientists tackled all aspects of the Arctic climate system. Comprehensive Arctic research incorporating multidisciplinary work and collaborations between observation and modeling had been realized. Since the top-down strategic targets were answered by the research themes in bottom-up manner, it became a unique and idealized construction as a research project.

General view of the project organization was as shown in Fig. 2.1 NIPR worked as a "core institute" under the Project Manager and operated a Project Steering Committee composed of senior research scientists most from universities and institutes outside of NIPR (members are on Table 2.1), which worked to make a selection of Research Themes, discuss and approve total and annual research plans and budgets, made an advice for the road mapping to the research targets and controlled the progress. In order to promote collaborations among Research Themes, the Coordinator was assigned (Kumiko Takata, NIES). JAMSTEC was an "associated institute" in

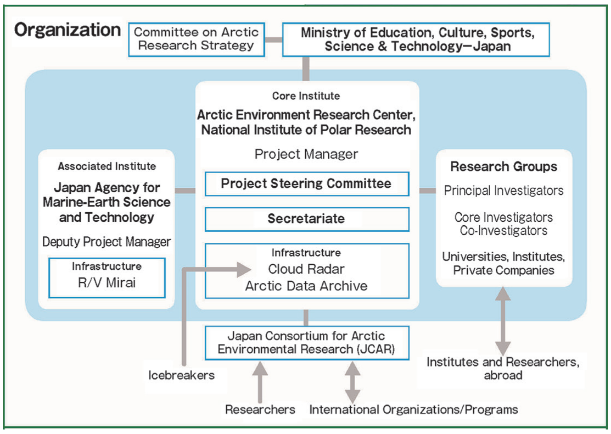

Fig. 2. 1 Project organization.

Table 2. 1 Members of Project Steering Committee

Role	Name	Affiliation	Title	Term
	Tamotsu Igarashi	RESTEC	Senior Researcher	
	Motoyoshi Ikeda	Hokkaido University	Professor Emeritus	
	Kou Izumiyama	North Japan Port Consultants (Co., Ltd.)	Senior Researcher	
	Gen Inoue	Nagoya University, STEL	Visiting Professor	
	Keiji Imaoka	Yamaguchi University	Associate Professor	Since July 2012
	Hiroshi Kanzawa	Nagoya University, Graduate School of Environment	Professor	
	Hiroshi Kanda	NIPR	Professor Emeritus	Till March 2013
	Akio Kitoh	University of Tsukuba	Senior Reseacher	
	Shuhei Takahashi	Okhotsuk Sea Ice Science Museum of Hokkaido	Director	
	Takuji Nakamura	NIPR	Diputy Direccter	
	Hisashi Nakamura	The University of Tokyo, ASTRC	Professor	
	Mitsuo Fukuchi	Hokkaido University, Tokyo Office	Director	
Acting Chair	Yoshiyuki Fujii	NIPR	Professor Emeritus	From Oct. 2011
Deputy PM	Masao Fukasawa	JAMSTEC	Executive	
	Yasushi Fujiyoshi	Hokkaido University	Professor Emeritus	
	Takehiro Masuzawa	Shizuoka University	Professor Emeritus	Since April 2013
Vice Chair	Tetsuzo Yasunari	Nagoya University, HyARC	Professor Emeritus	Till March 2013
Chair PM	Takashi Yamanouchi	NIPR	Diputy Director/ Professor Emeritus	
	Tomoaki Wada	Bando Kobe Youth Science Museum	Director	

charge of operating R/V "Mirai" as one of the infrastructures under the Deputy Project Manager. NIPR supplied other infrastructures such as cloud radar, foreign ice breakers and Arctic Data archive System (ADS), and supported JCAR through the activities of executive secretary.

Equipment and infrastructures

In order to investigate cloud 3-D profile (particle size, ice/ water content, vertical speed) following the requirements of the project, cloud radar was installed at Ny-Ålesund, Svalbard in September 2013. The radar "FALCON-A" was 95 GHz FM-CW (Frequency Modulated Continuous Wave) cloud profiling Doppler radar with 2 antennas (specifications shown in Table 2.2 and photo in Fig. 2.2), developed by Chiba University, following the prototype of FALCON-I developed 10 years ago (Takano et al., 2010). The research observatory "Rabben" in Ny-Ålesund, Svalbard, was established by NIPR in 1991 under the cooperation with Norwegian Polar Institute (Yamanouchi et al., 1996), and maintained since then and also supplied for the usage in this project; long term observations of atmospheric science and field observation of terrestrial ecosystems have been conducted.

The Arctic cruise of R/V Mirai in 2012 was operated as one of the major infrastructures of the project. Other cruises were also conducted during the project in 2013, 14 and 15 to the open water area of the Arctic Ocean. Though Mirai was already deployed, she was not an ice-

Table 2. 2 Specifications of cloud radar, FALCON-A

Radar Specifications	
Center frequency	94.84 GHz
Antenna power	~1 W
Observation height	Up to 15 km (nominal)
Range resolution	48 m (10 m minim.)
Beam width	0.2 ° (15 m at 5 km)
Doppler width	±3.2 m/s (nominal)
Time interval	10 sec (nominal)

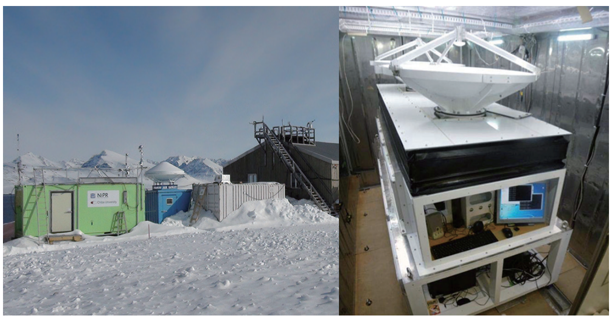

Fig. 2. 2 Cloud radar, FALCON-A, at NIPR station in Ny-Alesund, Svalbard. Radar is settled inside the container (left green color, right two antennas and electronics; photo by T. Takano).

breaker, and could not go into sea ice area. Several cruises of foreign icebreakers, Louis S. St-Laurent, Amundsen and Sir Wilfrid Laurier of Canadian Coast

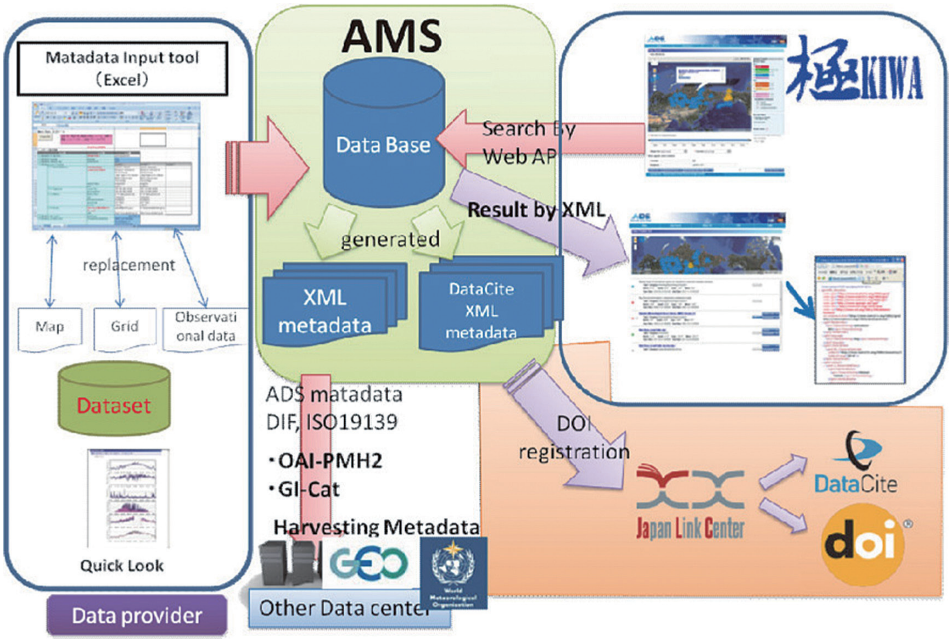

Fig. 2. 3 ADS system configuration

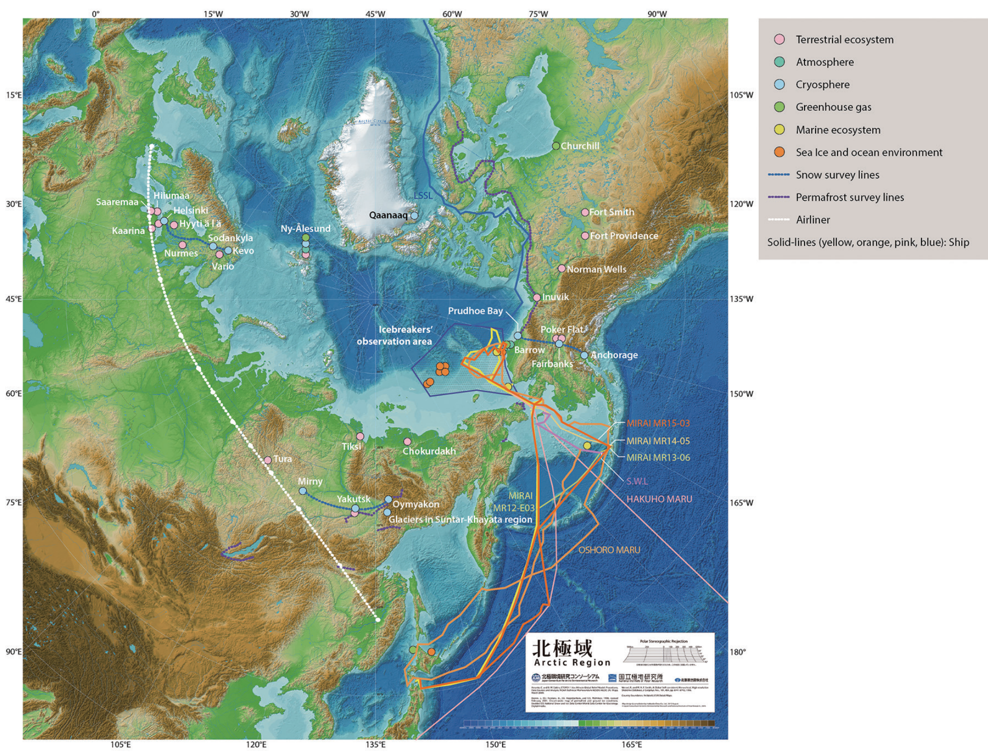

Fig. 2. 4 Map of GRENE-Arctic observation activities.

Guard, were prepared partly for the use of this project. Without cost, Korean icebreaker, Araon, was also used under collaboration and training vessel "Oshoro-maru" of School of Fisheries, Hokkaido University was also used with collaboration. Several mooring buoys were deployed for general use of the project.

The third item was Arctic Data archive System (ADS) which intended to collect, manage (control) and open those data obtained through observations and model simulations in the project. ADS was composed of three parts, 1) ADS Metadata registration System (AMS) and Key service for Inter Working Arctic data (KIWA) which was a research data registration system and Metadata search service (Fig. 2.3), 2) online visualization application (VISION) for climate, satellite and simulation data, and 3) Visualization service to view satellite data (VISH-

OP) for semi-real-time polar environment observation, monitoring and sea ice prediction. Also, the ADS joined the project to invest *doi* numbers to dataset to encourage data registration.

Deployment of Pan Arctic observations

Pan Arctic observations had been performed within GRENE Arctic Project at Ny-Ålesund, Svalbard, Skandinavia, Russian Siberia, Alaska, U. S. A., Northern Canada, Greenland and Arctic Ocean (Fig. 2.4). At Ny-Ålesund, cloud profiling radar was installed since September 2013, and long time continuous observation with several intense observations was made.

Promoting international cooperation and capacity building

In order to promote international cooperation and capacity building which are indispensable to the Arctic climate research, the project provided supports for young scientists to visit institutions in the Arctic countries, and made feasible to join the international cooperative projects. This issue was conducted in FY2014, following the comments from review committee. Public call was made and among 16 applications, 12 were accepted with 8 to visit University of Alaska, Fairbanks, U. S. A., and 4 to visit universities in Canada, which belong to ArticNet. For this activity, NIPR-Office was settled in International Arctic Research Center, University Alaska, Fairbanks and accommodation was also kept in the city of Fairbanks.

In order to contribute to the activities of Arctic Committee (AC), expert scientists were dispatched to those meetings, such as AC Working Group CAFF (Conservation of Arctic Flora and Fauna) or its Arctic Biodiversity Congress, AMAP (Arctic Monitoring and Assessment Program) and Arctic Circle.

References:

Takano, T., Yamaguchi, J., Abe, H., Futaba, K., Yokote, S., Kawamura, Y., Takamura, T., Kumagai, H., Ohno, Y., Nakanishi, Y., Nakajima, T., 2010. Development and performance of the millimeter-wave cloud profiling radar at 95 GHz: sensitivity and spatial resolution. Electron. Commun. Jpn,93 (3), 257–262.

Yamanouchi, T., Aoki, S., Morimoto, S., Wada, M., 1996. Report on atmospheric science observations at Ny-Ålesund, Svalbard. Mem. Natl Inst. Polar Res., Spec. Issue, 51, 153–163.

3. Arctic warming amplification (AA)

As for the strategic target 1, Modeling Theme, Terrestrial Theme, Atmosphere Theme, Glaciology Theme and Greenhouse Gas Theme joined together to work on the aim of "understanding the mechanism of warming amplification in the Arctic". It is already clear that the Arctic is sensitive to the climate change and global warming is greatly amplified in the Arctic. However, since at high latitudes, global solar radiation has a large seasonal variation, and it is necessary to consider the seasonal variation of the climate processes such as ice-albedo feedback and so on. Also, many processes are interrelated complicatedly, it is needed to analyze not only ice-albedo feedback but also each of number of processes overall. First of all, Fig. 3.1 shows vertical distribution of linear trends of temperature change in recent 33 years (1979–2013) from ERA-interim reanalysis data. Except for the large amount in the winter stratosphere, most warming appears in the lower troposphere in the Arctic and contribution of sea ice decline is pointed out (Serreze et al., 2009; Screen and Simmonds, 2010). However, warming in the summer Arctic seems to be limited.

3. 1. Arctic warming processes and its seasonality in climate models

Although single process of AA had been discussed in many studies made before, systematic evaluation of the relative importance of each process, interaction of processes and seasonality of each process were not commonly made. Here, quantifying the relative importance of individual effects was made as one of the essential steps toward an understanding of the underlying mechanisms (Yoshimori et al., 2014a, b). Feedbacks were quantified in two different versions of an atmosphere-ocean GCM under idealized transient experiments based on an energy balance analysis that extends from the surface to the top of the atmosphere. To conduct this analysis, a "feedback-response analysis method" (CFRAM; Lu and Cai, 2009) was applied not only to annual mean but also to different seasons. The GCM used in the study were the Model for Interdisciplinary Research on Climate version 4, medium resolution and version 5 (MIROC4m and MIROC5). Fig. 3.1.1 shows the underlying processes considered in the paper (Yoshimori et al., 2014a, b).

Yoshimori (2014), following Yoshimori et al. (2014a), showed seasonality of individual processes of AA in Fig.

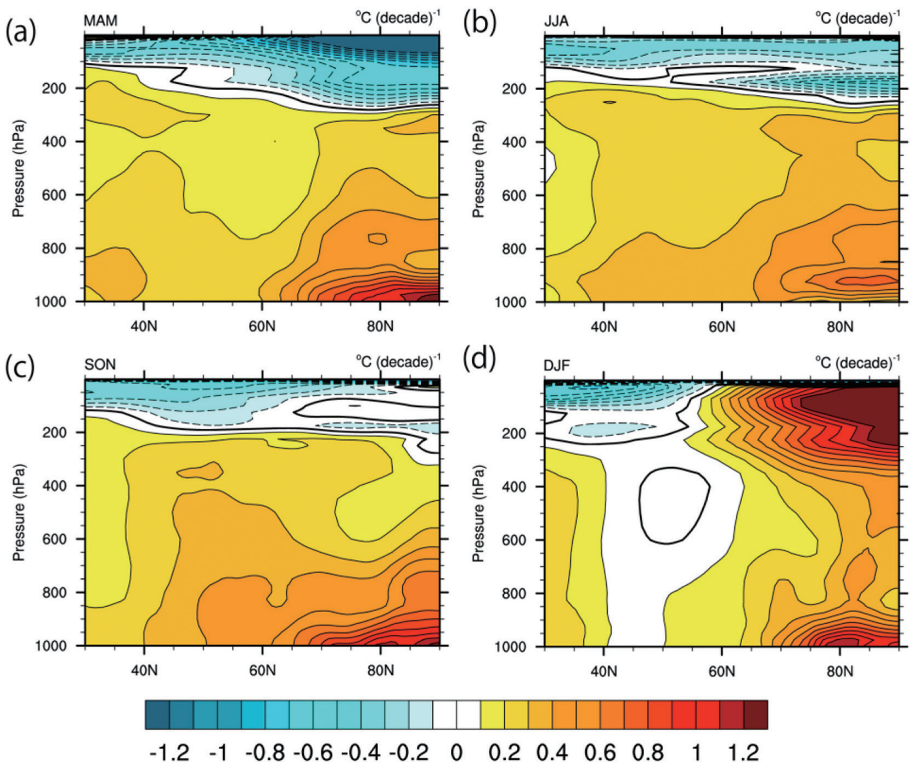

Fig. 3. 1 Vertical distribution of linear trends of temperature change in recent 33 years (1979–2013) from ERA-interim reanalysis data (Yoshimori, 2014).

3.1.2. These are the results of experiments for two conditions, preindustrial control and an 1% annually increasing CO_2 experiment (twice the level of initial concentration reached at 70 years and the 20 year average from years 61 to 80 was used for the analysis). AA is referred to an enhanced warming of the Arctic compared to the rest of the world, and the contributing processes to the AA are quantified by an Arctic amplification index (*AAI*) defined as

$$AAI_j = \left(\Delta T_j^{70N-90N} - \Delta T_j^{90S-90N}\right) / \Delta T_{SIM}^{90S-90N} \tag{3.1}$$

where ΔT_j denotes the partial temperature change induced by the jth feedback process and ΔT_{SIM} is simulated total temperature change. The superscripts denote the domain of the average. A positive *AAI* represents the process that maintains anomalous temperature contrast between the Arctic and the rest of the globe. Increase in surface temperature then AA over the Arctic is the smallest in summer but the largest in winter. Over the Arctic Ocean in summer, ice-albedo feedback due to sea ice retreat, over the Arctic land area, ice-albedo feedback due to snow melting (retreat), respectively, has the largest tendency to warm the surface; however, the surface warming is smallest because of the large heat uptake by the open ocean. In autumn and winter, the heat stored in the Arctic Ocean in summer is released into the atmosphere. Also, cloud feedback enhance the warming in autumn to winter. Moreover, there are a number of other factors that contribute to warming the surface: strong vertical stability in the atmosphere traps warming close to the surface; increased low-level clouds enhance the greenhouse effect by trapping more longwave radiation; surface warming sensitivity is larger in colder regions than in warmer regions due to the effect (non linearity) of the Stefan-Boltzmann law; and so on. As a consequence, the largest AA occurs in winter.

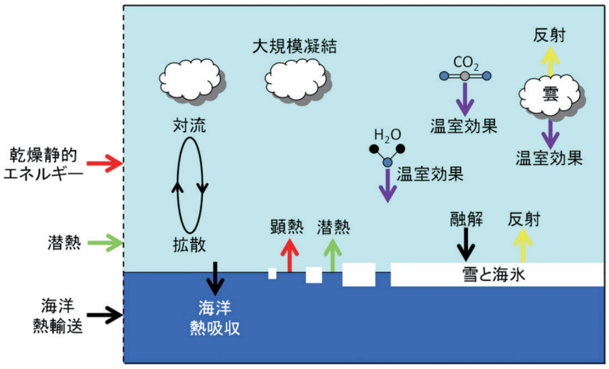

Fig. 3. 1. 1 Physical processes contribute to AA which were quantified in Yoshimori et al. (2014a, b) (Yoshimori, 2014).

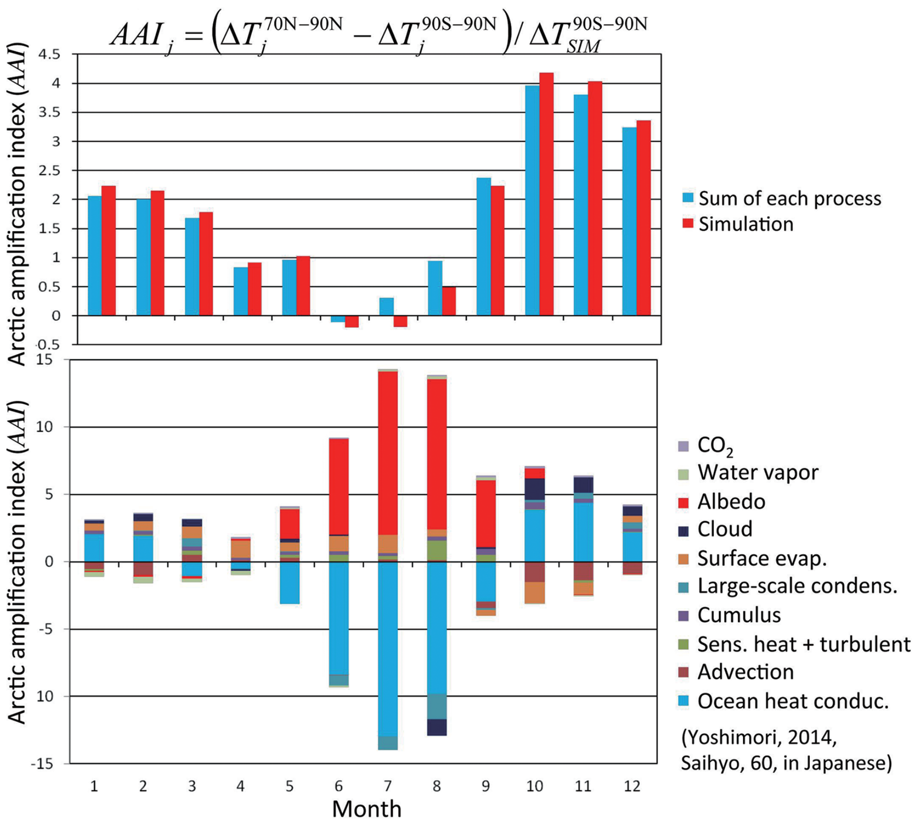

Fig. 3. 1. 2 Seasonality of Arctic amplification (Yoshimori, 2014) made from Yoshimori et al. (2014a). a) AA based on total of individual processes and simulations. b) Contributions of each process on AA.

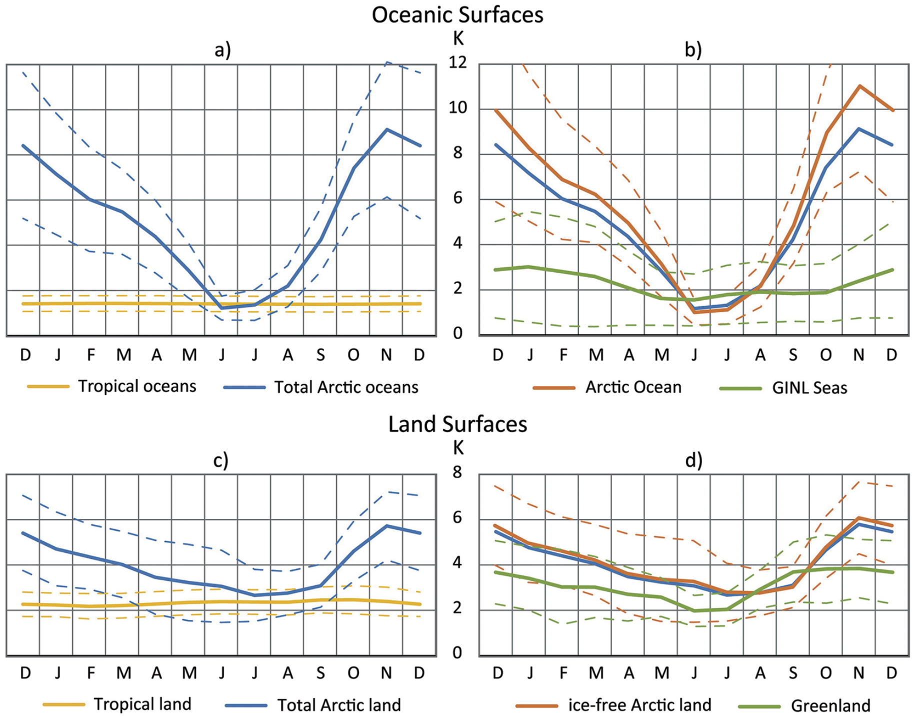

Fig. 3. 1. 3 Surface temperature changes averaged (a) over Arctic and tropical oceans, (b) over the GINL Seas and the Arctic Ocean, (c) over Arctic and tropical land areas, and (d) over Greenland and the ice-free Arctic land. Solid lines represent the ensemble-mean values; dashed lines indicate the mean dispersion among models (plus or minus one std deviation around ensemble mean) (Laine et al., 2016).

For the similar objective, Laine et al. (2016) conducted a multi model analysis. The roles of different factors contribution to local surface warming are quantified using the “radiative kernel method" applied at the surfacc after 100 years of global warming under a representative concentration pathway 4.5 (RCP4.5) scenario simulated by 32 climate models from phase 5 of the Coupled Model Intercomparison Project (CMIP5). The warming factors and their seasonality for land and oceanic surfaces were investigated separately and for different domains within each other surface type where mechanisms differ. AA is defined as the ratio of temperature changes in the Arctic (latitudes greater than 60°N) relative to the tropics (between 30°S and 30°N). The overall oceanic domain north of 60°N is called the Arctic oceans in this study, and it is further separated into the Greenland-Islandic-Norwegian-Labrador (GINL) Seas and the Arctic Ocean. Also, the land surface north of 60°N (domain referred to as Arctic land) is separated into Greenland and the rest of the domain, ice-free Arctic land. These separations of the Arctic ocean and land area were performed because mechanisms were found to be very different in these separate regions.

Fig. 3.1.3 shows seasonality, both over Arctic land and oceans, the mean warming is the largest during boreal winter, with a peak in November, and minimum during summer. In terms of amplitude, the seasonal cycle of surface warming is larger over oceanic surfaces than over land surfaces in the Arctic region. Over the oceans, the total Arctic mean warming (blue line) is mostly influensd by the Arctic Ocean (orange line) compared to the GINL Seas (green line) where seasonal variability is much smaller, as the former domain is more than 3 times larger in area than the latter. Over land, the total Arctic mean (blue line) is mostly determined by the ice-free Arctic land (orange line) compared to Greenland (green line) where seasonality is also smaller, as the former area is about 6 times larger than the latter.

Fig. 3.1.4a shows the decomposition of surface temperature changes over the Arctic Ocean for the different months of year. The sum of positive contributions is the largest during winter month with a peak in November, whereas the sum of negative contributions is the largest in summer, explaining most of the seasonality of surface temperature changes (black line). Most factors exhibit a clear seasonal cycle, the largest, seasonal amplitudes being related to the albedo and other surface effects. The positive albedo effect is the largest in summer, with a peak of +5°C in July, linked with a large retreat of the mean sea ice cover and a large solar irradiance, whereas

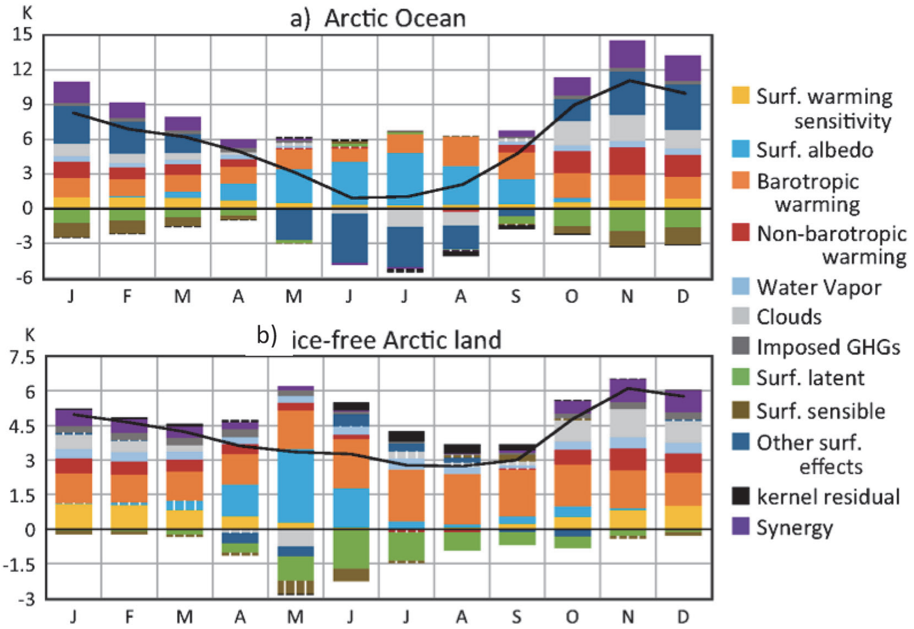

Fig. 3. 1. 4 Contributions (colored bars) to surface temperature changes (black line) for Arctic Ocean (a) and for ice-free Arctic land (b) (Laine et al., 2016).

it has no effect in winter when solar irradiance is weak or nonexistent. Other surface effects have a strong negative contribution in summer, partly balancing, the albedo feedback, and as strong positive effect in winter. The different terms of the decomposition suggest that the main contributor to overall energy absorption in summer is associated with the larger warming of the mixed layer, and to a lesser extent with a larger melting of sea ice in early summer and larger vertical mixing in late summer. The excess release of heat in winter seems mostly associated with an enhanced cooling of the mixed layer and, to a lesser extent, with a larger sea ice formation balanced by increased vertical heat mixing as winter progresses.

Cloud feedback has the warming effect up to +2.5°C in winter and a cooling effect in summer. It is consistent with an increased mean cloud cover over the Arctic Ocean in the models, leading to both increased greenhouse and parasol effects, favoring backward LW radiation in winter but decreasing incoming SW radiation in summer. Other changes in cloud properties (e.g., the amount of phase of condensates or the mean altitude or depth of clouds) may also play a role in the total cloud feedback.

Contribution to surface temperature changes over the ice-free Arctic land are shown in Fig. 3.1.4b. Contribution factor amplitudes are smaller than over oceans in the Arctic region. The seasonality of factors is more complex than over the Arctic Ocean, with different contributions peaking at different times of the year. The albedo feedback peaks in spring over the ice-free Arctic land, similar to over the GINL Seas, but differently from over the Arctic Ocean where it peaks in summer. The feedback is due to a large snow cover retreat in spring than in summer, since snow is fully melted at mid summer. We can therefore consider that this difference in the timing of the albedo feedback between the Arctic Ocean and the ice-free Arctic land can be indirectly attributed to a difference in their mean latitude. A large snow cover difference is also found in fall as snow starts to accumulate later in late twenty-first-century runs, but solar irradiance is weaker than in spring and only results in a small secondary peak in albedo feedback.

The timing of the cloud feedback is also partly different from over the Arctic Ocean, with the weak or negative contributions occurring in spring rather than in summer. The positive cloud contribution during the cold season, consistent with a larger cloud cover, is similar for both surface types. Cloud property changes other than the cloud cover itself may also play a role in the total cloud feeclback. The latent heat flux effect is very different between the ice-free Arctic land and the Arctic Ocean, with increased evaporation occurring mostly in summer over the former domain and in winter for the latter. Finally, other surface effects have much less impact of the surface warming over land than over oceans.

The largest warming over the ice free Arctic land during the coldest months is attributed to many positive contributions peaking at this time of the year and to weak cooling factors, whereas the minimum found in July-August is associated with weaker warming factors, especially albedo and surface warming sensitivity, nonbarotropic warming, cloud or synergy effects, and a relatively large latent cooling.

Arctic amplification in a multi-decadal time scale

Using a simple energy balance model (EBM), Tanaka and Tamura (2016) discussed the natural variability and linear warming trend due to the increasing radiative forcing of CO_2. Based on the fact that the variation of ice albedo feedback causes the Arctic amplification, a hypothetical experiment was conducted by introducing a multi-decadal variability of the ice albedo feedback in reference to the observed long-term variation of the global mean temperature. The rapid warming during 1970-2000 could be explained by the superposition of the natural variability and the background linear trend. It was shown that the recent AO negative pattern of EOF-1 with the warm Arctic and cold mid-latitude was in good agreement with planetary albedo change, indicating negative anomaly in high latitudes and positive anomaly in mid-latitudes. EOF-2 showed the Arctic amplification pattern, with warming in the Arctic and cooling in Siberia.

3. 2. Heat transport

The role of atmospheric heat transport and regional feedbacks

While the surface albedo feedback is often referred to as the explanation of the enhanced Arctic warming, the importance of the enhanced heat transport from the lower latitudes has also been reported in previous studies (e.g., Graversen and Brutu, 2016). Here, Yoshimori et al. (2017) made an attempt to understand how the regional feedbacks in the Arctic are induced by the change in atmospheric heat transport and vice versa.

The model used in the study is an atmospheric general circulation model (GCM) coupled to a mixed-layer slab ocean model, identical to that used in Yoshimori et al. (2014b), and the atmospheric model component is identical to that of the coupled atmosphere-ocean GCM, MIROC4m, used in Yoshimori et al. (2014a). The ocean model component has a constant depth of 50 m and solves only the thermodynamic equation and does not calculate the circulation. Experiments conducted in the study are illustrated in Fig. 3.2.1, where AS- means the

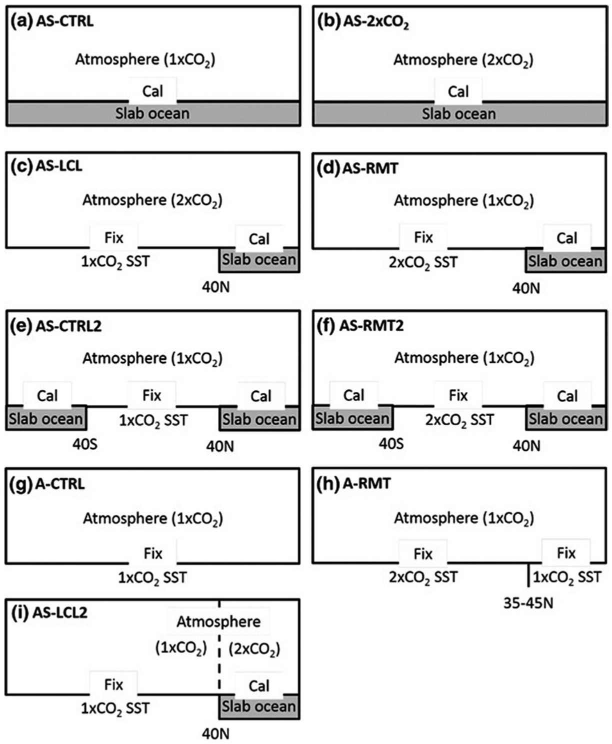

Fig. 3. 2. 1 Illustration of the experiments. “Fix” and “Cal” stand for fixed and calculated lower boundary conditions of the atmosphere (i.e., SST and sea ice conditions), respectively (Yoshimori et al., 2017).

atmospheric-slab ocean model and A- means simply an atmospheric model without slab ocean model. Two experiments, AS-CNTL2 and AS-RTM2 (Fig. 3.2.1e, f), are conducted to investigate the reason for the asymmetric polar warming of Northern and Southern hemisphere. Experiments are integrated for 60 years, and the last 30 years are used for the analysis except for Fig. 3.2.1e and f; while A- experiments are integrated for 40 years, and the last 30 years are used for the analysis. In order to decompose the simulated temperature change to contributions of individual processes, climate feedback-response analysis method (CFRAM) is used (Lu and Cai, 2009; Yoshimori et al., 2014a, b). The CFRAM solves the energy with SW and LW denoting shortwave and longwave radiation, respectively.

Fig. 3.2.2 shows the zonal and annual mean atmospheric temperature change from the control simulation. In the CO_2 doubling experiment with the global slab ocean model, well-known features of enhanced warming near the Arctic surface and tropical upper atmosphere are simulated (Fig. 3.2.2a). The warming is also enhanced near surface at the Southern Hemisphere (SH) high latitudes, though, to a lesser degree compared to the NH counterpart. The NH mid-high latitudes show, on the other hand, a limited warming in response to the CO_2

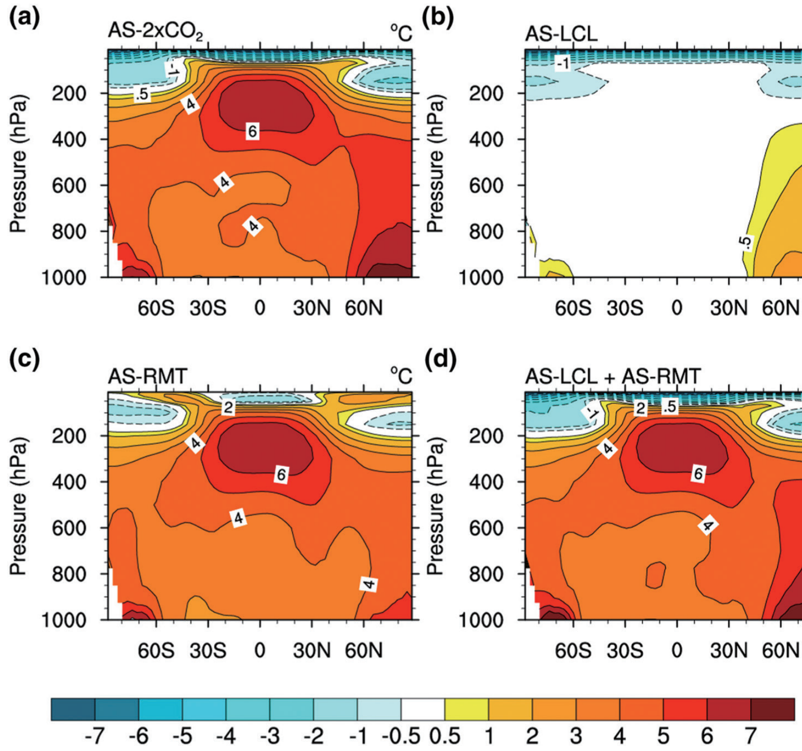

Fig. 3. 2. 2 Zonal and annual mean air temperature changes in the atmosphere from the control experiments (°C): a) AS-2xCO_2; b) AS-LCL; c) AS-RMT; d) the sum of the changes in AS-LCL and AS-RMT (Yoshimori et al., 2017).

forcing when the sea surface in other latitudes are fixed at 1xCO_2 conditions (Fig. 3.2.2b). Much of the full response seen in the global slab ocean model experiment (Fig. 3.2.2a) is captured by the experiment forced by the remote surface warming (Fig. 3.2.2c). The addition of warming in the two experiments isolating the remote and local effect (Fig. 3.2.2b, c) reproduces the full response reasonably well although small differences are discernible (Fig. 3.2.2a, d). This linearity suggests that the comparison of the two sensitivity experiments (AS-LCL and AS-RMT) is meaningful in the context of sensitivity measurement of local and remote influence.

All experiments exhibit least warming in summer (June-July-August). The maximum warming occurs in November except for the experiment with sea ice surface conditions fixed at the NH mid-high latitudes (A-RMT), where the warming occurs unsurprisingly by a similar magnitude throughout the year.

Fig. 3.2.3 shows the partial surface temperature change with respect to the control simulation averaged over the Arctic region for individual months diagnosed using the CFRAM technique. Only albedo feedback (ALB) and surface heat uptake (RESS) terms are explicitly displayed here with the rest term, the “Others”. The simulated change (SIM) is well reproduced by the sum of all terms diagnosed by the CFRAM technique (SUM). In AS-2xCO_2, AS-LCL and AS-RMT, the albedo feedback which tends to warm the surface in summer is nearly cancelled by the surface heat uptake that represents the energy consumed for the ocean warming and sea ice melting. The seasonal evolution of the Arctic surface warming is characterized by the absorption of heat anomaly in summer and its release in winter, consistent with previous studies (Yoshimori et al., 2014a, b; Fig. xx above). There are other terms that significantly contribute to winter warming in the AS-RMT, however.

“Other” terms in Fig. 3.2.3 is presented individually in Fig. 3.2.4 for A-RMT and AS-RMT. A-RMT reveals how the atmospheric dynamics induced by the remote surface warming tends to warm the Arctic surface while the difference of the two experiments reveals how the NH mid-high latitude surface response feeds back to the Arctic surface warming. Fig. 3.2.4a shows that the increased poleward transport of DSE (DYN) and LH (LSC) warms the Arctic atmosphere which in turn tends to warm the surface. In addition, the increased water vapor transport tends to warm the Arctic surface through greenhouse effect of water vapor (WVP) and clouds (CLDL). The moisture source of increased water vapor and clouds most likely originates from remote regions and is transported horizontally via the atmosphere. The fractional contribution of water vapor, clouds and large-scale con-

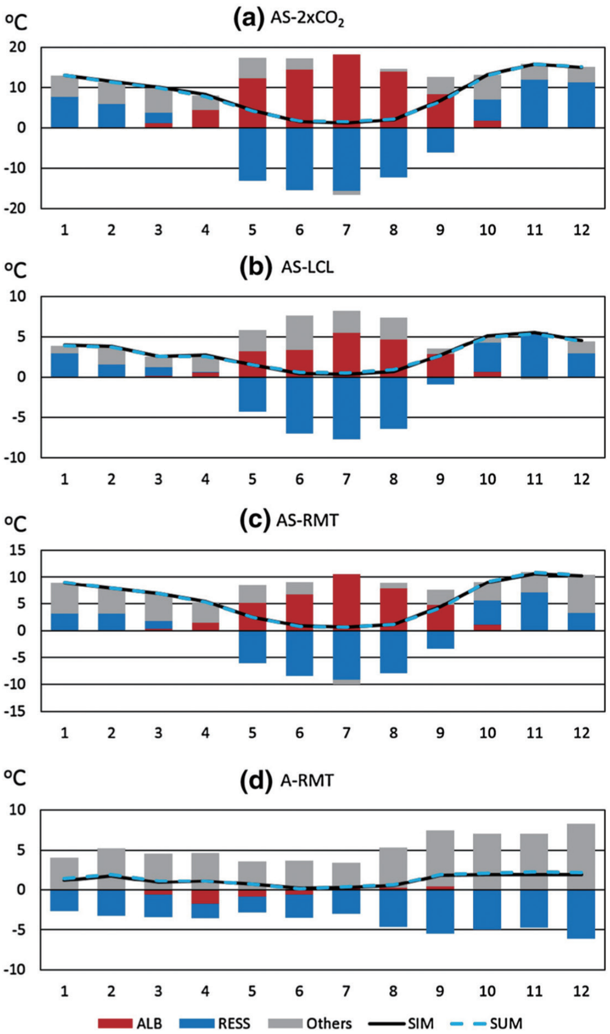

Fig. 3. 2. 3 Monthly partial surface temperature changes with respect to the control experiments diagnoses using the CFRAM technique (°C): a) AS-2xCO$_2$; b) AS-LCL; c) AS-RMT; and d) A-RMT. *ALB* albedo feedback, *RESS* snow-ice melting and ocean heat uptake, *OTHERS* other terms, *SUM* sum of all terms of the partial temperature change (*SUM=ALB+RESS+OTHERS*), and *SIM* simulated skin temperature change. The partial temperature change in the vertical axis is averaged to the north of 70°N (Yoshimori et al., 2017)

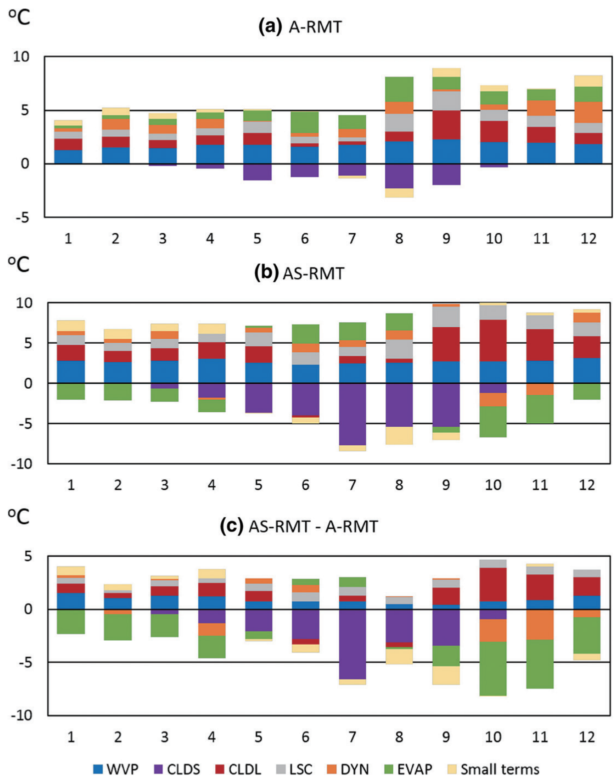

Fig. 3. 2. 4 Monthly partial surface temperature change of selected terms ("Others" in Fig. 3.2.3) with respect to the control experiment diagnosed using the CFRAM technique (°C): a) A-RMT; b) AS-RMT; and c) the difference between AS-RMT and A-RMT. *WVP* water vapor, *CLDS* shortwave cloud, *CLDL* longwave cloud, *LSC* large scale condensation, *DYN* advection and *EVAP* evaporative cooling. The partial temperature change in the vertical axis is averaged to the north of 70°N (Yoshimori et al., 2017)

densation to the total Arctic surface temperature change amounts to about 58% while dynamical heating and evaporative cooling contribute 18 and 17%, respectively, on the October-November-December average. As the increase in the northward atmospheric DSE and LH transport at 70°N are about equal, the LH transport appears to be much more effective in warming the Arctic surface through the greenhouse effect of water vapor and clouds as also found by Graversen and Burtu (2016).

Once the sea surface is allowed to respond, an enhanced greenhouse effect of clouds is further strengthened and contributes positively to the Arctic warming (CLDL in Fig. 3.2.4c). Also the sun-shade effect by

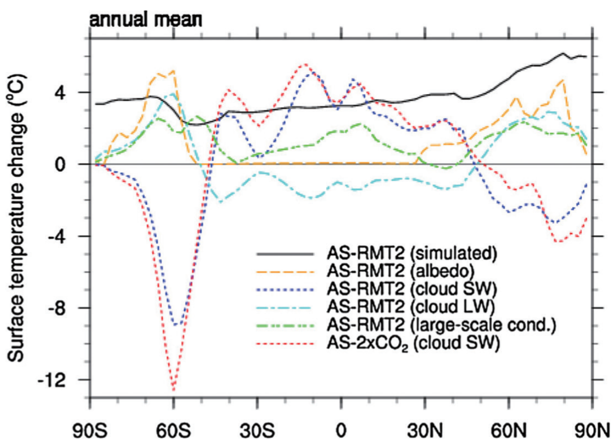

Fig. 3. 2. 5 Zonal and annual mean surface temperature change with respect to the control experiments. The black solid line represents the simulated surface temperature change in AS-RMT2 and other lines represent the partial surface temperature change in AS-RMT2 or AS-2xCO$_2$ diagnosed using the CFRAM technique (°C). SW and LW denote shortwave and longwave components, respectively (Yoshimori et al., 2017).

clouds become substantial in summer (CLDS in Fig. 3.2.4 b, c).

Given the approximate symmetry in the increased atmospheric heat transport to the NH and SH high latitudes in AS-CO_2 and the importance of remote forcing in the Arctic warming, one may wonder why the Southern Oceans does not warm as much as the Arctic Ocean (Fig. 3.2.2a). To seek the answer to this fundamental question, two additional experiments (AS-CTRL2 and AS-RMT2) are conducted. The black solid line in Fig. 3.2.5 represents simulated surface temperature changes and the asymmetric polar warming between AS-RMT2 and AS-CTRL2. While the albedo, large-scale condensation and LW cloud terms contribute to the warming roughly at the same magnitude between the Arctic and Southern Ocean, the SW cloud term exhibits a striking difference between the two regions. The large cooling effect by clouds in the Southern Ocean is explained by an increase in the cloud amount associated with the solid to liquid phase change of cloud condensate and consequent increase in cloud life time under warming, as elaborated by Ogura et al. (2008a, b) and discussed by Yoshimori et al. (2009).

From the observations at Ny-Ålesund, Svalbard, Yamanouchi (2019) explained the warm-moist air intrusion from the lower latitudes to the Arctic in enhancing cloud and water vapor longwave radiation to warm the Arctic. This mechanism was one of the realizations of the process proposed by Yoshimori et al. (2017).

3. 3. Clouds

Cloud feedback related to sea ice

As shown in the previous section, one of the major processes of AA is cloud feedback, which increases greenhouse effect and surface warming in autumn-winter. Abe et al. (2016) investigated the effect of sea ice reduction on the increase of cloud cover and enhancement of AA. Historical simulations using a coupled atmosphere-ocean general circulation model, MIROC5, which was used in the Coupled Model Intercomparison Project Phase 5 (CMIP5) were analyzed. Simulations are performed from 1850 to 2005 using anthropogenic forcing recommended by CMIP5 project, having five ensemble members with different initial conditions.

Results are compared between two periods 1976–1985 and 1991–2005. The decrease in the simulated Arctic sea ice area (SIA) in all months and the maximum reduction in September, consistent with observations (Comiso et al., 2008) and probably due to recent global warming, are found (Fig. 3.3.1a). As for the simulated cloud cover averaged over the Arctic Ocean (Fig. 3.3.1b), low-level cloud cover is at maximum of 50% in summer and continuously decreases during fall and winter, reaching a minimum in April. The simulated seasonal amplitude of the total cloud cover was similar to that of the low-level clouds. The simulated Arctic cloud cover for fall, winter and sprig increased between two periods (1976–1985 and 1996–2005), although the change was not substantial.

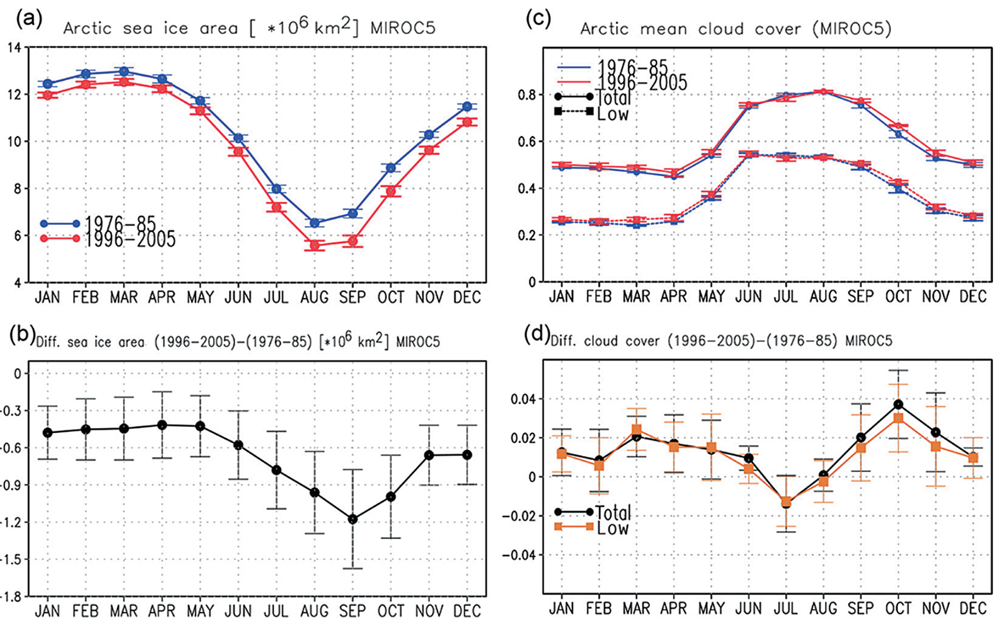

Fig. 3. 3. 1 Seasonal cycle of (a) Arctic mean sea ice area averaged over the periods 1976–1985 and 1996–2005 in MIROC5; (c) identical to (a) except for the total and low cloud covers. The unit of sea ice area is 10^6 km^2 (Abe et al., 2016).

The largest increase in simulated cloud cover in October agrees with previous studies using satellite data and climate model simulations (Liu et al., 2012; Vavrus et al., 2011; Wu and Lee, 2012).

The cloud radiative forcing (CRF) is examined since cloud cover changes could affect the energy balance through the CRF. During the fall, the downward longwave radiation by clouds may play a more important role in the surface energy balance than in the lower latitudes because of the reduced or absent incoming shortwave radiation. An increase in cloud cover in the Arctic Ocean should increase the downward longwave radiation at the surface; a positive change in CRF for the surface downward longwave radiation could occur with the substantial reduction in seaice concentration. In addition, an increase in the downward longwave radiation because of increased water vapor and air temperature is also an important factor contributing to Arctic warming (Rinke et al., 2013).

The change in CRF for the surface downward longwave radiation (ΔCRF_{SDLR}) and clear sky surface downward longwave radiation (ΔCS_{SDLR}) between the periods 1976–1985 and 1996–2005 was examined for the ΔSI- grids with a substantial sea ice reduction (a linear trend in sea ice concentration of less than −0.1 decade^{-1}) and ΔSI+ grids without a substantial sea ice reduction (a linear trend in sea ice concentration exceeding −0.1 decade^{-1}) in each month (Fig. 3.3.2a). Positive ΔCS_{SDLR} was dominant in the ΔSI- case when compared with the ΔSI+ case, particularly during fall, winter and spring. This positive ΔCS_{SDLR} resulted from both warming and moistening due to the increased open ocean and global warming can largely affect the surface energy balance in the grids with substantially reduced sea ice concentration.

ΔCRF_{SDLR} in the ΔSI- case were also large and positive from September to April; the changes in the ΔSI+ case were small. This result indicate that the increased CRF was not negligible and potentially contributed to the increased radiation energy in the surface in the grids with substantially reduced sea ice concentration, but the large positive ΔCS_{SDLR} was more dominant than ΔCRF_{SDLR}.

To evaluate the relative importance of the changes in CRF to the changes in clear sky downward longwave radiation, an index was defined as the ratio of ΔCRF_{SDLR} to ΔCS_{SDLR} as shown in Fig. 3.3.2b. The sign of the indexes was the same as that of ΔCRF_{SDLR} since ΔCS_{SDLR} was positive in all the months. The indexes for the ΔSI- case was negative in summer, increased approximately from 0.4 to 0.5 during September-December, reached a maximum (~0.7) in January-March and increased in Spring (Fig. 3.2.2b).

An increase in the cloud cover as a result of reduced sea ice enhanced the surface downward longwave radiation. The indexes during the period October-December showed that the all-sky surface downward longwave radiation in the ΔSI- cases increased by approximately 40–60% compared with the clear sky surface downward

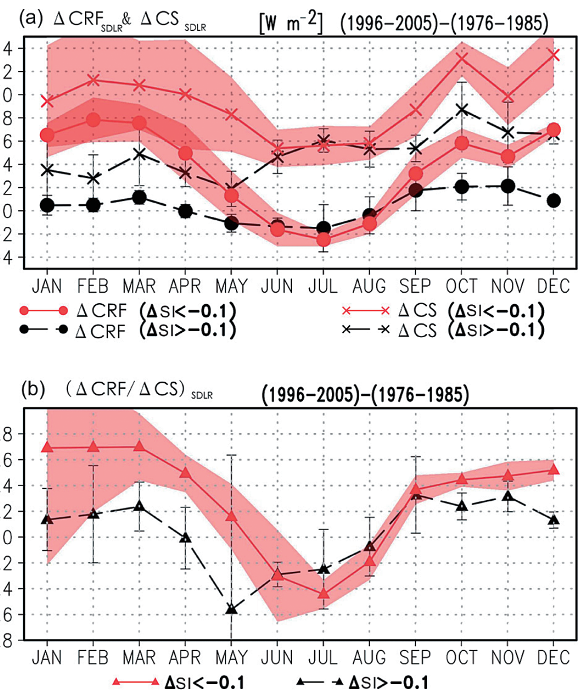

Fig. 3. 3. 2 Annual time series of (a) the change in (crosses) the CRF in surface downward longwave radiation (ΔCRF_{SDLR}) and (closed circle) clear sky surface downward longwave radiation (ΔCS_{SDLR}) between the averages for 1976–2005 and 1996–2005 in the MIROC5 simulations and (b) the index (($\Delta CRF/\Delta CS)_{SDLR}$, the ratio of ΔCRF_{SDLR} to ΔCS_{SDLR}). The solid red (broken black) lines indicate the ΔSI- (ΔSI+) case. See the text for the definition of the index. Shading and error bars indicate the standard deviations for the ensemble members in the ΔSI- and ΔSI+ cases, respectively (Abe et al., 2016).

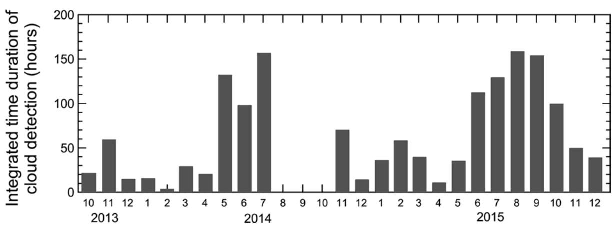

Fig. 3. 3. 3 An integrated time duration in which "in-cloud" data were obtained at the Zeppelin Observatory during each month. No data were obtained between August and October 2014 due to construction of the observatory (Koike et al., 2019).

longwave radiation. The indexes in the ΔSI- cases were larger than those in the ΔSI+ cases, although the index in the ΔSI- grids in November was not clearly distinguished from that in the ΔSI+ grids. Thus, considering the reduction in sea ice in October, the change in the CRF due to reduced sea ice was not disregarded as a factor affecting Arctic warming, contrary to Rinke et al. (2013). With regard to the feedback between sea ice and clouds, the effects of cloud cover on sea ice are also considerable. This study focused on the changes in Arctic cloud cover as a result of reduced sea ice; however, unable to observe an effect of increased cloud cover on sea ice reduction.

In-situ measurements of microphysical properties of clouds

Koike et al. (2019) made two years of continuous in situ measurements of microphysical properties of Arctic low-level clouds at the Mount Zeppelin Observatory (78°56′N, 11°53′E), in Ny-Ålesund, Spitsbergen. Frequency of cloud detections was as Fig. 3.3.3, the integration time durations during which in-cloud data were obtained for each month. The monthly median value of the cloud particle number concentration (N_c) showed a clear seasonal variation as in Fig. 3.3.4: Its maximum appeared in May–July (65±8 cm^{-3}), and it remained low between October and March (8±7 cm^{-3}). At temperatures warmer than 0°C, a clear correlation was found between the hourly N_c values and the number concentrations of aero-

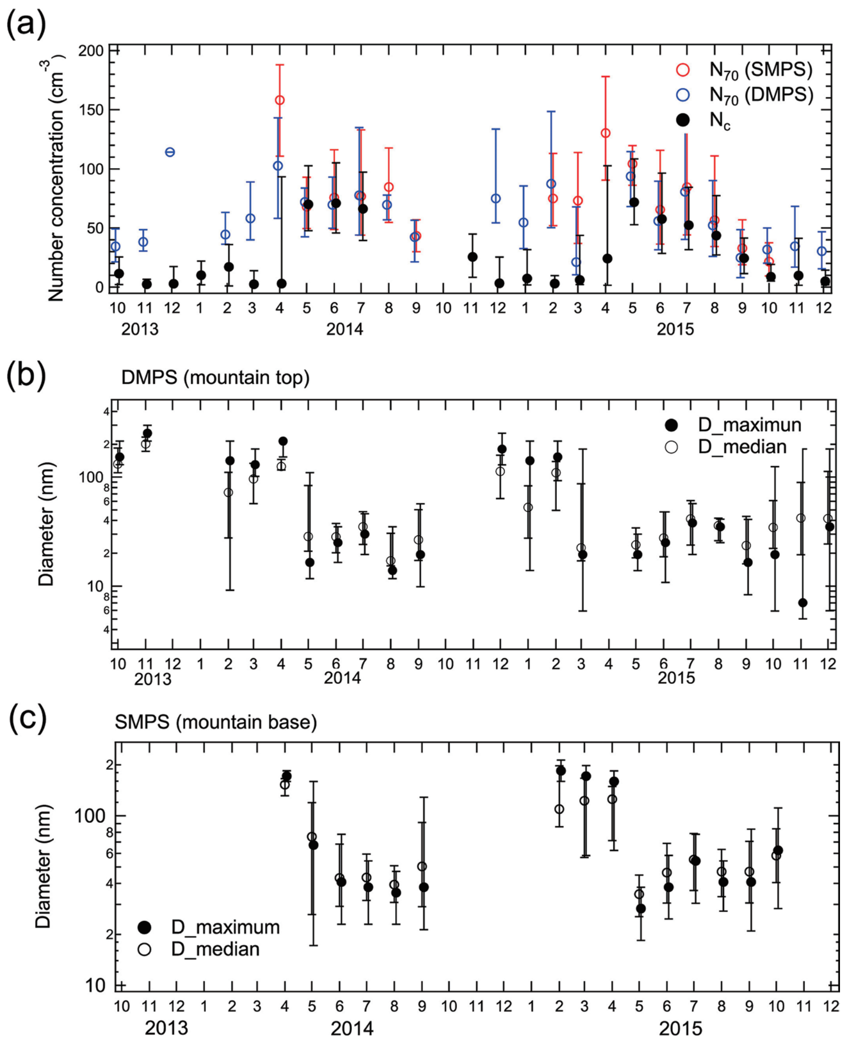

Fig. 3. 3. 4 (a) A time series of the monthly median values of the N_c and N_{70} data. Vertical bars indicate the 25th–75th percentiles. No cloud data were obtained between August and October 2014 due to construction of the observatory. (b) A time series of the monthly median values of the median diameter of aerosol size distribution, where the integrated aerosol number concentrations greater and smaller than this diameter are equal (open circles) for the DMPS (mountaintop) measurements. The diameters of the maximum concentration of aerosol size distributions (dN_a/dlog$D$) are also shown (closed circles). Vertical bars indicate the 25th–75th percentiles. (c) Same as (b) but for the SMPS (mountain base) aerosol measurements. DMPS = differential mobility particle sizer; SMPS = scanning mobility particle sizer (Koike et al., 2019).

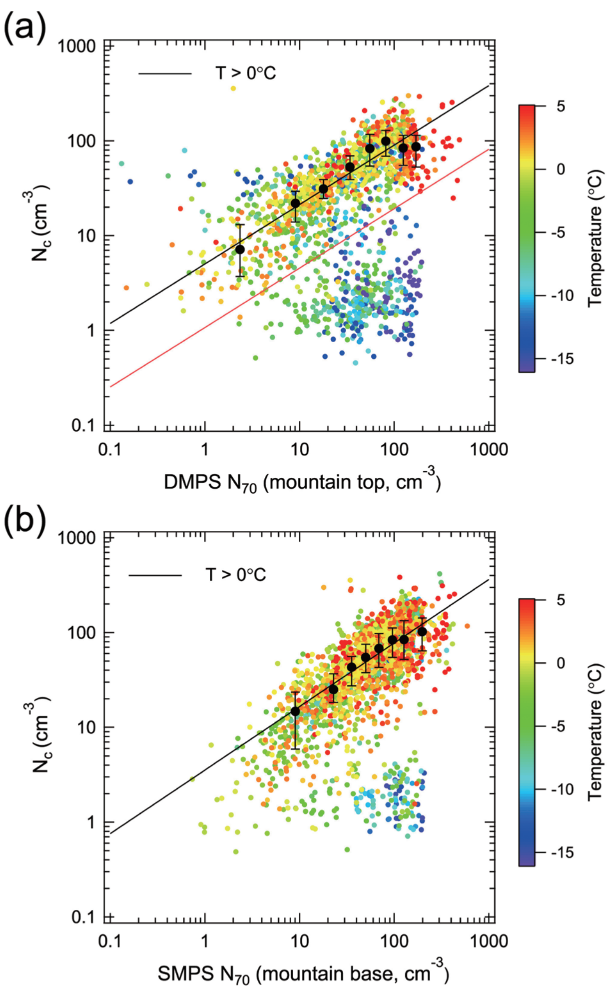

Fig. 3. 3. 5 A scatter plot of one-hour data between N_{70} and N_c. (a) DMPS-derived N_{70} (mountaintop) and (b) SMPS-derived N_{70} (mountain base) are used. Colors of the data points indicate the temperature at the Zeppelin Observatory. Black circles and vertical bars indicate median values and 25th–75th percentiles, respectively, for data obtained with $T > 0°C$. They are calculated within the individual data ranges, in which a similar number of data were obtained. The red line in (a) denotes the threshold values used to separate the "CCN-controlled" and "CCN-uncontrolled" data sets (above and below this line, respectively). DMPS = differential mobility particle sizer; SMPS = scanning mobility particle sizer; CCN = cloud condensation nuclei (Koike et al., 2019).

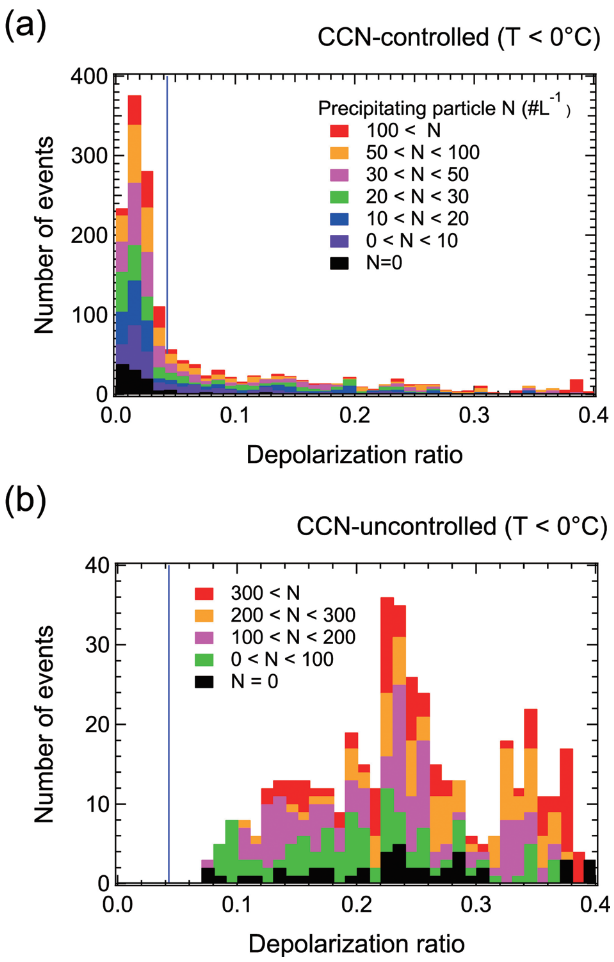

Fig. 3. 3. 6 A histogram of the depolarization ratios at altitudes of 450, 480, and 510 m measured by the micropulse lidar (at the AWI or Rabben Observatories, before and after March 2015, respectively; Table 1 and Figure 1b) when (a) CCN-controlled and (b) CCN-uncontrolled clouds were observed at Zeppelin ($T < 0°C$). Five-minute lidar data were used. The vertical line (a depolarization ratio of 0.043) indicates the threshold value used to distinguish spherical (liquid droplets) and nonspherical (ice) particles in this study. The colors denote the number concentrations of the precipitating particles (r = 25–775 μm) measured by the MPS. Note that different color scales are used for a and b. AWI = Alfred Wegener Institute; CCN = cloud condensation nuclei; MPS = Meteorological Particle Sensor (Koike et al., 2019).

sols with dry diameters larger than 70 nm (N_{70}), which are proxies for cloud condensation nuclei (CCN) (Fig. 3.3.5). When clouds were detected at temperatures colder than 0°C, some of the data followed the summertime N_c to N_{70}relationship, while other data showed systematically lower N_c values. The lidar-derived depolarization ratios (micropulse lidar; Uchiyama et al., 2014) suggested that the former (CCN-controlled) and latter (CCN-uncontrolled) data generally corresponded to clouds consisting of supercooled water droplets and those containing ice particles, respectively (Fig. 3.3.6). The CCN-controlled data persistently appeared throughout the year at Zeppelin. The aerosol-cloud interaction index (ACI=$d\ln N_c/(3 d\ln N_{70})$) for the CCN-controlled data showed high sensitivities to aerosols both in the summer (clean air) and winter–spring (Arctic haze) seasons (0.22±0.03 and 0.25±0.02, respectively). The air parcel model calculations generally reproduced these values. The threshold diameters of aerosol activation (D_{act}), which account for the N_c of the CCN-controlled data, were as low as 30–50 nm when N_{70} was less than 30 cm^{-3}, suggesting that new particle formation can affect

Arctic cloud microphysics.

3. 4. Other factors contribute to AA

Black carbon in the atmosphere

In the Arctic, the effects of black carbon (BC) include both the warming from absorption of solar radiation in the atmosphere and absorption of radiation from deposition on snow/ice. The Arctic warming from BC is highly variable with season of emission, physical transport into the Arctic, and the deposition to snow and ice. In addition, processes that emit BC also co-emit other particles and gases that lead to sulphate and organic carbon aerosols. Sand et al. (2016) estimated the total equilibrium Arctic surface temperature response to all (natural and anthropogenic) global 2010 emissions of SLCFs (short-lived climate forcers) to be −0.44 K, with a model range of −1.02 to −0.04 K, using chemical transport models. Of this 0.48 (0.33–0.66) K is due to BC in atmosphere and snow, −0.18 K is due to organic carbon, −0.85 K is due to sulphate and 0.05 K is due to tropospheric ozone.

However, estimates by climate models of the effects of BC on Arctic warming are still highly uncertain, in part because measurements of the spatio-temporal distribution of the mass concentration of BC (M_{BC}) in the atmosphere are limited and not sufficiently accurate. In the GRENE Arctic, new precise measurements were started by Sinha et al. (2017). A continuous soot monitoring system called COSMOS was deployed, which is a filter-based instrument equipped with an inlet heated at 300°C to remove non-refractory components from the aerosol phase (Miyazaki et al., 2008; Kondo et al., 2011). The measurements of absorption coefficients, b_{abs} by COSMOS, b_{abs} (COSMOS), and the derived M_{BC} (COSMOS) values were made by using a PM_1 impactor inlet (i.e., with a size cutoff at an aerodynamic diameter D_p of about 1 µm). Using a particle soot absorption photometer (PSAP), a long term measurement was conducted at Barrow Alaska (71.32°N, 156.61°E) by the National Oceanic and Atmospheric Administration (NOAA) (Hirdman et al., 2010), and at Ny-Ålesund, Svalbard operated by the Norwegian Polar Institute (Sharma et al., 2013). However, these studies did not perform detailed error analyses, and measurements obtained by filter-based absorption techniques need to be corrected for the effects of co-existing non-BC aerosol particles in the filter medium, because ambient aerosols comprise a complex mixture of light-absorbing and non-absorbing particles. Absorption coefficients measured by a PSAP, b_{abs} (PSAP), were scaled by comparing with mass concentration of BC, M_{BC} (COSMOS), measured by COSMOS. Finally, the scaled PSAP measurements were used to derive the long-term variations of M_{BC} (PSAP) in these sites.

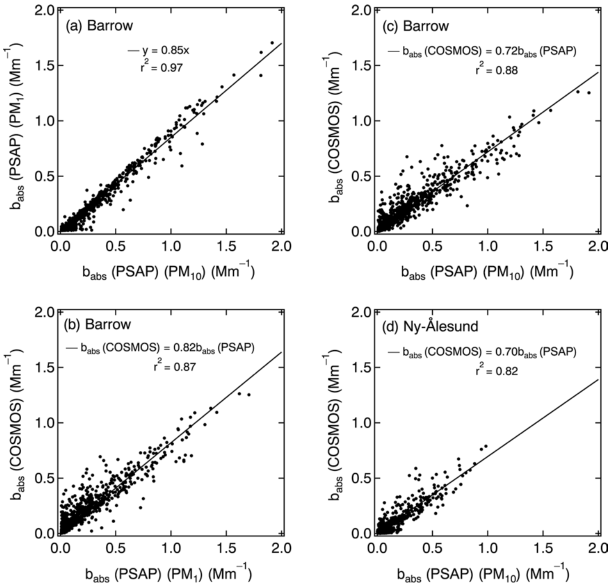

Fig. 3. 4. 1 Scatter plots between daily mean (a) b_{abs} (PSAP) for PM_1 and b_{abs} (PSAP) for PM_{10} and between daily mean b_{abs} (COSMOS) and b_{abs} (PSAP) for (b) PM_1 and (c) PM_{10} at Barrow during 2012–2015. (d) Scatter plot between daily mean b_{abs} (COSMOS) and b_{abs} (PSAP) for PM_{10} at Ny-Ålesund during 2012–2014 (Sinha et al., 2017).

At first, as shown in Fig. 3.4.1a, b_{abs} (PSAP) for PM_1 was highly correlated with b_{abs} (PSAP) for PM10 at Barrow. At Ny-Ålesund, there was no particle size cutoff for the PSAP data. However, since it is unlikely that a substantial number of particles with D_p > 10 µm was included in the PSAP measurements, these data were referred to as PM_{10} data for comparison with COSMOS data. Here comparisons of b_{abs} (COSMOS) were made with b_{abs} (PSAP) (PM_1) at Barrow (Fig. 3.4.1b) and with b_{abs} (PSAP) (PM_{10}) at Ny-Ålesund (Fig. 3.4.1d) and propotional coefficient (slope of the correlation) β was derived for each comparison.

Then it became possible to derive the mass concentration of BC by using the b_{abs} (PSAP) data applying these empirically determined relationships. The scaled M_{BC} (PSAP) is

$$M_{BC}\ (PSAP) = \beta \times b_{abs}\ (PSAP) / MAC\ (COSMOS), \quad (3.2)$$

where MAC (COSMOS) ($m^2\ g^{-1}$) is mass absorption cross section, and equal to 8.73 $m^2\ g^{-1}$ for these cases. Time series of daily mean M_{BC} (COSMOS) and M_{BC} (PSAP) for the entire period (2012–2015) of COSMOS

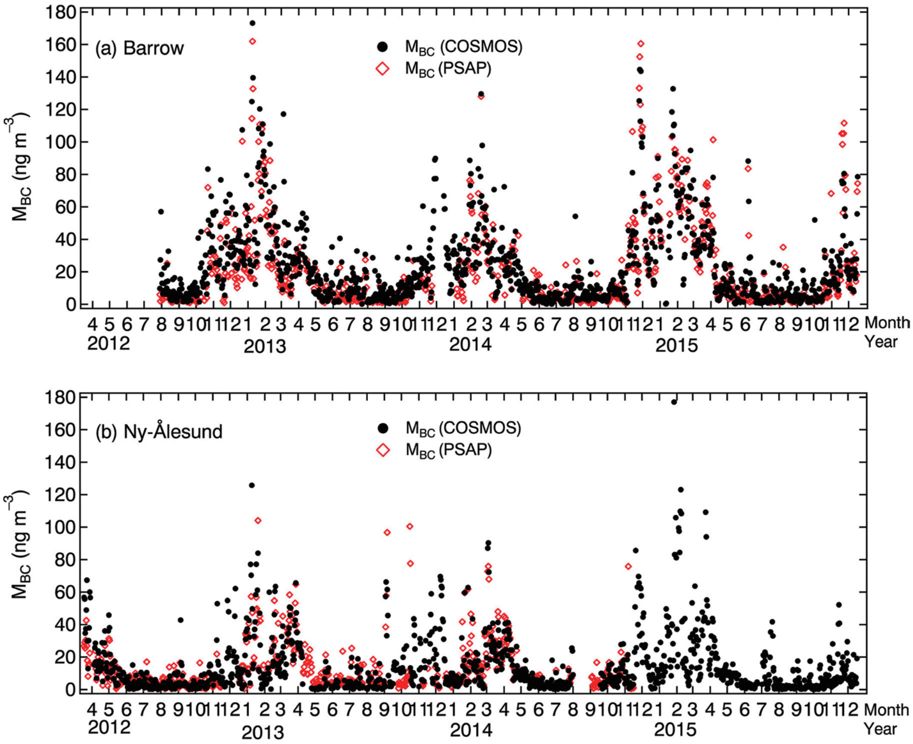

Fig. 3. 4. 2 Time series of daily mean MBC (COSMOS) and MBC (PSAP) at (a) Barrow (2012–2015) and (b) Ny-Ålesund (2012–2015) (Sinha et el., 2017).

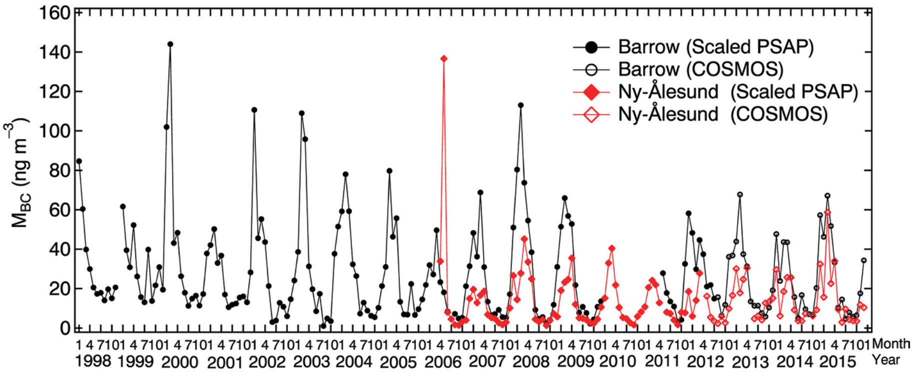

Fig. 3. 4. 3 Time series of monthly mean MBC (PSAP) values at Barrow (January 1998 to July 2012) (closed circles) and Ny-Ålesund (April 2006 to March 2012) (closed diamonds). The series are extended to December 2015 with MBC (COSMOS) values at Barrow (open sirces) and Ny-Ålesund (open diamonds). The gap in the PSAP data at Barrow from January 2010 to April 2011 was caused by an instrument malfunction (Sinha et al., 2017).

measurements at both sites were examined in Fig. 3.4.2 to evaluate the consistency of these two instruments. The temporal variations of M_{BC} (COSMOS) and M_{BC} (PSAP) were generally well correlated over wide ranges of values, as expected from the high correlation between b_{abs} (PSAP) and b_{abs} (COSMOS) as shown in Fig. 3.4.1. The time series qualitatively shows the degree of the differences between individual daily mean values of M_{BC} (COSMOS) and M_{BC} (PSAP). The difference between monthly mean M_{BC} (COSMOS) and M_{BC} (PSAP) values was generally less than 10 ng m^{-3} and agreed to within 5% and 2% at Barrow and Ny-Ålesund, respectively.

M_{BC} reached a maximum in winter and a minimum in summer, as shown by previous studies. At Barrow, mean M_{BC} (COSMOS) was 38.4±26.0 ng m^{-3} in winter and 9.3±12.0 ng m^{-3} in summer between 2012 and 2015, whereas at Ny-Ålesund during these years, mean M_{BC} (COSMOS) was 22.3±21.0 ng m^{-3} in winter and 6.2±7.9 ng m^{-3} in summer.

It is important to investigate year-to-year variations of M_{BC} in the Arctic with reliable data sets because variations in BC emissions and transport pathways can be reflected in M_{BC} changes. Sinha et al. (2017) examined time series of monthly mean M_{BC} (PSAP) from January

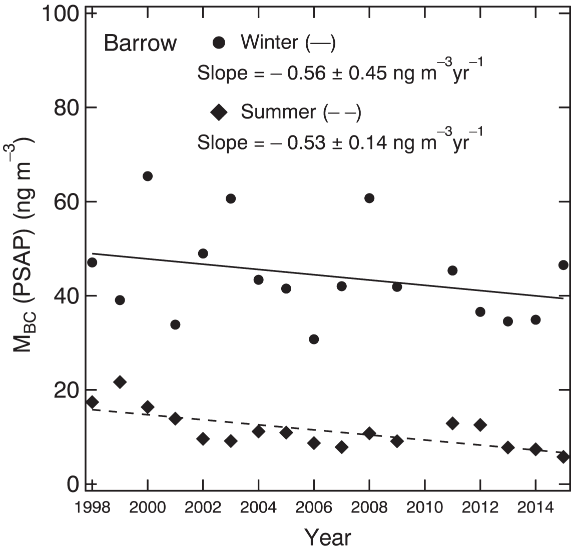

Fig. 3. 4. 4 Time series of monthly mean MBC (PSAP) in winter (November-April) and summer (May-October) during 1998–2015 at Barrow. The circles (winter) and diamonds (summer) represent seasonally averaged MBC (PSAP) values. The regression lines were obtained by applying the least-squares method to the MBC (PSAP) time series (Sinha et al., 2017).

1998 to July 2012 at Barrow and from April 2006 to March 2012 at Ny-Ålesund. Monthly mean M_{BC} (COSMOS) values at these sites also partly overlap these time series and extend them up to December 2015 as shown in Fig. 3.4.3. In winter, M_{BC} showed year-to year variations of up to a factor of two with a relative variability of about 22%. In summer, M_{BC} was much lower than it was in winter, and year-to-year variability in M_{BC} was correspondingly lower, was about 36% in summer. Year-to-year variability can be caused by variations in BC emissions, especially those due to biomass burning, as well as by differences in the transport pathway and the degree of the wet deposition of BC during transport.

Sinha et al. (2017) also examined the long-term trends in M_{BC}. The least squares method was applied to time series of MBC (PSAP) averaged over winter (November to April) and summer seasons (May to October) from 1998 to 2015 to obtain regression lines as seen in Fig. 3.4.4. The slopes were −0.56±0.17 ng m^{-3} yr^{-1} (−1.3%/yr) with r^2=0.10 for winter and −0.53±0.17 ng m^{-3} yr^{-1} (−4.7%/yr) with r^2=0.50 for summer. The lack of statistical reliability is due to the large year-to-year variability in M_{BC} (PSAP) especially in winter, which potentially includes the year-to-year variability of MAC (PSAP). No similar trend analysis of the Ny-Ålesund data was performed owing to the lack of M_{BC} (PSAP) data with sufficient reliability prior to 2006.

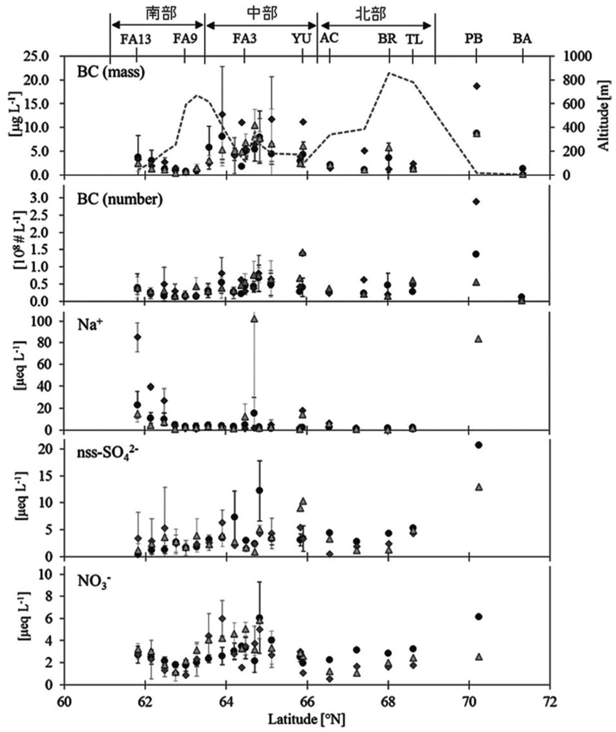

Fig. 3. 4. 5 Latitude distribution of mean BC and ion concentrations obtained during 2012 and 2015 in Alaska. ● shows whole layer, ◆ surface layer 0–2 cm, △ layer 2–10 cm, and vertical bars for 1σ (Tsukagawa et al., 2016).

BC in snow

Black carbon (BC) particles influence the radiation budget of the earth's surface by changing the albedo of snow through the deposition of BC on it. The importance of BC in snow has long been discussed; however, the accuracy of measurements of BC in snow has remained low, and measurement data were limited. Most measurements before used the filter method, which are liable to be uncertain due partly to the capturing efficiency and to the contamination of light absorbing aerosols other than BC. Here, Tsukagawa et al. (2016) measured BC concentrations in snow using a single particle soot photometer (SP2), which is based on the laser-induced incandescence technique. Moreover, normal SP2 measurement is liable to underestimate the concentration due to the limited wavelength region under 800 nm, wide range-SP2 (WR-SP2) was used to cover up to 4 μm (Mori et al., 2016).

Seasonal snow-cover samples were collected from Alaska in late February or early March during 2012–2015. Sampling points distributed from Anchorage to Fairbanks along the George Parks Highway, Poker Flat, Yukon River, Arctic Circle, Cold Foot, Brooks Mountain and Toolik Lake along Dalton Highway up to Prudhoe Bay, and then Barrow. Snow samples were collected

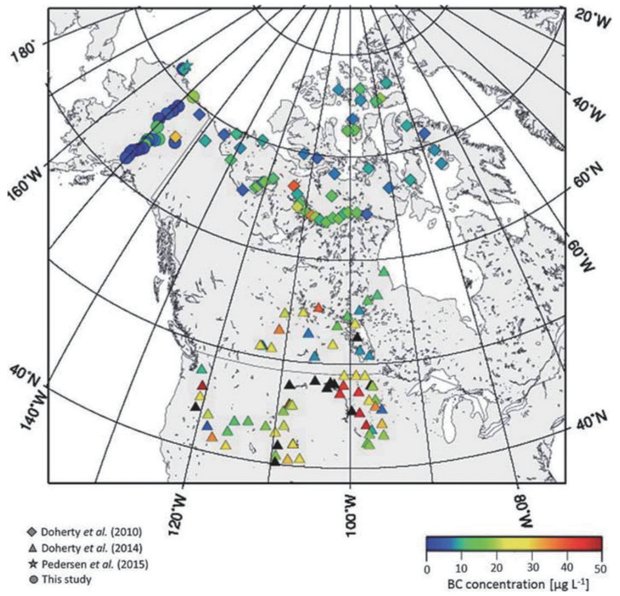

Fig. 3. 4. 6 BC concentrations in the surface snow by the present study and comparison with other former studies (Doherty et al., 2010; Doherty et al., 2014; Pedersen et al., 2015), (Tsukagawa et al., 2016).

from the surface to 2 cm depth, 2–10 cm depth and the whole snow layer. From the whole snow layer, BC concentrations were 0.4–13.6 μg L^{-1}, 0.2–21.4 μg L^{-1} and 0.2–15.0 μg L^{-1}, for 0–2 cm and 2–10 cm depth, respectively. Fig. 3.4.5 shows the latitudinal distribution of BC concentrations, together with the altitude and other ion concentrations. South of 69°N, BC concentration was the lowest around Alaska Range. BC concentration was high around Fairbanks, and at the north of Arctic Circle except Prudhoe Bay, lower than at Fairbanks. BC concentration was highest at Prudhoe Bay, by the anthropogenic emission due possibly to the oil drilling station. BC concentrations for the surface snow layers were similar or higher than those for whole snow layers and latitudinal distributions were similar. Except for Barrow and Prudhoe Bay along the transect of Alaska, BC mass concentrations for whole layer were largest in the middle part, three times higher than southern part and two times higher than northern part in average. Across Alaska Range, BC concentrations change greatly, and middle part is affected by anthropogenic emission from the city Fairbanks.

BC concentrations derived by Tsukagawa et al. (2016) were compared with other former results. As shown in the map of Fig. 3.4.6, the present results generally show lower values compared to other studies. Since they are using different measurement technique, filter method, it is rather difficult to coincide with the present study. BC in snow still has many uncertainties, and further study is needed.

Aoki et al. (2014) under the "Snow Impurity and Glacial Microbe effects on abrupt warming in the Arctic" (SIGMA) Project (2011–2015), collaborated with the GRENE Arctic, examined the effect of light-absorbing snow impurity concentration on northwest Greenland Ice Sheet (GrIS). The role of light-absorbing snow impurity concentration to the recent snow melt in GrIS was discussed and concluded that enhancement of the snow surface impurities occurred in the observation period, which can be explained by the effect of sublimation/ evaporation and snow melt amplification associated with drastic melting.

Then, Sinha et al. (2018) made accurate measurements of the concentration and size distributions of BC in snow that could be compared with model calculations reliably.

Glacier microorganisms-cryoconite

Although not in the Arctic but in Himalaya, Koshima et al. (1993) found the biological activities would accelerate the glacier melting. Surface dust contains products such as the organisms themselves, their dead remains and decomposed organic matter. Since these organic particles have relatively small single scattering albedo, yet are large in volume, they are optically effective on the surface albedo. Such biogenic surface dust on glacial ice is known as "cryoconite", which is first named by the arctic explorer, A. E. Nordenskjöld (1875), and it exerts a significant impact on the albedo of the ablation surface on some glaciers (Takeuchi et al., 2001). In the spectrum consideration, Takeuchi (2009) presented the reflectances (350–1050 nm in wavelength) of the glacier surface on Gulkana Clacier, Alaska Range, at six different elevations from May to September 2001. The temporal and spatial variations in spectral reflectance are discussed in terms of physical properties and impurities of snow and ice. The result clearly showed the relationship between spectral albedo reduction and surface dust (cryoconite) increase relative to the change of the surface conditions from snow to ice (Fig. 3 and 4 of Takeuchi, 2009). Mean amount of cryoconite increased up to 60 g m^{-2} in some altitude range in late summer.

Within GRENE Arctic, the group studied cryoconite in northwest Greenland and Suntar-Khayata Mountain Range in Russian Siberia. The Greenland Ice Sheet, the second largest continuous body of ice in the world, has been reported to be losing mass. Increased surface melt-

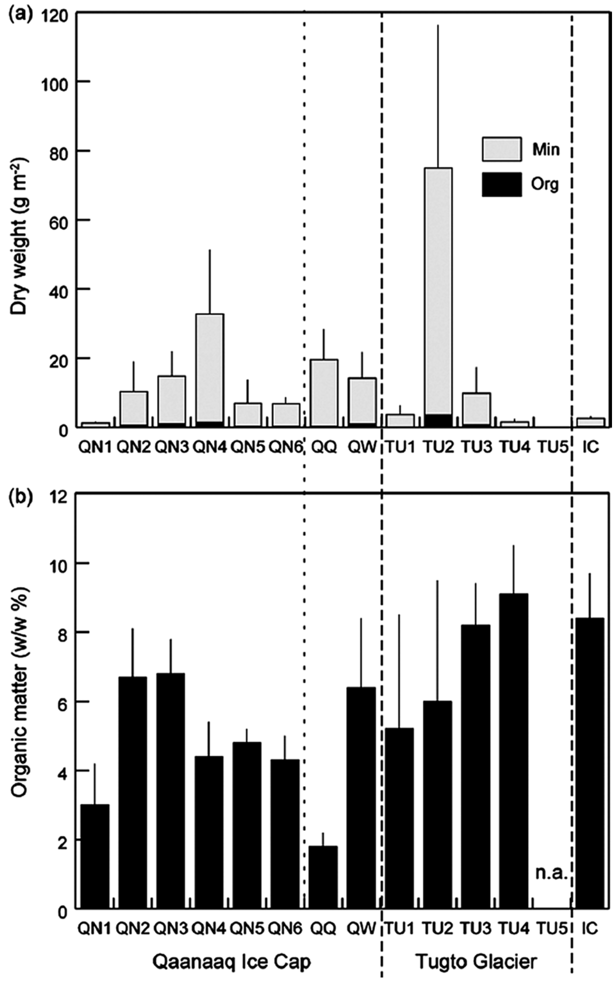

Fig. 3. 4. 7 (a) Mean amount of impurities (dry weight g m^{-2}) on the surface and (b) organic matter content (dry weight percentage) in impurities of all study sites on Qaanaaq Ice Cap and Tugo Glacier. Error bar is standard deviation (Takeuchi et al., 2014).

ing is a significant factor in the mass loss and is likely caused by temperature rise and reduction of surface albedo. The surface albedo of the Greenland Ice Sheet varied spatially, in particular, a part of the bare ice surface appeared to be particularly dark. That area is referred to as the dark region and is particularly prominent in the middle-west Greenland from MODIS images (Wientjes and Orlemans, 2010).

Takeuchi et al. (2014) investigated spatial variations in impurities (cryoconite) on the glacier surface on Qaanaaq Ice Cap and Tugo Glacier in the northwest Greenland in the melting season of 2012 (Fig. 3.4.7). The abundance of impurities ranged from 0.36 to 119 g m^{-2} on the bare ice surface and from 0.01 to 8.7 g m^{-2} on the snow surface of the study sites. There wa no significant difference in the abundance between the Qaanaaq Ice Cap and Tigo Glacier. The abundance of impurities on the Qaanaaq Glacier was greater in the middle part than in the lower part and upper snow area. These distributions were also confirmed from satellite data. The Landsat 7 satellite image showed that surface reflectivity varied across the Qaanaaq Ice Cap, and although it was generally higher at mid-elevations, it was highest about 0.68–0.72 near the terminus, decreased up-glacier to a minimum 0f 0.25–0.30 at an elevation if 800–900 m, then gradually increased up-glacier to the maximum of 0.60–0.68 m.

The reason impurities were more abundant in the middle area of glaciers is discussed. The distribution may be explained by supply and removal processes of mineral particles and/or biological process of cryoconite formation. Dust supply from mineral-rich layers in the ice may result in such spatial variation. Altitude variations in the microbial production rate and/or those in algal communities also could affect the variation. Since cryoconite granules, which are the main components of the impurities on the ice area, are formed by entanglements of filamentous cyanobacteria, their distribution could also result in abundant cryoconite in the area. Smaller amounts of impurities in the upper area may be due to smaller biomass of snow algae, which is commonly observed on glaciers and results from physical conditions such as shorter duration of melt season. To understand which factors determine the abundance of impurities, further studies are necessary. The organic matter contents in the impurities in the lower snow area were comparable to those in the ice area, suggesting that red snow algae are likely to be main constitution of the impurities. The red snow algae has been commonly observed on polar glaciers and they often bloom in the area closed to the firn line, which is consistent with the observation in the study. Thus, the bloom of red snow algae may largely control the spatial distribution of impurities in the snow surface on the glaciers.

The abundance of impurities on glaciers in the northwest Greenland revealed in the study was comparable to those on the other glaciers in polar or sub-polar regions. For examples, the abundance on the ablation surfaces have been reported to be 1.14±1.60 g m^{-2} for Canadian Arctic, 23.0±13.3 g m^{-2} for Alaska and 38.8±25.6 g m^{-2} for Patagonia and they are roughly equal to those for the northwest Greenland in the present study, 18.8±21.6 g m^{-2}. On the other hand, the abundance was much smaller than those of Asian mountain glaciers (Fig. 3.4.8).

Changes in physical conditions of glaciers due to climate warming such as expansion of bare ice area, melt snow surface and length of melt season, may affect abun-

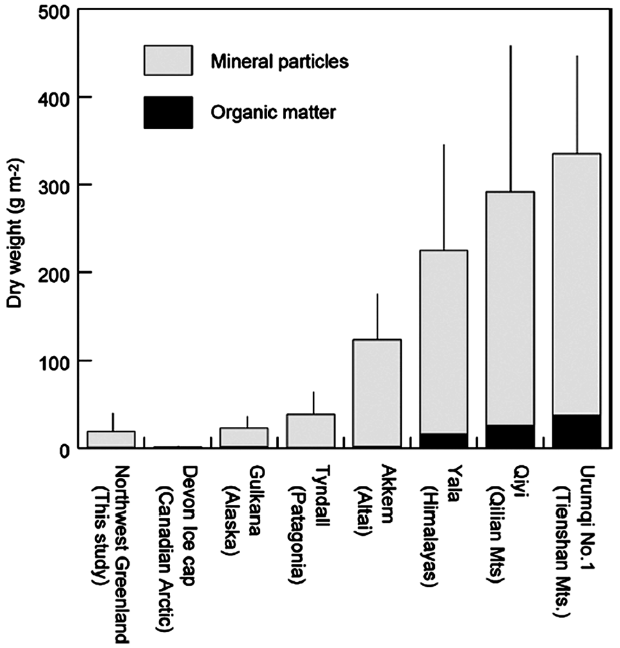

Fig. 3. 4. 8 Comparison of abundance of impurities (cryoconite) on the ablation surface of glaciers in the world. Error bar is standard deviation. Dry weight fraction of mineral and organic matter in the impurities were shown in the graph (Takeuchi et al., 2014).

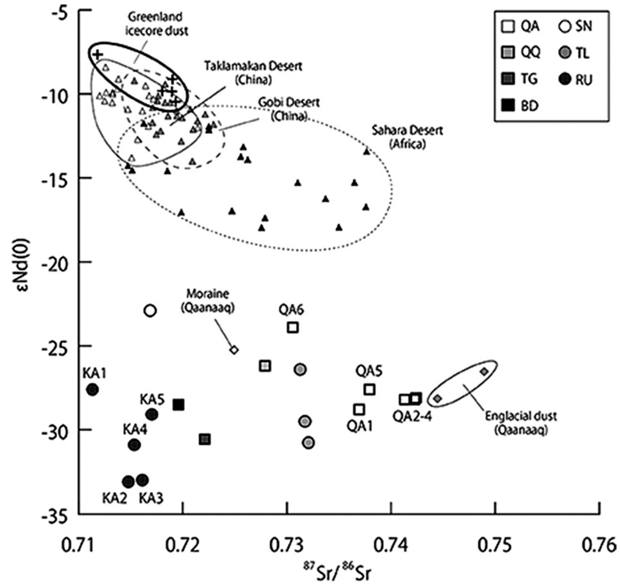

Fig. 3. 4. 9 Sr-Nd isotopic ratios of silicate minerals in cryoconites and those of moraine and englacial dust on and around the Qaanaaq Glaciers, and loess and sand reported in the Asian and African regions (Nagatsuka et al., 2016).

dance and distribution of impurities on the glaciers. Which means that cryoconite may have a feedback effect on the Arctic warming.

In order to better understand the source of minerals on the dark-colored ice, located in the Greenland Ice Sheet ablation zone, Nagatsuka et al. (2016) analyzed the Sr and Nd isotopic ratios of minerals in cryoconite. Recently, the area of dark-colored ice covered by cryoconites has expanded on the Greenland Ice Sheet. One of the possible causes of dark ice expansion is an increase in cryoconite abundance on the ice surface. Because mineral dust is the major constituent of cryoconite (Takeuchi et al., 2014), it is important to know its sources and the processes by which it accumulates on the ice sheet. The minerals in cryoconite may also affect the microbial production on the glacial surface, which is another contributor to the cryoconite mass. Because glacial microbes are likely to incorporate nutrients from mineral dust and dissolved components in snow and ice, the minerals on an ice sheet and/or glacier could affect their biomass by supplying nutrients.

There are different possible sources of the mineral dust in the cryoconite on the Greenland Ice Sheet. The mineral dust in ice cores from Greenland originated from the Sahara in Africa. On the other hand, the dust deposited on the ablation area was locally derived from wind-blown sediments and/or englacial melt-out debris. Stable isotopic rations of strontium ($^{87}Sr/^{86}Sr$) and neodymium ($^{143}Nd/^{144}Nd$ or εNd(0)) can reveal the source and transport process of mineral dust in cryoconite. Sr and Nd are commonly contained in trace amounts in natural materials such as rocks and water as well as in organisms. Their isotopic ratios vary greatly, depending on their geological origin and the ratios rarely change during transportation in the atmosphere or after deposition as sediment. Sd and Nd isotopic ratios and mineral compositions of cryoconite collected from seven glaciers in geographically separated regions in northwest and southwest Greenland are analyzed. The variations in the isotopic ratios and compositions are discussed in terms of the sources of silicate minerals found on the glaciers.

According to previous studies, there are three possible sources of minerals in cryoconites on the Greenland Ice Sheet: (1) dust transported by wind from the local area, probably the nearby tundra; (2) englacial dust that was deposited in the past in the accumulation area, traveled through the ice sheet and outcropped again in the ablation zone; or (3) long-range transported dust from distant deserts (Wientjes and Oerlemans, 2010; Takeuchi et al, 2014). The minerals in the cryoconite are likely to be a mixture of those from the three different sources. Results are shown in Fig. 3.4.9, the Nd isotopic ratios of the cryoconites analyzed in this study were significantly lower than those of distant deserts but were close to those of the moraine and englacial dust on and around the glaciers. This suggests that the silicate minerals in the cryoconites are probably not derived from Asia and African desearts [source (3)] but mainly from the area surrounding the glaciers.

The mineralogical composition of the cryoconites also supports the predominance of local dust on the glaciers. Nagatsuka et al. (2014) revealed that cryoconites on the Qaanaaq, Qaqortaq, Tugo, Bowdoin and Sun Glaciers contained much lower amounts of clay minerals compared to Asian desert sand (Fig. 3.4.8).

Finally, Takeuchi et al. (2015) investigated characteristics of impurities and their impact on the ablation of Glacier No. 31 in the Suntar-Khayata Mountain Range in Russian Siberia during summer 2014. Of the glacierised regions in the Arctic latitudes, those within Russia are some of the least studied. There are a number of glaciers in the mountain ranges in Arctic and sub-Arctic regions in eastern Siberia, Russia, and Suntar-Khayata Mountain Range lies near the coldest core of Oymyakon, east of Yakutsk. Positive degree-day factors (PDDFs) obtained from 20 stakes measurements distributed across the glacier's ablation area varied from 3.00 to 8.55 mm w.e. K^{-1} day^{-1}. The surface reflectivity measured with a spectrometer as a proxy for albedo, ranged from 0.09 to 0.62 and was negatively correlated with PDDF, suggesting that glacier ablation (melting) is controlled by surface albedo (absorption of shortwave radiation) on the studied glacier. Mass of total insoluble impurities on the ice surface varied from 0.1 to 42.5 g m^{-2} and was not correlated with surface reflectivity (Fig. 3.4.10), suggesting that albedo is not directly conditioned by the mass of the impurities. The lack of correlation between surface reflectivity and total mass of impurities is probably due to a smaller density of the organic matter including algal cells compared with that of inorganic impurities. Some of the data showing higher reflectivity and greater impurities in Fig. 3.4.10 can also be explained by greater contents of white transparent mineral particles, such as quartz and feldspar, in the impurities, which have a lower light absorbency. Microscopy of impurities revealed that they comprised mineral particles, cryoconite granules and ice algal cells filled with dark-reddish pigments. As shown in Fig. 3.4.10 (B), there was a significant negative correlation between surface reflectivity and algal biomass or organic matter, suggesting that the ice algae and their products are the most effective constituents in defining glacier surface albedo. The results suggest that the melting of ice surface was enhanced by the growth of ice algae, which increased the melting rate 1.6–2.6 times grater than that of the impurity free bare-ice.

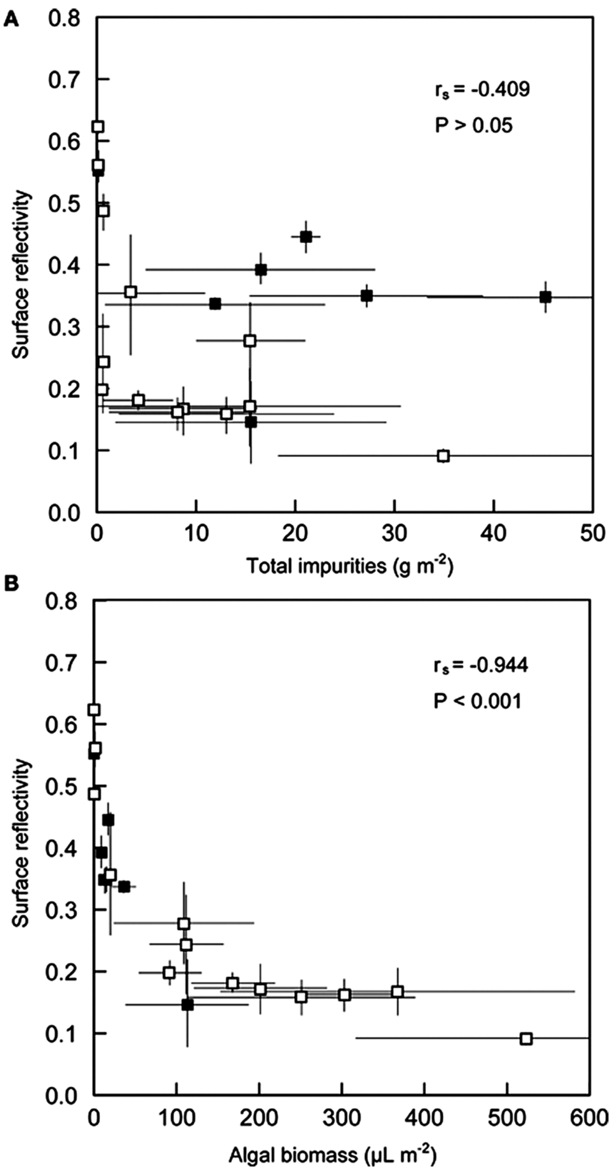

Fig. 3. 4. 10 Relationships between surface reflectivity and total impurities (A) and algal biomass (B) on the ice surfaces of Glacier No. 31. The correlation was not statistically significant between surface reflectivity and total impurities (A), but significant between surface reflectivity and algal biomass (B). Open and solid marks indicate Sites A and B, respectively. Error bars indicate standard deviation of measurements of surface reflectivity and impurities at each stake (Takeuchi et al., 2015).

Snow cover extent

Snow cover is an essential geophysical parameter for understanding the Earth's climate system. Its high shortwave albedo and longwave emissive properties significantly impact Earth's climate via the radiation budget. Snow cover also plays an important role as a thermal in-

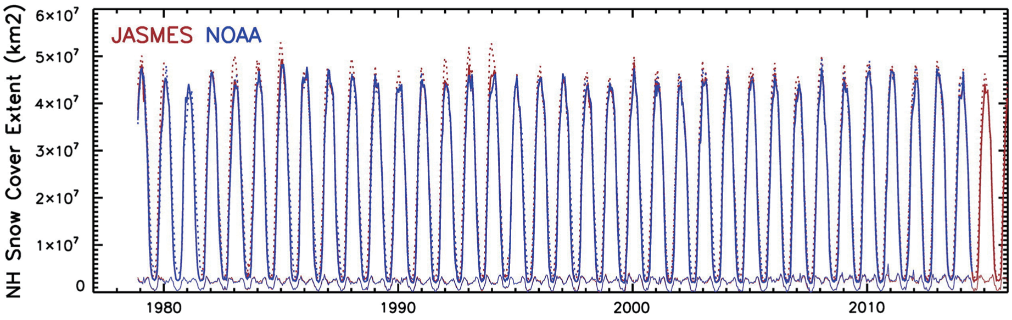

Fig. 3. 4. 11 Time series plot of Northern Hemisphere snow cover extent (SCE) of JASMES (red color) and NOAA (blue color) from November 1978 to December 2015. Dotted lines indicate primary SCE (PMSCE) and solid lines denote error-adjusted SCE (EASCE) (Hori et al., 2017).

sulator in cold continental areas, and snow cover itself provides regional terrestrial drainage and fresh water to downstream oceans during melt seasons. Hori et al. (2017) developed a long term Northern Hemisphere (NH) daily 5-km snow cover extent (SCE) product, released on the website "JAXA Satellite Monitoring for Environmental Studies (JASMES)", by the application of a consistent objective snow cover mapping algorithm to data from historical optical sensors on polar orbiting satellites from 1978 to 2015. In this study, radiance data acquired with the AVHRR on TIROS/NOAA series satellites and MODIS were used. Of these sensors, MODIS has the ability to calibrate observed radiance and thus the MODIS data were used without additional calibration; however, AVHRR cannot calibrate radiances in the visible and near-infrared spectral bands in orbit. These sensors are known to degrade over the course of satellite operational life span after being launched. The effect of the AVHRR sensor degradations on radiance was simply corrected by observing a reference target, Dome C on the Antarctic Ice Sheet, where the surface reflectance is considered to be unchanging. Also compared are the NOAA/NCDC climate data record (CDR) weekly snow charts from January 1978 to June 2014 (hereafter, NOAA SCE) in order to explore possible differences in the long-term trends.

Bi-monthly NH SCEs were derived from the weekly SCE maps of JASMES and NOAA in two ways. In the first, an ordinary direct method was used that sums the snow pixels area in a weekly SCE map to determine the total weekly SCE, primary product of SCE (PMSCE), in the NH. In addition to this direct method, also an error-adjusted SCE (EASCE) was estimated from the SCE map by using the accuracy data of the SCE map derived with in-situ station data. Fig. 3.4.11 shows the long-term variations of the NH PMSCE (dotted line) and EASCE (solid line) derived from the JASMES (red color) and NOAA (blue) SCE products during the 1978–2015 period. The SCE from both data sets exhibit typical periodic annual cycles with local maxima and minima in January and July, respectively. The confidence intervals (CI) also exhibit periodic cycles, becoming high in melting and snow-onset seasons when NH SCE changes rapidly.

Fig. 3.4.12 shows the time series of seasonally averaged PMSCEs derived from the JASMES (solid lines with filled circles) and NOAA (broken lines) products. Fig. 3.4.12(b) shows the time series of the PMSCE (exactly the same plot as in Fig. 3.4.12(a)) and EASCE from JASMES (dotted line with square symbols), and Fig. 3.4.12(c) is the same as Fig. 3.4.12(b) but for those derived from NOAA (similar time series plots of monthly averages of all the SCEs (PMSCE) and EASCE). In addition, a linear regression equation with the slope and intercept was calculated for each SCE. The linear regression lines for statistical significant linear trends are plotted in the figures, with a solid line for PMSCE and a broken line for EASCE.

NOAA's seasonally averaged PMSEs exhibit negative trends in spring and summer but positiove trends in winter and autumn, whereas the NOAA EASCEs exhibit negative trends in all seasons (Fig. 3.4.11(a) and (c)) with the following slopes: PMSCE (EASCE) of +50.4 (−24.7), −74.5 (−12.5), −82.4 (−21.2) and +59.3 (−37.8) km^2/yr in winter, spring, summer and autumn, respectively. Basically, the negative trends of the seasonally averaged EASCEs of NOAA are also consistent with those of JASMES, which suggests that the error-adjustment approach that takes into account the area proportion of snow cover and the accuracy of the SCE maps evaluated with in-situ snow data succeeds in generating consistent SCEs from the JASMES and NOAA products.

On the other hand, the JASMES SCEs (both the PMSCE and the EASCE shown in Fig. 3.4.11b) exhibit neg-

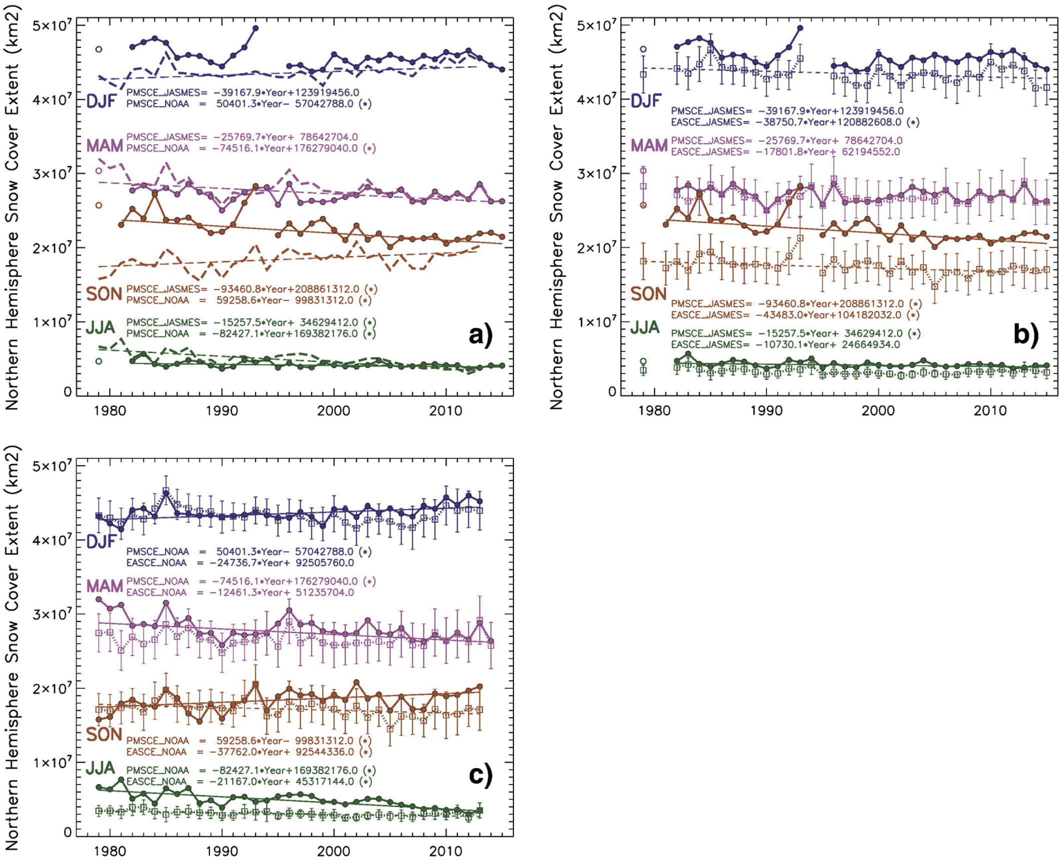

Fig. 3. 4. 12 Time series of (a) seasonally averaged Northern Hemisphere snow cover extent (PMSCE) derived from JASMES (solid lines with filled circles) and NOAA (broken lines), (b) seasonally averaged PMSCE and error-adjusted SCE (EASCE; dotted lines with square symbols) derived from JASMES, and (c) the same plots as in (b) but for those derived from NOAA. The equations for the PMSCE of JASMES were derived from the data for the 1981–2015 period only (filled circles). We plotted only those regression lines of statistically significant linear trends (Kendall-Mankind test a > 0.05). Error bars on the EASCE plot denote the confidence intervals averaged for individual seasons (Hori et al., 2017).

ative trends in all seasons as follows: PMSCE (EASCE) of −39.1 (−38.8), −25.8 (−17.8), −15.3 (−10.7) and −93.5 (−43.5) km^2/yr in winter, spring, summer and autumn, respectively. The trend of autumn EASCE is smaller than that of the PMSCE, which suggests an overestimation of the autumn trend by JASMES's original SCE (i.e., PMSCE). However, the autumn slope of the error-adjusted SCE (EASCE) is still the largest of all the seasons, which indicates that it is the main driver for the shrinkage of snow cover in the NH.

As a result, although there are some systematic positive biases of the JASMES SCE in winter and autumn, the signs of the trends do not change before and after the error adjustment of the SCE, which indicates that the JASMES PMSCE has more stable temporal accuracy compared with the NOAA SCE case. In addition, the EASCE derived from JASMES and NOAA exhibit consistent trends, which reveal that the shrinkage of the NH SCE due to global warming has steadily continued in all seasons at least since the 1970s.

In another application example, the annual snow cover duration (SCD) was estimated. The SCD is the sum of the temporal fraction of snow cover within each bi-monthly period, for every year and every pixel. Fig. 3.4.13a and b shows the 30-year average and trend, respectively, of the SCD in the NH (1982–2013, excluding 1994 and 1995). Fig. 3.4.13c is the same as Fig. 3.4.13b except that it shows only the area of the statistically significant SCD trend (Kendall-Mankind test with a > 0.05). Basically, the satellite-derived SCD trends to shorten significantly in western Eurasia (shortening one to two months over three decades) and also trends to shorten weekly in the center of Siberia, Alaska and eastern North America. On the other hand, the SCD seems to lengthen in parts of China, the Himalayas and in North America in the western mountain region (the Rokies) and a small portion of the Canadian Arctic Archipelago. By analyzing the snow onset and end dates from the JASMES SCE data, it was found that most of significant SCD shortening trends observed in western Eurasia occurred due to a

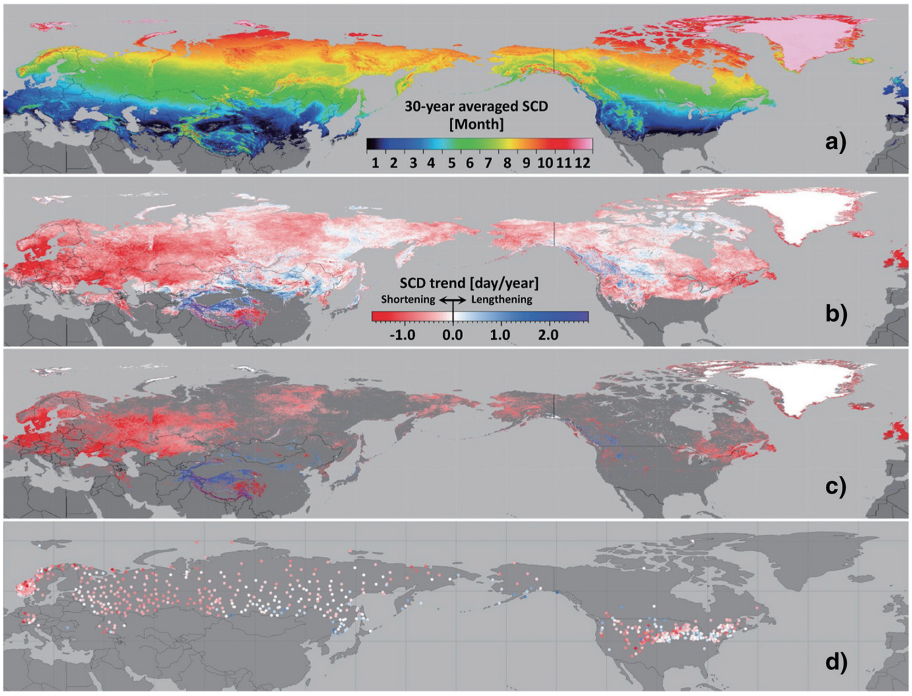

Fig. 3. 4. 13 Spatial distributions of the (a) 30-year average (1982–2013, excluding 1994 and 1995) of snow cover duration (SCD, in month), (b) 30-year trend of SCD (day/year) in the Northern Hemisphere derived from the long-term satellite-derived SCE, (c) the same as (b) except that only the areas with statistically significant SCD trends (Kendall-Mankind test a > 0.05) are shown, and (d) SCD trend derived from in-situ snow data measured at the ground stations that have complete annual snow depth observation records during the 32- year analysis period (Hori et al., 2017).

trend of later onset dates of the first snow in autumn or early winter seasons and weak contribution by a trend of earlier spring end dates.

Fig. 3.4.13d shows plots of the SCDs (filled circles) derived from the selected in-situ stations. Although the magnitudes of in-situ derived SCD trends tend to be smaller than those derived from satellite data, the spatial pattern of the SCD trends seem to be quite consistent. That is, there are negative trends in the western Eurasia Continent and positive trends in some parts of eastern Asia and North America.

References:

Abe, M., Nozawa, T., Ogura, T., Takata, K., 2016. Effect of retreating sea ice on Arctic cloud cover in simulated recent global warming. Atmos. Chem. Phys., 16, 14343–14365, doi:10.5194/acp-16-14343-2016.

Aoki, T., Matoba, S., Yamaguchi, S., Tanikawa, T., Niwano, M., Kuchiki, K., Adachi, K., Uetake, J., Motoyama, H., Hori, M., 2014. Light-absorbing snow impurity concentrations measured on Northwest Greenland ice sheet in 2011 and 2012. Bull. Glaiol. Res., 32, 21–31, doi: 10.5331/bgr.32.21.

Comiso, J. C., Parkinson, C. L., Gersten, R., Stock, L., 2008. Accelerated decline in the Arctic sea ice cover, Geophys. Res. Lett., 35, L01703, doi:10.1029/2007GL031972.

Doherty, S. J., Warren, S. G., Grenfell, T .C., Clarke, A. D., Brandt, R. E., 2010. Light-absorbing impurities in Arctic snow. Atmos. Chem. Phys., 10, 11647–11680.

Doherty, S. J., Dang, C., Hegg, D. A., Zhang, R., Warren, S. G., 2014. Black carbon and other light-absorbing particles in snow of central North America. J. Geophys. Res., 119, 12807–12831.

Graversen, R.G., Burtu, M., 2016. Arctic amplification enhanced by latent energy transport of atmospheric planetary waves. Q. J. R. Meteorol. Soc. 142, 2046–2054. https://doi.org/10.1002/qj.2802.

Hirdman D., Sodemann, H., Eckhardt, S., Burkhart, J. F., Jefferson, A., Mefford, T., Quinn, P. K., Sharma, S., Ström, J., Stohl, A., 2010. Source identification of short-lived air pollutants in the Arctic using statistical analysis of measurement data and particle dispersion model output. Atmos. Chem. Phys., 10, 669–693.

Hori, M., Sugiura, K., Kobayashi, K., Aoki, T., Tanikawa, T., Kuchiki, K., Niwano, M. and Enomoto, H., 2017: A 38-year (1978–2015) Northern Hemisphere daily snow cover extent product derived using consistent objective criteria from satellite-borne optical sensors. Remote Sens. Environ., 191, 402–418.

Koike, M., Ukita, J., Strom, J., Tunved, P., Shiobara, M., Vitale, V., Lupi, A., Baumgardner, D., Ritter, C., Hermansen, O., Yamada, K., Pedersen, C. A., 2019. Year-round in situ measurements of Arctic low-level clouds: Microphysical properties and their relationships with aerosols. J. Geophys. Re., 124, 1798–1822, https://doi.org/10.1029/2018JD029802.

Kondo, Y., Sahu, L., Moteki, N., Khan, F., Takegawa, N., Liu, X., Koike, M., Miyakawa, T., 2011. Consistency and traceability of black carbon measurements made by laser-induced incandescence, thermal-optical transmittance, and filter-based photo-absorption techniques. Aerosol Sci. Technol., 45, 295–312.

Koshima, S., Seko, K. and Yoshimura, Y., 1993: Biotic acceleration of glacier melting in Yala Glacier, Langtang Region, Nepal Himalaya. Snow and Glacier Hydrology (Proceedings of the Kathmndu Symposium, November 1992). IAHS Publ. no. 218, 309–316.

Laine, A., Yoshimori, M., Abe-Ouchi, A., 2016. Surface Arctic amplification factors in CMIP5 models: land and oceanic surfaces, seasonality. J. Clim. 29, 3297–3316. doi:10.1175/JCLI-D-15-0497.1

Liu, Y., Key, J. R., Liu, Z., Wang, X., Vavrus, S. J., 2012. A cloudier Arctic expected with diminishing sea ice. Geophys. Res. Lett., 39, L05705, doi:10.1029/2012gl051251.

Lu, J. H., Cai, M., 2009. A new framework for isolating individual feedback processes in coupled general circulation climate models. Part I: formulation. Clim. Dyn. 32, 873–885. doi:10.1007/s00382-008-0425-3.

Miyazaki, Y., Kondo, Y., Sahu, L. K., Imaru, J., Fukushima, N., Kanno, A., 2008. Performance of a newly designed continuous soot monitoring system (COSMOS). J. Environ. Monit., 10, 1195–1201.

Mori, T., Moteki, N., Ohata, S., Koike, M., Goto-Azuma, K., Miyazaki, K., Kondo, Y., 2016. Improved technique for measuring the size distribution of black carbon particles in liquid water. Aerosol Science and Technology, 50(3), 242–254. doi.org/10.1080/02786826.2016.1147644.

Nagatsuka, N., Takeuchi, N., Uetake, J. and Shimada, R., 2014: Minealogical composition of cryoconite on glaciers in northwest Greenland. Bull. Glaciol. Res., 32, 107–114.

Nagatsuka, N., Takeuchi, N., Uetake, J., Shimada, R., Onuma, Y., Tanaka, S. and Nakano, T., 2016: Variations in Sr and Nd isotopic ratios of mineral particles in cryoconite in western Greenland. Frontiers in Earth Science, 4:93. Doi: 10.3389/feart.2016.00093.

Nordenskjöld, N. E., 1875. Cryoconite found 1870, July 19th–25th, on the inland ice, east of Auleitisvik Fjord, Disco Bay, Greenland. Geological Magazine, Decade 2, 2, 157–162.

Ogura, T., Emori, S., Webb, M. J., Tsushima, Y., Yokohata, T., Abe-Ouchi, A., Kimoto, M., 2008a. Towards understanding cloud response in atmospheric GCMs: the use of tendency diagnostics. J. Meteorol. Soc. Jpn, 86, 69–79. doi:10.2151/jmsj.86.69

Ogura, T., Webb, M. J., Bodas-Salcedo, A., Williams, K. D., Yokohata, T., Wilson, D. R., 2008b. Comparison of cloud response to CO_2 doubling in two GCMs. Sola, 4, 29–32. doi:10.2151/sola.2008-008

Pedersen, C.A., Gallet, J. –C., Ström, J., Gerland, S., Hudson, S. R., Forsström, S., Isaksson, E., Berntsen, T. K., 2015. In situ observations of black carbon in snow and the corresponding spectral surface albedo reduction. J. Geophys. Res., 120, 1476–1489.

Rinke, A., Dethloff, K., Dorn, W., Handorf, D., Moore, J. C., 2013. Simulated Arctic atmospheric feedbacks associated with late summer sea ice anomalies, J. Geophys. Res.-Atmos., 118, 7698–7714.

Sand, M, T. K. Berntsen, K. von Salzen, M. G. Flanner, J. Langner and D. G. Victor, 2016: Response of Arctic temperature to changes in emission of short-lived climate forcers. Nature Climate Change, 6, 286–289, DOI: 10.1038/NCLIMATE2880.

Screen, J. A., Simmonds, I., 2010. The central role of diminishing sea ice in recent Arctic temperature amplification. Nature, 464, 1334–1337, doi:10.1038/nature09051.

Serreze, M. C., Barrett, A. P., Stroeve, J. C., Kindig, D. N., Holland, M. M., 2009. The emergence of surface-based Arctic amplification. Cryosphere, 3, 11–19, doi:10.5194/tc-3-11-2009.

Sharma, S., Ishizawa, M., Chan, D., Lavoué, D., Andrews, E., Eleftheriadis, K., Maksyutov, S., 2013. 16-year simulation of Arctic black carbon: Transport, source contribution, and sensitivity analysis on deposition. J. Geophys. Res., 118, 943–964, doi:10.1029/2012JD017774.

Sinha, P. R., Kondo, Y., Koike, M., Ogren, J., Jefferson, A., Barrett, T., Sheesley, R. J., Ohata, S., Moteki, N., Coe, H., Liu, D., Irwin, M., Tunved, P., Quinn, P. K., Zhao, Y., 2017. Evaluation of ground-based black carbon measurements by filter-based photometers at two Arctic sites. J. Geophys. Res., 122, 3544–3572, doi.org/10.1002/2016JD025843.

Sinha, P. R., Kondo, Y., Goto-Azuma, K., Tsukagawa, Y., Fkuda, K., Koike, M., Ohata, S., Moteki, N., Mori, T., Oshima, N., Førland, E. J., Irwin, M., Gallet, J. –C., Pedersen, C. A., 2018. Seasonal progression of the deposition of black carbon by snowfall at Ny-Ålesund, Spitsbergen. J. Geophys. Res., 123, 997–1016, https://doi.org/10.1002/2017JD028027.

Takeuchi, N., 2009: Temporal and spatial variations in spectral reflectance and characteristics of surface dust on Gulana Glacier, Alaska Range. J. Glaciol., 55, 701–709.

Takeuchi, N., Koshima, S. and Seko, K., 2001: Structure, formation and darkening process of albedo-reducing material (cryoconite) on a Himalaya Glacier: A granular algal mat growing on the glacier. Arctic, Antarctic, Alpine Research, 33, 115–122.

Takeuchi, N., Nagatsuka, N, Uetake, J., Shimada, R., 2014: Spatial variations in impurities (cryoconoite) on glaciers in northwest Greenland. Bull. Glaciol. Res., 32, 85–94.

Takeuchi, N., Fujisawa, Y., Kadota, T., Tanaka, S., Miyairi, M., Shirakawa, T., Kusaka, R., Federov, A. N., Konstantinov, P., Ohata, T., 2015. The effect of impurities on the surface melt of a glacier in the Suntar-Khayata Mountain Range, Russian Siberia. Frontiers in Earth Science, 3, 82. Doi: 10.3389/feart.2015.00082.

Tanaka, H. L., Tamura, M., 2016. Relationship between the Arctic oscillation and surface air temperature in multidecadal time-scale. Polar Science, 10, 199–209, doi.org/10.1016/j.polar.2016.03.002.

Tsukagawa, Y., Goto-azuma, K., Kondo, Y., Sugiura, K., Ohata, S., Mori, T., Moteki, N., Koike, M., Hirabayashi, M., Dallmayer, R., Enomoto, H., 2016. Black carbon concentrations in snow in Alaska. Seppyo, 78(6), 459–478 (in Japanese with English abstract).

Uchiyama, A., Yamazaki, A., Shiobara, M., Kobayashi, H., 2014. Case study on microphysical properties of boundary layer mixedphase cloud observed at Ny-Ålesund, Svalbard: Observed cloud microphysics and calculated optical properties on 9 June 2011. *Polar Science*, 8, 57–72. https://doi.org/10.1016/j.polar.2013.11.001

Vavrus, S., Holland, M. M., Bailey, D. A., 2011. Changes in Arctic clouds during intervals of rapid sea ice loss. Clim. Dynam., 36, 1475–1489, 2011.

Wientjes, I. J., Orlemans, J., 2010. An explanation for the dark region in the western melt zone of the Greenland ice sheet. The Cryosphere, 4, 261–268, doi: 10.5194/tc-4-261-2010.

Wu, D. L., Lee, J. N., 2012. Arctic low cloud changes as observed by MISR and CALIOP: Implication for the enhanced autumnal warming and sea ice loss. J. Geophys. Res., 117, D07107, doi:10.1029/2011JD017050.

Yamanouchi, T., 2019. Arctic warming by cloud radiation enhanced by moist air intrusion observed at Ny-Ålesund, Svalbard. Polar Science, 21, 110–116, https://doi.org/10.1016/j.polar.2018.10.009.

Yoshimori, M., 2014. Arctic warming amplification. Saihyo, J. Hokkaido Branch, Jpn Meteorol. Soc., No. 60 (in Japanese).

Yoshimori, M., Yokohata, T., Abe-Ouchi, A., 2009. A comparison of climate feedback strength between CO_2 doubling and LGM experiments. J. Clim., 22, 3374–3395. doi:10.1175/2009jcli2801.1.

Yoshimori, M., Abe-Ouchi, A., Watanabe, M., Oka, A., Ogura, T., 2014a. Robust seasonality of Arctic warming processes in two different versions of the MIROC GCM. J. Clim., 27, 6358–6375, doi:10.1175/jcli-d-14-00086.1.

Yoshimori M, Watanabe M, Abe-Ouchi A, Shiogama H, Ogura T, 2014b. Relative contribution of feedback processes to Arctic amplification of temperature change in MIROC GCM. Clim Dyn 42, 1613–1630. doi:10.1007/s00382-013-1875-9.

Yoshimori, M., Abe-Ouchi, A., Laine, A., 2017. The role of atmospheric heat transport and regional feedbacks in the Arctic warming at equilibrium. Clim. Dyn. doi 10.1007/s00382-017-3523-2.

4. Arctic and mid-latitude link

Within the recent Arctic abrupt warming, impacts to the mid-latitude are also noticed. As for these mid-latitude links, there are may discussions such as 6 reviews already exist, Vihma (2014), Walsh (2014), the National Academy of Sciences (2014), Cohen et al. (2014), Barnes and Screen (2015) and Orverland et al. (2015), but still many questions are left on (1) what is the mechanism to connect Arctic warming or sea ice retreat and mid-latitude extreme weather and (2) is the signal from the Arctic to mid-latitude meaningful or only the result of natural variability (Overland, 2016)? In case of North America, signal to noise ratio is especially small and it is not clear if the signal overcomes the natural variability. As for the east Eurasia and Japan, impacts of sea ice decrease on the mid-latitude weather is much solid. Honda et al. (2009) by reanalysis and numerical experiments, clearly showed the stationary Rossby wave response to the increased turbulent heat flux resulting from summer Arctic sea ice reduction intensifies the winter Siberian high that brings cold air outbreaks. Following this results, Inoue et al. (2012) explained actual synoptic mechanism in detail that the intensification of Siberian high would occur following the shift of cyclone route to the north in Siberian coast and made this relation very solid. After then, Japanese weather forecaster began to remind the relation with the Arctic for the forecast of extreme winter weather in Japan.

4. 1. Robustness of Arctic sea ice influence on the Eurasian cold winters

Over the past decade, severe winters occurred frequently in mid-latitude Eurasia, despite increasing global- and annual-mean surface air temperatures. Observations suggest that these cold Eurasian winters could have been instigated by Arctic sea ice decline, through excitation of circulation anomalies similar to the Arctic Oscillation. In climate simulations, however, a robust atmospheric response to sea ice decline has not been found, perhaps owing to energetic internal fluctuations in the atmospheric circulation. Here, Mori et al. (2014) used a 100-member ensemble of simulations with an atmospheric general circulation model driven by observation-based sea ice concentration anomalies to show that a result of sea ice reduction in the Barents-Kara Sea (BKS), the probability of severe winter has more than doubled in central Eurasia. In these simulations, the atmospheric response to sea ice decline is approximately independent of the Arctic Oscillation.

To clarify the relationship between the sea ice concentration (SIC)-driven atmospheric response and internal fluctuations of circulation, the dominant modes of variability governing winter surface air temperature (SAT) anomalies over Eurasia were extracted by applying empirical orthogonal function (EOF) analysis to DJF-mean SAT anomalies (1979–2013) in the reanalysis, over longitude 0°–180°, latitude 20°N–90°N (Fig. 4.1.1). The first mode (EOF1), accounting for 31% of total variance, represents a pattern of uniform warming over the entire Eurasian continent, accompanied by a meridional sea level pressure (SLP) dipole over the North Atlantic (Fig. 4.1.1a). The hemispheric circulation pattern resembles the North Atlantic Oscillation (NAO) or the Arctic Oscillation (AO), and the associated principal components (PC1) are highly correlated with the AO index (r=0.85) (Fig. 4.1.1c). The second mode (EOF2), accounting for 23% of the total variance, is characterized by a "Warm Arctic and Cold Eurasia" (WACE) pattern, straddled by positive SLP anomalies, which corresponds to an intensified Siberian High on its western edge (Fig. 4.1.1b). A markedly linear trend with positive slope (0.45/decade) is shown by the principle components (PC2; Fig. 4.1.1d), strongly tied to the winter SIC anomaly averaged in the BKS. Therefore, it is evident that WACE represents SAT variation associated with the SIC anomaly in the BKS and serves as a distinct mode of variability, independent of the AO.

The relative importance of these two modes to the occurrence of severe winters over Eurasia was examined by a scatter plot of PC scores (Fig. 4.1.1e), categorized by SAT anomalies over central Eurasia. The plot shows that almost all severe winters coincided with a negative phase of the AO and with a positive phase of the WACE. Therefore, the severe winters in central Eurasia can be explained by combination of these two modes. From combined 200-member AGCM ensembles, a comparison of the probability density functions (PDFs) of PCs calculated separately for low-ice (LICA) and high-ice (HICE) demonstrates that the polarity of WACE in the model tends to be more positive in LICE and more negative in HICE runs (Fig. 4.1.1f).

The dependence of the ensemble-mean response over central Eurasia on ensemble size reveals that the robust

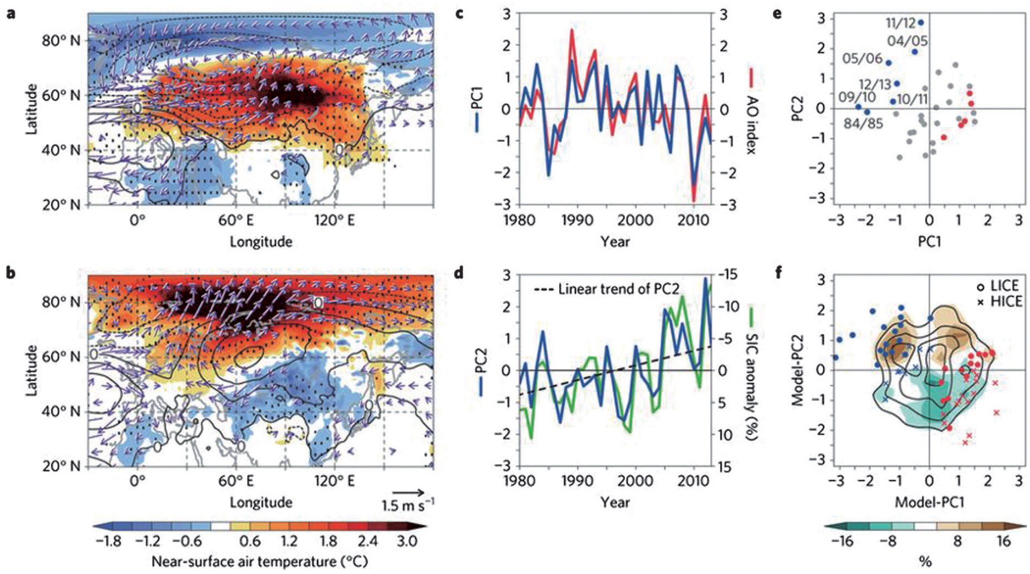

Fig. 4. 1. 1 Two leading mode governing winter SAT anomalies over Eurasia. a, b, DJF-mean SAT, SLP (contours, 1 hPa interval, negative contours are dotted) and near-surface wind (vector) anomalies in ERA-interium, regressed on normalized PC1 (a) and PC2 (b). Stippling indicates regions exceeding 95% statistical confidence. c, d, PC time series, AO index and SIC anomaly in the BKS (axis reversed). e, f, scatter plot of PCs for reanalysis (e) and simulation (f). Blue and red marks indicate cold and warm winters, respectively, grey marks in e indicate winters that were warm nor cold. Two-dimensional PDF of 200 members (contours, 3% interval) and differences between LICE and HICE PDFs (shading) are imposed in f (Mori et al., 2014).

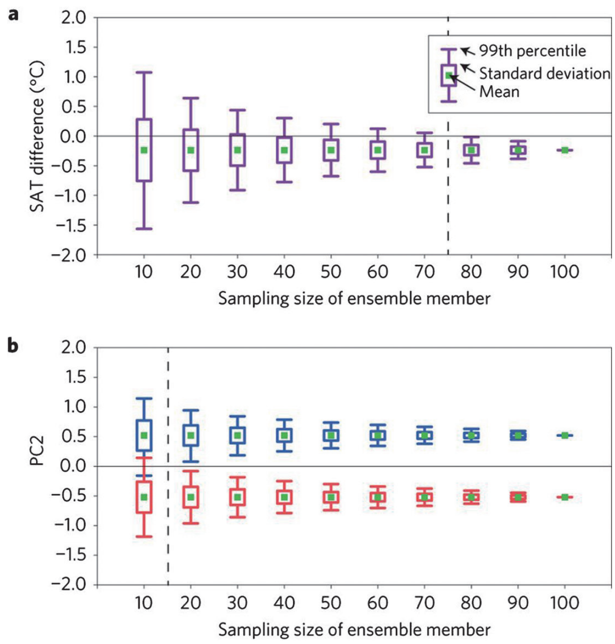

Fig. 4. 1. 2 Robustness and dependence of signal detection on ensemble size. Box-and-whisker plots of the ensemble-mean SAT difference between LICE and HICE experiments (former minus latter) averaged over central Eurasia (a) and ensemble-mean PC2 scores for LICE (blue) and HICE (red) experiments (b), shown as a function of ensemble size. Boxes and whiskers indicate ranges of one standard deviation and the 99th percentile, respectively, and are estimated based on bootstrap random sampling (100,000 times). Vertical dashed lines indicate the minimum number of ensemble members required for robust signal detection − that is, at the 99% confidence level (Mori et al., 2014).

SAT response ($p \leqq 0.01$) to SIC anomalies in the BKS, in terms of sign, could not be detected with less than 80 ensemble members (Fig. 4.1.2a). This small signal-to-noise ratio justifies the production of a large ensemble for signal detection. By contrast, in terms of polarity of PC2, the robust response to SIC anomalies could be detected with just 20 ensemble members (Fig. 4.1.2b), which implies that the effect of the AO on SAT anomalies weaken the signal-to-noise ratio. This partly explains the weaker ensemble-mean anomalies in the AGCM compared to the reanalysis.

Previous modeling studies that investigated possible impacts of sea-ice changes on the atmosphere suggest that the circulation response to sea-ice reduction has a negative AO/NAO like structure in winter. This may not be inconsistent with our results, because our AGCM simulation also shows a slight increase in frequency of the negative AO in LICE compared to HICE. However, the SIC-forced signal represented by a shift of the AO PDF is considerably smaller than for the WACE. Therefore, SAT anomalies associated with the AO are regarded as noise rather than signal in this analysis.

Given that the observed sea ice decline largely reflects the global warming signature, and that it will continue to decline in the future, one might expect the frequency of cold winters to increase as well, by the mechanism presented above. To examine this possibility, 22 climate simulations performed by the Coupled Model Intercomparison Project Phase 5 (CMIP5) model ensembles were analyzed for the period 1979–2098. Results indicate the frequency of severe winters may not increase, but rather decrease towards the end of the century, despite sea ice decline in the BKS. The contribution of the positive WACE trend to the cooling of Eurasia is identified, but a positive AO trend overcomes the cooling effect and results in a gradual SAT increase over central Eurasia. Therefore, the frequent occurrence of cold winters may be temporary phenomena in a transitional phase of eventual global warming, although projection uncertainty remains, owing partly to the insufficient number of ensemble members in CMIP5.

4. 2. Stratosphere path way

The paper by Nakamura et al. (2015) examined the possible linkage between the recent reduction in Arctic sea ice extent and the wintertime Arctic Oscillation (AO)/north Atlantic Oscillation (NAO). Observational analyses using the ERA- interim reanalysis and merged Hadley/Optimum Interpolation Sea Surface Temperature data reveal that a reduced (increased) sea ice area in November leads to more negative (positive) phases of the AO and NAO in early and late winter, respectively. The atmospheric response to observed sea ice anomalies was simulated using a high-top atmospheric general circulation model (AGCM for Earth Simulator, AFES version 4.1). The results from the simulation revealed that the recent Arctic sea ice reduction resulted in cold winters in mid-latitude continental regions, which linked to the anomalous circulation pattern similar to the negative phase of AO/NAO phase, and increased cold air advection from the Arctic to the mid-latitudes.

First, observational evidence was examined for a relationship between wintertime atmospheric and Arctic sea ice variations. Since sea ice has a much longer memory than the atmosphere, the lag-correlations were calculated between the DJF mean AO index and the sea ice area (SIA) index in the preceding months. The maximum correlation, between November SIA and the DJF mean AO indices, exceeded the 95% confidence level, was seen.

Fig. 4.2.1 shows anomalies of 3-month mean geopotential height at 500 hPa (Z500) from October-November-December (OND) to January-February-March (JFM) regressed on the time series of the November-December

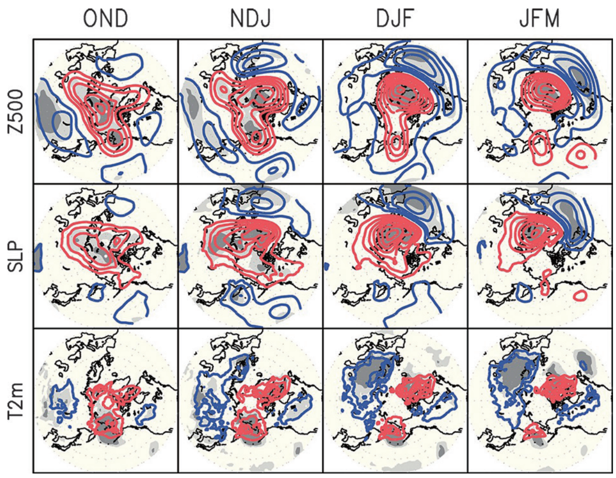

Fig. 4. 2. 1 (Top) 3-month mean geopotential height anomalies at 500 hPa (Z500) during (from left to right) OND, NDJ, DJF and JFM. These anomalies are lag regression coefficients against the normalized SIA index in November. Note that the sign of the coefficients is reversed so that red (blue) corresponds to positive (negative) anomalies when Arctic sea ice decreases. The contour interval is 5 m, and the zero line is omitted. Light and heavy shading indicate statistical significance of over 95% and 99%, respectively. (Middle) Regression coefficients of sea level pressure with a contour interval of 0.5 hPa. (Bottom) Regression coefficients of 2-m temperature with a contour interval of 0.5 K (Nakamura et al., 2015).

Arctic sea ice area. Most of the regressed anomalies show positive anomalies in the Arctic Ocean region but negative anomalies at mid-latitudes. This structure of the geopotential height anomaly resembles the negative phase of the AO/NAO pattern. Consistent with this result, regressions of sea level pressure (SLP) anomalies shown in Fig. 4.2.1 (middle row) have persistent positive anomalies in the Arctic Ocean region and negative anomalies at mid-latitudes.

Climatological impact of recent ice reduction from model results

The control run (CNTL) was performed with a 5-year monthly varying climatology of SST and SIT for the early period (1979–1983). A perturbed run (N.ICE) used the same SST as CNTL but SIT climatology for the late period (2005–2009). Both runs used the same initial conditions (the January 1979 monthly mean from JRA-25/JCDAS). 60-year integrations was carried out after 11-year spin-up. The differences between the 60-year averages of CNTL and N.ICE were examined. By this experimental design, only the sea ice difference is responsible for atmospheric differences without any influences from other external forcings such as SST variations. Fig. 4.2.2 shows the NH temperature response in

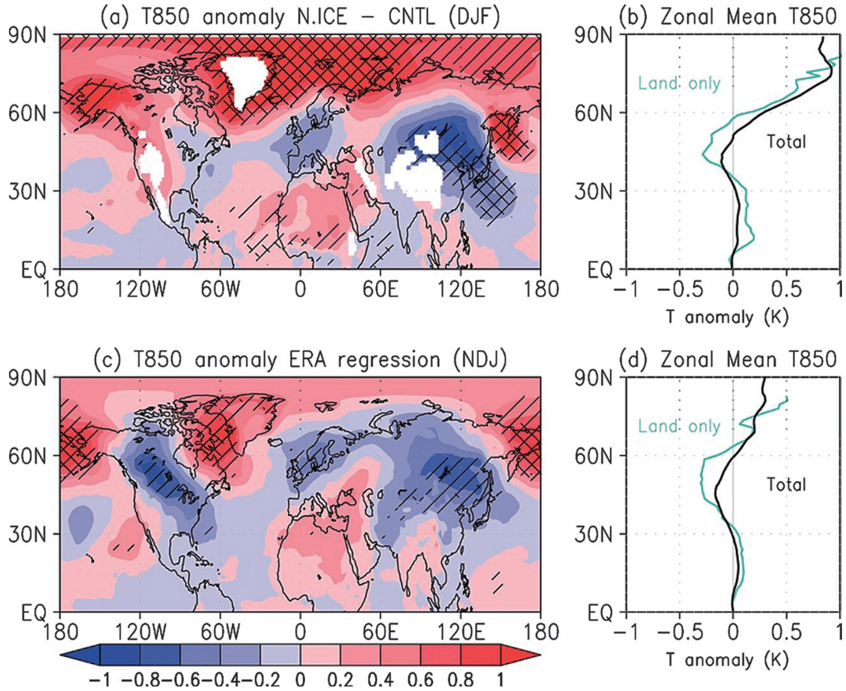

Fig. 4. 2. 2 (a) DJF mean temperature anomalies at 850 hPa of N.ICE against CNTL. Hatched and double-hatched areas indicate statistical significance (*t*-test) at the 95% and 99% confidence levels, respectively. (b) Zonal mean temperature anomalies. Black and light blue lines indicate the glaobal mean and land-only mean, respectively. (c and d) As for (a) and (b), but for the regressed field of ERA-interim in NDJ upon November SIA index. Values corresponding to −1.0σ of SIA index are shown (Nakamura et al., 2015).

N. ICE relative to CNTL, and its zonal mean, respectively. Significant cold anomalies are found in eastern Siberia and warm anomalies over the Arctic Ocean and the Sea of Okhotsk. The zonal mean temperature response shows large warm anomalies in the polar region. In mid-latitudes, while the zonal mean temperature response shows small anomalies, anomalies averaged only over land are clearly negative. The area-weighted temperature response over the NH mid-latitudes (30–60°N) is nearly zero, −0.01 K. However, averaging only over the land area gives −0.10 K, with a minimum of −0.29 K at 44.1°N. In comparison, Fig. 4.2.2c presents regressed fields of observed NDJ mean temperatures at 850 hPa associated with the normalized time series of November sea ice area. Warm anomalies in the Arctic and cold anomalies over mid-latitude land are also found. Continental cold anomalies are located in North America, Europe, and eastern Siberia. Simulated spatial pattern of the cold anomalies resemble the observed pattern, although for the simulation, there are no significances in North America and less in Europe. The area-weighted temperature response averaged over the NH mid-latitudes (30–60°N) is −0.09 K, with a minimum of −0.17 K at 45.0°N; averaged only over land, this becomes −0.18 K. with a minimum of −0.30 K at 49.5°N. Those results strongly suggest that the recent sea ice reduction contributes to the cooling of the NH continents.

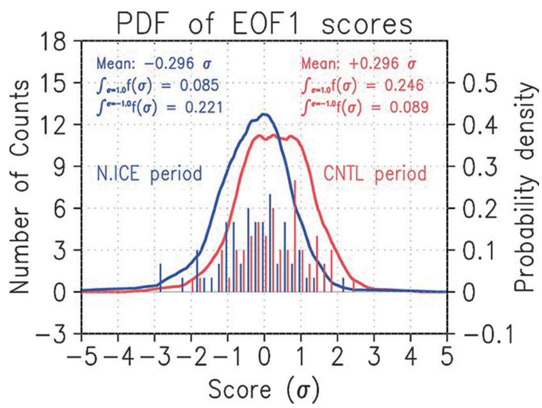

Fig. 4. 2. 3 Histogram of the EOF1 score from the combined EOF (0.2s bins); red and blue bars indicate the CNTL and N.ICE periods, respectively. The horizontal axis shows scores for the center of each bin. The vertical axis on the left hand side indicates the number of counts for each bin. Lines indicate the probability density function (PDF) estimated from the EOF1 score for the CNTL (red) and N.ICE (blue) periods, respectively. The vertical axis on the right-hand side indicates probability density. The mean score and the integral of the PDF above (below) 1.0σ (−1.0σ) are shown in the panel in the colors corresponding to CNTL and N.ICE (red and blue, respectively) (Nakamura et al., 2015).

It was found that the stationary Rossby wave response to the sea ice reduction in the Barents Sea region induced this anomalous circulation. It was also found that a positive feedback mechanism resulting from the anomalous

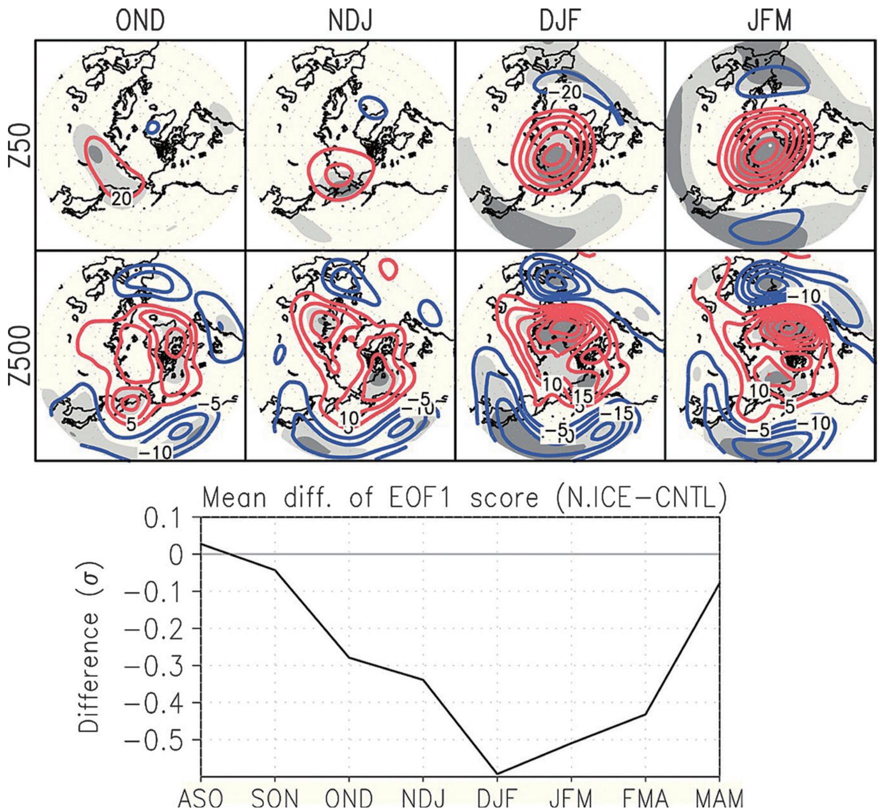

Fig. 4. 2. 4 Geopotential height anomalies of N.ICE with respect to CNTL in OND, NDJ, DJF and JFM at 50 hPa (upper row) and 500 hPa (lower row). The contour interval is 5 m, and the zero line is omitted. Light and heavy shading indicate statistical significance (*t*-test) at the 95% and 99% confidence levels, respectively (Nakamura et al., 2015).

meridional circulation that cooled the mid-latitudes and warmed the Arctic, which added an extra heating to the Arctic air column equivalent to about 60% of the direct surface heat release from the sea ice reduction.

The vertical motion induced by ice reduction warms the Arctic and cools mid-latitudes. Such an anomalous meridional circulation caused by stationary wave drag is accompanied by a weakening of the polar vortex, which shows variability that is strongly related to the AO/NAM. The contribution of Arctic sea ice reduction to the AO/NAM signals was estimated. To do this, an EOF analysis was applied to the 3-month men Z500 data from the 60-year results of the CNTL and N.ICE runs, and to the Z500 data from N.ICE combined with those from CNTL. Using this combined EOF analysis, the modulation of AO/NAM was evaluated as a response to recent sea ice reduction.

For a more quantitative estimate of the modulation of the primary mode, the probability density function (PDF) of the EOF1 score was examined using the nonparametric density estimation technique. Fig. 4.2.3 shows histograms and associated PDFs of combined EOF1 scores for the CNTL and N.ICE periods. The probability density for positive scores is larger over the CNTL period than over the N.ICE period. The probabilities of positive scores larger than 1.0σ were 24.6% and 8.5% for the CNTL and N.ICE periods, respectively. On the other hand, the probabilities for scores less than −1.0σ were 8.9% and 22.1% for the CNTL and N.ICE periods, respectively. Furthermore, while the PDF of CNTL is skewed to the right (skewness=0.175), that of N.ICE is skewed to the left (skewness=−0.096). This finding supports the more frequent appearances of a strong negative phase of the AO/NAM during the N.ICE period. The results also indicate that strong positive AO/NAM events occur less frequently (<50%) in association with a negative shift of the AO/NAM due to the Arctic sea ice reduction, and vice versa.

Finally, the seasonal evolution of the impact of sea ice reduction was estimated on NH climate fields. The panels of Fig. 4.2.4 compare the Z50 and Z500 anomalies of the N.ICE run with the CNT run from the OND to JFM periods. In the stratosphere, while positive anomalies are only evident in far-eastern Russia in the OND and NDJ periods, large positive anomalies are found in the Arctic surrounded by negative anomalies in the mid-latitudes in the DJF and JFM periods. This indicates the weakening of the polar vortex in mid to late winter. In comparison,

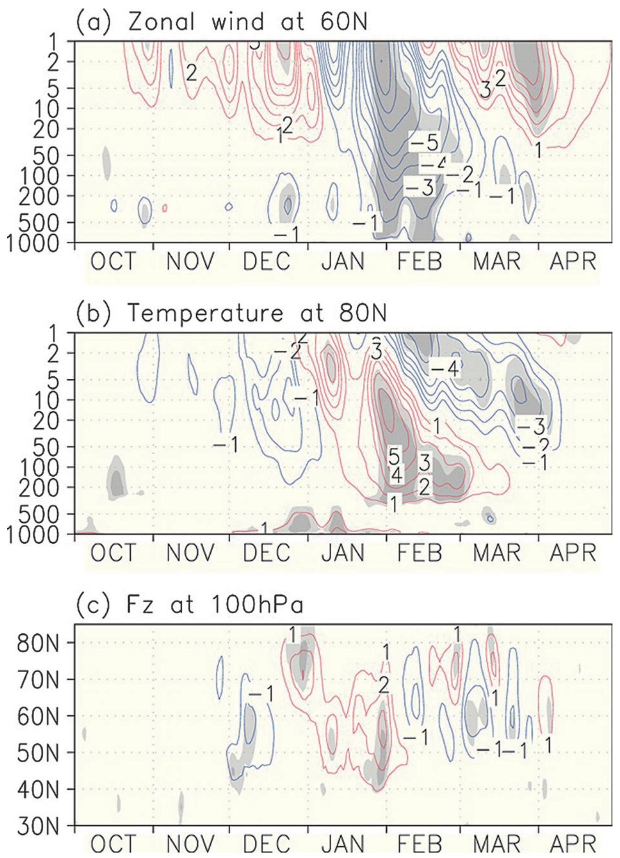

Fig. 4. 2. 5 Winter seasonal evolution of anomalies of N.ICE with respect to CNTL for (a) zonal mean zonal wind at 60°N (m s^{-1}), (b) zonal mean temperature at 80°N (K), and (c) vertical component of EP flux (10^4 m^2 s^{-2}) at 100 hPa. Contour shading intervals are as in Fig. 4.2.4 (Nakamura et al., 2015).

negative AO-like anomalies appear throughout the troposphere and strengthen toward late winter. The simulated seasonal evolution in the troposphere resembles that observed. The simulated weakening of the polar vortex in the stratosphere in the mid to late winter implies a role of the stratosphere in deepening the tropospheric annular mode.

Figs. 4.2.5a and b show daily anomalies (N.ICE minus CNTL) of zonal mean zonal wind at 60°N and temperature at 80°N, respectively. Significant deceleration of the polar night jet and a corresponding stratospheric warming anomaly are seen at the end of January. The signals propagate downward and penetrate into the troposphere in February. Fig. 4.2.5c shows a time-latitude cross-section of the vertical component of the EP flux anomaly through the lower stratosphere (100 hPa). A positive anomaly exist around 70°N at the end of December and around 50°N in January, indicating an intensification of the propagation of the planetary wave from the troposphere to the stratosphere. The intensified upward propagation of the planetary wave causes the deceleration of the polar night jet and the polar stratospheric warming, which later propagates downward to the troposphere. The simulated behavior is consistent with downward propagation of the stratospheric signature induced by the planetary wave modulation (Baldwin and Dunkerton, 1999, 2001). The results from this high-top model experiment suggested a critical role of the stratosphere in deepening the tropospheric annular mode and modulation of the NAO in mid to late winter through stratosphere-troposphere coupling.

Vertical planetary wave propagation

Extending the results of Nakamura et al. (2015), Jaiser et al. (2016) aim to provide detailed information on vertical planetary wave propagation and thus the coupling between stratosphere and troposphere by means of the comparison between the model experiment of Nakamura et al. (2015) and the ERA-Interim reanalysis data with respect to low and high sea ice conditions in the Arctic. A particular focus in on timing and regional characteristics of both upward and downward propagation of signals.

In winter, planetary waves are allowed to propagate from the troposphere into the stratosphere due to the prevalence of westerly winds in these layers. The corresponding vertical component of planetary scale EP flux is shown in Fig. 4.2.6 as the difference between low and high sea ice conditions. This illustrates the change in the vertical propagation of planetary waves. The polar cap average (65°N–85°N and 0°E–360°E) of vertical EP flux difference NICE minus CNTL in the AFES experiment (Fig. 4.2.6a) is positive starting in November and continues throughout December, at which the positive signal enters the stratosphere. Similar anomalies are present in ERA-Interim (Fig. 4.2.6b), but show less significance and are more disturbed by short periods of negative vertical EP flux differences. Upward propagating planetary waves are generated in the troposphere underpinning the relationship to sea ice changes. Later they reach the stratosphere and interact with the polar vortex.

In the difference between the N.ICE and CNTL run (Fig. 4.2.6a) strong negative planetary-scale EP flux anomalies start in mid-January. The signal is significant in the troposphere, while it is more disturbed in the stratosphere. This continues into February, when a significant negative anomaly becomes visible from the lower stratosphere down to the troposphere. The negative anomaly is related to an interruption of upward propagat-

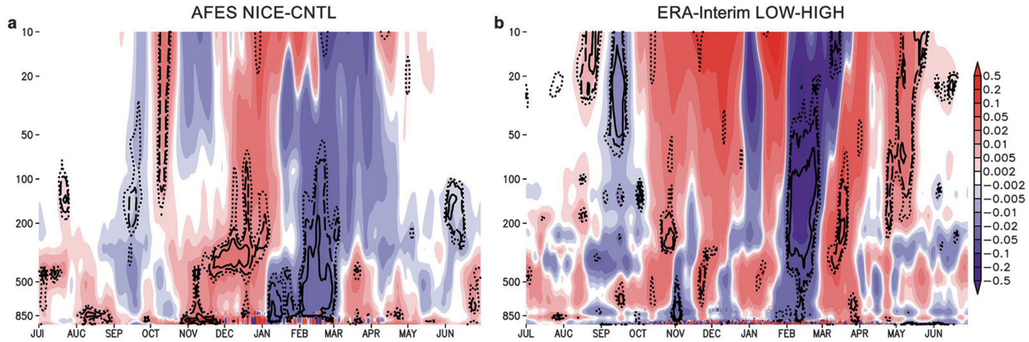

Fig. 4. 2. 6 Vertical component of planetary scale EP flux (m^2 s^{-2}) averaged over 65°N–85°N and 0°E–360°E as 21 day running mean time vs. height plot. (a) AFES N.ICE minus CNTL, (b) ERA-Interium low ice minus high ice period. Significance on 90% (dotted), 95% (dashed) and 99% (solid) level marked in black contours (Jaiser et al., 2017).

ing planetary waves for low ice conditions. While in the CNTL run, planetary waves still propagate into the stratosphere in February, this is not the case in N.ICE run. The absence of vertical wave propagation is an indication of a stratospheric polar vortex breakdown. In the ERA-Interim data (Fig. 4.2.6b), the negative anomaly clearly starts in the beginning of February without preceding negative anomalies in the troposphere or stratosphere. Again, the vertical propagation of planetary waves into the stratosphere is reduced under low sea ice conditions with weak indication of actual downward EP flux.

The role of stratosphere in the Arctic midlatitude climate linkage

Nakamura et al. (2016a) showed that midlatitude surface signals as a response to the Arctic sea ice reduction disappeared when artificially suppressing stratospheric wave mean flow interaction, based on numerical experiments using a high-top atmospheric general circulation model that has already shown sea ice impacts on the stratosphere highly consistent with observations. The results confirm the active role of the stratosphere in the Arctic midlatitude climate linkage. Then, from a posteriori analysis we argue that an observed reduction in sea ice alone can sufficiently affect atmospheric circulation to influence surface climate via the stratospheric pathway.

The atmospheric general circulation model for Earth simulator (AFES) version 4.1 was used with the model top about 60 km. Three sensitivity experiments (*FREE*, *RS10* and *RS30*), each consisting of two perpetual model runs (high sea ice (*HICE*) and low sea ice (*LICE*) using sea ice conditions of Early (5 year average of 1979–1983) or Late (2005–2009) periods. The Merged Hadley-National Oceanic and Atmospheric Administration/Optimum Interpolation sea surface temperature (SST) and sea ice concentration (SIC) data sets for period 1979–2011 were used for the boundary conditions of the model. The *FREE* experiment was the same as the sensitivity experiment performed in the previous study by Nakamura et al. (2015), in which sea ice conditions during the Early and Late periods were used as the boundary conditions for high sea ice (*HICE*) and low sea ice (*LICE*) runs, respectively.

The *RS10* experiment differed from *FREE* in that the zonal mean zonal wind above 10 hPa was restored at every time step by relaxation toward the climatology of the daily annual cycle in the *HICE* run of *FREE* with a maximum relaxation timescale of 1 day. Relaxation forcing τ^{-1} was zero ($\tau=\infty$) at and below the lowest level of 10 hPa and increased linearly up to 1.0 d^{-1} (τ=1 day) at the higher level of 3.16 hPa, and was 10 d^{-1} above that level. The *RS30* experiment was the same as *RS10* except that the lowest level was 31.6 hPa and the higher level was 10 hPa.

The simulated responses to sea ice reduction in the Arctic region was evaluated by subtracting the HICE results from the LICE results. In the FREE experiment, the geopotential height anomalies in the upper troposphere at the 300 hPa averaged over December-February clearly showed the negative AO phase pattern, which is characterized by positive anomalies over the Arctic and negative anomalies in surrounding regions (Fig. 4.2.7b). At 2 m height, large negative (cold) air temperature anomalies were found over the Siberia, and less significant negative anomalies were seen over the Europe and northeastern North America region (Fig. 4.2.7c). These results are highly consistent with observations that following a low summertime sea ice cover in the Arctic, the wintertime

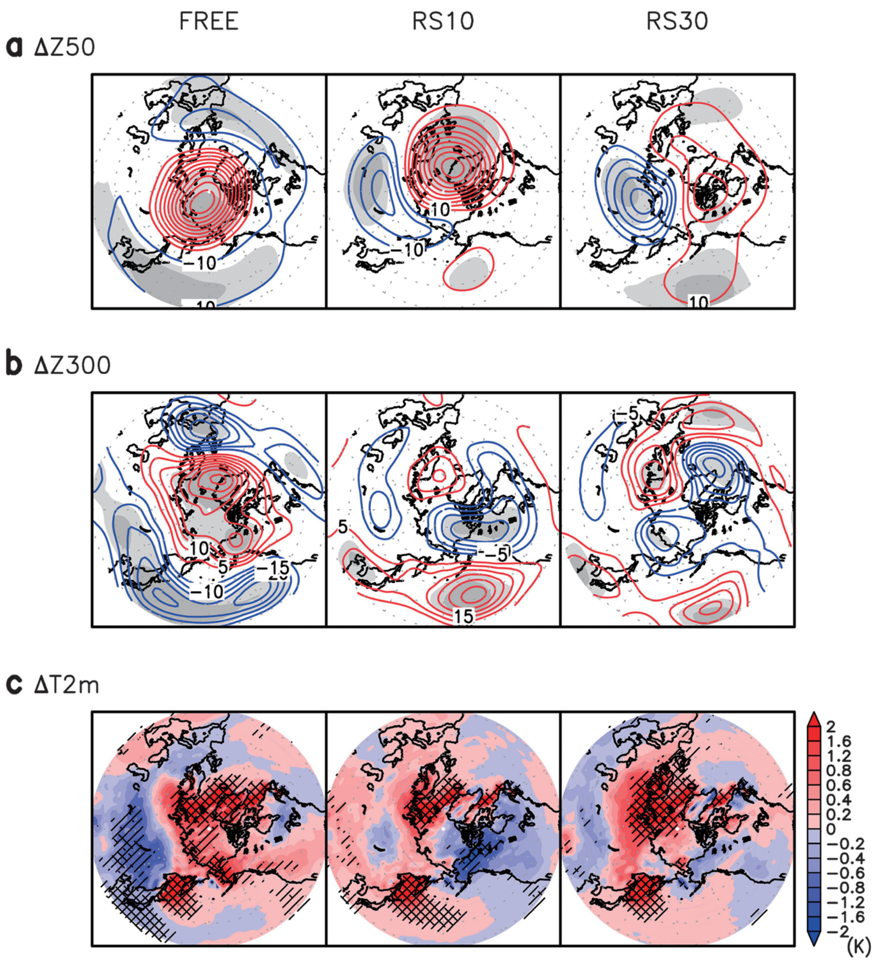

Fig. 4. 2. 7 December-February averaged anomalies (*LICE* minus *HICE*) of (a) geopotential height at 50 hPa (in m); (b) geopotential height at 300 hPa (m); and (c) temperature at 2 m height (K) in the (from left to right) *FREE*, *RS10* and *RS30* experiments. *LICE* and *HICE* runs indicate perpetual model simulations with annual cycle of low (2005–2009) and high (1979–1983) sea ice conditions, respectively. In (a) and (b), red (blue) contours indicate amplitudes of the positive (negative) anomaly, with the zero line omitted. Light and heavy grey shades indicate statistical significance greater than 95% and 99%, respectively. In (c), red (blue) shading indicates positive (negative) anomalies. Hatching (cross hatching) indicates statistical significance greater than 95% (99%) (Nakamura et al., 2016a).

AO tends to be in its negative phase, which brings severe winter weather to Europe and the North Atlantic sector. In the stratosphere the signal of the negative AO phase was marked in the geopotential height anomalies at 50 hPa (Fig. 4.2.7a).

When restoration was applied, the stratospheric AO signal was not so different (*RS10*) or was slightly weakened (*RS30*). In contrast, no clear AO signal at 300 hPa (Fig. 4.2.7b) nor any significant cold anomalies (Fig. 4.2.7c) was seen in eastern Siberia. Instead, a significant cold anomaly was seen over northwestern North America only in *RS10*. These results show that by damping stratospheric variations, the tropospheric response to the sea ice reduction was modified in such a way that the negative AO-like pattern and its associated cold anomalies in the troposphere were much subdued or even absent in the experiments with restored stratospheric circulation. Furthermore, the surface temperature anomalies differ among three experiments except for warm anomalies over ice reduction regions, suggesting large natural fluctuations of the temperature responses that hinder to detect sea ice impacts on the surface (Mori et al., 2014).

Central to stratosphere-troposphere coupling is a dynamical process by which planetary-scale waves propagate upward, followed by weakening of the stratospheric polar vortex and the downward progress of its signal back to the troposphere (Baldwin and Dunkerton, 2001; Nishii et al., 2011). These components were all clearly identified as responses to sea ice reduction in the *FREE* experiment. During December-March, an increase in anomalies in the vertical component of the Eliassen-Palm (E-P) flux (Fz) at 100 hPa averaged over the 50–80°N (a measure of the upward propagation of planetary-scale wave activity) just prior to a period of negative anoma-

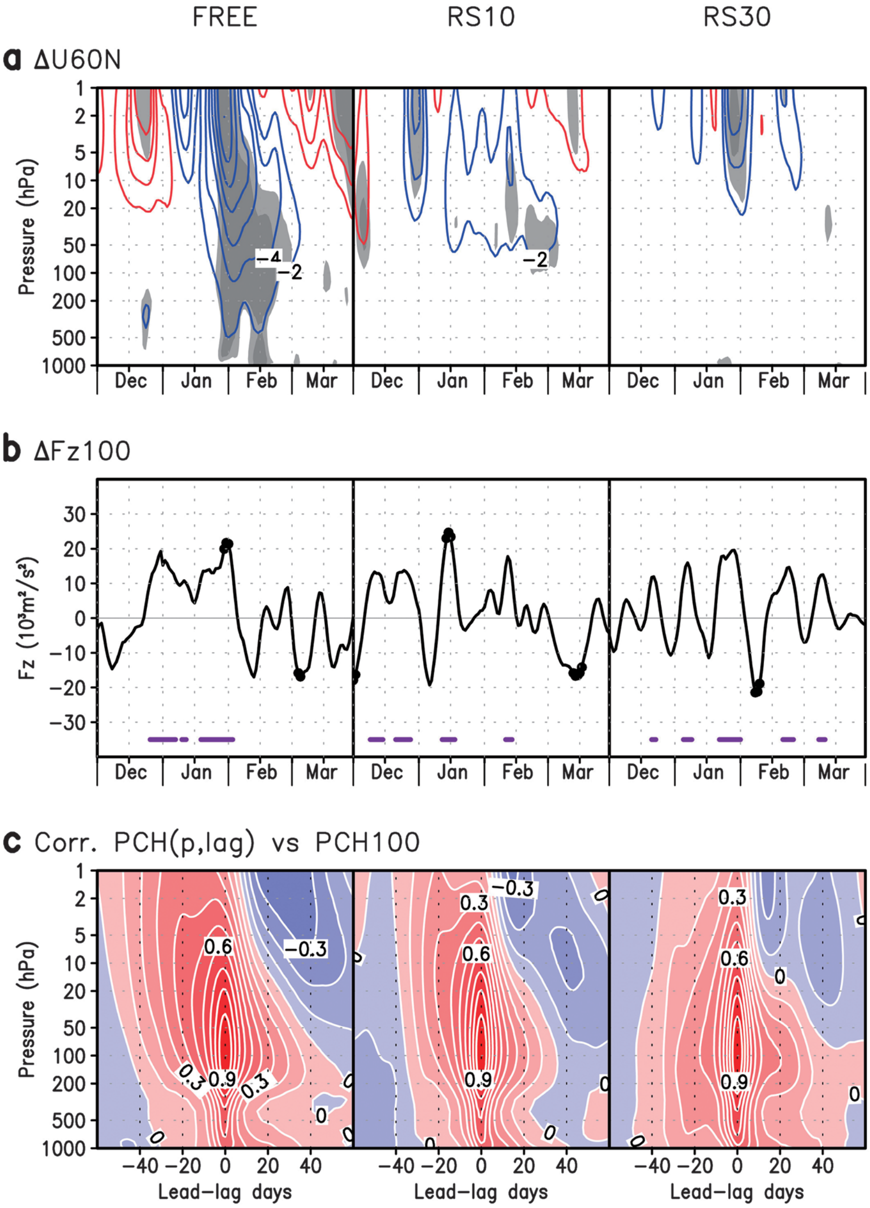

Fig. 4. 2. 8 (a) Time-height cross sections of daily mean anomalies (*LICE* minus *HICE*) of zonal mean wind at 60°N. Red (blue) contours indicate amplitudes of the positive (negative) anomaly, with the zero line omitted. Light and heavy grey shades indicate statistical significance greater than 95% and 99%, respectively; the contour interval is 2.0 m s^{-1}. (b) Time series of daily anomalies of F_Z (vertical component of the Eliassen-Palm flux) at 100 hPa averaged ver 50–80°N. Black dot indicates the statistical significance greater than 95%. Purple line segments signify periods when the F_Z anomaly exceeded 10^4 m^2 s^{-2}. (c) Lead-lag correlation coefficients of polar cap height (PCH) at various pressure levels with PCH at 100 hPa. Red (blue) shading indicates positive (negative) correlations; contour interval is 0.1 (Nakamura et al., 2016a).

lies in the zonal mean winds at 60°N in the upper stratosphere was followed 1 to 3 weeks later by downward propagation of the stratospheric signals to the troposphere (Fig. 4.2.8a and b). These temporal characteristics were further captured by a lead-lag correlation map of polar cap height (PCH) anomalies (Fig. 4.2.8c). From the reference height of 100 hPa, the upper stratosphere PCH anomalies led by up to 2 weeks, and the tropospheric PCH anomalies lagged on a much shorter timescale; together they indicate slow downward propagation of the stratospheric signal and faster coupling between the lower stratosphere and the troposphere.

These signatures were much reduced in *RS10*. Although similar negative wind anomalies in the stratosphere appeared after some intensification of upward wave propagation in December and January, their amplitudes were smaller, and the signal was less significant compared with the signatures in FREE. Importantly, the signal no longer reached the troposphere (Figs. 4.2.8a and b). In RS30, there was no significant downward propagation of the stratospheric signal (Fig. 4.2.8a). One might think that the stratosphere-troposphere coupling

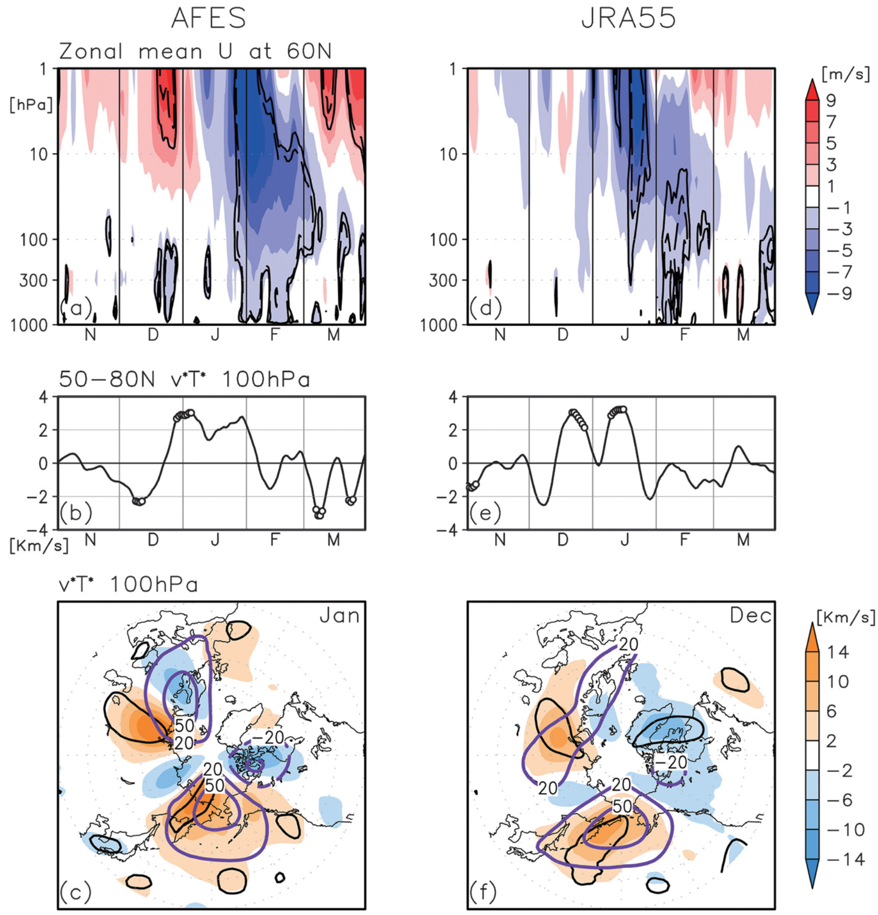

Fig. 4. 2. 9 AGCM differences (NICE-CNTL) in (a) a time-height cross section of zonal-mean zonal wind at 60°N (shading; m s^{-1}), (b) a time series of 50–80°N mean poleward eddy heat flux at 100 hPa (K m s^{-1}), and (c) January-mean poleward eddy heat flux at 100 hPa (shading; K m s^{-1}). NICE reflects the light ice conditions of the 2005–2009 period, whereas CNTL is for the heavy ice conditions of 1979–1984. The purple contours in c indicate the climatological (CNTL) poleward eddy heat flux. The JRA-55 anomalies of detrended (d) time-height cross section of zonal-mean zonal wind at 60°N (shading; m s^{-1}); (e) time series of 50–80°N mean poleward eddy heat flux at 100 hPa (K m s^{-1}); and (f) December mean poleward eddy heat flux at 100 hPa (shading; K m s^{-1}) for 1979–2015, regressed on the normalized December mean Barents-Kara (15–90°E, 70–85°N) SIC index, are also shown. Note that the sign of the coefficients is reversed. The purple contours in Fig. 4.2.9f indicate the climatological poleward eddy heat flux. The horizontal axes in Figs. 4.2.9a, b, d and e indicate the months. The solid (dashed) black lines in Figs. 4.2.9a, c, d and f indicate the statistical significance at the 90% (95%) level. The circles in Fig. 4.2.9b and eindicate the statistical significance at the 95% level (Hoshi et al., 2017).

would be weak in the restored experiments. On the contrary, at zero lag stratosphere-troposphere coupling was seen in all three experiments (Fig. 4.2.8c). Thus, one of the reasons for the lack of a tropospheric signal in *RS10* is that the signal in the lower stratosphere was too weak; this was caused by the unrealistically weak amplitudes of the anomalies in the upper stratosphere, which therefore no longer propagated to the lower stratosphere. The fact that the lead-lag structure in the upper stratosphere was degraded in a stepwise manner with restoration (Fig. 4.2.8c) provides strong evidence for an active stratospheric dynamic role and at the same time suggests the importance of the upper stratosphere.

Relationships between increased poleward eddy heat fluxes and upward propagating wave structure

Details of the characteristics of upward planetary wave propagation associated with Arctic sea ice loss under present climate conditions were examined by Hoshi et al. (2017) using reanalysis data and simulation results. The study used the Hadley Center Sea Ice and Surface Temperature data set version1, and the Japanese 55-year Reanalysis (JRA-55) for the analysis period of 1979–2015. Also, data from the model simulations presented in Nakamura et al. (2015) were used, in which Arctic sea ice loss sensitivity experiments were conducted using the AGCM for the Earth Simulator (AFES). The experiments consisted of a pair of model runs, each integrated over the same annual cycle repeatedly for 60 years using the same climatological forcings and boundary conditions except for Northern Hemisphere sea ice. One run (CNTL) used sea ice concentration (SIC) averaged over the high sea ice period of 1979–1983, and the other (NICE) used SIC averaged over low sea ice period of 2005–2009.

The poleward eddy heat flux is defined as v^*T^*, where v and T are the meridional wind and air temperature, respectively, and superscript * denotes the deviation from the zonal mean. Poleward eddy heat flux is a key indicator of the upward propagation of planetary scale waves, as it is proportional to the vertical component of the Eliassen-Palm flux in the transformed Eulerian mean framework. Nishii et al. (2009) decomposed the observed poleward eddy heat flux into three terms. Following their scheme, poleward eddy heat flux anomalies simulated in the AGCM experiments are decomposed as follows:

$$[v^*T^*]_{\mathrm{NICE-CNTL}} = [v_c^*\ T_a^*] + [v_a^*\ T_c^*] + [v_a^*\ T_a^*]_a, \tag{4.2.1}$$

where the subscripts c and a denote the climatological mean and anomaly, respectively, and the square brackets denote a 60 year temporal average. The first and second terms are referred to as the linear terms in temperature anomaly and in meridional wind anomaly, respectively. They represent poleward eddy heat flux anomalies formed by interactions between the climatological planetary wavefield and anomalous temperature and meridional wind fields, respectively. The last term is referred to as the nonlinear term, which is from both anomalous fields.

Figs. 4.2.9 a and b show the time evolution of AGCM daily-mean anomalies of zonal-mean zonal wind at 60°N and poleward eddy heat flux averaged over 50–80°N at 100 hPa, respectively. Negative zonal wind anomalies first appear in the upper stratosphere in early January, and significant signals subsequently propagate downward to the surface level in late January and February (Fig. 4.2.9a). An increase in poleward eddy heat flux in late December and January precedes the weakening of the polar vortex (Fig. 4.2.9b). Quantitatively, the increase in the poleward eddy heat flux averaged over January is about 19% of its climatological (CNTL) value. When these results are compared with the coefficients from the regression of JRA-55 on the December Barentz-Kara Sea SIC index, there is striking resemblance in features such as the increased poleward eddy flux in December and January (Fig. 4.2.9d) and weakened stratospheric polar vortex and subsequent downward propagating signal (Fig. 4.2.9d). Kim et al. (2014) and Nakamura et al. (2015) found similar results using slightly different methodologies on different data sets.

A question then arises as to whether there are any preferred locations for enhanced poleward eddy heat flux. There are indeed two centers of action in the poleward eddy heat flux climatology at the 100 hPa level (purple contours in Figs. 4.2.9c and f). One is situated near the Barents-Kara Sea and the other over the Bering region, appearing consistently in both simulation and JRA-55 results. The January-mean poleward eddy heat flux anomalies from the simulations (Fig. 4.2.9c) and from the regression coefficients corresponding to 1 standard deviation of the December-mean Barents-Kara Sea SIC index (Fig. 4.2.9f) are also shown. For both simulations and reanalysis data, positive poleward eddy heat flux anomalies appear in eastern Eurasia and its vicinity. In addition, there is an area located approximately south of the Barents-Kara Sea (central Eurasia region) with significant positive poleward eddy heat flux anomalies (Figs. 4.2.8a and f). This is part of a dipole pattern with an area of negative flux anomalies situated to the west. Comparing the location of this dipole pattern with respect to the climatological center, it was noted that the reduction in Arctic sea ice leads to a shift and strengthening of the region of positive poleward eddy heat flux in central Eurasia.

It was investigated how the spatial and temporal characteristics of poleward heat flux, and therefore of the upward propagation of planetary waves, are modulated in response to the present-day reduction in Arctic sea ice. Both the AGCM simulations and the reanalysis data revealed that the increased poleward eddy heat fluxes at the lower stratospheric level in the central Eurasia and east Eurasia regions result from Arctic sea ice loss. These increases in two regions are due to constructive coupling of the climatological planetary wave structure with anomalous meridional wind and temperature fields, respectively, which are dynamically linked through the propagation of stationary Rossby waves emanating from the Barents-Kara Sea region. This study provides a detailed three-dimensional picture of the way the recent Barents-Kara sea ice loss has modified the poleward eddy heat flux field in the lower stratosphere and subsequently affects the stratospheric wave structure, which likely

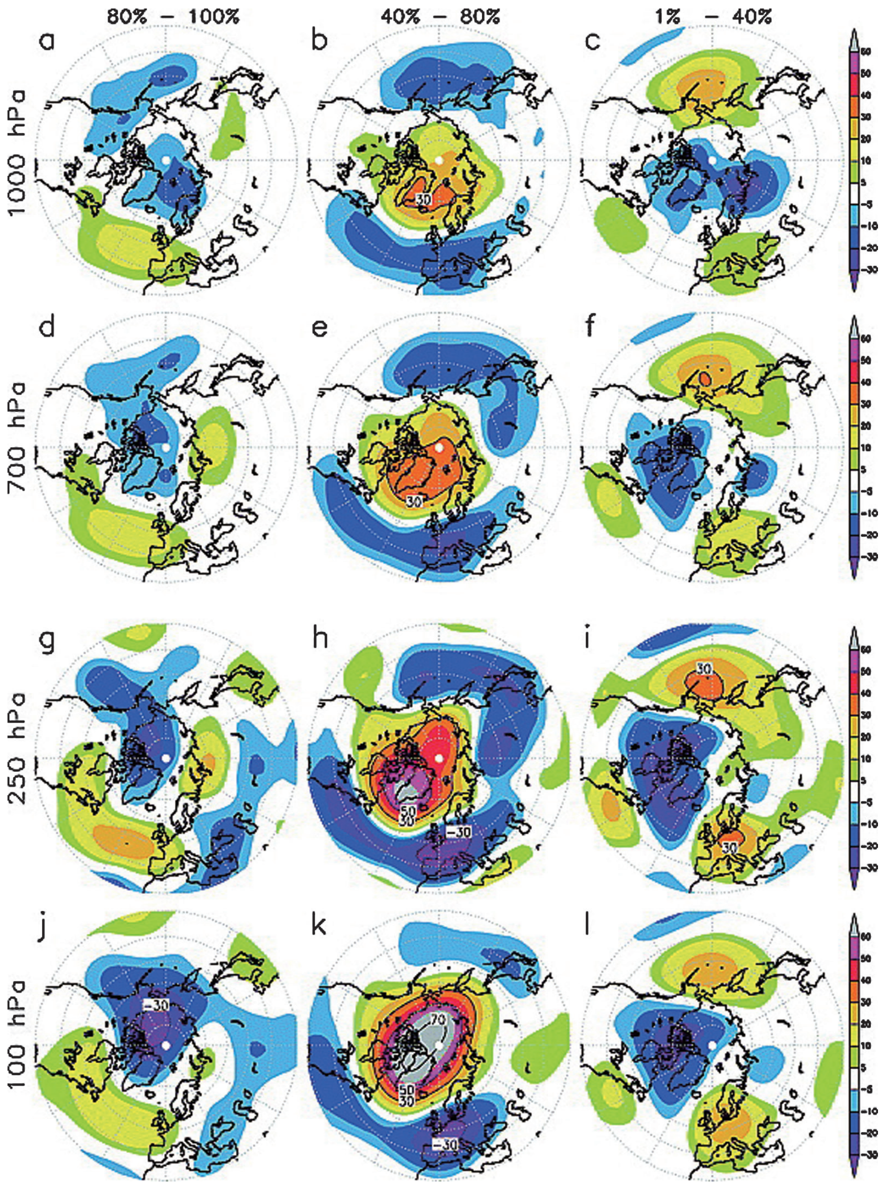

Fig. 4. 3. 1 Change in the geopotential height (gpm) at (a–c) 1000 hPa, (d–f) 700 hPa, (g–i) 250 hPa and (j–l) 100 hPa pressure levels as response to Barents-Kara sea ice transitions from 100% to 80%, 80% to 40% and 40% to 1% for February (Petoukhov and Semenov, 2010).

plays a key role in the Arctic-midlatitude climate linkages under present climate conditions.

4. 3. Future trends

A link between reduced Barents-Kara (B-K) sea ice and cold winter extremes over northern continents had already been discussed by Petoukov and Semenov (2010). They suggested that high-latitude atmospheric circulation response to the B-K sea ice decrease is highly nonlinear and characterized by transition from anomalous cyclonic circulation to anticyclonic one and then back again to cyclonic type circulation as the B-K sea ice concentration gradually reduces from 100% to ice free conditions. For the discussion, six simulations were performed with the ECHAM5 atmospheric general circulation model, developed at the Max Planck Institute for Meteorology. Sea ice concentration (SIC) in all six simulations was assigned to the 1987–2006 climatological mean data everywhere except for the B-K sector (30–80°E, 65–80°N). SIC in this sector in May through October was assigned to the 1987–2006 climatology in all six simulations, whereas November through April SIC was set to six different constant values, namely, 100, 80, 60, 40, 20 and 1% in six corresponding simulations.

The patterns of geopotential height anomalies through the troposphere (Fig. 4.3.1) principally differ from the corresponding anomalies associated with the negative NAO, in case of 80% to 40% SIC decrease (Fig. 4.3.1b, e and h) and from the positive NAO, in the events of

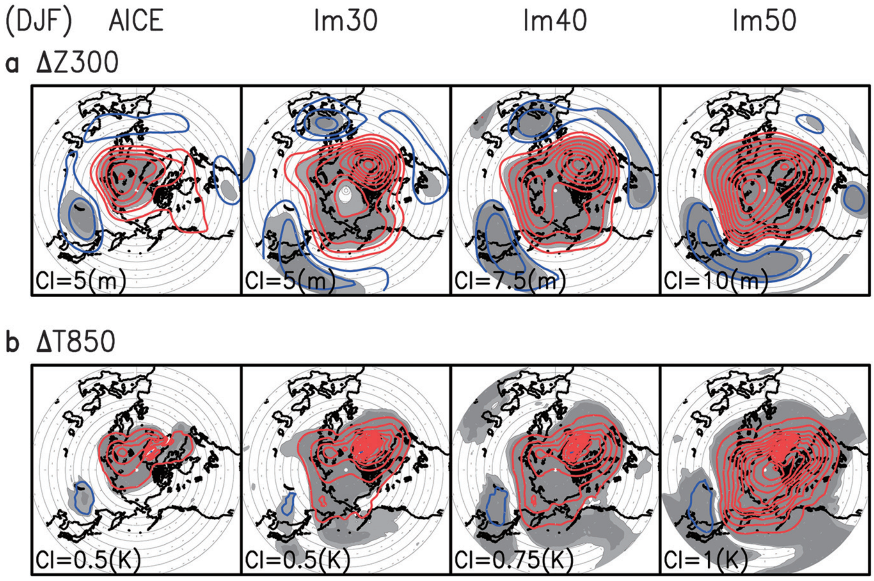

Fig. 4. 3. 2 Differences in the 150 year average of the (a) geopotential height at 300 hPa (m) and (b) temperature at 850 hPa (K) in December-January-February. Anomalies of (from left to right) *AICE*, *Im30*, *Im40* and *Im50* runs from the *CNTL* run are shown. A positive (negative) anomaly is indicated by red (blue) contours. The zero line is omitted and the contour interval is displayed at the bottom left corner of the plot. Statistical significance greater than 95% and 99% are indicated by light and heavy gray shading, respectively. *CNTL*, high ice period, 1979–1983; *AICE*, low ice period, 2005–2009; *Im30*, *Im40* and *Im50*: decrease of 30, 40 and 50 cm, respectively, from the *CNTL* (Nakamura et al., 2016b).

100% to 80% (Fig. 4.3.1a, d and g) and 40% to 1% (Fig. 4.3.1c, f and i) SIC reduction. Fig. 4.3.1b, e and h demonstrate, in particular, the counterclockwise turn of the anomalous blocking-like structure around the pole as compared to the canonic negative NAO pattern. The positive anomaly expands far deep to the south with increase in height. At the same time, both 100% to 80% and 40% to 1% SIC transitions trigger a development of the anomalous atmospheric circulation structures turned, relative to the positive-NAO structure, counterclockwise around the pole in the lower and middle troposphere (compare Figs. 4.3.1a and d and Figs. 4.3.1c and f). This is due to the lower-troposphere heat anomaly in the B-K sector as a source of the indicated anomalous atmospheric circulation structures. In the upper troposphere and lower stratosphere, a spatial pattern of the geopotential height anomaly still resembles the counterclockwise-turned positive NAO pattern in the case of 40% to 1% SIC decrease (Fig. 4.3.1i and l). Meanwhile, unlike the positive NAO structure, the anomalous Z250 and Z100 patterns for the 100% to 80% SIC decrease are practically in the opposite spatial phase to their counterparts in the lower- and middle-troposphere over the Barents Sea Region (compare Fig. 4.3.1 a and g).

Atmospheric responses to a reduction in Arctic sea ice

In this study, Nakamura et al. (2016b) examined how the impacts of climate on Arctic sea ice changes are modified during the transition from present-day conditions to ice-free conditions. They conducted four sensitivity experiments using the idealized assumption that Arctic sea ice is reduced to the ice-free condition in a stepwise manner. Then, an atmospheric general circulation model (AGCM) was adopted that has successfully captures the negative AO-like responses to a reduction in sea ice (Nakamura et al., 2015, 2016a; Jaiser et al., 2016). The comparison of the atmospheric responses to gradual changes in sea ice improves the understanding of the underlying mechanism of the association between sea ice and the AO. 150 year integrations were performed of a control run (*CNTL*), high ice period 1979–1983, and four perturbed runs, referred to as anomalous ice (*AICE*), low ice period, 2005–2009, *Im30*, decrease of 30 cm from *CNTL*, *Im40*, decrease of 40 cm from *CNTL* and *Im50*, decrease of 50 cm from *CNTL*, indicating an ice-free condition over the Arctic Ocean in all seasons.

The winter Northern Hemisphere (NH) atmospheric response to a reduction in present-day sea ice clearly showed a negative AO-like pattern in the upper tropospheric height anomaly (ΔZ300; Fig. 4.3.2a, *AICE*). The corresponding near-surface temperature response (ΔT850) was indicative of a warm anomaly over the Atlantic side of the Arctic Ocean, due to the reduction in sea ice in that area, and a cold anomaly over eastern Si-

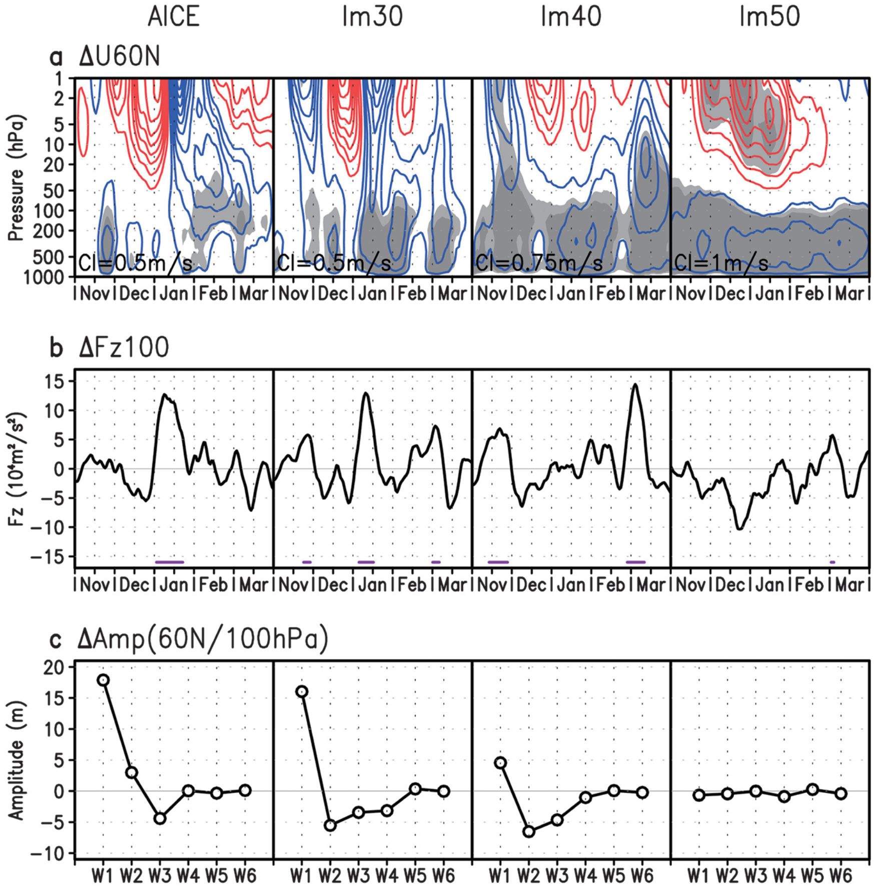

Fig. 4. 3. 3 (a) Daily evolutions of zonal mean zonal wind anomalies (respective runs minus *CNTL*) at 60°N. The contours and shading are the same as those in Fig. 4. 3. 2. (b) Daily evolutions of F_Z (i.e., vertical component of the Eliassen-Palm (E-P) flux) anomalies at 50–80°N and 100 hPa. Periods when the F_Z anomaly exceeded 5 x 10^4 m^2 s^{-2} are indicated by a purple line. (c) Anomalies of amplitude (i.e., square root of the power) decomposed into wave 1 to wave 6 components of January geopotential height at 60°N and 100 hPa (nakamura et al, 2016b).

beria (Fig. 4.3.2b, *AICE*). Even when sea ice thickness (SIT) was further reduced artificially as described above, the tropospheric responses showed negative AO-like patterns with amplitudes that increased as more sea ice was reduced (Fig. 4.3.2b, *Im30*, *Im40* and *Im50*). The experiments showed that the negative AO-like pattern intensifies with a reduction in Arctic sea ice. This appears to be consistent with current studies that presented a negative phase shift of the AO induced by the recent Arctic sea ice reduction (Nakamura et al., 2015). Some studies have emphasized the role of stratosphere-troposphere coupling on the association between sea ice and the AO (Jaiser et al., 2016; Nakamura et al., 2016a). However, stratospheric responses vary depending on the location of sea ice anomalies. Therefore, the role of the stratosphere was clarified in our experiments.

The intensification of the upward wave propagation and subsequent stratospheric polar vortex weakening occurred sporadically in *Im30* and *Im40* (Fig. 4.3.3a and b). Conversely, the negative tropospheric anomalies of the zonal wind were relatively large and significant, suggestive of independent tropospheric processes that differed from stratosphere-troposphere coupling. This independence between the stratosphere and troposphere was most obvious in *Im50* (Fig. 4.3.3a), in which the stratospheric polar vortex strengthened from November to February, consistent with the reduced upward wave propagation (Fig. 4.3.3b).

To examine why the intensity of the stratosphere-troposphere coupling weakened with increasing sea ice reduction, a wave number analysis was applied to the January mean height field in the lower stratosphere, an important level that connects the troposphere with the stratosphere through upward planetary-scale wave propagation (Nakamura et al., 2016a). January was chosen due to the clear contrast between the *AICE* and *Im50* cases. The wave number 1 amplitude of the 100 hPa geopotential height at 60°N was magnified clearly by 18 m (i.e., geopotential meter) in *AICE* (Fig. 4.3.3c). While the wave 1 amplitudes were magnified by 16 and 5 m in

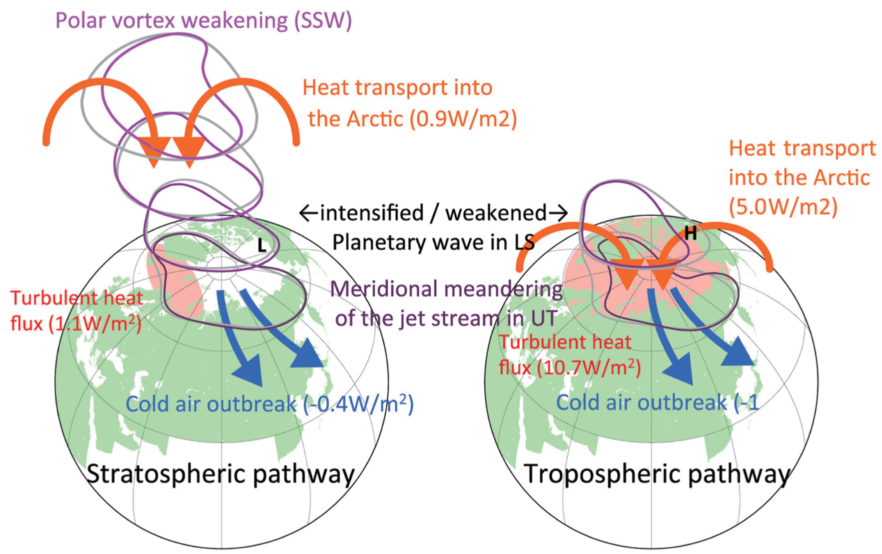

Fig. 4. 3. 4 Schematic diagram of two physical processes connecting Arctic sea ice loss and negative Arctic Oscillation (AO)-like response. (left) The stratospheric pathway corresponding to the *AICE* case in January. (right) The tropospheric pathway corresponding to NDJFM *Im50* case. Typical characteristics of the circumpolar jet stream at 10, 30, 100 and 300 hPa (only 100 and 300 hPa in the right plot) corresponding to the *high* and *low* sea ice cases are shown by grey and purple lines, respectively. Anomalous atmospheric heating due to associated meridional circulation changes and the turbulent heat flux are given in units of W m^{-2}. SSW, sudden stratospheric warming; LS, lower stratosphere; UT, upper troposphere (Nakamura et al., 2016b).

Im30 and *Im40*, respectively, no change was observed in *Im50*. This suggests that the wave 1 structure corresponding to a typical planetary-scale wave was responsible for the stratospheric polar vortex weakening. Therefore, it was suggested that the intensification (suppression) of the climatological Siberian trough in the lower stratosphere could strengthen (weaken) stratosphere-troposphere coupling, which has a role in the association between sea ice and the AO in accordance with features of the recent Arctic amplification.

Two processes are proposed that control the association between Arctic sea ice changes and the polarity of the winter AO, which are described below and drawn in Fig. 4.3.4.

1. The stratosphere-troposphere coupling process is dominated by an intensified climatological planetary-scale wave structure (Fig. 4.3.4, stratospheric pathway). This is mainly due to the intensification of the lower stratospheric Siberian trough associated with a reduction in Arctic sea ice on the Atlantic side of the Arctic Ocean. The results are consistent with recent studies that demonstrated the role of the stratosphere in the association between sea ice and climate observed in the most recent decade (Nakamura et al., 2016a). The results support that there are different stratospheric responses to different locations of surface heat sources.
2. The tropospheric process is controlled by the eddy heat flux due to a planetary-scale wave response in the troposphere (Fig. 4.3.4, tropospheric pathway). Increased meandering of the tropospheric jet stream, corresponding to the response of the stationary Rossby wave to Arctic sea ice reduction (Honda et al., 2009; Inoue et al., 2012; Nakamura et al., 2015), induces a negative AO-like pattern. Although the issue of longtitudinal dependency remains, the associated eddy momentum flux response is consistent with the conventional understanding of AO dynamics.

4. 4. Is the conclusion solid?

Even many studies have been done in GRENE Arctic Project on “Arctic and mid-latitude link”, the conclusions of series of studies are not clear. Mori et al. (2014) and Nakamura et al. (2015) tackle this topic squarely; however, the both conclusions seem not to be fully consistent. Mori et al. stressed that the link was due to two different elements, AO/NAO and WACE, and the latter was due to Barentz-Kara Sea ice retreat but the former was due mainly to natural variability. On the other hand, Nakamura et al. (2015) explained the WACE as an expression of AO/NAO, and focused to the pathway through the stratosphere. Nakamura et al. (2015) refer to Mori et al. (2014) only for the fact and do not make a discussion on the difference of the link.

After GRENE Arctic Project, still many discussions are continued. Mori et al. (2019a, b) made a clear evaluation of the weakness of simulations in describing the linkage compared to the observations; however, question was raised (Screen and Blackport, 2019). There is a growing debate about the strength of the influence of Arctic warming versus that of other regions, and those discussions were listed up as a "Nature Research collection" from 4 Nature related journals (Nature communications, 2019). One from the collection, Cohen et al. (2019), gave a wide review for the topic as "divergent consensus", and this phrase is a good expression of the topic at present.

References:

Baldwin, M. P. and Dunkerton, T. J., 1999. Downward propagation of the Arctic Oscillation from the stratosphere to the troposphere. J. Geophys. Res., 104 (D24), 30,937–30,946, doi: 10.1029/1999JD90445.

Baldwin, M. P. and Dunkerton, T. J., 2001. Stratospheric harbingers of anomalous weather regimes. Science, 294, 581–584, doi: 10.11126/ science.1063315.

Barnes, E. A., Screen, J. A., 2015. The impact of Arctic warming on the midlatitude jet-stream: Can it? Has it? Will it? WIREs Clim. Change 6 (3), 277–286, http://dx.doi.org/10.1002/wcc.377.

Cohen, J., Screen, J. A., Furtado, J. C., Barlow, M., Whittleston, D., Coumou, D., Francis, J., Dethloff, K., Entekhabi, D., Overland, J., Jones, J., 2014. Recent Arctic amplification and extreme midlatitude weather. Nat. Geosci. 7 (9), 627–637, http://dx.doi.org/10.1038/ngeo2234.

Cohen, J. and 31 others, 2019. Divergent consensuses on Arctic amplification influence on midlatitude severe winter weather. Nature Clim. Change, 10, 20–29, doi.org/10.1038/s41558-019-0662-y.

Honda, M., Inoue, J., Yamane, S., 2009. Influence of low Arctic sea-ice minima on anomalously cold Eurasian winters. Geophys. Res. Lett. 36, L08707. http:// dx.doi.org/ 10.1029/ 2008GL037079.

Hoshi, K., Ukita, J., Honda, M., Iwamoto, K., Nakamura, T., Yamazaki, K., Dethloff, K., Jaiser, R. and Handorf, D., 2017. Poleward eddy heat flux anomalies associated with recent Arctic sea ice loss. Geophys. Res. Lett., 44, 446–454, doi: 10.1002/2016GL071893.

Inoue, J., Hori, M. E., Takaya, K., 2012. The role of Barents sea ice in the wintertime cyclone track and emergence of a warm-Arctic cold-Siberian anomaly. J. Clim. 25, 2561–2568. http:// dx.doi.org/ 10.1175/ JCLI-D-11-00449.1.

Jaiser, R., Nakamura, T., Handorf, D., Dethloff, K., Ukita, J. and Yamazaki, K., 2016. Atmopheric winter response to Arctic sea ice changes in reanalysis data and model simulations. J. Geophys. Res., 121, 7564–7577.

Kim, B.-M., Son, S.-W., Min, S.-K., Jeong, J.-H., Kim, S.-J., Zhang, X., Shim, T. and Yoon, H.-J., 2014. Weakening of the stratospheric polar vortex by Arctic sea-ice loss. Nat. Commun., doi: 10.1038/ncomms5646.

Mori, M., Watanabe, M., Shiogama, H., Inoue, J. and Kimoto, M., 2014: Robust Arctic sea-ice influence on the frequent Eurasian cold winters in past decades. Nature Geoscience, 7, 869–873.

Mori, M., Kosaka, Y., Watanabe, M., Nakamura, H., Kimoto, M., 2019a. A reconciled estimate of the influence of Arctic sea-ice loss on recent Eurasian cooling. Nature Clim. Change, 9, 123–129, doi.org/10.1038/s41558-018-0379-3.

Mori, M., Kosaka, Y., Watanabe, M., Taguchi, B., Nakamura, H., Kimoto, M., 2019b. Reply to: Is sea-ice-driven Eurasian cooling too weak in models?. Nature Clim. Change, 9, 937–939, doi.org/10.1038/s41558-019-0636-0.

Nakamura, T., Yamazaki, K., Iwamoto, K., Honda, M., Miyoshi, Y., Ogawa, Y., Ukita, J., 2015. A negative phase shift of the winter AO/NAO due to the recent Arctic sea-ice reduction in late autumn. J. Geophys. Res. 120, doi:10.1002/2014JD022848.

Nakamura, T., Yamazaki, K., Iwamoto, K., Honda, M., Miyoshi, Y., Ogawa, tomikawa, Y. and Y., Ukita, J., 2016a. The stratospheric pathway for Arctic impacts on midlatitude climate. Geophys. Res. Lett., 43, 3494–3501, doi: 10.1002/2016GL068330.

Nakamura, T., Yamazaki, K., Honda, M., Ukita, J., Jaiser, R., Handorf, D. and Dethloff, K., 2016b. On the atmospheric response experiment to a Blue Arctic Ocean. Geophys. Res. Lett., 43, 10,394–10,402, doi: 10.1002/ 2016GL070526.

National Academy of Sciences, 2014. Linkages between Arctic Warming and Mid-latitude Weather Patterns. The National Academies Press, Washington, DC.

Nature communications, 2019. A tug-of-war over the mid-latitudes (Editorial). Published online, 09 Decemmber 2019, 1–2, doi.org/10.1038/s41467-019-0.

Nishii, K., Nakamura, H. and Miyasaka, T., 2009. Modulations in the planetary wave field induced by upward-propagating Rossby wave packets prior to stratospheric sudden warming events: A case study. Q. J. R. Meteorol. Soc., 135, 39–52, doi: 10.1002/qj.359.

Nishii, K, Nakamura, H. and Orsolini, Y. J., 2011. Geographical dependence observed in blocking high influence on the stratospheric variability through enhancement or suppression of upward planetary-wave propagation. J. Climate, 24, 6408–6423.

Overland, J. E., 2016. A difficult Arctic science issue: Midlatitude weather linkages. Polar Science 10, 210–216, http://dx.doi.org/10.1016/ j.polar.2016.04.011.

Overland, J. E., Francis, J. A., Hall, R., Hanna, E., Kim, S.-J., Vihma, T., 2015. The melting Arctic and midlatitude weather patterns: are they connected? J. Clim. 28, 7919–7932, http:// dx.doi.org/ 10.1175/ JCLI-D-14-00822.1.

Petoukhov, V. and Semenov, V., 2010. A link between reduced Barents-Kara sea ice and cold winter extremes over northern continents. J. Geophys. Res., 115, D21111, doi: 10.1029/ 2009JD013568.

Screen, J. A., Blackport, R., 2019. Is sea-ice-driven Eurasian cooling too weak in models? Nature Clim. Change, 9, 934–936, doi.org/10.1038/s41558-019-0635-1.

Vihma, T., 2014. Effects of Arctic sea ice decline on weather and climate: a review. Surv. Geopys. 35, 1175–1214, http: // dx.doi.org/ 10.1007/ s10712-014-9284-0.

Walsh, J. E., 2014. Intensified warming of the Arctic: causes and impacts on middle latitudes. Glob. Planet. Change 117, 52–63, http:// dx.doi.org/ 10.1016/ j.gloplacha2014. 03.003.

5. Sea ice distribution and Arctic sea routes

We have proposed empirical method to estimate timing of disappearance of sea ice, and proposed a simple model using just sea ice motion to evaluate volume transportation of upper ocean circulation, so called "Beaufort Gyre", that delivers the heat into the central Arctic Ocean and affects fate of sea ice. Analyses using in-situ and satellite observation data have clarified that volume transportation of the oceanic Beaufort Gyre is determined by past sea ice motion from about four years previously. We have also constructed methods to derive the timing of the disappearance of sea ice associated with rafting of sea ice from satellite-derived high-accuracy sea ice motion data. We also conducted a study using a high-resolution numerical Arctic Ocean model to reveal the structure of the heat transport system from the Atlantic to the Arctic, and the impact of meso-scale eddies on the advance/retreat of sea ice cover.

Another important theme of ours is seasonal-scale sea ice prediction, which is necessary for a decision of whether or not to take the Arctic route. We have improved the statistical method of the prediction using satellite remote-sensing data. In 2015, our prediction provided a good forecast of the timing of summer ice retreat and the spatial pattern of the minimum ice cover. Our activity regarding the Arctic sea route included many other themes, such as the optimal routing of ships, engineering studies on ship/ice interaction, ship icing, economic evaluations, and a proposal of scenarios for the use of Arctic sea routes. With these multidisciplinary efforts, studies for realizing the sustainable use of Arctic sea routes have advanced greatly during the GRENE Arctic Climate Change Research Project.

5. 1. Sea ice distribution by ocean heat transport and rafting of sea ice

Sea ice retreat and ocean circulation

In recent years, the anomalous sea ice retreat into the central Arctic basin has been mainly observed in the Pacific sector of the Arctic Ocean. First year ice has replaced multi year ice as the dominant sea ice type in the Arctic Ocean. In this situation, the thickness of first year ice at the melt onset, which is influenced by sea ice growth in winter, is an important precondition of whether or not sea ice can survive during the following summer. The sea ice growth in winter is influenced by thermohaline stratifications in the upper ocean. In the Pacific sector of the Arctic Ocean, one of the major heat inputs to the upper ocean just beneath the surface mixed layer is primarily controlled by advection of the warm Pacific Summer Water (PSW). PSW is transported into the Canadian Basin (Fig. 5.1.1) by the oceanic Beaufort Gyre (OBG), driven by winds and sea ice motions. Therefore, the volume transport of the OBG is a key parameter to determine upper oceanic heat contents in the basin.

In the case of the upper ocean circulation driven by only Ekman pumping without any wave propagation and lateral vorticity inputs, the upper ocean circulation simul-

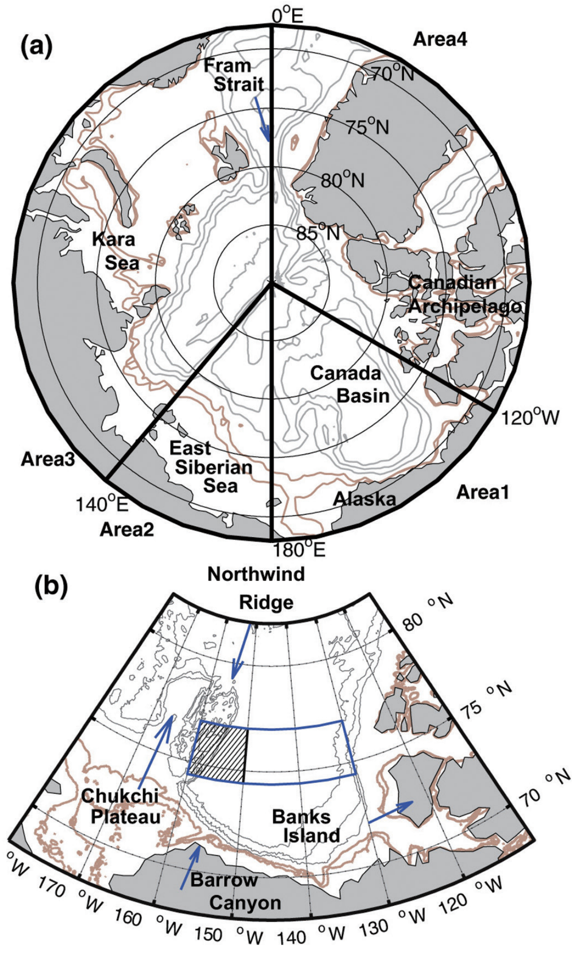

Fig. 5. 1. 1 Bottom topography of study area. Grey (brown) contours indicate seafloor topographies deeper (shallower) than 1000 m (100 m), contour interval 1000 m (50 m). a) The Arctic Ocean. Area 1-4 show the areas for which time series of the areal sea ice area (SIA) shown in Fig. 5.1.2b were calculated. b) The Canada Basin. The zonal band in the blue box, 74.4°–77°N, 130°–160°W, shows the area for which time series of δ x u_W and δ x u_I, shown in Fig. 5.1.3b and c, were calculated. The black hashed box, 74.4°–77°N, 150°–160°W, is the area used to calculate time series f the spatial average of ocean dynamic height (ODHc) shown in Fig. 5.1.3d (Yoshizawa et al., 2015).

taneously responds to surface forcing. The observational evidence, however, showed that the spatial pattern of the OBG did not correspond to that of the overlying sea ice gyre. As such, the spatial inconsistency suggests that there was a time lag in the response of the OBG relative to surface forcing. Therefore, the time scale of this delayed oceanic response significantly influences oceanic heat transportation into the basin and the resulting sea ice variations. As a first step toward understanding oceanic influences on sea ice variations, Yoshizawa et al. (2015) examined the relative contributions of past surface forcing to the current state of the OBG. The quantitative result enables to forecast volume transports of the OBG within a time scale that is shorter than the delayed oceanic response.

The hydrographic data used were collected under the Joint Western Arctic Climate Studies (JWACS) with Canadian Coast Guard Ship (CCGS) Louis S. St-Laurent (LSSL) 2002–2008 and R/V Mirai 2002, 2004 and 2008, and under the Korea-Polar Ocean in rapid transition (K-PORT) expedition with the Korean icebreaker ARAON 2011 and 2012. Also data from XCTD stations, collected during CCGS LSSL 2009–2012, were used. Sea ice concentration data were analyzed derived from the NASA team algorithm (Cavalieri et al., 1984), provided by the NSIDC. Sea ice motion data were calculated by the maximum cross correlation method, the so-called particle image velocimetry method (Adrian, 1991), for brightness temperature images obtained from AMSR-E (Kamoshida and Shimada, 2010), mainly using 89 GHz channel data gridded onto a polar-stereo projection (2.08 × 2.08 km).

Fig. 5.1.2a shows time series of the sea ice area (SIA) in September in the area north of 68°N (hereafter referred to as the entire Arctic Ocean). SIA did not show a constant reduction trend, but accompanied rapid reduction events in 1989–1990, 1998, 2007 and 2012. First, it was investigated whether these events occurred in the entire Arctic Ocean or were dominated by specific regions. Fig. 5.1.2b shows time series of SIA in the four distinct areas (area 1–4 depicted in Fig. 5.1.1a). The rapid reduction in 1989–1990 was led by the reduction in the eastern hemisphere in the Arctic Ocean (areas 2 and 3), where the sea ice motion is characterized by the transpolar sea ice drift (blue and black curves in Fig. 5.1.2b). The reduction in this region is interpreted as discharges of sea ice through the Fram Strait, which correlate with variations of climatic indices such as the Arctic Oscillation

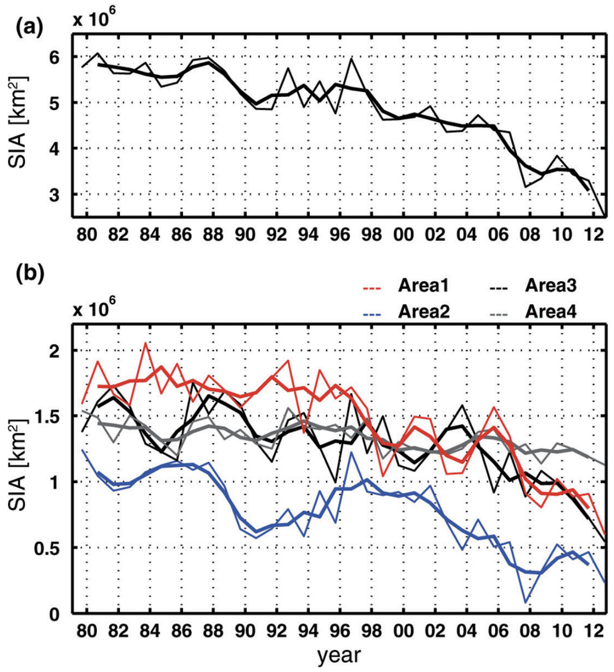

Fig. 5. 1. 2 Time series pf SIA (km^2) in September, a) in the entire Arctic Ocean, the area north of 68°N, b) in the individual four area depicted in Fig. 5.1.1a: area 1 (120°–180°W, red curve), area 2 (140°–180°W, blue), area 3 (0°–140°E, black), and area 4 (0°–120°W, grey). Thick and thin curves denote 3-year running mean values and annual values, respectively (Yoshizawa et al., 2015).

(AO). In this period, in contrast, no significant change was observed in the western hemisphere (areas 1 and 4; red and grey curves in Fig. 5.1.2b). The second rapid reduction in 1998 was led by a regional reduction in the Canadian Basin (area 1; red curve in Fig. 5.1.2b), without significant changes in other areas (blue, black and grey in Fig. 5.1.2b). These regional contrasts suggest that the mechanism of sea ice reduction differs from region to region.

After 1998, the SIA reduction trends in areas 1, 2 and 3 (red, blue and black curves in Fig. 5.1.2b), and also in the entire Arctic Ocean (Fig. 5.1.2a), were much larger than those before 1998. In 2012, SIA in the entire Arctic Ocean hit a new minimum record.

During 1998–2006, before the anomalous sea ice reduction in 2007, an embayment-shaped sea ice retreat into the basin was observed in the western Canada Basin, and in other areas, the ice edges were still located in the shelf regions or on the shelf slopes. During 2007–2012, in the East Siberian and Kara Seas, the ice edge moved offshore but did not enter into the basin deeper than 500m. In the Canada Basin, however, the open water area was enlarged northward along the Northwind Ridge and the Chukchi Plateau, where the major pathway of

PSW was identified (Shimada et al., 2001; Steele et al., 2004). This retreat pattern suggests that the oceanic heat carried by the OBG is a key element to understanding the regional sea ice change in the Canada Basin.

Oceanic influences on sea ice reduction in the Canada Basin

Shimada et al. (2006) explained that the strengthening of the OBG in the late 1990s was initiated by the strengthening of basin-scale sea ice motion due to less friction of the sea ice cover against the Alaskan Beaufort coast, and then more oceanic heat, leading to the substantial sea ice reduction, was delivered into the deep Canada Basin. Here, attempt was made to identify which parameters have controlled the observed temporal variations of the summer SIA in recent years.

First of all, features of spatial distributions of the OBG were briefly mentioned, in order to introduce how the volume transport can be evaluated by surface forcing data. Based on the Sverdrup relation, the vertically averaged volume transport of the OBG would be given by just the surface torque. Fig. 5.1.3b and c show time series of curls of 10 m winds and sea ice velocities, $\nabla \times u_W$ and $\nabla \times u_I$, averaged for the ice-covered period from November to June in the zonal band, in the blue box depicted in Fig. 5.1.1b, respectively.

During 1979–1996, $\nabla \times u_W$ increased (Fig. 5.1.3b), while there were no significant changes in both $\nabla \times u_I$ (Fig. 5.1.3c) and SIA in the Canada Basin (Fig. 5.1.3a). This suggests that vorticities of surface winds did not penetrate into sea ice under the heavy ice condition during this period (Shimada et al., 2006). From 1997 to 2004, $\nabla \times u_I$ decreased (Fig. 5.1.3c) coherently with a decrease in $\nabla \times u_W$ (Fig. 5.1.3b). This suggests that the ratio of the sea ice velocities, which are tangential to wind vectors, to the wind velocities, which is a proxy of the kinematic coupling between atmosphere and sea ice (Kimura and Wakatsuchi, 2000), was getting larger than that before 1997. When the anomalous summer sea ice reduction was observed in 2007–2008 (Fig. 5.1.3a), both $\nabla \times u_W$ and $\nabla \times u_I$ decreased substantially, i.e., clockwise rotation was strengthened (Fig. 5.1.3b, c).

After 2009, $\nabla \times u_W$ rebounded to the value observed around 2004 or in the mid 1980s (Fig. 5.1.3b). $\nabla \times u_I$ also rebounded after 2009, but the rebound did not reach the levels of the 3-year running mean values before 2007 (Fig. 5.1.3c). Even though the curls rebounded, SIA in the Canada Basin continued to decrease after 2009 (Fig.

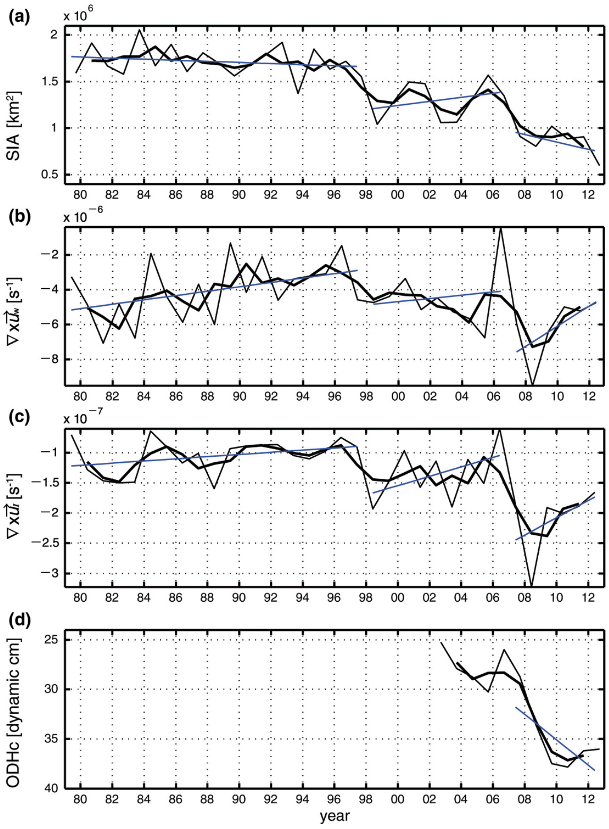

Fig. 5. 1. 3 Time series of a) SIA (km^2) in September in the Canada Basin (area 1 depicted in Fig. 5.1.1a); b) spatial averages of $\nabla \times u_W$ (s^{-1}) in the ice-covered period (November-June) in the zonal band in the blue box depicted in Fig. 5.1.1b; c) the same as (b), but for $\nabla \times u_I$ (s^{-1}); d) spatial averages of ODH (dynamic cm) at 100 dbar relative to 800 dbar in summer (July–September) in the black hashed box depicted in Fig. 5.1.1b, ODHc. The z-axis in (d) is inverted. In (a)–(d), thick and thin curves denote 3-year running mean values and annual values, respectively. Blue straight lines denote trends of each observed variable in 1979–1997, 1998–2006 and 2006-2012, calculated by a least-squares technique (Yoshizawa et al., 2015).

5.1.3a). This implies that the observed variations of SIA in the Canada Basin cannot be explained by just the surface forcing, and some oceanic delayed processes, i.e., “ocean inertia” effects, may be necessary to interpret the observed SIA variations after 2007–2008. Before examining the delayed temporal response of the OBG to the surface forcing, recent variations of the OBG were reviewed, as well as the heat content in the subsurface layer (25–150 m) in the western Canada Basin where the warm PSW is delivered.

Changes in the OBG and ocean heat content

Fig. 5.1.4 by Yoshizawa et al. (2015) shows ocean dynamic height (ODH) distributions at 50, 100 and 150 dbar relative to 800 dbar in the summers (July-September) of 2004, 2008, 2011 and 2012 (color). For these

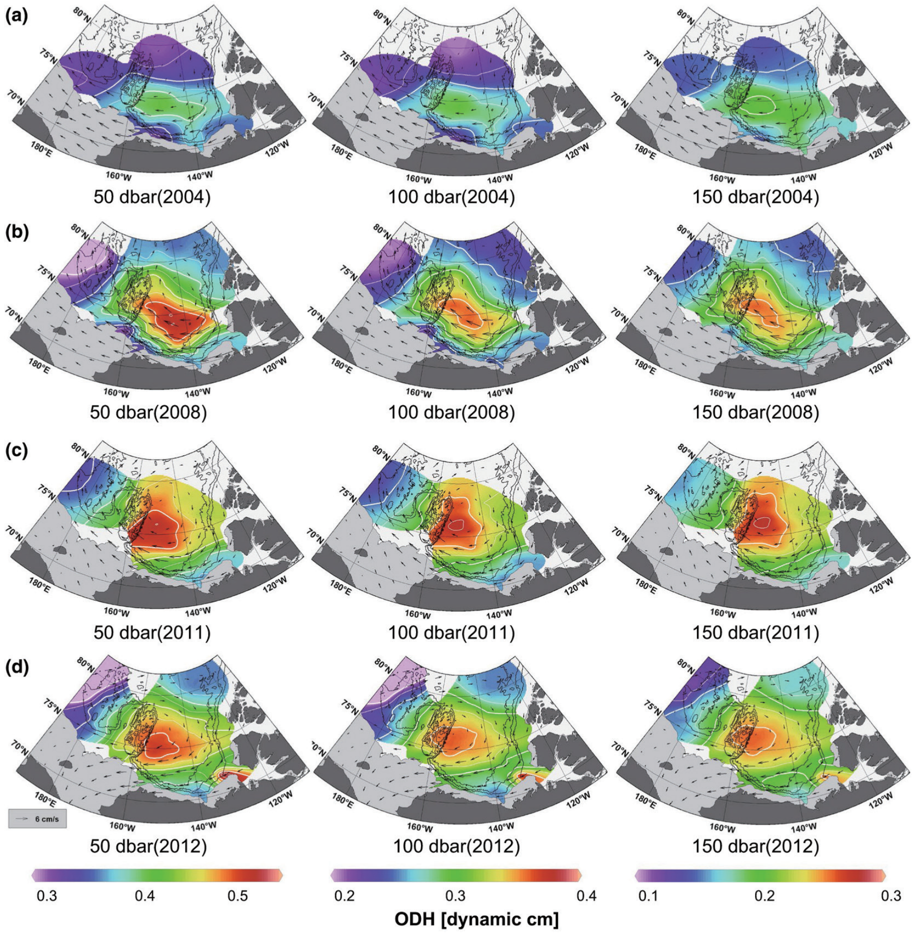

Fig. 5. 1. 4 Spatial distributions of ODH (color, dynamic cm) at 50, 100 and 150 dbar relative to 800 dbar in summer (July–September) of a) 2004, b) 2008, c) 2011 and d) 2012, and sea ice motions (vector, cm s^{-1}) in preceding ice-covered period (November–June) (Yoshizawa et al., 2015).

four summers, hydrographic observations covering the OBG region are available. Sea ice motions in preceding ice-covered periods (November-June) are also overlaid as vectors. In the summers of 2004, 2011 and 2012, ODH showed patterns that were almost the same at the three levels (Fig. 5.1.4a, c, d). In the summer of 2008, however, the pattern of ODH at 50 dbar (left panel of Fig. 5.1.4b) slightly differed from the patterns at the deeper levels of 100 and 150 dbar (center and right panels of Fig. 5.1.4b). The center of the OBG at 50 dbar in 2008 was not localized just east of the Northwind Ridge, but showed a zonally broad pattern extending southeastward, toward the Canadian Beaufort Sea (left panel of Fig. 5.1.4b). The freshwater inputs arising from the melting of multi-year ice anomalously increased in the summers of 2007 and 2008 in the Canadian Beaufort Sea (Yamamoto-Kawai et al., 2009). These freshwater inputs would cause the broadening of the pattern of ODH at 50 dbar observed in the summer of 2008.

At 100 and 150 dbar, northward currents in the zonally narrow area of the Northwind Ridge and the Chukchi Plateau were observed in all 4 years (color in center and right panels of Fig. 5.1.4a-d), while overlying sea ice motions were westward in thes regions, i.e., sea ice velocity vectors were perpendicular t the direction of the oceanic geostrophic flows (vector in Fig. 5.1.4). Such discrepancies in the spatial patterns of the oceanic and sea ice gyres support the notion of a significant role of finite amplitude seafloor topographic features, the Northwind Ridge and the Chukchi Plateau, in the formation of the OBG, as pointed out by Sumata and Shimada (2007). In such cases, the difference in ODH values between the center and rim of the gyre is proportional to the volume transport, based on the Sverdrup relation. Here, the ODH value can be assumed near the stable center of the OBG as a proxy of the volume transport. Here, the spatial average of ODH was defined in the black hashed box depicted in Fig. 5.1.1b as a proxy of the northward volume transport. The subscript c denotes the "center" of the OBG.

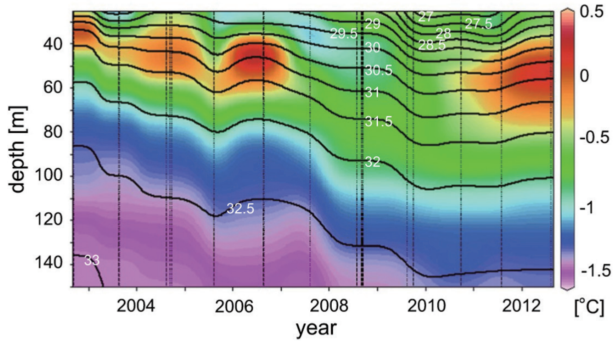

Fig. 5. 1. 5 Hovmoeller diagram of depth-averaged potential temperature (color, °C) and salinity (black contour), using spatially averaged values in the region near Northwind Ridge, the black hashed box depicted in Fig. 5.1.1b (Yoahizawa et al., 2015).

Fig. 5.1.3d shows temporal variations of ODHc at 100 dbar, which correspond to the lower level of the PSW layer, relative to 800 dbar. The z-axis in the figure was inverted. The annual value of ODHs increased remarkably from 2007 to 2010 (thin curve in Fig. 5.1.3d). This shape was similar to those of the 3-year averaged ∇x u_W and ∇x u_I in 2006–2009 (thick curve in Fig. 5.1.3b, c), but ODHc showed time lags of about 2 years relative to the curls. Trends of these observed variables in 2007–2012 indicate that both the loss of SIA (blue line in Fig. 5.1.3a) and the volume transport of the OBG (blue line in Fig. 5.1.3d) increased, while clockwise rotations of winds and sea ice motions decreased (blue lines in Fig. 5.1.3b, c). This suggests that the OBG rather than the surface forcing has much more immediate impact on the change in SIA.

Fig. 5.1.5 shows time series of potential temperature and salinity near the Northwind Ridge. The thickness of the PSW layer (29.5<S<32.5; Steele et al., 2004) associated with the oceanic thermal condition affecting the overlying sea ice cover, increased from 2007 to 2010. The thickness was nearly unchanged after 2009, even when the negative vorticity inputs by surface forcing decreased after 2009 (Fig. 5.1.3b, c). This suggests that the delayed response of the OBG to surface forcing is a potential candidate for maintaining lateral heat fluxes to the basin. This delayed oceanic response enables us to forecast the upper ocean state from the surface forcing in past years.

Estimation of sea ice rafting

The summer sea ice reduction in the Arctic Ocean has been accelerated since the late 1990s, and continuous reduction of sea ice has encouraged interests in developments of the Arctic sea routes. However, robust sea ice often remained through summer locally in the Arctic coastal region used for the shipping routes, in spite of the decline of the total amount of the summer sea ice area (SIA). The prediction of the persistence of such robust sea ice during summer is essential information for making decision of utilization of the Arctic sea routes. The balance between the winter sea ice growth and the summer sea ice melting is critical to whether sea ice can persist or not through summer. The amount of the sea ice growth during winter can be a reasonable indicator of the persistence of the sea ice in the subsequent summer.

Ignoring thermodynamic sea ice growth and melting and focusing on mechanical sea ice growth, temporal variations of sea ice volume due to divergence/convergence of sea ice motion was related to the function describing redistributions of the sea ice thickness due to rafting processes by Yoshizawa (2016). When the convergent sea ice motion increases ice thickness mechanically via rafting processes, SIA will be reduced to conserve mass of sea ice. Based on this relationship, a proxy of mechanical sea ice growth was introduced using the satellite-derived sea ice velocity and coverage data.

Daily averaged sea ice velocity data was calculated from satellite-measured brightness temperature images obtained by AMSE-E and AMSAR 2. To validate the performance of the method to estimate sea ice trajectories by using satellite-derived sea ice motion data, locations of the ice-tethered profiler (ITP) buoy detected by GPS are used (http://www.whoi.edu/website/itp). Also sea ice concentration (SIC) data were derived using NASA team algorithm 2. A proxy of sea ice type was obtained from Gradient Ratio (GR), introduced by Cavalieri et al. (1984) by the following equation,

$$GR_{(a/b)V} = \{T_a(V) - T_b(V)\} / \{T_a(V) + T_b(V)\}, \quad (5.1.1)$$

where $T_a(V)$ and $T_b(V)$ are brightness temperature of the vertical polarized frequencies a and b. Although GR does not identify actual sea ice thickness, GR distinguishes multi year ice (MYI) from first year ice (FYI) by difference of their salinity, and relatively small (large) values represent old (young) ice.

The mean sea ice motion from November to April in the AMSR-E period consisted of the clockwise sea ice Beaufort Gyre over the Canada Basin and transport drift stream (TDS) of sea ice flowing from the Pacific sector (vectors in Fig. 5.1.6). The western branch of the sea ice Beaufort Gyre connected to TDS of sea ice in the Chukchi Sea. This suggests that MYI was transported from the upstream regions of these sea ice motion, i.e., the

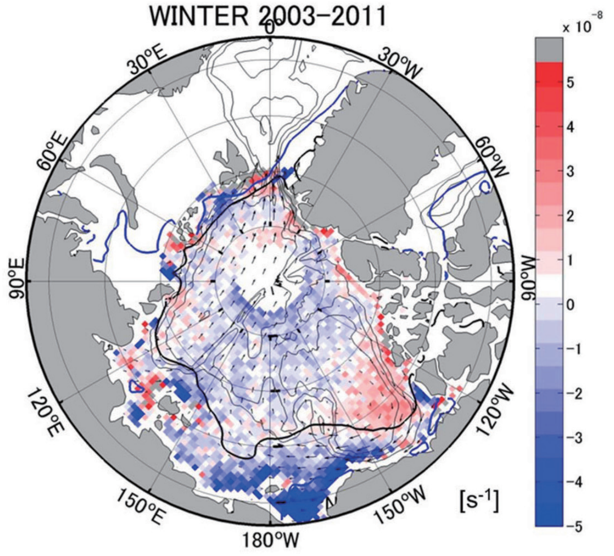

Fig. 5. 1. 6 The spatial distribution of the divergence of sea ice motions (s^{-1}, *color*) in winter (November–April) of the AMSR-E period (2002/2003–2010/2011), with mean sea ice velocities (cm s^{-1}, *vectors*). The values are averaged at each grid cell in which sea ice velocities are defined (Yoshizawa, 2016).

northern Canada Basin, to downstream regions, even in the late 2000s when MYI coverage decreased in the downstream region. In the Pacific sector, the convergent field of sea ice motions is found in the coastal regions from Pt. Barrow to the East Siberian Sea, where the divergent field is found in the eastern half of Canada Basin (color in Fig. 5.1.6). On the other hand, such characteristic divergence/ convergence fields are not found in the basin area. This suggests that sea ice rafting caused by the convergence of sea ice motions is dominant in the coastal regions rather than the basin area, and sea ice traveling the coastal regions would likely to experience mechanical growth due to rafting than traveling the basin area.

To assess influences of mechanical sea ice growth during winter on sea ice condition in the subsequent spring, it should be estimated along sea ice trajectories by a Lagrangian approach. Without thermodynamic sea ice growth, SIC is reduced to conserve sea ice mass, when convergence of sea ice motions increases sea ice thickness via rafting processes. It can be interpreted that *SIC* ($t + \Delta t$) exceeds 100% due to the sea ice convergence over Δt, thickness increases by $\{SIC(t + \Delta t) - 100\}$%. In this constraint, sea ice thickness can be estimated. Con-

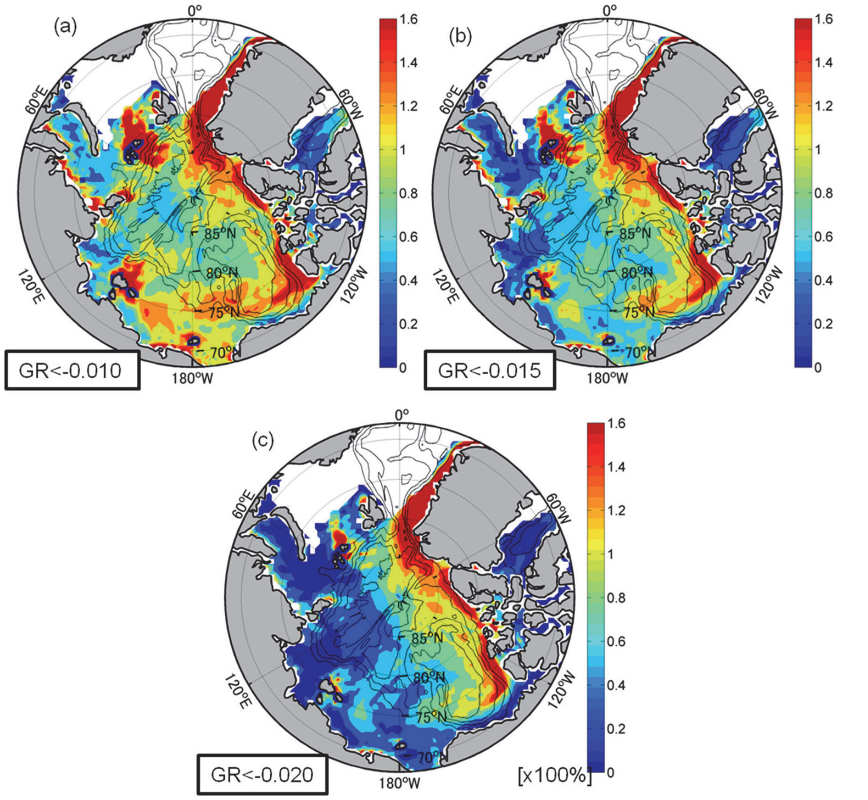

Fig. 5. 1. 7 Spatial distributions of EV [x100%] in spring, on 1 May, averaged for the AMSR-E period. The values of EV were calculated by Eq. (5.1.2) in **a** Case 1 ($GR_{threshold} = -0.010$), **b** Case 2 ($GR_{threshold} = -0.015$), **c** Case 3 ($GR_{threshold} = -0.020$) (Yoshizawa, 2016).

vergent motions of new ice such as grease ice does not contribute to mechanical sea ice growth, only mechanical growth of relatively thick ice was focused on. Influence of new ice are eliminated from the estimation of mechanical sea ice growth by using *GR*. Thresholds are set on GR, then the convergence of sea ice motions are ignored when GR exceeds the thresholds. Since $GR_{(36/06)V}$ was much sensible to differences between MYI and FYI than $GR_{(36/18)V}$ (Krishfield et al., 2014), $GR_{(36/06)V}$ was used as thresholds in this estimation. The values of $\{SIC(t + \Delta t) - 100\}$% are integrated along Lagrangian sea ice trajectories as follows,

$$EV(t + \Delta t) = \int_0^{t+\Delta t} \{SIC(t + \Delta t) - 100\}\, dt, \qquad (5.1.2)$$

when $SIC(t + \Delta t) > 100\%$ and $GR(t) < GR_{threshold}$.

The integrated values from eq. (5.1.2) is introduces as “effective convergence (EV)” that contributes to mechanical sea ice growth during winter.

Fig. 5.1.7 shows spatial distributions of EV on 1 May averaged for the AMSR-E period, which were calculated using different thresholds of $GR_{(36/06)V}$. Hereafter, EV on 1 May is defined as “EV in spring”. The values of EV in case 2 and 3 (Fig. 5.1.7b, c) were smaller than that in case 1 (a) due to decreasing the MYI coverage in the AMSR-E period. In all cases, sea ice with relatively large EV zonally distributed in the coastal region in the Pacific sector (the southern Canada Basin, the Chukchi Sea and the East Siberian Sea). These regions are known as choke-points of the Arctic sea routes. This suggests that locations of sea ice with large mechanical growth just before summer are important to whether these choke-points can be used as the shipping route or not. In addition, the large EV was found in the region around the Franz Josef Land.

In fact, in the region from the southern Canada Basin to the East Siberian Sea, the spring EV in case 3 and the summer (July–September) SIC are correlated with each other with a correlation coefficient > 0.58, which is significant at 90% confidence level. This means that mechanical sea ice growth during winter is a dominant process in determining the summer SIC variations in these choke-points several months ahead of the summer using only satellite-derived data.

5. 2. Estimation of thin ice thickness and sea ice production

Sea surface heat flux is the most important factor to determine the sea ice distributions; however, both interact together. Since the thick sea ice acts to suppress air-sea heat transfer, open water area and thin sea ice area such as polynya and marginal ice zone are the most important area where large surface heat flux emerges, and large amount of sea ice is produced and then affects the distributions of sea ice in other regions. Heat fluxes at the surface of thin sea ice depend on the thickness of sea ice, then it is important to estimate sea ice thickness for understanding the heat budget and sea ice distributions in the Arctic Ocean.

Sea ice thickness

Iwamoto et al. (2013) developed an algorithm for estimating thin ice thickness in the Chukchi Sea using Advanced Microwave Scanning Radiometer - Earth Observing System (AMSR-E) data, applicable not only to the coastal polynyas but also to the marginal sea ice zone (MIZ). The algorithm is based on comparisons between the polarization ratio (PR) of AMSR-E brightness temperatures from the 89 and 36 GHz channels (PR_{89} and PR_{36}) and the “thermal ice thickness” which is estimated from heat budget calculation using the ice surface temperature from clear-sky Moderate-Resolution Imaging Spectrometer (MODIS) infrared data. AMSR-E has twice the spatial resolution of Special Sensor Microwave/Imager (SSM/I) data and can therefore resolve polynyas at a smaller scale. Although the spatial resolution of the 89 GHz data (6.25 km) is twice that of the 36 GHz data (12.5 km), the 89 GHz data can be contaminated by atmospheric water vapor and clouds.

Ice thickness was estimated from the conductive heat flux through the ice based on the heat budget analysis at the ice surface with observed atmospheric data from ERA-Interim and ice surface temperature from MODIS thermal infrared data (Drucker et al., 2003), and called “MODIS thermal ice thickness”. To compare the ice thickness with the AMSR-E data, the MODIS 1.1 km gridded thermal ice thickness is mapped onto the 12.5 and 6.25 km AMSR-E grid. Pixels with false thin ice signal due to cloud were removed in the analyses.

The relationship between thermal ice thickness and the polarization ratio,

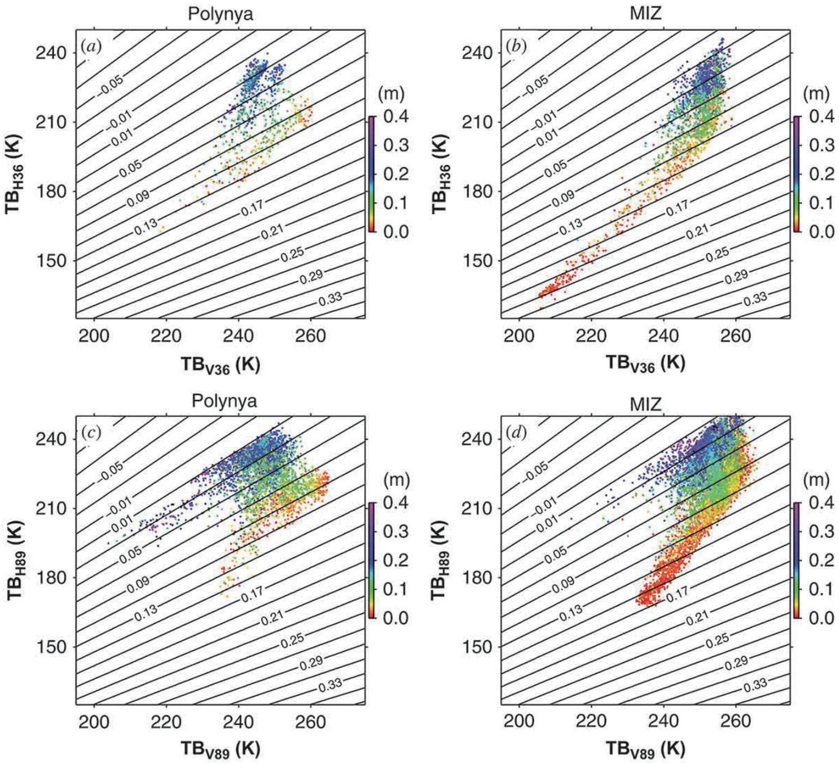

Fig. 5. 2. 1 Scatter plot of horizontal and vertical polarization components of the AMSR-E brightness temperature, with the thermal ice thickness denoted by the colors for the case of (a) 36 GHz from the 11 polynya cases, (b) 36 GHz from the 9 MIZ cases, (c) 89 GHz from the 11 polynya cases and (d) 89 GHz from the 9 MIZ cases. The contours indicate the isolines of PR (Iwamoto et al., 2013).

$$PR = (TB_V - TB_H)/ (TB_V + TB_H), \tag{5.2.1}$$

where TB_H and TB_V are the horizontally and vertically polarized brightness temperatures, respectively. The open water area under the cloud corresponds to the area with $PR_{36} > 0.15$ and $PR_{89} > 0.11$. On the other hand, the area with a PR < 0.04 corresponds to the thicker ice area with thickness > 0.2 m for both PR_{36} and PR_{89}. Fig. 5.2.1 shows the scatter plots of horizontal versus vertical polarizations of the AMSR-E brightness temperature on a pixel-by-pixel basis, with the thermal ice thickness denoted by colors, for 11 polynya cases and 9 MIZ cases. As mentioned earlier, the brightness temperature measured by passive microwave radiometer is thought be related to the ice thickness through the correlation between the brightness temperature and the surface salinity of ice. Fig. 5.2.1 demonstrates that similar color (thickness) distributes parallel to the isolines of PR, particularly in the thickness range < 0.2 m. The thickness has obviously a much stronger correlation with the PR than with the individual polarization component. Fig. 5.2.1 shows that the use of PR is reasonable for detecting and estimating thin ice thickness, as has been done in previous studies. However, the relationship between the PR and the ice thickness tends to be obscured in the thickness range > 0.3 m, probably because of the influence of snow cover and dynamical ice growth on the thick ice regime.

Fig. 5.2.2 shows the scatter plot of the PR and thermal ice thickness for the 11 polynya cases (blue dots) and 9 MIZ cases (green dots). From the scatter plot, exponential relationship was proposed by Martin et al. (2004). Tamura et al. (2007) and Nihashi et al. (2009) instead adopted a linear fit. Here, following Tamura and Oshima (2011), both an exponential and linear fit for the relationship between PR and ice thickness were adopted. Because the PR value is not sensitive to the MODIS thermal ice thickness in the thicker ice range (small PR range), an ice thickness estimation including a small PR range would misinterpret thick ice as thin ice. Therefore, the fitting was carried out for the plotted data with the thickness of < 0.3 m. These fitted curves and lines were used to estimate thin ice thickness from PR for ice thickness of < 0.2 m. From the fitting, the following equations for ice thickness h_i were obtained from PR_{36} and PR_{89}, respectively,

$$h_i = \exp [\ 1/ (206\ PR_{36} - 5.4)\ ] - 1.02, \tag{5.2.2}$$

$$h_i = -2.32\ PR_{36} + 0.307, \tag{5.2.3}$$

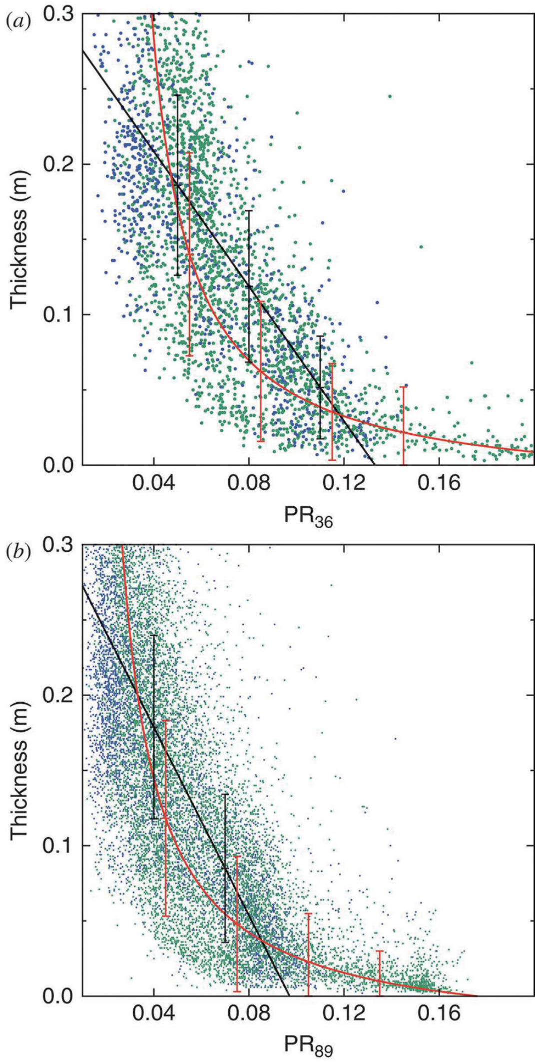

Fig. 5. 2. 2 Scatter plot of the PR value and the thermal ice thickness for (a) PR36 and (b) PR89 from the 11 polynya cases (blue dots) and the 9 MIZ cases (green dots), The red and black lines show the fitting curves of eq. (5.2.2) and (5.2.4) and eq. (5.2.3) and (5.2.5), respectively. The vertical lines with crossbars show the standard deviation of the thermal ice thickness with respect to the fitting curve and line (Iwamoto et al., 2013).

$$h_i = \exp\left[\, 1/\,(218\, PR_{89} - 3.0)\,\right] - 1.03, \quad (5.2.4)$$

$$h_i = -3.06\, PR_{36} + 0.306. \quad (5.2.5)$$

Eqs. (5.2.2) and (5.2.3) and eqs. (5.2.4) and (5.2.5) are superimposed in Figs. 5.2.2a and b, respectively, with the standard deviation for every 0.02 segment of PR. From Fig. 5.2.2a and b, the exponential-fitting seems to be more suitable representation of the plots than the linear-fitting in both PR_{36} and PR_{89}.

The very thin ice signal covers the open water area that is indicated from the ice concentration map, suggesting that only equation (5.2.2) or (5.2.4), the open water area tends to be judged as a thin ice area. Therefore, an open water mask was required to determine the ice-free area. Also, 89 GHz data have a tendency to be influenced by water vapor in the atmosphere. The microwave emissions from the surface have a tendency to be depolarized by the water vapor and the cloud liquid water in the atmosphere through absorption and emission processes and the effect is larger for the higher frequency data. A water vapor correction was applied on a pixel-by-pixel basis for PR_{89} using the relationship showing those pixels influenced by water vapor, and were treated as missing pixels. A seamless data set without missing pixels could be obtained by substituting the thickness from the PR_{36} for the missing PR_{89} pixels. Generally, a coastal polynya is covered with relatively uniform ice, whereas an MIZ consist of open water and ice floes with relatively low ice concentration, particularly in the melting season. The thin ice algorithm sometimes judges areas of lower ice concentration as thin ice because the open water presents a PR value close to that of thin ice. A method of ice

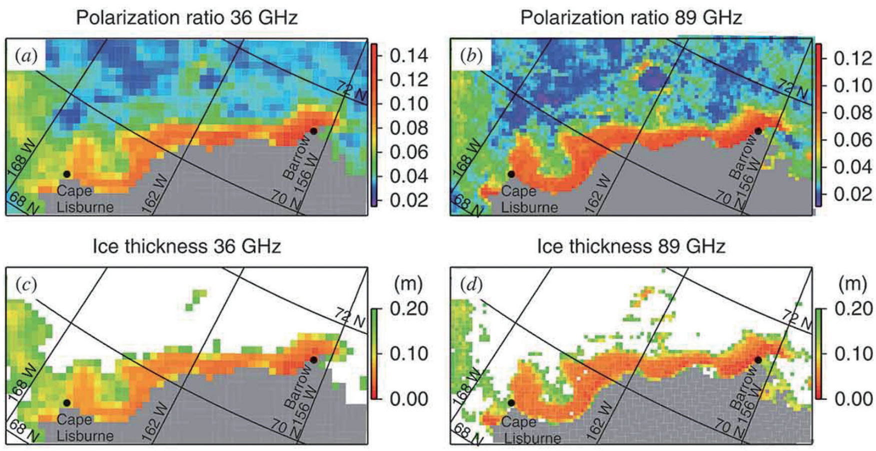

Fig. 5. 2. 3 Spatial distribution of (a) PR36 and (b) PR89, and (c) ice thickness from PR36 with eq. (5.2.2) and (d) PR89 with eq. (5.2.4), for the Chukchi polynya on 8 February 2007. The white pixels show the thickness of > 0.2 m in (c) and (d) (Iwamoto et al., 2013).

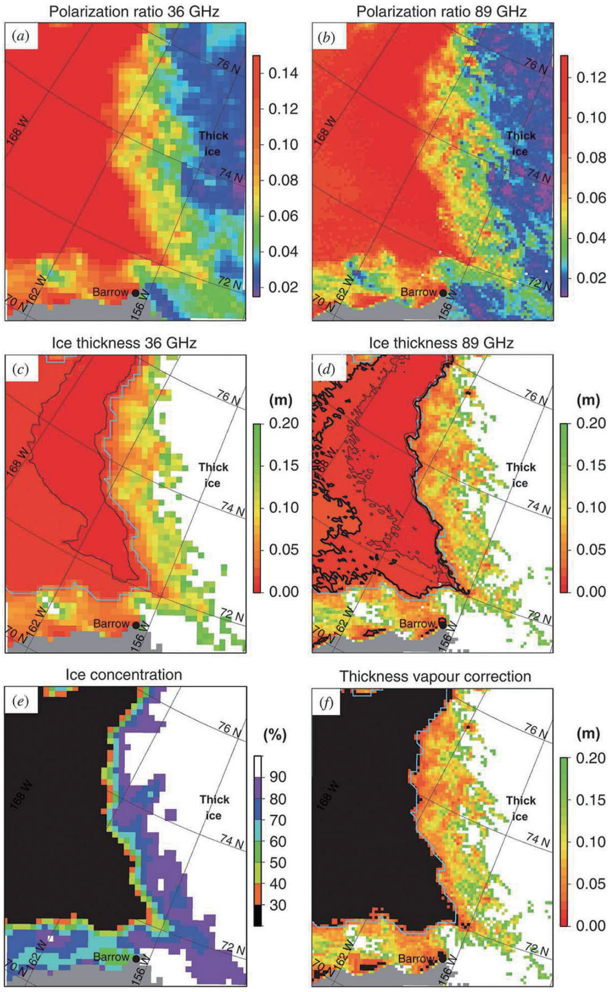

Fig. 5. 2. 4 Maps of sea ice for the MIZ in the Chukchi Sea on 7 November 2007. Spacial distribution of (a) PR36 and (b) PR89, (c) ice thickness from PR36 with eq. (5.2.2), (d) ice thickness from PR89 with eq. (5.2.4), (e) Bootstrap Based Algorithm (BBA) ice concentration and (f) ice thickness from PR89 with both open water mask and water vapor correction. The white pixels indicate an ice thickness of > 0.2 m. The blue and thick black lines show the ice edge defined by the BBA ice concentration of 30% and by the threshold PR89 of 0.11, respectively in (c), (d) and (f). The solid lines show the contour lines of the ice thickness of 0.01 m in (c) and (d) (Iwamoto et al., 2013).

thickness estimation was proposed that excludes the effect of the open water fraction in an AMSR-E grid cell, in the combination with the ice concentration algorithm.

Fig. 5.2.3 shows the spatial distribution of ice thickness from PR_{36} with eq. (5.2.2) and PR_{89} with eq. (5.2.4), respectively for the polynya case. The coastal polynya is well represented, particularly from PR_{89} (Fig. 5.2.3d). Fig. 5.2.4c and d show the thickness distribution for the MIZ case from PR36 and PR_{89}, respectively. However, the very thin ice signal covers the open water area that is indicated from the ice concentration map (black area in Fig. 5.2.4e), suggesting that, only from eq. (5.2.2) or

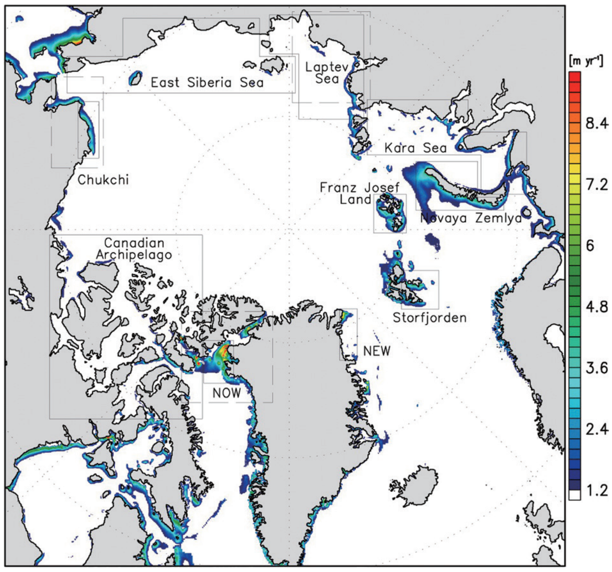

Fig. 5. 2. 5 Annual cumulative sea ice production, represented by the ice thickness, averaged over the nine winters (September–May) of 2002/2003–2010/2011. The areas with the ice production of < 1.2 m yr^{-1} are not colored (Iwamoto et al., 2014).

(5.2.4), the open water area tends to be judged as a thin ice area. Therefore, an open water mask was required to determine the ice-free area.

Sea ice production

Persistent areas of thin sea ice in the form of coastal polynyas and marginal ice zones (MIZs) are crucially important as regions of enhanced ice production and brine rejection in the polar oceans during freezing periods. New and improved estimates of sea ice production in the Arctic Ocean were derived from AMSR-E satellite and atmospheric reanalysis (ERA-Interim) data for the period 2002–2011. Following the ice thickness data obtained in the foregoing paragraphs (Iwamoto et al., 2013), ice production over thin ice areas was estimated by Iwamoto et al. (2014) from heat budget analysis, assuming that all of the heat loss goes into ice formation. Under the assumption that there is no oceanic heat flux from below, the volume of ice production V in given by

$$V = H/\,(\rho_i\,L_f), \qquad (5.2.6)$$

where H is the heat loss at a thin ice surface, ρ_i (= 920 kg m^{-3}) is the ice density and L_f (= 0.334 MJ kg^{-1}) is the latent heat of fusion of sea ice. If there is oceanic heat flux from below, calculated ice production will be overestimated. Therefore, this mapping would provide the upper bound of the ice production. For the longwave radiation, turbulent and conductive flux calculations, the same em-

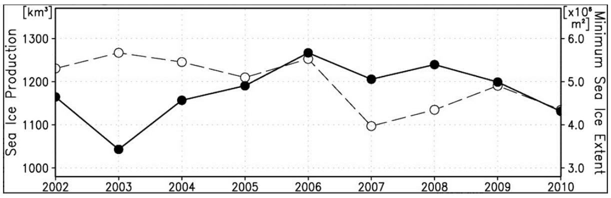

Fig. 5. 2. 6 Time series of sum of the annual cumulative sea ice production in the 10 major Arctic coastal polynyas for 2002/2003–2010/2011 (Iwamoto et al., 2014).

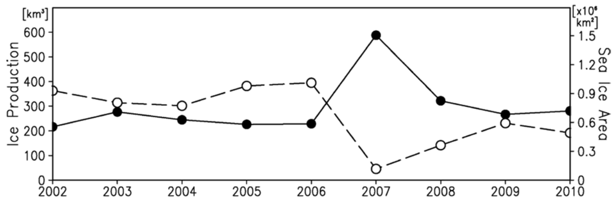

Fig. 5. 2. 7 Time series of sea ice area on 30 September (dashed line) and cumulative sea ice production integrated over the areas from October to November (solid line) for 2002–2010 (Iwamoto et al., 2014).

pirical and bulk formulae as those used in the estimation of MODIS thermal ice thickness. Shortwave radiation is assumed to be completely absorbed in the thin surface layer.

Here, the annual cumulative ice production in a polynya was defined as production in the region in which the polynya regularly forms, including ice production due to fall freeze-up. Fig. 5.2.5 shows the resultant annual cumulative ice production in the Arctic Ocean, averaged over the winter months (September–May) of 2002/2003–2010/2011. High ice production is largely confined to the major Arctic coastal polynyas, e.g., the North Water (NOW) polynya, Chukchi polynya and along the coast of Novaya Zemlya, Frantz Josef Land and Svalbard. Among the major polynyas, the NOW polynya has by far the highest production rate with the maximum rate reaching ~ 13 m yr^{-1} in Smith Sound..

Fig. 5.2.6 compares total cumulative ice production in the 10 major polynyas with annual minimum sea ice extent in the Arctic Ocean during the period 2002–2010. The average total ice production was about 1180±70 km^3. The magnitude of minimum sea ice extent anomaly may result in either a positive or negative annual ice production anomaly, depending on which mechanism is dominant; delay in the onset of freezing could reduce the production. On the other hand, loosened pack ice offshore could promote polynya opening and thus production. Based on the present mapping, there is no obvious relationship between total ice production and summer ice extent, at least during this period, probably because both effects act oppositely.

The ice production in this study is smaller in all coastal polynyas than that from Tamura and Oshima (2011), who conducted quite similar study from SSM/I data with lower resolution. Since the AMSR-E thin ice algorithm with its finer resolution and the landfast ice detection mask can better resolve the polynyas and the ice production compared with SSM/I data (Tamura and Oshima), the estimation in this study is expected to more realistically map ice production. The land fast ice along Alaskan coast in the Chukchi polynya is detected in the present algorithm, while all of the landfast ice area is judged as thin ice area in Tamura and Oshima algorithm. Such misclassification in Tamura and Oshima partly causes the overestimation of ice production in the nearshore area in the Chukchi polynya and Laptev polynya. The open water mask for PR89 thickness in the present algorithm also contributes to better resolve the open water area in the NOW polynya, because the area tends to be judged as thin ice area in Tamura and Oshima algorithm, resulting in the overestimation of ice production.

The recent reduction in summer Arctic ice extent is remarkable in the Pacific sector, which would affect the ice production in MIZ in this region, especially in the early stage of freezing period. The area from the western Beaufort Sea to the East Siberian Sea was focused on, away from the continents and large islands by 100 km. Fig. 5.2.7 shows the relationship between the ice production in the MIZ of this area from October to November and the sea ice area on 30 September for each year. The production in the MIZ has clear negative correlation with the summer ice extent. Particularly in 2007, when the summer ice extent in the Arctic Ocean showed the minimum during this analysis period, ice production reached about 600 km^3, which corresponds to about twice as large as the ice production in other years. This amount also corresponds to about half of the total annual ice production in the major 10 coastal polynyas, suggesting that the retreat of summer ice extent results in the larger amount of the sea ice production in the central Arctic Ocean. In accordance with the drastic northward shift of the ice edge location at the beginning of freezing period in 2007, significant ice production occurred at much higher latitudes in 2007. Particularly from the Beaufort Sea to Chukchi Sea, the area within which the production exceeds 0.6 m yr^{-1} occurs in the deep basin north of the shelf break, whith production > 1.0 m yr^{-1} occurring over the Canada Basin. These results demonstrate that the reduction of summer ice extents shift the high ice production area from the continental shelf near the coast to the deeper basin. The direct supply of dense water to the Basin due to ice production in the MIZ may change salinity and density structures in the ocean. This suggests that the retreat of summer ice extent might change the ocean structure, specifically deepening the winter mixed layer through brine rejection by strong ice production.

5. 3. Heat budget and sea ice processes in polynya

With ongoing retreat and thinning of Arctic sea ice and growing commercial interest in resource extraction and marine navigation, there is an increasing demand for observational data of ice thickness and velocity. In the paper by Mahoney et al. (2015), data collected as part of the Seasonal Ice Zone Observing Network (SIZONet) acquired near Barrow, Alaska, during the 2009/10 ice season, were combined to make novel comparisons between coincident and co-located observations of sea ice from above and below, measurements of ice thickness and velocity.

Two moorings (B1 and B2) were deployed, B1 at 71.23°N, 156.88°W on 5 August 2009 and retrieved on 29 July 2010, B2 at 71.23°N, 157.65°W on 7 August 2009 and retrieved on the same day as B1. These moorings each comprised an Ice Profiler Ice Profiling Sonar (IPS) and Acoustic Doppler Current Profiler (ADCP) as well as a conductivity-temperature (C-T) recorder and a temperature-pressure (T-P) recorder (Fig. 5.3.1). The IPSs are used to measure the draft of the sea ice passing overhead while the ADCPs measure current velocity profile of the overlying water column and, of particular relevance here, the velocity of the ice through bottom tracking.

Sea ice thickness was measured from above using airborne electromagnetic sounding by electromagnetic (EM) induction sensor to determine the distance from the towed instrument, known as an EM-bird, to the water surface. On 12 April 2010, airborne electromagnetic flight was made over the sea ice near Barrow over mooring B2 with helicopter. The EM-bird was flown at an altitude of ~15 m, giving an effective sampling footprint of ~70 m. Each EM measurement is thus a mean value of ice and snow thickness over the area and will therefore tend to underestimate the maximum thickness of ice ridges, though it can be expected to give an accurate measure

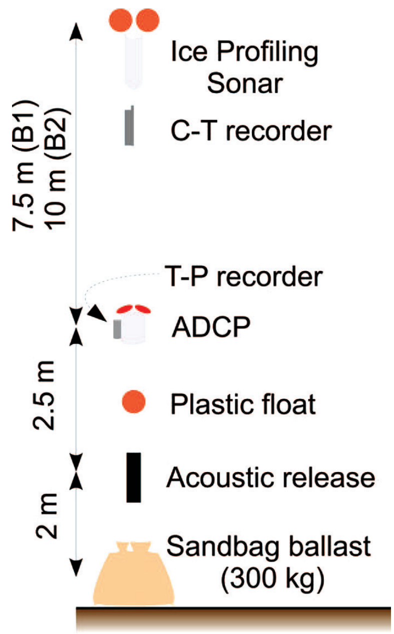

Fig. 5. 3. 1 Configulation of SIZONet moorings deployed near Barrow in 2009/10. Distances indicate approximate rope lengths between mooring components (Mahoney et al., 2015).

of the overall ice volume.

Here, the comparisons of EM and IPS measurements were made by calculating their probability distributions using all data that fall within 10 km of mooring B2. Fig. 5.3.2 shows the distributions of EM-derived ice and snow thickness and IPS-derived ice draft, binned into 0.05 m intervals. Both distributions have pronounced modes, which represent the thickness and draft of level undeformed ice. The EM data indicate a modal combined thickness of ice and snow of 1.6±0.025 m, while the IPS data show a modal ice draft of 1.35±0.025 m. To better match the footprints of the two instruments, a 70 m smoothing filter was applied to the IPS data. This smoothing changes the shape of the tail of the IPS draft distribution (Fig. 5.3.2) to more closely resemble that of the EM data. Finally, a conversion factor from ice draft to total thickness was determined as 1.20±0.01 m (Fig. 5.3.3). Then the ice thickness of level sea ice near mooring B2 at 1.48±0.09 m, with a snow depth of 0.12±0.09 m.

Supercooled water and frazil ice in polynya

Due to the lack of an insulating ice cover when open water is maintained, heat loss and thus ice production rate are at a maximum during episodes of supercooling and associated frazil ice formation. Under cold and windy conditions, sea ice is initially generated as small mm- or µm-scale or dendritic crystals, called frazil ice.

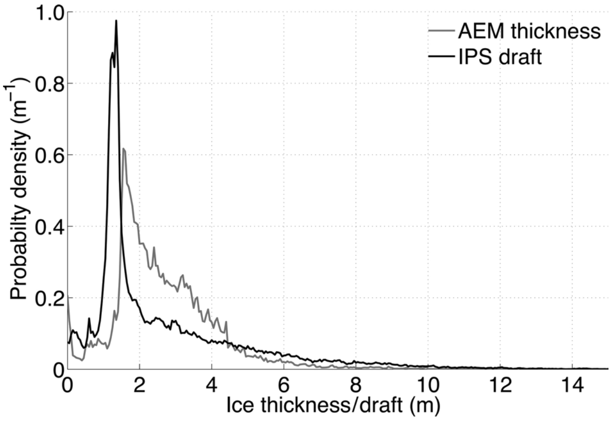

Fig. 5. 3. 2 Probability distribution of combined ice and snow thickness (EM) and ice draft (IPS) derived from all measurements within 10 km of mooring B2 (Mahoney et al., 2015).

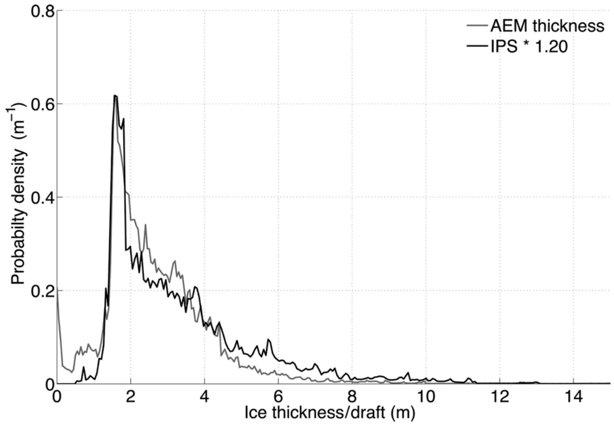

Fig. 5. 3. 3 Probability distribution of combined ice and snow thickness (EM) and 70 m smoothed, isostatically adjusted ice draft (IPS*1.20) derived from all measurements within 10 km of mooring B2 (Mahoney et al., 2015).

Laboratory experiments have shown that underwater frazil ice formation occurs in association with supercooled water resulting from large surface heat loss under turbulent conditions with strong wind (Ushio and Wakatsuchi, 1993). However, in situ observations of supercooling and underwater frazil ice formation have been hampered by logistical challenges in polar oceans.

Formation of supercooled water and frazil ice was studied by Ito et al. (2015) in the Chukchi Sea coastal polynya off Barrow, Alaska, in winter 2009/10, using moored salinity/temperature sensors and Ice Profiling Sonar (IPS) data already discussed in the previous paragraph (Mahoney et al., 2015) along with satellite data. This study covers the sea ice production from the in-situ data, which was already shown from remote sensing data such as explained in the previous section (Iwamoto et al., 2014). This study might provide the first IPS observation of underwater frazil ice in the ocean, using a newly developed profile mode option. The IPS is capable of much higher temporal observation than the upward-looking sonar. On the basis of these observations, the formation processes of supercooled water and frazil ice were discussed to improve our understanding of the processes governing high ice production rates in a coastal polynya.

Fig. 5.3.4 shows the time series of the mooring data with sea ice and atmospheric conditions from AMSR-E and ERA-Interim during December 2009 to February 2010. During this period, two persistent coastal polynya events occurred at or in the immediate vicinity of the mooring sites (Fig. 5.3.4a and d). These polynya events lasted for 10–15 days and were associated with strong offshore winds (> 10 m s^{-1}; Fig. 5.3.4g); one event took place during the period 20 December 2009 to 1 January 2010 and the other during the period 10–25 February. On 20–21 and 23–26 December, during the former event, episodic potential supercooling occurred coincidentally at 30 m depth for B1 and at 40 m depth at B2 (Fig. 5.3.4 a and b). These supercooling events occurred at both sites at the same time, reducing the likelihood of the observed supercooling being caused by contamination of the conductivity cell by ice. During the latter persistent polynya event, potential supercooling of ~ 10 mK was observed on 8 February at B1 and on 19–20 February at B2. All these episodic supercooling events occurred when the heat loss was 200–600 W m^{-2} to the stmosphere (Fig. 5.3.4c). Therefore, it is likely that these supercooling events are caused by strong direct surface cooling.

On the other hand, even when the polynya was not open, specifically for 10–18 December and 4–28 January, coincident potential supercooling of ~ 15 mK persisted for 1–3 weeks at the two mooring sites. Under the sea ice cover of thick ice, the heat loss is small and thus insufficient to create supercooled water at depth. According to the ADCP data collected at 40 m depth at B2 (Fig. 5.3.4e), a northeastward current of 0.35–0.45 m s^{-1} (30–40 km d^{-1}) started to be dominant from ~1 week before the events and persisted for the first half of the events. Although the polynya was closed at the mooring locations, the AMSR-E ice thickness data show that other coastal polynyas had formed ~400–600 km to the southwest in these periods. Thus, the potentially supercooled water masses were likely advected from these polynyas. According to temperature and salinity data from the conductivity and temperature (C-T) recorders (the data at B2 are shown in Fig. 5.3.4f), all the supercooling events ended with the advection of saltier and warmer Atlantic

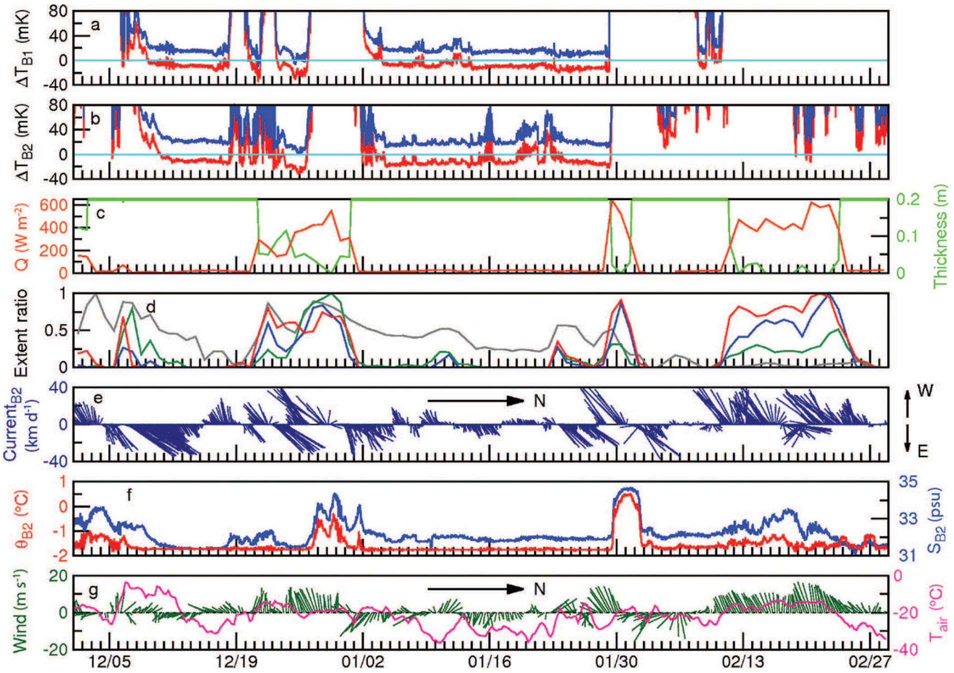

Fig. 5. 3. 4 Time series of the mooring data with AMSR-E and meteorological data, during 1 December 2009 to 28 February 2010. (a) The water temperature relative to in situ freezing point (blue) and the potential temperature relative to the surface freezing point (red) at 30 m depth at B1 from C-T recorder. The light blue line is the freezing point. (b) Same as (a) at 41 m depth at B2. (c) AMSR-E ice thickness (green) and calculated heat loss (orange) at B2. (d) Polynya extents expressed as the sum of thin-ice (< 0.2 m) area for regions I (red), II (blue), III (green) and IV (grey), normalized by the maximum extent in winter. (e) The ocean current (3 hour mean) from the ADCP measurement at 40 m depth at B2. (f) The potential temperature (red) and salinity (blue) at 40 m depth at B2. (g) 2 m air temperature (pink) and the 10 m wind (green) from the ERA-Interim data at the gridpoint closest to B2. Thick marks correspond to 0:00 UTC (Ito et al., 2015).

Water from the northeast.

Fig. 5.3.5 a shows the time series of range and profile data at B2 on 20 February when potential supercooling was ovserved in association with a coastal polynya at the mooring locations. These IPS signals were interpreted as frazil ice based on several lines of evidence presented below. According to the Advanced Synthetic Aperture Radar (ASAR) image, the region around the mooring sites show relatively high backscatter, which indicates rough surfaces corresponding to a wind-roughened sea surface with capillary waves and wind waves. According to the AMSR-E data, the region around the mooring site shows polarization ratio close to that of the open-water area. Further, the ERA-Interim data show strong offshore wind on that day (Fig. 5.3.4a). While the most prominent signals occurred on 20 Febryary with deep potential supercooling (Fig. 5.3.4b), such underwater signals were observed at B2 during the period of 12–22 February, which corresponds exactly to the active polynya period (Fig. 5.3.4c) with strong offshore winds prevailing (Fig. 5.3.4g). During the entire mooring data record for 2009/2010, such long-term underwater signals were observed only in this period. Considering all of these facts, the observed targets in the IPS profile data at B2 are considered to be frazil ice. This is likely the first detection of underwater frazil ice in sea water by an IPS.

On the other hand, on 20–21 and 23–26 December during periods of in situ and/or potential supercooling at both moorings, underwater targets were not detected except fairly close to the ocean surface. Fig. 5.3.5b shows the data obtained by the IPS at B1. According to the AMSR-E ice thickness data on this day, the ice thicknesses around the mooring sites are ~0.02–0.05 m. Thus, the ice detected by the IPSs is probably thin sheet ice such as nilas.

Hybrid latent and sensible heat polynya

Following the detection of signals of frazil ice formation accompanied by supercooled water and vanishing the signals with the arrival of warm Atlantic Water (AW) in the Barrow Coastal Polynya (BCP) by Ito et al. (2015), it was suggested that the BCP, which is known as a latent heat polynya, may have characteristics of a sensible heat polynya as well. Hirano et al. (2016) examined the nature of BCP using data from year-long under-ice moorings (Mahoney et al., 2015) already used in above paragraph, satellite-derived products (sea ice concentration and production rate), atmospheric reanalysis data and tracer experiment results from a high-resolution pan-Arctic ice-ocean model.

The BCP is located within the pathway of Pacific-origin water entering the Canada Basin via Barrow Canyon.

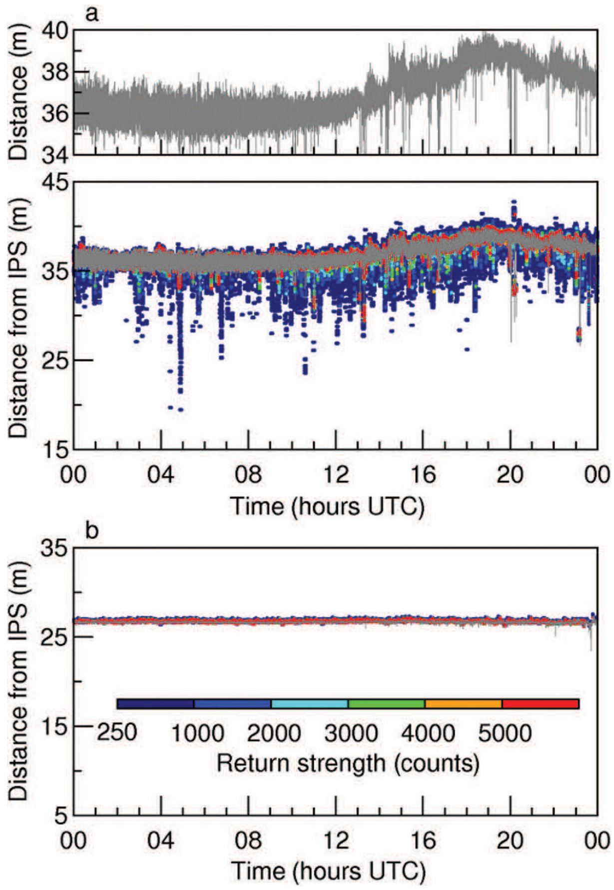

Fig. 5. 3. 5 Time series of range (gray line) and profile (color dots) data obtained by the IPS (a) at B2 on 20 February 2010 and (b) at B1 on 25 December 2009. The vertical axis shows the distance between the IPS and each target. Dot color indicates return strength (in counts) of the profile data (see color bar in (b) for their values). The upper panel of (a) shows the range data in an enlarged vertical scale (Ito et al., 2015).

In addition, the Chukchi shelf-Canada Basin interaction occasionally occurs through upwelling of warm AW around Barrow Canyon. Therefore, various water masses are expected to be present on the shelf region around Barrow Canyon due to the seasonal variability of Pacific-origin water and/or the upwelling of AW. Fig. 5.3.6 shows the relationships of temperature (relative to freezing point T_f) and salinity at B2 (41 m) from August 2009 to July 2010. Except for the upwelling events of warm water described below, the observed temperature and salinity of Pacific Summer Water (PSW) were near the freezing point and ~32, respectively. The water temperature increased after June, Pacific Summer Water (PSW) was then dominant in this region. AW signals were frequently found from October to early June as shown in shifts toward the upper right in Fig. 5.3.6, although they were less clear in April. Except for summer and early fall when PSW was dominant, these AW signals resulted from the upwelling caused by northeasterlies blowing in the direction of Barrow Canyon.

Time series of wind, SIC and ice production from November to May are shown in Figs. 5.3.7a and b. The SIC started increasing in mid-November and decreasing in late April, and then dropped to zero in June. Considering this seasonal variability, the ice-growth period around Barrow Canyon in 2009/2010 is defined to be from mid-November to mid-May. During this period, the region around Barrow Canyon was almost entirely covered by sea ice (i.e., SIC is 100%) except for BCP events defined below. The dominant winds during the BCP events were commonly northeasterly (toward 240°on average). These northeasterly winds resulted from a pressure pattern dominated by the Aleutian Low and Beaufort High. Their direction was almost parallel to the Barrow Canyon with an offshore component near Barrow. For each BCP

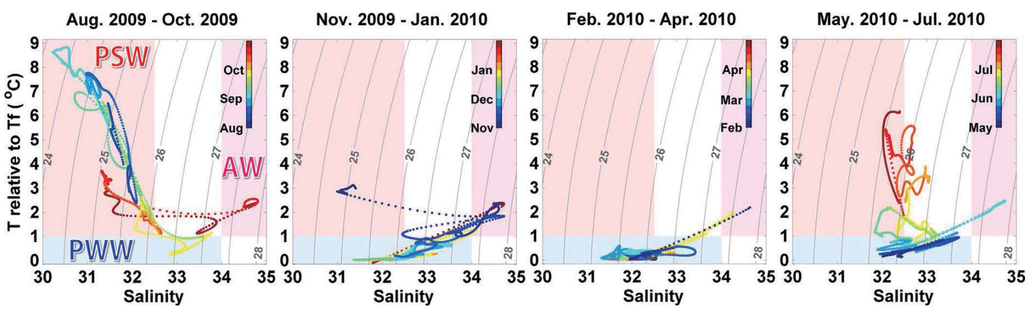

Fig. 5. 3. 6 Relationship between temperature (relative to freezing point) and salinity at 41 m of B2 from August 2009 to July 2010 after applying a tide killer filter. Colors of dots indicate time in each month. Red, light blue and pink-shaded areas represent water mass classifications for Pacific Summer Water (PSW; $T > T_f + 1$°C with $S < 32.5$), Pacific Winter Water (PWW; $T < T_f + 1$°C with $S < 34$) and Atlantic Water (AW; $T > T_f + 1$°C with $S > 34$). The gray contours denote potential density surfaces (Hirano et al., 2016).

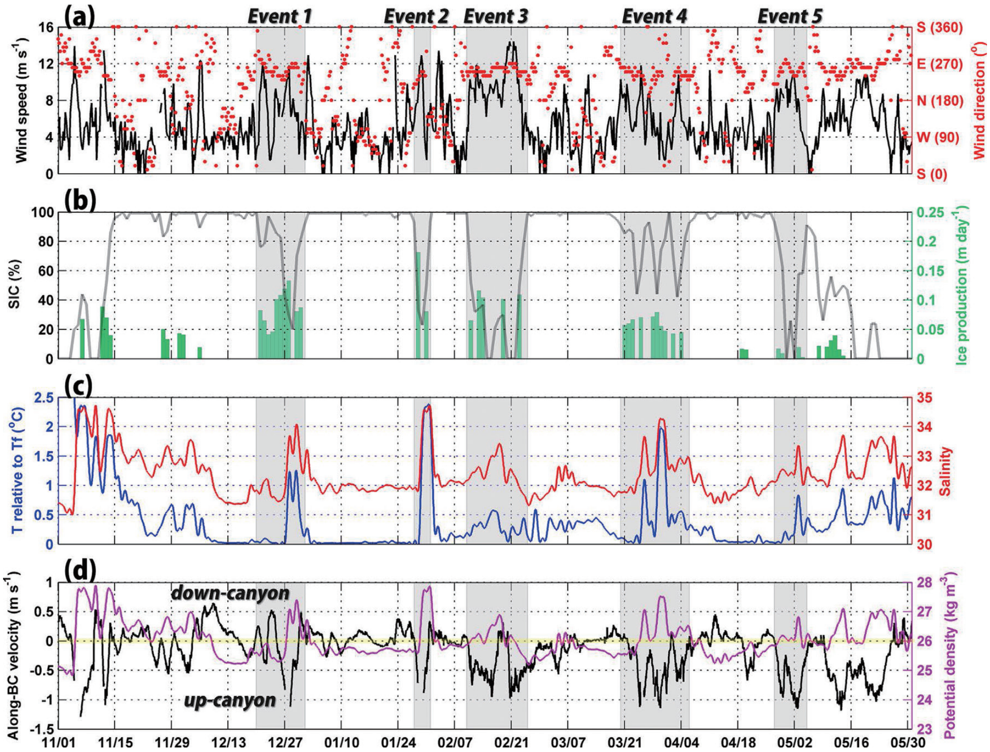

Fig. 5. 3. 7 Time series of (a) wind speed (solid line) and direction (red dots) at Barrow Willey-Post Airport, (b) sea ice concentration (solid line) and production rate (green bar) at the AMSR-E grid point, (c) temperature relative to freezing point (blue) and salinity (red) at 41 m after applying a tide killer filter, (d) along-BC velocity at 11 m (balck, positive values indicate down-canyon flows) and potential density at 41 m (purple). Blanks in d represent the flagged data. Shadings represent periods of BCP events. Data at B2 are shown in c and d (Hirano et al., 2016).

event, active ice production occurred with rates of 0.005–0.10 m d^{-1} and maximum exceeding ~0.15 m d^{-1} (Fig. 5.3.7b, green bars) if the open water mask of AMSR-E is assumed to be correct. This is a remarkable feature of the BCP events.

Figs. 5.3.4c and d show time series of temperature, salinity and potential density obtained at B2 (41 m). During the BCP events, warm and saline (dense) AW appeared at the moorings, with the most prominent signals of $T > T_f + 2$°C, $S > 34$ and $\sigma\theta > 27$ kg m^{-3} (Figs. 5.3.6, 5.3.7c and d). Whenever the BCP was open, it is reasonable to consider that the temperature is vertically uniform and near the freezing point over the shallow shelf (Fig. 5.3.7c). In contrast, the upwelling warm water is considered to be present below the surface mixed layer, resulting in two-layer thermal structure.

Dominant northeasterly winds over the BCP region induce two different phenomena as follows: (1) sea ice divergence causing the formation of the BCP and (2) upwelling of warm saline water, originationg from the mouth of Barrow Canyon and the southern Canada Basin, compensating surface Ekman flow toward the offshore. Thus, the combination of the coastline orientation around the Barrow and the location of Barrow Canyon along with prevailing northeasterly winds can result in both enhancement and inhibition of ice production in the BCP. Unless the upwelled warm water outcrops, upward heat transport accompanied by vertical mixing into the surface mixed layer is required to suppress ice production and/or to melt sea ice. Such upward heat transport transforms the BCP into a sensible heat polynya in which heat loss mostly goes into cooling of the water column and/or suppression of ice growth. Fig. 5.3.7d shows a time series of ocean current along the Barrow Canyon (63°; along-BC velocity) at B2 (11 m). Down-canyon flow toward the Canada Basin was up to ~0.5 m s^{-1}. However, each time the BCP started forming, up-canyon flow toward the BCP region gradually strengthened and reached its maximum of up to ~1 m s^{-1} nearly coincident with the local SIC minimum (Fig. 5.3.7b). In addition, the up-canyon flow corresponded with higher potential density, likely caused by the upward displacement of density surfaces due to the upwelling.

The reduction of ice production by the ocean heat transport from below was estimated with and without the open water mask (figure not shown). The difference between the two estimates considered to be roughly equivalent to the amount of suppressed ice production by ocean heat transform from below. The ocean heat transport had the largest impact on ice production for Event 3 when the open water area became vast. Specifically, ice production was suppressed by almost half, compared to that without the open water mask, when the open water area was largest on 22 February. Throughout the ice-growth period in 2009/2010, ice production in the BCP is estimated to decrease by ~17% due to ocean heat transport from the upwelled warm water. Another point to note is that polynya events end up with ice formation, because reduced northeasterly wind forcing (Fig. 5.3.4a) weakens upwelling and subsequent intensive heat loss cools the upwelled water down to the freezing point.

Heat budget analysis of Arctic sea ice variation

Kashiwase et al. (2017) showed the dominance of heat input through the open water fraction on sea ice loss and its variation, which is a necessary condition for ice-ocean albedo feedback, based on the relationship between sea ice retreat and heat budget over the ice-covered area. Then the specific trigger of the feedback effect was explored and examined whether ice melt is in fact amplified significantly by this feedback and whether the drastic reduction in summer ice extent can be explained by this feedback, based on the combined analysis of satellite observations and a simplified ice-ocean model. Fan shaped area in the Pacific Arctic sector was selected as the main study area (Fig. 5.3.8). This area experienced the largest reduction in summer sea ice extent and volume anywhere in the Arctic beginning in the 2000s. Interannual variation of ice retreat in this region explains about 86% of the variance over the Arctic Ocean.

For the ice-covered area defined by ice concentration > 15%, the daily heat budget was analyzed for the water and ice surfaces from 1979 to 2014. Since net heat flux at the water surface (F_w) is much larger than that at the ice surface (F_i), the amount of heat input into the upper ocean was focused on through the open water fraction (Q_u), and this heat was compared with the volume of sea ice melt (Q_m) which was calculated from the observed decrease of ice area, accounting also for the decrease by ice advection (A_{dv}). In the calculation of Q_u, the analysis area varies as the ice retreats. It should be noted that, since most of the sea ice area exceeds 80% ice concentration even in summer, the total heat input at the ice surface is comparable to that at the water surface and thus contributes significantly to ice melt. In this paper, it was assumed heat input at the sea ice surface resulting in sur-

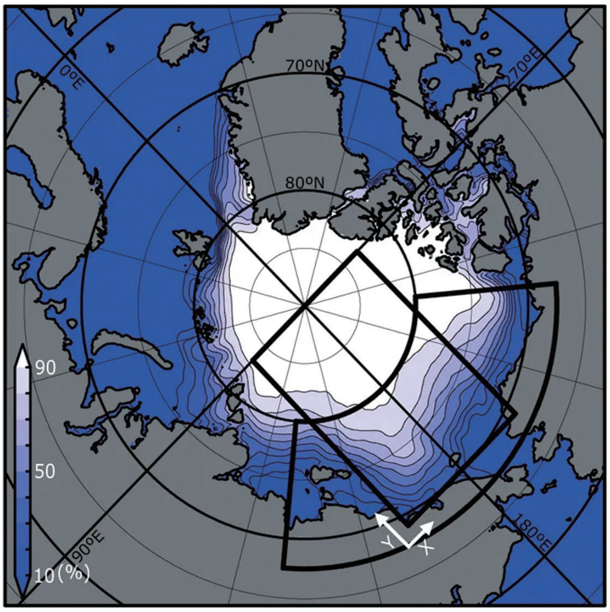

Fig. 5. 3. 8 Map of the Arctic Ocean with September sea ice concentration averaged from 1979 to 2014. The heat budget analysis and calculation of ice divergence were completed for the fan-shaped area. The simplified model was applied for the rectangular region. The map is drawn by GrADS 2. 0. 2 (Kashiwase et al., 2017).

face melt is exclusively used to reduce ice thickness. In calculation of Q_m and A_{dv}, a time dependent ice thickness which decreases from 1.4 m to 0.86 m was used through surface melt driven by Q_i (Fig. 5.3.9a).

Estimation from the heat budget analysis and satellite observations show that Q_u corresponds well with Q_m both for seasonal and interannual variations quantitatively (Fig. 5.3.9b, c and e). Correlation coefficients between Q_u and Q_m were statistically significant as 0.77, 0.85, 0.92 and 0.91 for the monthly mean from May to August, respectively (Fig. 5.3.9e). The correlation coefficient between yearly values is also statistically significant as 0.96 and 0.91 for detrended variations. However, results of the heat budget analysis have a relatively large uncertainty mainly due to the formation of melt ponds. It is noted that ice export from the fan-shaped area and its interannual variation (green lines in Figs. 5.3.9a and c) are much smaller than Q_u and Q_m. These results indicate that ice retreat in the Pacific Arctic is mainly due to the ice melt caused by heat input through the open water fraction, implying that the necessary condition for ice-ocean albedo feedback is satisfied in the study area.

The divergence in ice motion of the Pacific Arctic is determined mainly by the Transpolar Drift, the Beaufort Gyre and the migration of the ice edge. To deal with these factors simultaneously, the mean ice divergence

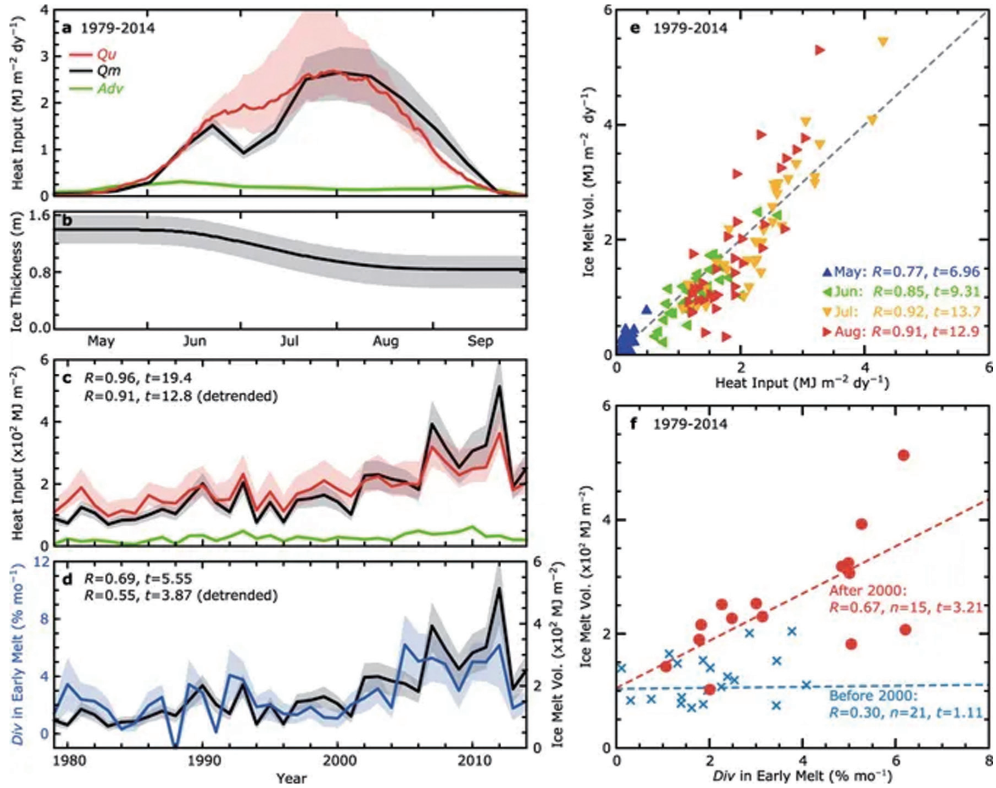

Fig. 5. 3. 9 Results of heat and sea ice budget analysis. (a) Seasonal evolution of mean ice thickness calculated from the surface melt by heat input at the ice surface. (b) Seasonal and (c) interannual variations in heat input through the open water fraction (*Qu*, red line), ice melt volume (*Qm*, black line), and the volume of ice export (*Adv*, green line). The volume of ice is converted to the heat required for the equivalent amount of ice melt. (d) Interannual variations of ice divergence (*Div*) averaged from mid-May to early-June (blue line) and *Qm*. (e) Scatter plot of *Qu* and *Qm*. Monthly means (May to August) for each year are plotted. (f) Scatter plot of *Div* averaged from early-May to mid-June versus *Qm*. Blue crosses and red circles indicate values before and after 2000, respectively. Dashed lines indicate the regression line for both periods. Uncertainties due to errors in the satellite observations are shown as shaded envelopes (Kashiwase et al., 2017).

over the analysis area (D_{iv}) was calculated using the ice drift velocity derived from satellite observations. Comparison between D_{iv} and ice retreat conditions show that D_{iv} during the melt season significantly correlates with the simultaneous/subsequent ice concentration and ice melt volume. Particularly, D_{iv} in the earliest stage of the melt season (from mid-May to early-June) has the highest correlation with sea ice retreat lagged by 1–2 months, with high correlation persiting through the end of August. Thus, the early D_{iv} is also well correlated with the yearly value of Q_m (Fig. 5.3.9d), with a correlation coefficient of 0.69 and 0.55 for detrended variations. These suggest that the divergent ice motion in the early melt season can be a trigger of ice melt acceleration through ice-ocean albedo feedback. After the 2000s, such relationship has likely become stronger, suggested by a much higher regression coefficient than that prior to 2000s (Fig. 5.3.9f).

Findings from this study show that the feedback effect triggered by early-season divergent ice motion plays a key role in the seasonal evolution and interannual variation of sea ice retreat in the Pacific Arctic, particularly since the early 2000s. In the early melt season, sea ice concentration sustains nearly 100% for both time periods, while, the fraction of multi year ice has decreased from 49 to 31%. This reduction affects sea ice dynamics, in particular through decrease in ice mechanical strength and internal forces, and increases in ice deformation rates. These outcomes in turn increase the momentum flux from the atmosphere to the ocean, and strengthen anticyclonic circulation in the Beaufort Gyre with a steeping sea surface height anomaly after the 2000s (Yoshizawa et al., 2015; shown in Section 5.1). As a result of such changes, ice drift speed has significantly increased, likely responsible for the increase in early summer D_{iv} from 1.9 to 3.7% mo^{-1}. Although the direct contribution of the increased divergence to reductions in ice concentration is quite small, heat absorption by the upper ocean through the end of August has gradually increased through ice-ocean albedo feedback, with an increase by a factor of up to 1.5 (from 153 MJ m^{-2} to 230

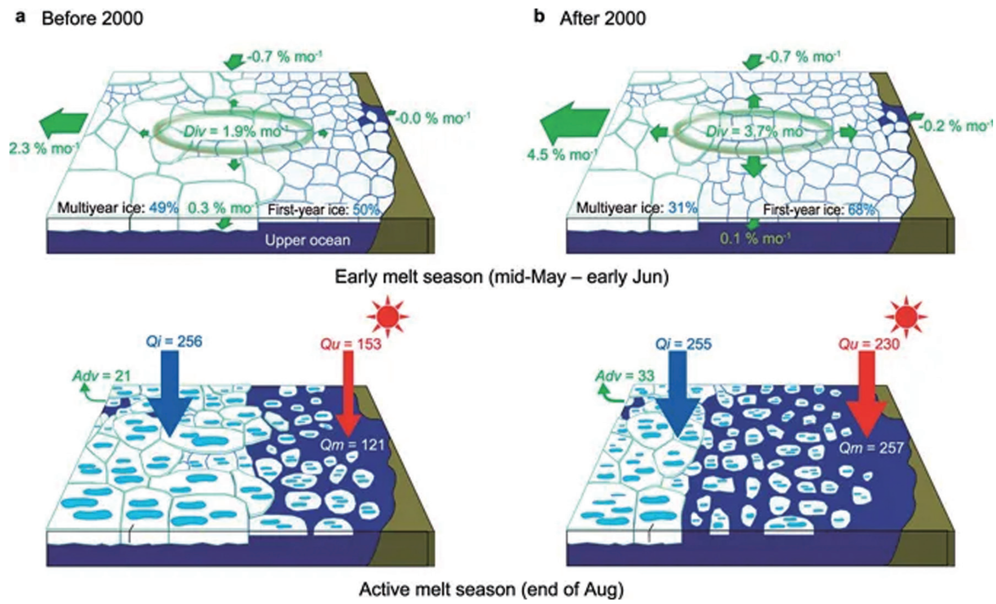

Fig. 5. 3. 10 Schematic of ice and heat budgets during seasonal ice retreat. Mean ice conditions and heat budgets for the two periods (a) 1979–1999 and (b) 2000–2014 are shown. Divergent ice motion in the early melt season induces a small reduction in ice concentration (upper panel). A key finding is that although the direct contribution of doubled divergent ice motion after 2000 to the ice concentration reduction is small, this trigger accelerates ice melt through the enhanced solar heat input over the open water fraction (ice-ocean albedo feedback) until the end of August (lower panel). All values in the lower panel are standardized as heat per unit area (MJ m^{-2} yr^{-1}), and the volume of ice is converted to the equivalent heat required for ice melt (Kashiwase et al., 2017).

MJ m^{-2}; Fig. 5.3.10). This increased heat uptake can explain about 70% of the observed 2.1-fold increase in sea ice melt (from 121 MJ m^{-2} to 257 MJ m^{-2}; Fig. 5.3.10). This contrast in the increase in annual ice melt compared to heat input is also evident in Fig. 5.3.9d, and is partly explained by the continuing decline in mean ice thickness.

This study provides a new perspective on the observed drastic ice reduction in demonstrating, through modeling and analysis of remote sensing data, that ice divergence in the early melt season is a key trigger for amplification of ice retreat through ice-ocean albedo feedback. This findings also suggest that early-season ice divergence is associated with a substantial skill for seasonal ice prediction.

5. 4. Modeling of circulation and physical processes of the Arctic Ocean

Basic model

Numerical modeling is key to deepening our understanding of the interaction between the Arctic and global climates. The study by Komuro (2014) focuses on the representation of the Arctic river water outflow and its impact on surface stratification. It is found that specifying weak surface mixing in a global ice-ocean coupled model has a considerable impact on the Arctic river water distribution and consequently on the Arctic stratification. The ice-ocean coupled model used in the study is Center for Climate System Research (CCSR) Ocean Component Model, version 4.5 (COCO4.5; Hasumi, 2015), which has also been employed as the ice-ocean component for the Model Interdisciplinary Research on Climate, version 5 (MIROC5; Watanabe et al., 2010). The model domain is global, with a horizontal grid size of approximately 60 km in the Arctic Ocean, and 17 vertical levels in the uppermost 250 m. The sea ice component includes a subgrid-scale sea ice thickness distribution, which greatly improves Arctic atmosphere-ocean heat exchange (Komuro and Suzuki, 2012).

The control experiment (CNTL) with the standard settings generally reproduces the largescale temperature and salinity structures, flow patterns and horizontal sea ice distribution. However, the CNTRL results have some biases in the Arctic Ocean. In particular the mixed layer is deeper than reality, and its improvement is one of the motivations of this study. The horizontal extent of the Beaufort gyre is also too small. In addition, the relatively coarse resolution puts limitations on the reproducibility of features such as coast currents. Three sensitivity experiments are performed: low vertical diffusivity K_V^b at all depths (LALL), low K_V^b at the surface (LSFC), and low K_V^b at surface with no wave-breaking mixing (LSNW). LALL employs a background value of K_V^b =

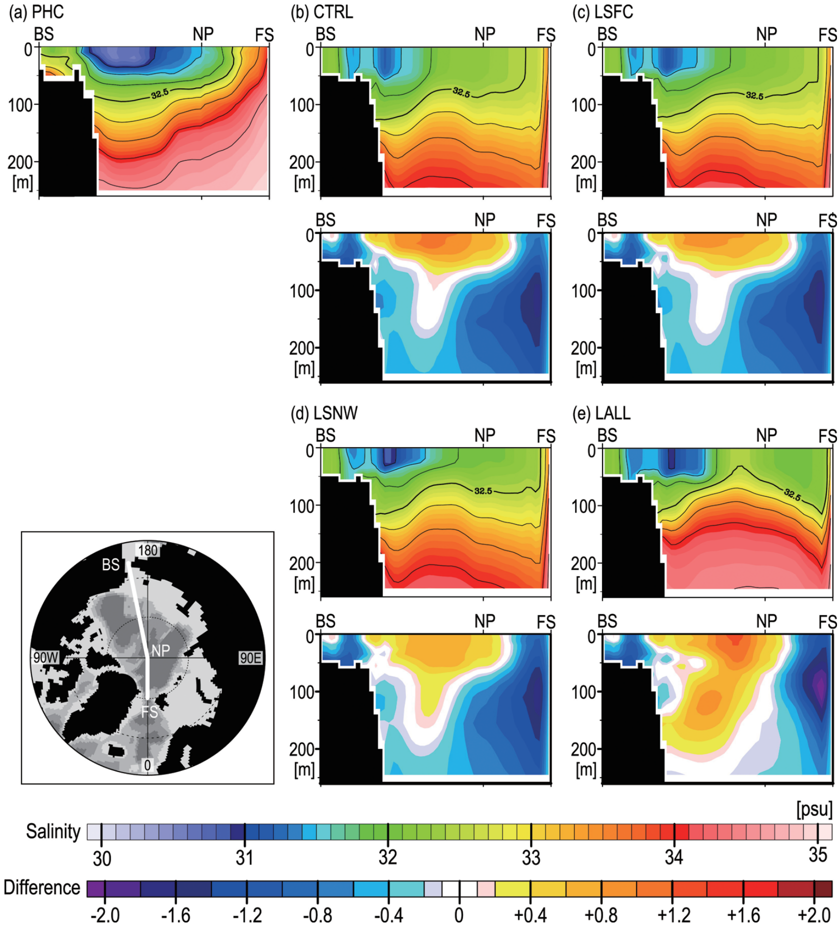

Fig. 5. 4. 1 Salinity for the uppermost 250 m along the section from the Bering Strait (BS) to the Fram Strait (FS). Note that NP stands for the North Pole. (a) PHC, (b) CTRL, (c) LSFC and (e) LALL (Komuro, 2014).

10^{-6} m^2 s^{-1} at all depths, which is approximately an order of magnitude smaller than that for CNTL in the surface layer.

Salinity cross sections of the uppermost 250 m across the Arctic basin are shown in Fig. 5.4.1 for the four runs and for the Polar Science Center Hydrographic Climatology (PHC; Steele et al., 2001). The climatological data show that surface water with low salinity (around 31 psu) extends out from the continental shelves. In CNTL, the volume of low salinity water is very small and it is trapped at the shelf break (Fig. 5.4.1b). In the other three experiments (LSFC, LSNW and LALL), low salinity water spreads out from the shelves, although to a smaller extent than in the climatology (Figs. 5.4.1c–e). The vertical salinity gradient at around 100 m in LALL is sharper and closer to the PHC data than in the other cases because of the low backgraound vertical diffusivity and is consistent with previous modeling studies with low vertical diffusion. Sea surface salinity in and around the Arctic Ocean shows similar behavior (not shown). Low-salinity water spreads out from the shelves in LSFC, LSNW and LALL, especially in the latter two cases. In these experiments, fresher surface water is also conspicuous in the coastal areas, where river water is added to the sea surface. The low-salinity water in the central Arctic Ocean seems to be connected to the fresh coastal water. These spatial patterns are also found in the PHC data.

Fig. 5.4.2 depicts the annual-mean fraction of the Arctic river water tracer along the section indicated in Fig. 5.4.1. The fraction is the lowest in CTRL, where the maximum appears below the sea surface (Fig. 5.4.2a). In the other cases, the fraction is higher and the maximum is at the surface (Fig. 5.4.2b–d). Thus the river water distribution in LSFC, LSNW and LALL is more realistic than that in CTRL, with LALL giving the best results.

The increase in the river water fraction in the surface layer is largely responsible for the surface freshening in these three cases. Changes are also found in sea ice thickness among the four cases, although the parameter settings for the sea ice component of the model are the same in all the experiments. Arctic summer (July–September) sea ice thickness in CTRL averaged over the Arctic Ocean is 242 cm. The sea ice thickens over most of the Arctic ice extent in all the cases. The fresher the

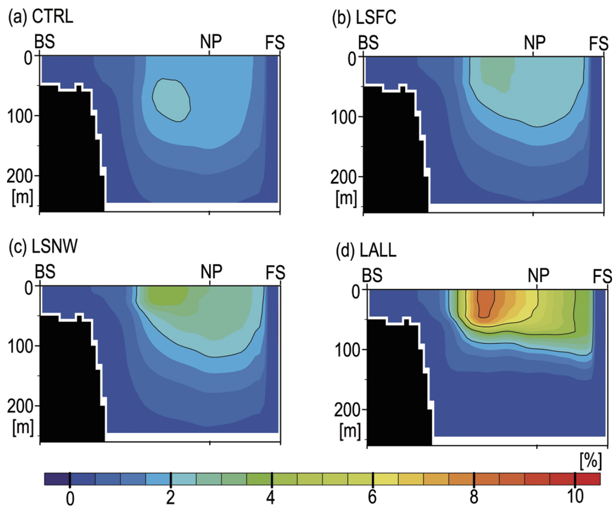

Fig. 5. 4. 2 Annual mean fraction of the Arctic river water tracer along the section shown in Fig. 5. 4. 1 for (a) CTRL, (b) LSFC, (c) LSNW and (d) LALL (Komuro, 2014).

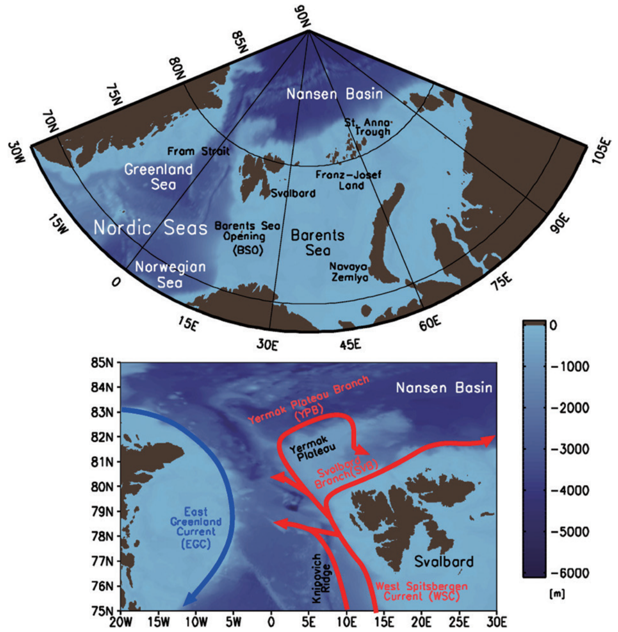

Fig. 5. 4. 3 (top) The bathymetry of the Nordic Seas, the Barents Sea and the Nansen Basin. (bottom) A shematic for the circulation of warm/salty Atlantic water (red arrow) and cold/fresh East Greenland Current (blue arrow) around the Fram Strait (Kawasaki and Hasumi, 2015).

surface salinity, the thicker the summer sea ice: the summer thickness averaged over the Arctic Ocean compared with that for CTRL is 17, 28 and 39 cm greater for LSFC, LSNW and LALL, respectively.

In summary, the representation of the surface low-salinity water is improved in the Arctic Ocean in all the cases with lower background K_V^b. LALL is the most realistic, but LSNW also performs well, particularly in the surface layer. The distribution of the river water tracer suggests that the concentration of river water in the surface layer leads to these improvements. In addition, the Arctic sea ice thickness is also sensitive to the change in background K_V^b.

Heat transport

Interannual variability of the Arctic sea ice is controlled not only by heating or cooling by the atmosphere but also by the heat flux from the ocean underneath as shown in the previous paragraph. Cold low salinity water originated in the river runoff covers the sea surface in the Arctic Ocean. Warm Pacific Water passing through the Bering Strait lies just below it, and a change of its behavior caused the recent drastic decline of Arctic sea ice (Shimada et al., 2006). Below Pacific Water, the Atlantic Layer Water is found (~150–400 m depth), which is originated from the Atlantic water entering through the Fram Strait and contains a larger amount of heat than Pacific Water. It melts the Arctic sea ice through the significant upward heat flux by the enhanced vertical mixing over the rough topography and double diffusion along the Barents and Laptev Slopes. For monitoring the water passing through the Fram Strait, many moorings have been deployed and repeated CTD observations have been conducted along 79°N (Schouer et al., 2008). On the other hand, the ocean circulation and its variability to the north of 79°N have not been described so clearly as those to the south due to the observational difficulty caused by sea ice (Fig. 5.4.3).

Kawasaki and Hasumi (2015) tried to reproduce the Atlantic water inflow (the West Spitsbergen Current (WSC) and eddy activity) to the Arctic Ocean as realistically as possible by using an ice-ocean model with high-horizontal resolution around the Fram Strait. Then, they examined the heat transport to the Arctic Ocean by the Atlantic water passing through the Fram Strait with focusing on: (1) the amount of heat removed by eddies, returning currents, and sea surface cooling, and (2) factors controlling the interannual variability of heat transport at the north of the Fram Strait (79°N).

The ice-ocean general circulation model employed in this study is COCO version 4.5 (Hasumi, 2015). The model domain is global. As the Rossby's deformation radius is ~10 km around the Fram Strait, effects of mesoscale eddies cannot be explicitly represented unless the horizontal grid size is significantly smaller than 10 km. As in the study of Kawasaki and Hasumi (2014; explained in Section 7.4), special high resolution is applied to the region of interest by placing the poles of the general curvilinear horizontal coordinates close to the region, on the Greenland and Scandinavian Peninsula. The horizontal resolution is eddy resolving (2–3 km) in the Fram Strait and the Barents Sea Opening (BSO), and is eddy permitting (3–10 km) around the Nordic Seas, the Barents Sea and the Nansen Basin (Fig. 5.4.4). The integrated period is from 1980 to 2010. The first 10 years (1980–1990) is for spin-up of sea-ice distribution and mean circulation in and around the Arctic Ocean.

The modeled temperature and salinity around the Fram Strait and the Barents Sea averaged in the shallow layer (0–300 m depth) and for 1993–2010 are displayed in Fig. 5.4.5. The warm, salty Atlantic water is transported northward by the Norwegian Atlantic Current in the Norwegian Sea. A part of the Norwegian Atlantic Current flows into the Barents Sea through the Barents Sea Opening (BSO) and the rest flows into the Nansen Basin through the Fram Strait. The Atlantic water entering the Barents Sea flows northeastward along several routes

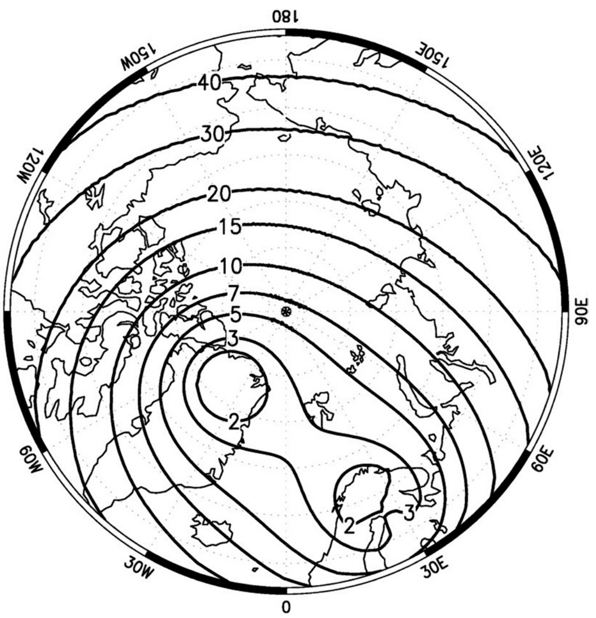

Fig. 5. 4. 4 Horizontal grid size of model (km) (Kawasaki and Hasumi, 2015).

constrained by the bathymetric structure on the shelf. This water reaches the Nansen Basin by passing between Frantz-Josef Land and Novaya Zemlya and through the St. Anna Trough. The net volume transports through the Fram Strait, the WSC and the BSO are 2.8, 7.1 and 2.4 Sv (Sv = 106 m^3 s^{-1}), respectively from the model and 2.0, 6.6 and 2.0 Sv, respectively from observations. All simulated volume transports are slightly larger than observed. The net southward volume transport at the Fram Strait is comparable with the net eastward volume transport at the BSO, which is consistent with observations.

The 17 year mean heat transports at the Fram Strait and the BSO are 58 and 88 TW, respectively, when −0.1°C is chosen as the reference temperature for the sake of comparison with previous observed estimates. In comparison to a mooring observation (16–41 TW in 1997–1999 and 40–50 TW in 2004–2006; Schauer et al., 2004, 2008), it is slightly higher at the Fram Strait. It is likely that the heat flux is overestimated in the model. The heat flux at the BSO is in the range of estimates by a mooring observation (73 TW) and an inverse model (103 TW). As the heat flux into the Nansen Basin through the St. Anna Trough is −12 TW (the negative value means that the temperature of passing water is less than −0.1°C), it is obvious that the Atlantic water flowing through the Fram Strait has larger contribution to the heat supply to the Nansen Basin than that through the Barents Sea. The temperature of the Atlantic water entering the Nansen Basin through the Barents Sea and St. Anna Trough is low because of the strong sea surface cooling on the way flowing northeastward on the shelf (Fig. 5.4.5a). On the other hand, the Atlantic water flowing through the Fram Strait toward the Nansen Basin retains a high-temperature property. As a consequence, the Atlantic water transported through the Fram Strait provides the Arctic Ocean with a larger amount of heat than that through the Barents Sea.

Mean meridional velocity and potential temperature

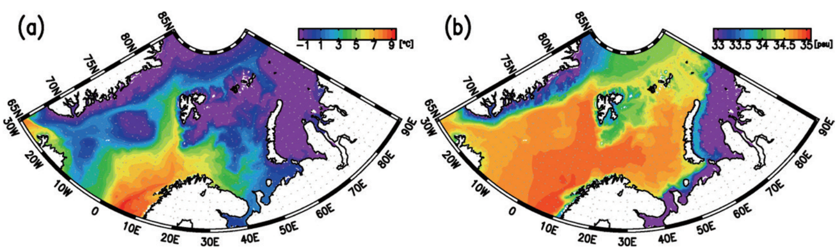

Fig. 5. 4. 5 Distribution of (a) potential temperature and (b) salinity averaged in the shallow layer (0–300 m depth) and for 1993–2010 (Kawsaki and Hasumi, 2015).

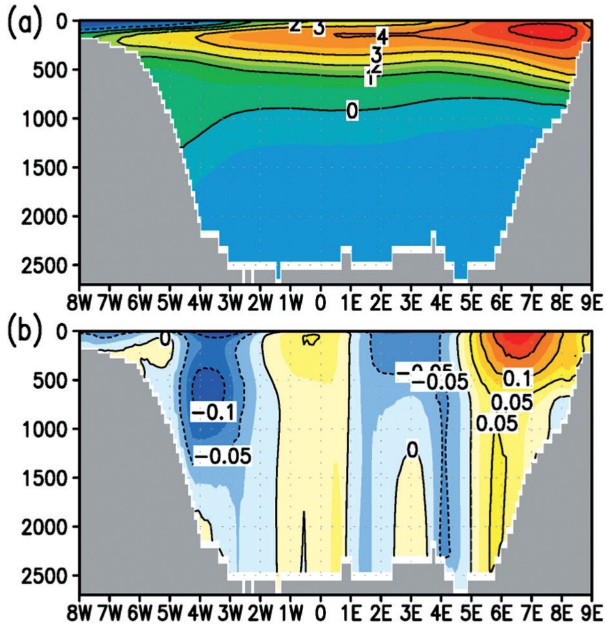

Fig. 5. 4. 6 Distributions across the Fram Strait (79°N) of (a) temperature and (b) meridional velocity averaged for 2002–2008 (in°C and m s^{-1}) (Kawasaki and Hasumi, 2015).

distributions at the Fram Strait (along 79°N) between 2002 and 2008 are shown in Fig.5.4.6. This period is selected for comparison with an observational study. The warm Atlantic water is transported northward by the WSC at the eastern Fram Strait (on the side of the Svalbard). On the other hand, the cold Polar Water is transported southward by the EGC at the western Fram Strait (on the side of the Greenland). This qualitative feature of currents is consistent with many observations, and only possible by the high-resolution experiments.

It was demonstrated that the interannual variability of heat flux toward the Nansen Basin is related to the Siberian high variability. The strengthen of Siberian high induces the weakening of Atlantic water inflow toward the Nansen Basin, and finally the sea ice in the Nansen Basin. Several recent studies showed that the Arctic sea ice retreat induces enhancement of winter Siberian high (Inoue et al., 2012; Tang et al., 2013; Mori et al., 2014). These studies suggested only the effect of the Arctic sea ice on the atmosphere (the Siberian high). This study presented the first scientific evidence of possible effect of atmospheric (the Siberian high) change on the oceanic heat flux. The linked variability of the Arctic sea ice and Siberian high should be examined by using a climate model.

5. 5. Prediction of the Arctic sea ice distributions

Monitoring of sea ice thickness

As for the support of ice navigation, sea ice area is not only the necessarily information but also sea ice thickness is indispensable. The ice draft algorithm for AMSR-E data is adapted from ice thickness measurement method using passive microwave radiometer Special Sensor Microwave Imager (SSM/I) data developed by Tateyama et al. (2002). The moored upward looking sonar (ULS) measurements are used to calibrate a coarse algorithm to estimate sea ice thickness using satellite microwave observations by Krishfield et al. (2014). The sea ice thickness detecting ability of a polarization ration PR36 was examined, calculated from 36 GHz brightness temperatures measured by ship mounted microwave radiometers on RV Shirase in the Antarctic. PR_{36} is calculated using the following equation (same stile as the eq. 5.2.1):

$$PR_{36} = (TB_{36V} - TB_{36H})/(TB_{36V} + TB_{36H}) \qquad (5.5.1)$$

where TB_{36V} and TB_{36H} are brightness temperatures of vertical and horizontal polarization of 36 GHz measured microwave radiometers, respectively. Fig. 5.5.1 shows the relationship between EM thickness and PR36 observed in the Lutzow-Holm Bay, East Antarctica on the way to the Syowa Station, extending from early summer melt to fall freezeup. A negative correlation between PR_{36} and EM thickness is shown by the figure; however,

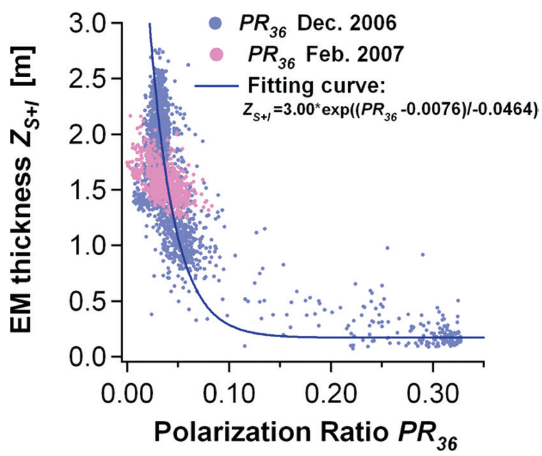

Fig. 5. 5. 1 The relationship between EM thickness and PR36 derived from observation in the Luzow-Holm Bay, East Antarctica (67–69°S and 38–40°E) in 2006–2007 Antarctic summer. The blue and pink dots mean the period of December 2006 and February 2007, respectively. The solid curve means regression curve (Krishfiel et al., 2014).

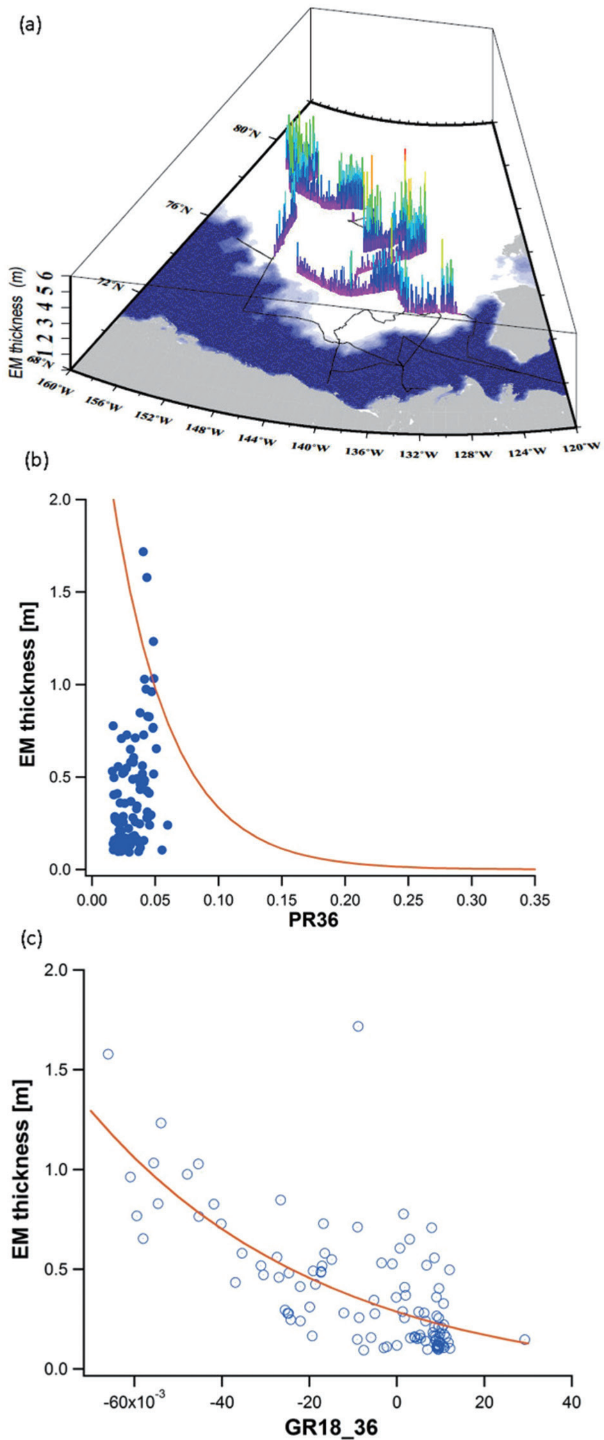

Fig. 5. 5. 2 (a) Distribution of sea ice thickness derived from AMSR-E and EM between 29 September and 12 October 2010, (b) relationship between EM thickness and PR_{36}, (c) relationship between EM thickness and GR_{18-36} (Krishfield et al., 2014).

only sensitive in the thickness of less than 1 m.

In the Arctic, sea ice thickness estimation using EM and microwave radiometers occurred during IJIS (International Arctic Research Center – Japan Aerospace Exploration Agency information System) cruise in the Beaufort Gyre. Fig. 5.5.2 shows a relationship with EM

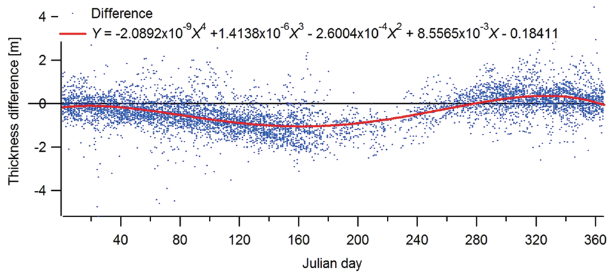

Fig. 5. 5. 3 Seasonal change of thickness difference between IJIS draft (from PR_{36} and GR_{6-36}) and ULS draft (Krishfield et al., 2014).

thickness derived from AMSR-E and EM. PR_{36} showed no relation to thickness of second-year and multiyear ice which has a fresh ice layer on the surface or deeper layer formed through summer melting season. Multiyear ice is characterized by greater penetration depth than first year ice because its properties include much lower salinity and less moisture. Though the physical theory on microwave signal variations with multiyear ic thickness is still uncertain, decreasing of gradient ratio (GR) may be attributed to volume scattering by deep snow on thicker ice. Here, GR between vertically polarized 18 and 36 GHz (as eq. 5.1.1):

$$GR_{18-36} = (TB_{36V} - TB_{18V})/(TB_{36V} + TB_{18V}) \qquad (5.5.2)$$

was compared with EM thickness in Fig. 5.5.2b. The figure shows a better sensitivity for the multiyear ice. This result suggests that GR_{18-36} changes with differences ice temperatures at each penetration depths of 18 and 36 GHz, and snow depth over the sea ice. PR_{36} and GR_{18-36} were calculated from AMSR-E brightness temperatures and compared with daily-averaged ice draft data derived from the ULS. Although AMSR-E PR_{36} and GR_{18-36} showed agreement with ULS draft in September, GR_{18-36} thickness showed saturation and significant underestimation in other months. The difference between 6 and 36 GHz is the most sensitive to ULS draft. So, PR_{36} was confirmed as the best sea ice thickness parameter for the first year ice and for older ice, GR_{6-36} was chosen as the parameter.

Fig. 5.5.3 shows the seasonal change of thickness difference between ULS draft and IJIS draft calculated using PR_{36} and GR_{6-26}. The thickness difference for all the years and all mooring points plotted together show significant seasonal variability with minimum in January and September. Underestimation error increases toward summer and causes a maximum in June. Overestimation error increases toward late autumn and causes a maximum in October. This suggests that existence of surface liquid water and surface salt drainage in summer and refreezing melt water contribute to large signal shifts on microwave radiation. To minimize the seasonal error empirically, the equation listed in Fig. 5.5.3 (red line) was applied.

Short-term sea ice prediction by high resolution regional model

In order to utilize the Arctic Sea Routes (ASR), accurate sea ice observations and predictions are vital to protect ships and offshore/coastal structures. Long-term, medium-term and short-term predictions are needed for safe navigation in the ASR. Long-term predictions – looking 20–30 years ahead – inform decisions regarding the construction of new icebreakers and ports. Medium-term predictions – about three to six months – contribute to deciding on whether to utilize the ASR or the conventional southern sea route in the coming summer navigation season. Finally, short-term predictions – one to two weeks – are used to choose the safest and shortest path in the Arctic Ocean once a ship enters ice-covered areas.

This study by De Silva et al. (2015) considers how numerical modeling can be used to make a short-term predictions of sea ice conditions. Numerical modeling of sea ice has become an important instrument for ice monitoring, understanding past conditions, explaining recently observed changes and making future predictions regarding the Arctic Ocean. Here, De Silva et al. (2015) aim to reproduce the short-term sea ice conditions in the ASR using mesoscale eddy-resolving ice-ocean coupled model, while explicitly treating the ice discrete characteristics in marginal ice zones. Ice discrete characteristics are introduced to the model using Sagawa's (2007) floe collision rheology. In addition, to minimize sea ice diffusion and improve the accuracy of locating ice edges, subgrid-scale ice motion (semi Lagrangian movements) was incorporated into the sea ice dynamics (Rheem et al., 2007). The ice-ocean coupled model developed in this study is based on a three-dimensional high-resolution regional model in the Sea of Okhotsk (Fujisaki et al., 2010) in which an ocean model is based on generalized coordinates, the Message Passing Interface version of the Princeton Ocean Model (POM; Mellor et al., 2002). The zonal and meridional grid spacings are approximately 25 × 25 km and 2.5 × 2.5 km for the whole-Arctic and high-

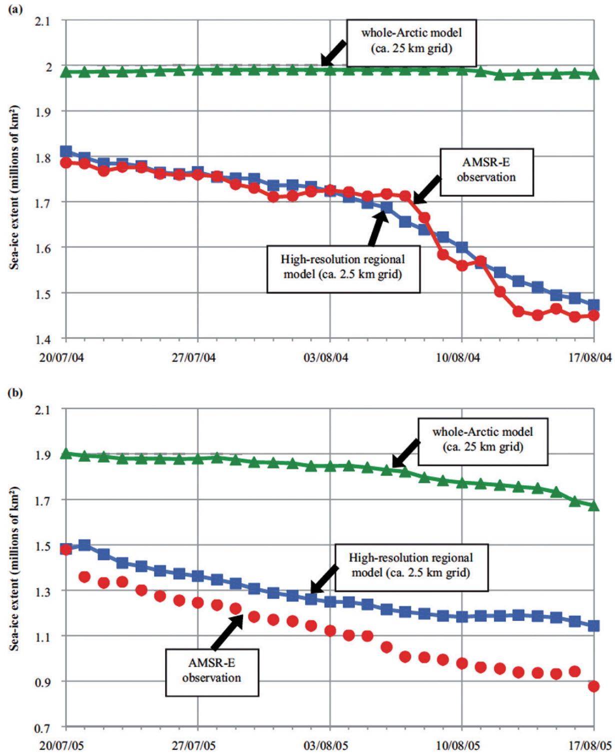

Fig. 5. 5. 4 Seaice extent from the whole-Arctic model with coarse grid, the Laptev Sea regional model with the fone grid and Advanced Microwave Scanning Radiometer-Earth Observing System (AMSR-E) satellite observations during (a) 20 July 2004 to 17 August 2004 and (b) 20 July 2005 to 17 August 2005. Area covered with ice concentration more than 15% taken into the comparison (De Silvia et al., 2015).

resolution regional models, respectively. The model domains for the high-resolution models are Laptev Sea region (LS) including the Laptev Sea and part of the Kara and East Siberian seas, and Chukchi Sea region (CS) including parts of the East Siberian and Chukchi seas. The European Center for Medium-Range Weather Forecast Re-Analysis Interim (ERA-Interim) six-hourly data from 2000 to 2011 are given as the atmospheric forcing.

Although the whole-Arctic model was able to capture sea ice conditions accurately, it cannot be used to accurately predict details of ice-edge locations and extents. Figs. 5.5.4 and 5.5.5 show a time series of sea ice extent in the LS and CS regions for short-term hindcast simulations in 2004 (when North-east Passage was closed) and 2005 (North-east Passage was open), respectively. In both the LS and Cs regions, computations are performed from 20 July to 17 August in both years. As shown in Fig. 5.5.4a, the sea ice extent simulated in the LS regional model varied from 1.8 × 10^6 km^2 to 1.4 × 10^6 km^2 within four week period in 2004 because of thermodynamics and dynamics activities. In the first two weeks, the computation shows a similar reduction pattern with

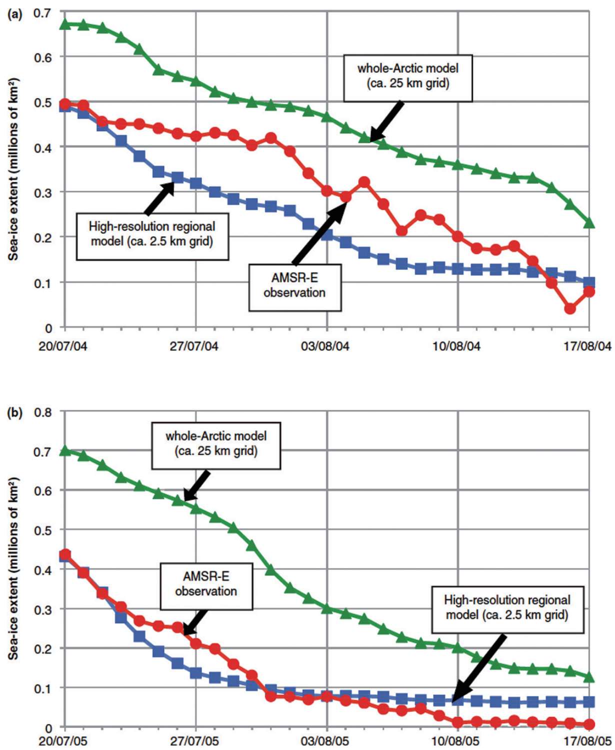

Fig. 5. 5. 5 Sea ice extent from the whole-Arctic model with coarse grid, the Chukchi Sea regional model with the fine grid and Advanced Microwave Scanning Radiometer-Earth Observing System (AMSR-E) satellite observations during (a) 20 July 2004 to 17 August 2004 and (b) 20 July 2005 to 17 August 2005. Area covered with ice concentration more than 15% taken into the comparison (De Silvia et al., 2015).

observations. In the third week, the observational sea ice extents show a dramatic reduction, but the model cannot capture such a dramatic reduction. At the end of the third week (11 August 2004), the model sea ice extent is almost equal to the observational results. But again in the fourth week, the model has drifted away from the observation. Fig. 5.5.4b shows the model sea ice extent variation from 1.5 × 10^6 km^2 to 1.1 × 10^6 km^2 in 2005. In contrast to 2004, when the North-east Passage was closed, the high-resolution regional model overestimates the sea ice extent compared to the observations in 2005. Instead of high-resolution computations, the coarse-grid whole-Arctic computation (extracted LS region) cannot reproduce the ice extent variations in both years. Sea ice in the whole-Arctic model was almost unchanged in 2004, while it showed a slightly decreasing trend throughout the 2005 computations.

As shown in Fig. 5.5.5, the sea ice extent in 2004 and 2005 varied in the CS region from 0.5 × 10^6 km^2 to 0.05 × 10^6 km^2 within the four weeks. However, the difference between the observations and the model is much larger (about 0.1 × 106 km^2) in 2004 than in 2005. In contrast to the LS region, the whole-Arctic simulation (extracted CS region) showed a similar decreasing trend in sea ice extent compared to the satellite observations in the CS region. Considering all the qualitative and quantitative comparisons of the regional model results, it is believed that the coarse-grid computation cannot be used to reproduce sea ice variations in summer accurately. But the fine-grid computation can reproduce sea ice variations accurately using satellite observations. However, even high-resolution computations are unable to follow the dramatic reduction of sea ice extents, such as shown in Fig. 5.5.4a.

There are several possible reasons for this discrepancy in the results between coarser and high-resolution grid computations. The first reason is mesoscale eddy-resolving capability. The second is that small-scale sea ice dynamics (converging and diverging process) were more correctly captured with the high-resolution models. The third possible reason is that the high-resolution computation well expresses the ice-albedo feedback process, which accelerates ice melting in the spring and summer.

Medium-range prediction of the summer Arctic sea-ice area

Recent reduction of summer sea ice cover in the Arctic has accelerated maritime transport using the Arctic sea routes. Sea ice prediction is essential to realize safe and efficient use of the route. We are trying to predict summer Arctic sea ice cover in spring by analyzing satellite observation data. This prediction focuses on the ice thickness in spring as preconditioning of the ice melting in summer. For this prediction, a daily-ice velocity product on a 60-km resolution grid is prepared using data by satellite passive microwave sensors AMSR-E and AMSR2.

Kimura et al. (2013) found that the winter divergence/convergence of the ice motion is strongly related to the summer ice cover in some regions. A daily-ice velocity data set has been prepared for winter season between 1 December and 30 April, which is the same one used in the study on the Southern Ocean (Kimura and Wakatsuchi, 2011), calculated from images of the AMSR-E satellite. Ice velocity is computed from the gridded brightness temperature of 89 GHz horizontal and vertical polarization channels which is binned to square pixels of 6.25 × 6.25 km by the National Snow and Ice Data Center (NSIDC). The procedure for detecting ice motion, which has been improved in the studies (e.g., Kimura and Wakatsuchi, 2000, 2004), is based on the maximum

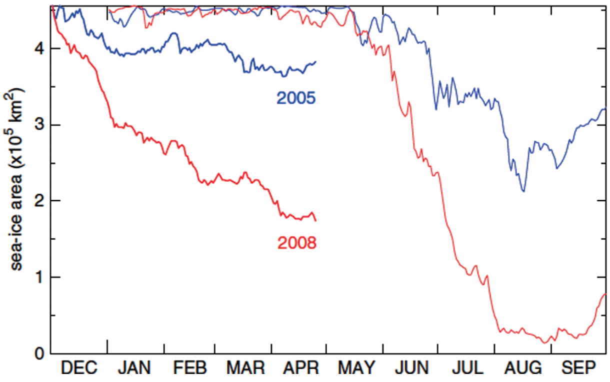

Fig. 5. 5. 6 Bold lines indicate the fraction of sea ice existing since before 1 December and the temporal evolution of the number particles within that part of the Beaufort Sea for 2005 and 2008. The unit of the particle number is converted to ice area (km^2) by multiplying by 37.5 × 37.5, under the assumptions that each particle represents a 37.5 × 37.5 km of area with 100% ice concentration and that ice melting during December and April is negligible. Thin lines show the corresponding total sea ice area within the same region calculated from the daily-ice concentration (Kimura et al., 2013).

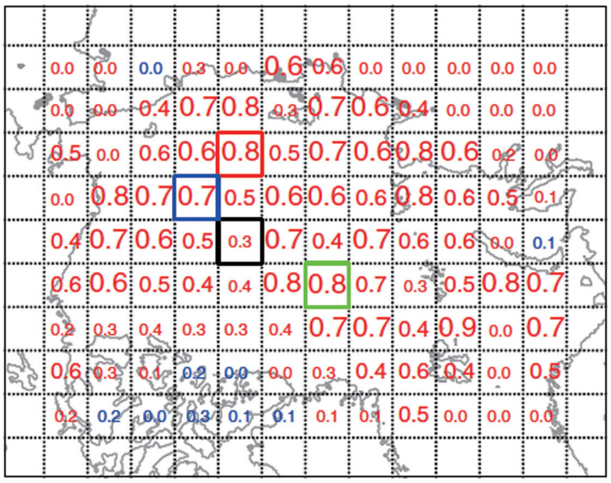

Fig. 5. 5. 7 Correlation coefficient between the number of particles on 30 April migrated from 1 December (NP4) and the total ice area on 10 September (IA9) of the same year for 108 domains, based on the nine years' data (Kimura et al., 2013).

cross-correlation method described by Ninnis et al. (1986) and Emery et al. (1991). After these processes, a daily-ice velocity data set was constructed without missing data over the sea ice area on a 37.5 × 37.5 km grid (6 × 6 of original 6.25 km square grid) for the nine year period 2003–2011.

To visualize the dynamic redistribution of sea ice, movement of particles spread over the ice covered area is calculated. About 10000 particles are arranged at an interval of 37.5 km over the ice area on 1 December of each year. Daily displacement of particles released on the day is calculated from AMSR-E derived ice velocity on one-day time steps. Since sea ice concentration within the Arctic is near 100% during winter, ice divergence and convergence yield new ice production and dynamical thickening, respectively. The spatial inhomogeneity of the particles distribution becomes significant with time. Though there are obvious interannual differences, particles generally become sparse in the Kara, Laptev and Beaufort seas in contrast to the convergence of ice particles in the East Siberian Sea. In the convergence area, the density of the particles becomes higher than initial distribution. This means that dynamic deformation and accompanied thickening of sea ice through rafting or ridging of ice floes is occurring. In contrast, ice divergence promotes the formation of leads and polynyas, which is associated with new ice production; it results in a higher fraction of thin ice compared with the convergence areas. As a result, ice thickness in divergence area becomes lower compared with convergence areas. Summer ice cover has a relation to the ice motion before spring probably through the dynamic change of ice thickness.

For example, in the Beaufort Sea, sea ice cover retreats between May and September in both 2005 and 2008 (Fig. 5.5.6). In 2008, more than 60% of the particles were exported from this region between 1 December and 30 April, that is, the ice area at the end of April consists of more than 60% thin ice produced after December. In response to the thinning, ice area in 2008 decreased rapidly after May. In contrast, in 2005 there was little export of ice during winter and the resulting predominantly thick ice resulted in the slow decrease of total sea ice area during the melting season.

This paragraph examines the relationship between the winter ice redistribution and summer ice area based on the nine years of 2003–2011 for 108 domains defined by 375 × 375 km^2 (10 × 10 pixels, 1.4 × 10^5 km^2). Here, two quantities are focused on, total ice area on 10 September (IA9) and the number of particles converted into the area on 30 April moved from 1 December (NP4): the unit of both is square kilometers. IA9 is calculated by adding up the ice concentration within each domain. Base on nine data points of the nine years' data, Fig. 5.5.7 shows the correlation coefficient between NP4 and IA9 of same year, for each domain. There are high correlation coefficients between the winter ice redistribution and summer ice area in several domains. The relationship is significant in 18 domains at a 95% confidence level, that is, domain with a correlation coefficient of more than 0.67.

Fig. 5. 5. 8 Observed ice cover on 11 September 2013, 2014 1nd 2015, overlapped by the predicted ice edge line for the same days. Ice edge location is defined by the 30% of ice concentration. By considering the initial ice thickness, accuracy of the prediction in 2015 becomes higher compared with 2013 and 2014 (Kimura and Yamaguchi, 2016).

The strong relationship in these domains supports the scenario that a greater ice divergence or outflow in winter and resulting thinner ice cover in spring contributes to the smaller ice area in summer.

There are other factors controlling the spring ice thickness. Small scale ice process such as ice thickening through rafting/ridging of ice floes and new ice production in leads, thermodynamic ice thickening/thinning, ice movement and melting attributed to the summer weather condition and so on are ignored in this study. The point is that even though these processes were not taken into consideration, the linear relation between the winter ice motion and summer ice cover is still significant in many regions with large interannual variability. Based on the linear relationship between NP4 and IA9, we can potentially improve the prediction of the summer ice area in spring by analyzing the satellite derived winter ice motion. This medium-term forecast looking several months ahead is useful for human activity in the Arctic, foe example to determine whether or not the shipping route through the Arctic – the Northern Sea Route – will be navigable.

Prediction capability

Following this study by Kimura et al. (2013), additional information of ice thickness from Krishfield et al. (2014) improved the forecast of summer ice extent. Kimura and Yamaguchi (2016) estimated provisional ice thickness on 30 April by particle density multiplied by the initial ice thickness only in the thick-ice (> 1.5 m) area and the highest correlation between the spring ice thickness and summer ice cover was acquired. By considering the initial ice thickness, accuracy of the prediction becomes higher compared with the prediction based on the particle density only (Fig. 5.5.8). Based on the analysis, first report of the summer ice prediction showing the ice concentration map for 1 July to 11 September is released in May on the website[*1] and Arctic Data archive System[*2] (ADS). After then, updated predictions are released at the end of June and July. Information of the predicted ice area was also sent to Sea Ice Outlook[*3].

5. 6. Navigation support systems

In order to support ship navigation in the Arctic sea routes, it is necessary to investigate the effects of sea ice and cold oceans on ships.

Ship icing

Marine disasters by ship icing occur frequently in cold regions. In recent years, the summer condition of the Arctic Ocean has been changing and expansion of the open water area on the Arctic sea routes increases the frequency of sea spray generation and marine icing, because the air temperature remains cold enough and con-

*1 http://www.1.k.u-tokyo.ac.jp/YKWP/ 2015article_e.html
*2 https://ads.nipr.ac.jp/vishop/
*3 https://www.arcus.org/sipn/sea-ice-outlook

ditions are suitable for sea spray icing. To address icing on the ship, liquid water content (LWC) of sea water is one of the important parameter. In order to address icing on ships, Ozeki et al. (2016) developed sea spray meters, the sea spray particle counter (SPC) and the marine rain gauge type spray gauge (MRS), for measuring the spray particles and the amount of spray. The SPC was originally developed for the measurement of drifting snow (Nishimura and Nemoto, 2005). The flux distribution and the transport rate could be calculated as a function of particle size. Based on the previous observation case (Ozeki and Adachi, 2013), the SPC was improved to be a seawater spray particle counter. The SPC measures particle size range from 100 to 1000 μm in diameter.

The marine rain gauge type spray gauge (MRS) consists of marine rain gauge and cylindrical spray trap. The marine rain gauge was developed to measure rainfall on ships that pitch and roll. It collects seawater spray or precipitation in a catchment funnel which has a cross sectional area of 100 cm^2, and the inside diameter of the funnel is 112 mm. The cylindrical spray trap was attached above the marine rain gauge to capture the seawater spray from the horizontal direction instead of precipitation. The amount of seawater spray is measured every minute and the smallest measurable unit is 0.1 mm.

The field tests were conducted on the r/v Shirase (icebreaker), when the vessel sailed in open water. The amount of seawater spray and the size and number of seawater particles were measured by an SPC and two MRSs during Japanese Antarctic Research Expedition (JARE) -55 and 56. To analyze the seawater spray characteristics, a correlation analysis was performed between the amount of seawater spray, the size and number of seawater particles and the wind velocity. According to the well known equation of the vertical distribution of liquid water content (e. g., Zakrzewski, 1987) in the seawater spray, it is expected that the amount of seawater spray depends on the relative wind velocity under a fixed height and a constant wave height condition. As shown in Fig. 5.6.1, the amount of seawater spray measured by the SPC was strongly related to the relative wind velocity at every observation point, although the fitting curve was not a quadratic expression.

To clarify the characteristics of the size of seawater particles on the deck, the wind velocity dependence of the particle size distribution was analyzed using the SPC data obtained in JARE-55 and -56. Fig. 5.6.2 shows the average spray particle size distributions by each relative

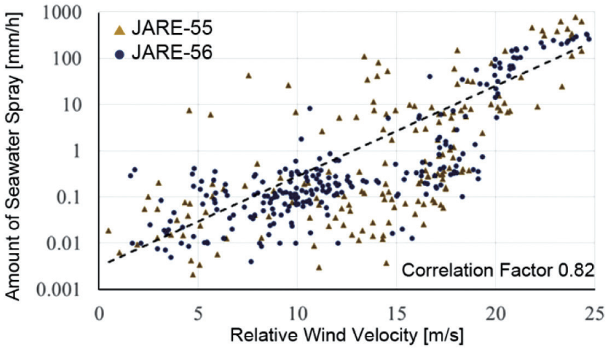

Fig. 5. 6. 1 Correlation diagram of the amount of seawater spray measured by the SPC and relative wind velocity (Ozeki et al., 2016).

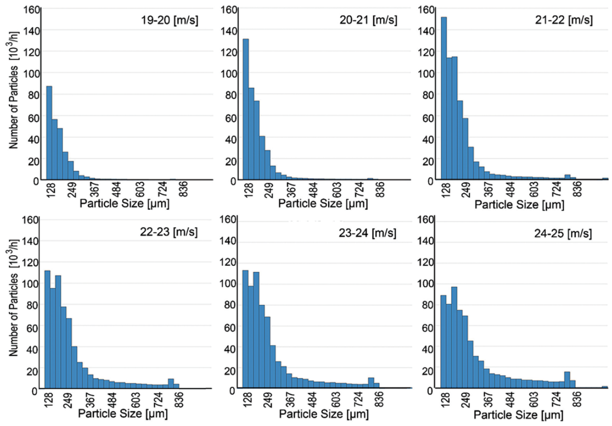

Fig. 5. 6. 2 Spray particle size distribution by each wind velocity (Ozeki et al., 2016).

wind velocity. It indicates that the particle size distribution becomes braod and the rate of large particle increase with increases in relative wind velocity. The large particles affect the increase of seawater spray volume strongly, because the volume of droplet is in proportion to the third power of the diameter of droplet. Therefore, the wind velocity dependence of the amount of seawater spray might include the effect of the shift of particle size distribution. On the other hand, when the relative wind velocity was lower than 19 m s^{-1}, the amount of seawater spray was very small, because the compass deck of large vessel was higher enough to reduce the drifted seawater spray under the low wind velocity condition. From these results, it may be concluded that the SPC measurement is superb way to analyze the particle size distribution of impinging seawater spray.

Optimal routing of ships

Takagi et al. (2014) formulated the selection of the sea route in the ice sea as the finding-path problem. Sea ice has caused a significant damage to vessels in the Arctic.

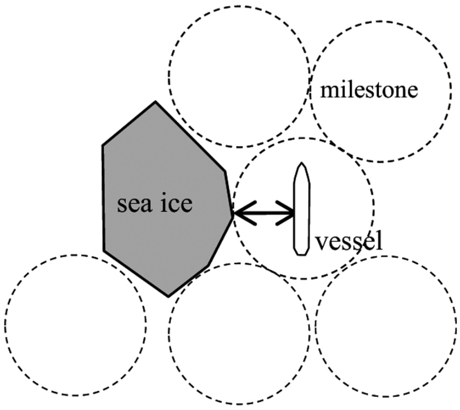

Fig. 5. 6. 3 Milestone of ship of circle (Takagi et al., 2014).

There have been over 200 reported damage events over the past 25 years. It is important to avoid the collision with sea ice, and to select the route to save the fuel and time safely. However, it is not easy to select the best sea route promptly and safely because the shape and distribution of sea ice are very complex. Probablistic roadmap method (PRM) is a popular path planning scheme that can find a collision-free path by connecting the start and goal through a roadmap constructed by drawing random node in the free configuration space. The PRM consists of two phases: a construction and a query phase. The construction phase have two processing before constructing the roadmap graph; construction free space and checking collision with the obstacles for all local paths. These processing needs a lot of calculation time. The paper presented new method that constructed a roadmap graph without these processings. The path between the start and goal was decided by using Dijkstra's Algorithm (Dijkstra, 1959) as a query. Experimental results showed the effectiveness of the proposed method.

To examine the proposed method by various concentration of sea ice, a sea ice in the algorithm described is presented as an irregular polygon inscribed into an ellipse. A sea ice is defined as a ratio of the minimum diameter of the circumscribed ellipse d_{min} to its maximum diameter d_{max}. To detect collision (intersection or one being inside another), it can be implemented using the polygonal ellipse-circle detection after stretching of the ellipses so that the other becomes a circle. Fig. 5.6.3 shows that the sea ice of various densities is generated. Dijkstra's algorithm is a graph search algorithm that solves the single-source shortest path problem for a graph with non-negative edge path costs, producing a shortest path tree. This algorithm is often used in routing and as a subroutine in other graph algorithms.

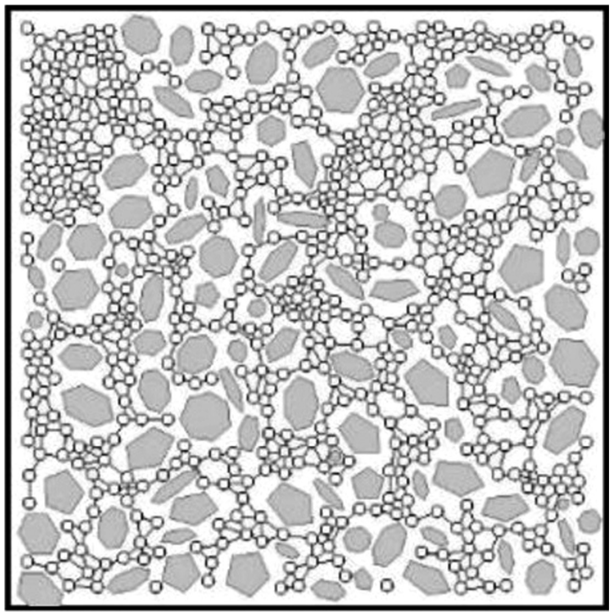

Fig. 5. 6. 4 Roadmap graph in ice cover modeling (Takagi et al., 2014).

Ordinary milestones are given by the point. The proposed method uses a circles as a milestone. The radius of the milestone is set in the distance where the vessel can navigate safely as in Fig. 5.6.3. Fig. 5.6.4 shows a roadmap graph with milestones in the sea ice that is constructed with the ice cover modeling. Each milestone does not overlap as shown in Fig. 5.6.3. It can be implemented using the circle-circle collision detection. And all paths between nodes don't come in contact with the sea ice.

Fig. 5.6.5 shows a binary image of vessel radar by the image processing. The range of the observation of this vessel radar is 3 NM. This image was obtained by Louis S. St-Laurent in the Arctic Ocean on August 26 of 2012. White parts show the sea ice, and black parts show the open water. It is not possible to obtain information of the height of the sea ice like ice ridge or ice berg from the radar image of the vessel. However, it is possible to get the distribution and size of the sea ice. Fig. 5.6.6 shows a roadmap graph of this radar image. All routes do not come in contact with the sea ice. The center of the circle is a point of the present position of the vessel. That is, it is a start point.

Ice in the Arctic is a very complex and dynamic material. It has a wide range of thickness, concentration, age and roughness. Moreover, ice conditions in the Arctic change throughout the year. Transport Canada has implemented a Regulatory Standard that is intended to minimize the risk of pollution in the Arctic due to damage of

Fig. 5. 6. 5 Binary image of vessel radar (Takagi et al., 2014).

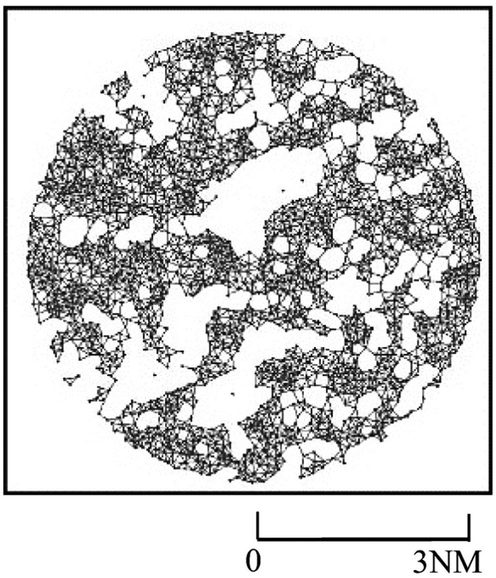

Fig. 5. 6. 6 Roadmap graph for radar image (Takagi et al., 2014).

vessel by ice. It is called "Arctic Ice Regime Shipping System (AIRSS)". AIRSS combines information on the ice conditions and a ship's capability in ice to assess the potential for damage from the ice. It uses the concept of an "Ice Regime" to characterize the ice. A ship is characterized by its "Vessel Class". The class of the vessel reflects its structural strength, displacement and power for breaking ice. The Vessel Class is determined by Transport Canada regulations based on the vessel's characteristics. The classes are designed as either "Type" vessels, which are designed for first-year ice or "CAC-Canadian Arctic Class" vessels which are designed for more severe ice conditions. It is not necessary to avoid all sea ices according to ship's capability.

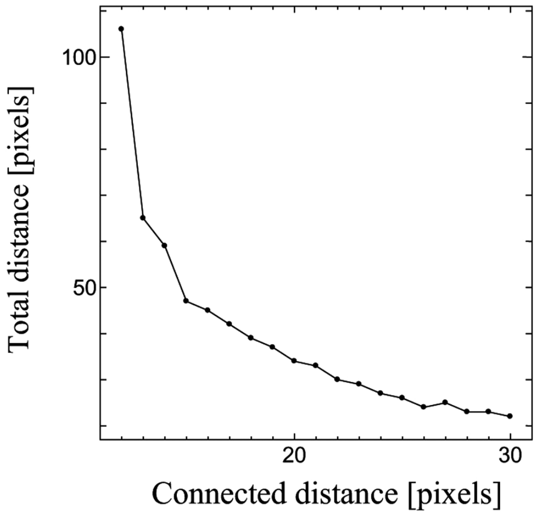

Fig. 5. 6. 7 Connected distance and total distance of sea route (Takagi et al., 2014).

Fig. 5.6.7 shows the relation between the connected distance between milestones and the total distance of the sea route. When the connected distance becomes long, the sea route shortens. Here, a method has been proposed that minimizes the distance to the goal point from the starting point. In the future, it is considered as an evaluation function such as time and fuel, depending on the size of the ship.

References:

Adrian, R. J., 1991. Particle imaging techniques for experimental fluid mechanics. Ann. Rev. Fluid Mech., 22, 261–304.

Cavalieri, D. J., Gloersen, P. and Campbell, W. J., 1984. Determination of sea ice parameters with the NIMBUS 7 SMMR. J. Geophys. Res., 89, 5355–5369.

De Silvia, L. W. A., Yamaguchi, H. and Ono, J., 2015. Ice-ocean coupled computations for sea-ice prediction to support ice navigation in Arctic sea routes. Polar Research, 34, 25008, http://dx.doi.org/10.3402/ polar.v34.25008.

Drucker, R., Martin, S. and Moritz, R., 2003. Observations of ice thickness and frazil ice in the St. Lawrence Island Polynya from satellite imagery, upward looking sonar and salinity/temperature moorings. J. Geophys. Res., 108, C53149, doi: 10.1029/ 2005JC003327.

Dijkstra, E. W., 1959. A note on two problems in connection with graphs. Numerische Mathematik 1, 269–271.

Emery, W. J., Fowler, C. W., Hawkins, J. and Preller, R. H., 1991. Fram Strait satellite image-derived ice motion. J. Geophys. Res., 96, 4751–4768.

Fujisaki, A., Yamaguchi, H., Mitsudera, H., 2010. Numerical experiments of air-ice drag coefficient and its impact on ice-ocean coupled system in the Sea of Okhotsk. Ocean Dynamics, 60, 377–394.

Hasumi, H., 2015. CCSR Ocean Component Model (COCO) Version 4.0. as of January 29, 2015. Atmosphere and Ocean

Research Institute, The University of Tokyo, Chiba, Japan.

Hirano, D., Fukamachi, Y., Watanabe, E., Oshima, K. I., Iwamoto, K., Mahoney, A. R., Eicken, H., Shimizu, D. and Tamura, T., 2016. A wind-driven, hybrid latent and sensible heat coastal polynya off Barrow, Alaska. J. Geophys. Res., 121, doi: 10.1002/ 2015JC011318.

Inoue, J., Hori, M. and Takaya, K., 2012. The role of Barents Sea in the winter cyclone track and emergence of a warm-Arctic cold-Siberia anomaly. J. Climate, 25, 2561–2568.

Ito, M., Oshima, K. I., Fukamachi, Y., Simizu, D., Iwamoto, K., Matsumura, Y., Mahoney, A. R. and Eicken, H., 2015. Observations of supercooled water and frazil ice formation in an Arctic coastal polynya from moorings and satellite imagery. Annals Glaciol., 56, 307–314, doi: 10.3189/ 2015AoG69A839.

Iwamoto, K., Oshima, K. I., Tamura, T. and Nihashi, S., 2013. Estimation of thin ice thickness from AMSR-E data in the Chukuchi Sea. Int. J. Remote Sensing, 34, 468–489.

Iwamoto, K., Oshima, K. I. and Tamura, T., 2014. Improved mapping of sea ice production in the Arctic Ocean using AMSR-E thin ice thickness algorithm. J. Geophys. Res., 119, 3574–3594, doi: 10.1002/ 2013JC009794.

Kamoshida, T. and Shimada, K., 2010. Long term sea ice motion dataset in the Arctic from SMMR, SSM/I and AMSR-E. Proceedings of the Second International Symposium on the Arctic Research (ISAR-2), December 2010, Tokyo, Japan, 125.

Kashiwase, H., Oshima, K. I., Nihashi, S. and Eicken, H., 2017. Ice divergence as a driver for Arctic ice-ocean albedo feedback on seasonal and interannual timescales. Science Data, 7, on revision.

Kawasaki, T., Hasumi, H., 2014. Effect of freshwater from the West Greenland Current on the winter deep convection in the Labrador Sea. Pcean Modelling, 75, 51–64.

Kawasaki, T., Hasumi, H., 2015. The inflow of Arctic water at the Fram Strait and its interannual variability. J. Geophys. Res. Oceans, 121, doi:10.1002/ 2015JC011375.

Kimura, N. and Wakatsuchi, M., 2000. Relationship between sea-ice motion and geostrophic wind in the Northern Hemisphere. Geophys. Res. Lett., 27, 3735–3788, doi: 10.1029/ 2000GL011495.

Kimura, N. and Wakatsuchi, M., 2004. Increase and decrease of sea ice area in the Sea of Okhotsk: ice production in coastal polynyas and dynamical thickening in convergence zones. J. Geophys. Res., 109, C09S03, doi: 10.1029/2003 JC001901.

Kimura, N. and Wakatsuchi, M., 2011. Large-scale processes governing the seasonal variability of the Antarctic sea ice. Tellus A, 63, 828–840.

Kimura, N. and Yamaguchi, H., 2016. Medium-term forecast of the Arctic sea-ice. Proceedings of the 31st International Symposium on Okhotsk Sea and Polar Ocean, 2016, 21–24 February 2016, Monbetsu, Japan, F-21, 186–187.

Kimura, N., Nishimura, A., Tanaka, Y. and Yamaguchi, H., 2013. Influence of winter sea-ice motion on summer ice cover in the Arctic. Polar Research, 32, 20193, http://dx.doi.org/10.3402/polar.v32i0.20193.

Komuro, Y., 2014. The impact of surface mixing on the Arctic river water distribution and stratification in a global ice-ocean model. J. Climate, 27, 4359–4370, DOI: 10.1175/ JCLI-D-13-00090.1.

Komuro, Y. and Suzuki, T., 2012. Impact of subgrid-scale ice thickness distribution on heat flux on and through sea ice. Ocean Modell., 71, 13–25, doi: 10.1016/ j.oceanmod. 2012.08.004.

Krishfield, R. A., Proshutinsky, A., Tateyama, K., Williams, W. J., Carmack, E. C., McLaughlin, F. A. and Timmermans, M.-L., 2014. Deterioration of perennial sea ice in the Beaufort Gyre from 2003 to 2012 and its impact on the oceanic freshwater cycle. *J. Geophys. Res. Oceans,* 119, 1271–1305, doi:10.1002/ 2013JC00899.

Mahoney, A. R., Eicken, H., Fukamachi, Y., Oshima, K. I., Simizu, D., Kambhamettu, C., Rohith, M. V., Hendricks, S. and Jones, J., 2015. Taking a look at both sides of the ice: comparison of ice thickness and drift speed as observed from moored, airborne and shore-based instruments near Barrow, Alaska. Annals Glaciol., 56, 363–372, doi: 10.3189/ 2015AoG69A565.

Martin, S., Drucker, R., Kwok, R. and Holt, B., 2004. Estimation of the thin ice thickness and heat flux for the Chukchi Sea Alaskan Coast Polynya from Special Sensor Microwave/Imager data, 1990–2001. J. Geophys. Res., 109, C10012, doi: 10.1029/ 2004JC002428.

Mellor, G. L., Hakkinen, S., Ezer, T. and Patchen, R., 2002. A generalization of a sigma coordinate ocean model and an intercomparison of model vertical grids. In N. Pinardi and J. Woods (eds), Ocean forecasting: conceptual basis and applications. Berlin, Springer, 55–72.

Mori, M., Watanabe, M., Shiogama, H., Inoue, J. and Kimoto, M., 2014. Robust Arctic sea-ice influence on the frequent Eurasian cold winters in past decades. Nat. Geosci., 7, 869–873.

Nihashi, S., Oshima, K. I., Tamura, T., Fukamachi, Y. and Saito, S., 2009. Thickness and production od sea ice I the Okhotsk Sea coastal polynya from AMsR-E. J. Geophys. Res., 114, C10025, doi: 10.1029/ 2008JC005222.

Ninnis, R. M., Emery, W. J. and Collins, M. J., 1986. Automated extraction of pack ice motion from advanced very high resolution radiometer imagery. J. Geophys. Res., 91, 10725–10734.

Nishimura. K. and Nemoto, M., 2005. Blowing snow at Mizuho station, Antarctica. Phil. Trans. R. Soc., A363, 1647–1662.

Ozeki, T. and Adachi, S., 2013. Field investigations of impinging seawater spray and spray icing on Icebreaker Soya. Proc. 28th Int. Symp. Okhotsk Sea and Sea Ice, 162–165.

Ozeki, T., Shiga, T., Sawamura, J., Yashiro, Y., Adachi, S. and Yamaguchi. H., 2016. Development of sea spray meters and an analysis of sea spray characteristics in large vessels. Proc. "6th Int. Ocean Polar Engineering Conference, Rhodes, Greece, 26 June-1 July 2016, 1335-

Rheem, C, K,, Yamaguchi, H. and Kato, H., 1997. Distribution mass/discrete floe model for pack ice rheology computation. J. Marine Sci. Tech., 2, 101–121.

Sagawa, G., 2007. Development of ice dynamic odel that takes account of floe collision and its validation in numerical sea ice forecast in the Sea of Okhotsk in Japanese). Phd thesis, University of Tokyo, pxx.

Schauer, U., Beszczynska-Mo¨ller, A., Walczowski, W., Fahrbach, E., Piechura, J. and Hansen, E., 2008. Variation of measured heat flow through Fram Starait between 1997 and 2006, in Arctic-Subarctic Ocean Fluxes. Edited by R. R. Dickson, J. Meincke and P. Rhines, Springer, Dordrecht, 66–85.

Shimada, K., Carmack, E. C., Hatakeyama, K. and Takizawa, T., 2001. Varieties of shallow temperature maximum waters in the western Canadian Basin of the Arctic Ocean. Geophys. Res. Lett., 28, 3441–3444.

Shimada, K., Kamoshida, T., Itoh, M., Nishino, S., CArmack, E., McLaughlin, F. A., Zimmermann, S. and Proshutinsky, A., 2006. Pacific Ocean inflow: influence on catastrophic reduction of sea ice cover in the Arctic Ocean. Geophys. Res. Lett., 33, L08605, doi: 10.1029/ 2005GL025624.

Steel, M., Morley, R. and Ermold, W., 2001: PHC: A global ocean hydrography with a high-quality Arctic Ocean. J. Climate, 14, 2079–2087, doi: 10.1175/ 1520-0442(2001) 014<2079: PAGOHW> 2.0.CO;2.

Steele, M., Morison, J., Ermold, W. Rigor, I., Ortmeyer, M. and Shimada, K., 2004. Circulation of summer Pacific halocline water in the Arctic Ocean. J. Geophys. Res., 109, C02027, doi: 10.1029/ 2003JC002009.

Sumata, K. and Shimada, K., 2007. Northward transport of Pacific summer water along the Northwind Ridge in the Western Arctic Ocean. J. Oceanogr., 63, 363–378.

Takagi, T., Tateyama, K. and T, Ishiyama, 2014. Obstacle avoidance and path planning in ice sea using Probablilistic Roadmap Method. Proc. 22nd IAHR Int. Symp. On Ice, Singapore, August 11 to 15, 2014, doi: 10.3850/978-981-09-0750-1_1259.

Tamura, T. and Oshima, K. I., 2011. Mapping of sea ice production in the Arctic coastal polynyas. J. Geophys. Res., 116, doi: 10.1029/ 2010JC006586.

Tamura, T., Ohshima, K. I., Markus, T., Cavalieri, D. J., Nihashi, S., Hirasawa, N., 2007. Estimation of Thin Ice Thickness and Detection of Fast Ice from SSM/I Data in the Antarctic Ocean. J. Atmos. Ocean. Tech. 24, 1757–1772.

Tang, Q., Zhang, X., Yang, X. and Francis, J., 2013. Cold winter extremes in northern continents linked to Arctic sea ice loss. Environ. Res. Lett., 8, 014036.

Tateyama, K., Enomoto, H., Toyota, T. and Uto, S., 2002. Sea ice thickness estimated from passive microwave radiometers. Polar Meteorol. Glaciol., 16, 15–31.

Ushio, S. and Wakatsuchi, M., 1993. A laboratory study on supercooling and frazil ice production processes in winter coastal polynyas. J. Geophys. Res., 98, 20321–20328, doi: 10.1029/ 93JC01905.

Watanabe, M. and Coathors, 2010. Improved climate simulation by MIROC5: Mean states, variability and climate sensitivity. J. Climate, 23, 6312–6335, doi: 10.1175/ 2010JCLI 3679.1.

Yamamoto-Kawai, M, McLaughlin, F. A., Carmack, E. C., Nnishino, S., Shimada, K. and Kurita, N., 2009. Surface freshening of the Canada Basin, 2003–2007: River runoff versus sea ice meltwater. J. Geophys. Res., 114, C00A05, doi: 10.1029/ 2008JC005000.

Yoshizawa, E., 2016. Estimations of ocean stratification and sea ice rafting: key factors in recent sea ice variations in the Arctic Ocean. Doctoral Thesis, Tokyo Kaiyo Daigaku (Tokyo University of Marine Science and Technology, March 2016, 67p.

Yoshizawa, E., Shimada, K., Ha, H-K., Kim, T-W., Kang, S-H. amd Chung, K-H., 2015. Delayed responses of the oceanic Beaufort Gyre to winds and sea ice motions: influences on variations of sea ice cover in the Pacific sector of the Arctic Ocean. J. Oceanogr., 71, 187–197, DOI 10.1007? s10872-015-0276-6.

Zakrzewski, W. P., 1987. Splashing a ship with collision-generated spray. Cold Regions Sci. Technol., 14, 65–83.

6. Evaluation of the impacts of Arctic change on marine ecosystems and fisheries

The Arctic Ocean has experienced significant warming, freshening and ocean acidification mainly caused by rapid reduction of sea ice. In the project Ecosystem Studies on the Arctic Ocean with Declining Sea Ice (ECOARCS) under GRENE Arctic as strategic target 3b, we investigated the impact of sea ice retreats on marine ecosystems.

6. 1. Ocean acidification and the maintenance mechanism of primary production

Ocean acidification

During the last decade, ocean acidification due to uptake of anthropogenic carbon dioxide (CO_2) has emerged as an urgent issue in ocean research (Orr et al., 2005). Increasing acidity and consequent changes in seawater chemistry are expected to impact the marine ecosystem and may threaten some organisms. Of particular concern is the impact on calcifying organisms, such as coralline algae, pteropods, bivalves and corals, because acidification lowers the saturation state (Ω) of calcium carbonate ($CaCO_3$) in seawater, which affects the ability to these organisms to produce and maintain their shells or skeletons. In fact, a decrease in Ω of water can cause enhanced mortality of juvenile shellfish and decreased calcification, growth, development and abundance of calcifiers.

The shallow shelf seas of the Arctic Ocean are known to be especially vulnerable to ocean acidification. Cold water dissolves more CO_2, large fresh water inputs from rivers and sea ice melt reduce calcium ion concentrations and alkalinity, the buffering capacity of seawater to added CO_2 (Yamamoto-Kawai et al., 2011), and respiration at the bottom of a salt stratified water column accumulates CO_2 in bottom water (Bates et al., 2009). Because of these characteristics both surface and bottom waters of Arctic shelf seas exhibit naturally low Ω compared to other ocean waters (Yamamoto-Kawai et al., 2013). The Chukchi Sea is one of these seas.

Yamamoto-Kawai et al. (2016) show results of ship-based observations in September–October of 2012 and early July of 2013 in the Chukchi Sea. In both years, sea ice concentration decreased to < 80% at the end of May and to < 30% at the beginning of June. Therefore, observations were carried out about 3 months and 1 month after the ice retreat in 2012 and 2013, respectively. Because of the difference in season as well as interannual variability in hydrographic conditions, distribution of Ω was largely different between two observations. By comparing with distributions of physical and biogeochemical parameters, factors controlling Ω will be discussed. Based on these results, reconstruction of seasonal variations of Ω in the bottom water was attempted in the southern Chukchi Sea by using data from a 2-year-round mooring observation between July 2012 and July 2014. Hydrographic data were collected in the Chukchi and Bering seas during the cruises of R/V Mirai of the Japan Agency for Marine-Earth Science and Technology (JAMSTEC) from 13 September to 14 October in 2012 (Kikuchi, 2012) and T/S Oshoro-Maru of Hokaido University from 3 July to 18 July in 2013 (Hirawake, 2013). Here, data from stations north of 66°N with a bottom depth shallower than 70 m were used. A mooring system was deployed in Hope Valley from 16 July 2012 to 19 July 2014. The system was first deployed at 67°42’ N, 168°50’ W from 16 July 2012 to 2 October 2012, and then moved slightly to the north at 68°02’4 N, 168°50’ W on 3 October 2012. On 20 July 2013, the system was recovered for maintenance and redeployed at the latter location until 19 July 2014. Bottom depth was 52, 59 and 60 m, respectively, for each deployment. Sensors for T, S, dissolved oxygen (DO), chlorophyll a and turbidity were equipped on the mooring at 7 m above the bottom.

Distribuitons of Ω in bottom waters of Chukchi Sea (Fig. 6.1.1) were significantly different between September–October 2012 (hereafter autumn 2012) and July 2013 (hereafter summer 2013). In autumn 2012, Ω in bottom water ranged from 0.3 to 2.0 for aragonite (Ω_{ar}) and from 0.5 to 3.2 for calcite (Ω_{ca}). Aragonite undersaturation (Ω_{ar} < 1; black circles in Fig. 6.1.1) was observed at stations off Pt. Barrow, in Hope Valley, in the Bering Strait and near the northern continental slope. The lowest Ω_{ar} was observed on 3 October 2012 in Hope Valley at 68°N, in the dome-like structure of bottom water with low T, high S and low dissolved oxygen (DO) (Nishino et al., 2016) with high total alkalinity (TA), high dissolved inorganic carbon (DIC) and high fCO_2 (fugacity of CO_2). Calcite undersaturation was also found in this dome. [Nishino et al. (2016) described the dome-like structure as a common feature found in this region associated with Hope Valley topographic depression, although water properties can

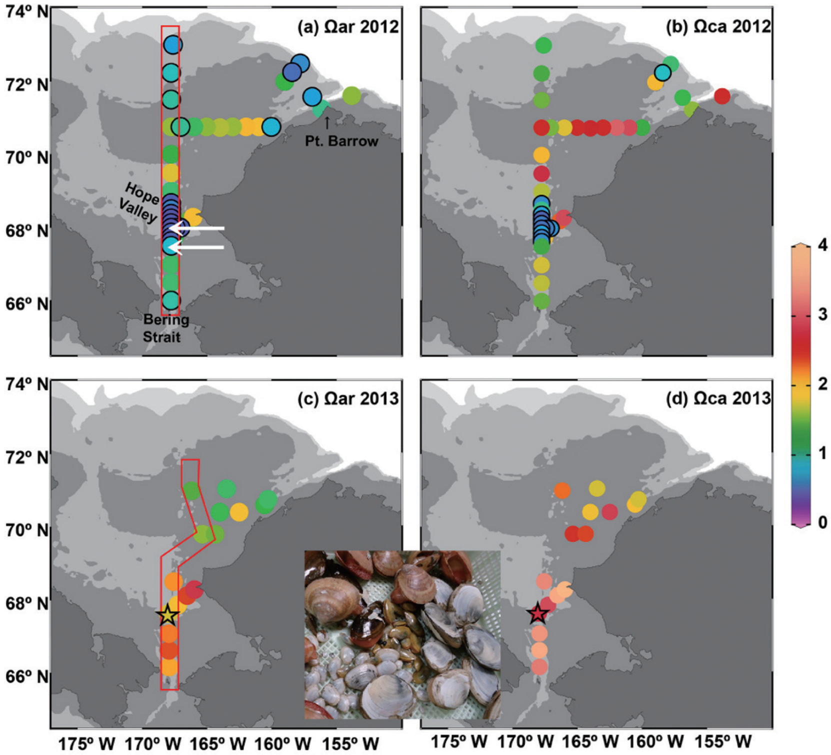

Fig. 6. 1. 1 Distribution of Ω_{ar} (a, c) and Ω_{ca} (b, d) in bottom water in September–October 2012 (a, b) and July 2013 (c, d). Circled stations were undersaturated with $CaCO_3$ minerals. White arrows indicate mooring sites. An insert photo shows bivalves collected by dredge trawl at a station marked with a star in July 2013 (Yamamoto-Kawai et al., 2016).

differ between years and seasons.]

In 2013, Ω in bottom water was 1.1–2.8 for aragonite and 1.4–4.4 for calcite: all of the observed waters were oversaturated with respect to aragonite and calcite (Fig. 6.1.1). Ω in bottom waters at these stations was slightly lower than stations north or south but still very oversaturated with respect to $CaCO_3$ (Ω_{ar} = 1.7−1.9; Ω_{ca} = 2.8−3.0). Waters with lower Ω_{ar} of 1.1−1.2 and Ω_{ca} of 1.8−1.9 were found in northern stations at around 71°N where *T* and DO were lower and fCO_2 was higher than in the south. These results show that variations in Ω in the Chukchi Sea bottom water are controlled largely by organic matter remineralization with minor contributions of *T* and *S*. In fact, low Ω waters were observed in regions off Pt. Barrow and Hope Valley, known as biological "hotspots" in the Chukchi Sea, characterized by high primary productivity, high export flux of organic matter to depth, a high respiration rate in sediment community and high benthic biomass (Nishino et al., 2016). Strong stratification prevents ventilation and accumulates more CO_2 in the bottom water.

Based on the analysis from the comparison of mooring and ship-based observations, the regression equations were applied to the mooring data in Hope Valley. The reconstructed Ω is shown in Fig. 6.1.2 together with *S*, *T*, DO and apparent oxygen utilization (AOU, the difference between saturated and observed concentrations of DO), with a range of −3.6 and +0.45 for aragonite and −0.57 and +0.71 for calcite. For the whole period, Ω ranged from 0.2 to 2.1 for aragonite and from 0.3 to 3.4 for calcite (Fig. 6.1.2). It was shown that the ship-based observations in autumn 2012 and summer 2013 captured low and high Ω periods, respectively. Seasonal variation of Ω mirrors that of DO, low in autumn due to stratification and respiration and high in spring and early summer due to photosynthesis. In the unusually stratified autumn 2012, bottom water Ω was ~0.3 for aragonite and ~0.5 for calcite. In 2013, Ω decreased after the ship-based observation in July, and intermittent aragonite undersaturation was predicted in August, September and October, although Ω was higher than in the same months in 2012. At the beginning of the cooling and convection periods in November–December 2012 and October–November 2013, ventilation of bottom water increased DO and Ω. Then, Ω in bottom water remained low during winter until the initiation of photosynthesis in May. Low Ω in winter is likely due to continued respiration by benthic organisms, as suggested by positive AOU. From spring to autumn, predicted large temporal variation in Ω suggests inhomogeneous distribution of undersaturated wa-

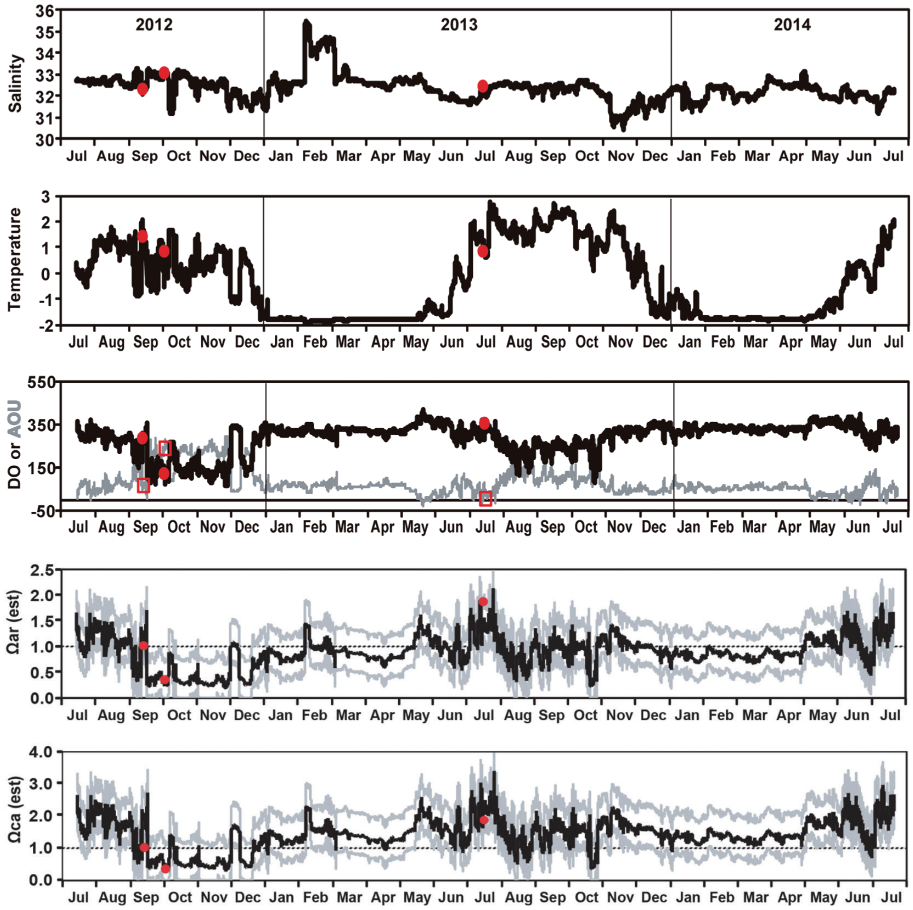

Fig. 6. 1. 2 Time series of salinity (S, top), temperature (T, second; °C) and dissoleved oxygen (DO, third; m mol kg^{-1}). Ω_{ar} (fourth) and Ω_{ca} (bottom) reconstructed from mooring data of T, S and AOU shown above. Gray lines in the fourth and bottom panels indicate ranges of −3.6 and +0.45 for aragonite and −0.57 and +0.71 for calcite. Red symbols indicate ship-based observations. In the third panel, red squares are ship-based data of AOU (Yamamoto-Kawai., 2016).

ters during this period. In winter, in contrast, variability in Ω is relatively small. This suggests that low Ω is a widespread feature during winter.

The reconstructed Ω suggests the frequent occurrence of aragonite undersaturation in the bottom water of the Chukchi Sea, not only in summer/autumn, but also in the winter months. In previous studies, continuous aragonite undersaturation has been observed in bottom waters in the Bering and Chukchi seas, but in limited seasons. The present study is the first to estimate year-round variability of Ω in the bottom water of the Chukchi Sea.

In order to roughly quantify the effect of anthropogenic CO_2 on the timing and duration of $CaCO_3$ undersaturation in the 2-year time series of Ω, estimation has been made on Ω in two cases: (1) the preindustrial period case with an atmospheric partial pressure of CO_2 (pCO_2) of 280 ppm, and (2) the future case with pCO_2 of 650 ppm (50 years later in the high CO_2 emission scenario (RCP8.5), and the end of the century in a moderate scenario (RCP6; IPCC, 2013)). For the preindustrial case, Ω ranged from 0.2 to 2.6 for aragonite and from 0.4 to 4.1 for calcite. For the future case, Ω ranged from 0.2 to 1.5 for aragonite and from 0.2 to 2.4 for calcite. This means that $CaCO_3$ undersaturation might have occurred, at least for aragonite, even with the productivity much lower than that occurring today and without perturbation by anthropogenic CO_2.

In terms of duration, the period of aragonite (calcite) undersaturation was estimated to be 3.9 (2.6) and 1.7 (0.3) months in the first and second year, respectively, in the preindustrial period case. By comparing with the original estimate of 7.5–8.6 months, it was suggested that the period of aragonite undersaturation has been significantly extended by an input of anthropogenic CO_2 by now. In the future case with an atmospheric pCO_2 of 650 ppm, the period of undersaturation is estimated to increase further to > 11 months for aragonite and half year for calcite. This analysis indicates that anthropogenic CO_2 has a significant impact on the duration of $CaCO_3$ undersaturation in the bottom water even though seasonal and interannual variations of Ω are mainly controlled by biological processes.

Biological hotspot

The southern Chukchi Sea is one of the most biologically productive regions of the world's ocean because of nutrients supplied by northward flow of Pacific-originating water advected over the shelves from the northern Bering Sea into the Arctic Ocean. Due to high primary productivity, a large quantity of organic matter descends to the seafloor as potential food for benthic communities, resulting in high benthic biomass. Consequently, large benthic feeders at high trophic levels, such as grey whales and walruses, also congregate there. Such a region of high biological activity is called a biological hotspot. Here Nishino et al. (2016) analyzed mooring and ship-based data obtained from a biological hotspot in the southern Chukchi Sea to understand the water mass characteristic (and temporal changes thereof) that influence phytoplankton biomass and productivity. Mooring data, including temperature (T), salinity (S), dissolved oxygen (DO), Chl *a* and turbidity near the bottom of the biological hotspot in the southern Chukchi Sea, were collected from July 2012 to July 2014 for the first time. The data were used to examine changes in water mass characteristics and phytoplankton biomass associated with spring and autumn blooms in this biological hotspot. Three temporally sequenced moorings (named SCH-12, SCH-12-2 and SCH-13) from 16 July 2012 to 19 July 2014 to aquire T, S, DO, Chl *a* and turbidity time series near the bottom of a biological hotspot located in Hope Valley of the southern Chukchi Sea (Fig. 6.1.3). Ship-based hydrographic surveys were conducted in the Chukchi Sea and Canada Basin from 13 September to 4 October 2012 and from 31 August to 4 October 2013 on board the R/V *Mirai* of the japan Agency for Marine-Earth Science and Technology, JAMSTEC (Fig. 6.1.3; Kikuchi, 2012 and Nishino, 2013).

The bottom waters in the Chukchi Sea are classified into Alaskan coastal water (ACW; $S < 31.8$, $T = 0$–4°C), Bering shelf – Anadyr water (BSAW; $S > 31.8$, $T = -1.0$–4°C), Bering winter water (BWW; $S = 32.4$–34.0, $T < -1.6$°C) and hypersaline water (HSW; $S > 34.0$ with freezing temperature of seawater, $T \sim -1.8$°C). The T and S characteristics from the mooring data (Fig. 6.1.4) indicate seasonal changes between these waters. The BSAW (BWW) was generally presented in summer and autumn (winter and spring) at the bottom of the mooring

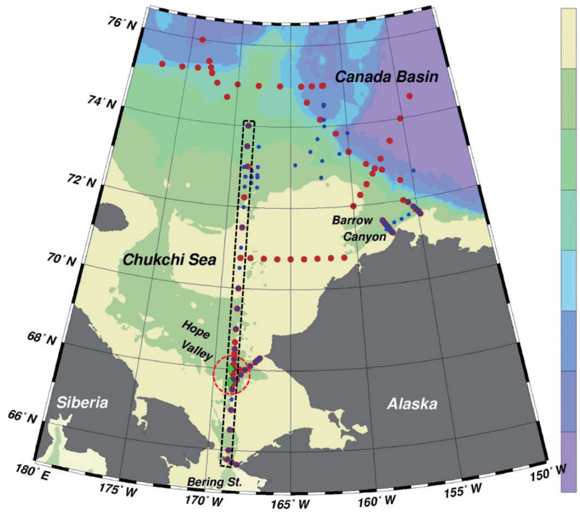

Fig. 6. 1. 3 Map showing the bathymetric features of the study area and the hydrographic stations for the R/V Mirai cruises in 2012 (red dots) and 2013 (blue dots). Green diamonds represent the SCH-12 (southern site) and SCH-12-2/SCH-13 (northern site) mooring sites. Data from the stations enclosed by black dotted lines were used for the illustrations of vertical sections shown in Fig. 6.1.5. The area enclosed by the red dotted circle is the southern Chukchi Sea biological hotspot, where the moorings were installed and detailed hydrographic surveys were conducted (Nishino et al., 2016).

site. DO concentration (blue line in Fig. 6.1.4) varied in response to the change in water masses. The BWW and HSW had high DO concentrations (> 300 μ mol kg^{-1}) because the waters undergo cooling and convection in winter with oxygen supplied from the atmosphere. On the other hand, there was a wide range of DO concentrations in BSAW. DO concentration was high (~ 300 μ mol kg^{-1}) in the beginning when the BSAW occupied the mooring site in July. Then it decreased gradually over time and had minimum values between September and November 2012 and between August and October 2013. Turbidity (red line in Fig. 6.1.4) was lowest in an annual cycle during winter and spring when BWW or HSW occupied the site. Then it increased sharply in May 2013 and 2014, when the DO concentration also increased. In July 2012 and 2013, when the BSAW began to occupy the site, turbidity became relatively lower and subsequently reached an annual maximum (10–15 FTU (Formazin Turbidity Units)) between September and November 2012 and between August and October 2013. The period of annual maximum turbidity corresponded with the period of annual minimum DO.

Chl *a* concentration (Fig. 6.1.4c) increased sharply in May, when sea ice still remained in the area, and the high concentration continued until July. The shrap increase in

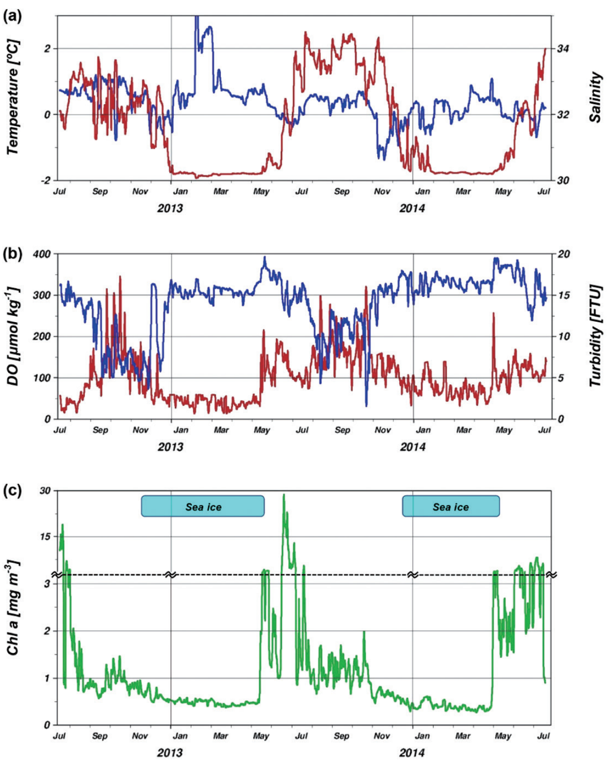

Fig. 6. 1. 4 Time series of (a) temperature (°C; red) and salinity (blue), (b) dissolved oxygen (DO, m mol kg^{-1}; blue) and turbidity (in Formazin Turbidity Units, FTSs; red) and (c) chrolophyll a (Chl a, mg m^{-3}; green). The data were obtained from the SCH-12, SCH-12-2 and SCH-13 moorings during 16 July 2012–19 July 2014. The vertical axis scale in (c) below the dotted line is exaggerated where the concentration is < 3 mg m^{-3}. Periods when sea ice concentration was > 50% at the mooring site are indicated by blue bars (Nishino et al., 2016).

Chl *a* in May was synchrony with the sharp increase in DO concentration and turbidity (blue and red lines in Fig. 6.1.4b, respectively). In addition, relatively high Chl *a* concentration (> 1 mg m^{-3}) were found in September–October 2012 and August–October 2013, although the concentrations were much lower than those in late spring to early summer (May–July). The time series of the turbidity data showed two peaks in accordance with annual variation in Chl *a* concentration, i.e. high turbidity in late spring and early summer and in autumn. However, turbidity was higher in autumn than in late spring and early summer, despite Chl *a* concentrations being lower in autumn.

The ship-based hydrographic and biogeochemical surveys were conducted in the Chukchi Sea and the Canada Basin during September to early October 2012 and 2013, when the mooring data indicated high Chl *a* and turbidity with low DO concentrations. The spatial distribution of Chl *a* integrated over the water column in 2012 showed that the quantity of Chl *a* was relatively high in the Bering Strait, Hope Valley and Barrow Canyon, where primary productivity in the water column was also high compared to that in the central Chukchi Sea and the Canada Basin. The high productivity regions are thought to be the biological hotspots. The quantity of Chl *a* in the water column in 2013 was higher everywhere compared to 2012, and the highest quantity was detected in Hope Valley. Despite being downstream from nutrient-rich water from the Bering Sea, the algal biomass and primary productivity in Hope Valley were comparable to or higher than those in the Bering Strait during both years.

A hydrographic section was obtained from Bering Strait to the shelf slope of the Chukchi Sea along 168°45' W across the biological hotspot of the southern Chukchi Sea at ~68°N on 13–17 September 2012 (Fig. 6.1.5). *T* and *S* (Fig. 6.1.5a) characterize the water mass distribution in this section. In the shelf area (from the Bering Strait to 72°N), ACW (S < 31.8, T > 4°C) was found at ~67 and 69–70°N in the upper layer (< ~20 m) and BSAW occupied the lower layer. Over the shelf slope (north of 72°N), BWW with near-freezing temperature was found at 73–74°N below a depth of ~40 m. The saline bottom water (> 33) around 72°N was classified as BSAW, but the water temperature was relatively low indicating that it was likely influenced by the adjacent BWW to the north. A dome-like structure of bottom water was found characterized by an uplifted isohaline (isopycnal) surface at ~68°N with lower T and higher S than those of the surroundings. This bottom water at ~68°N was also characterized by the lowest light transmission in this section (Fig. 6.1.5b). The light transmission was relatively low in the bottom water around 72°N, but it increased sharply in the BWW (73–74°N).

f_{SIM} was calculated wether the water was influenced by sea ice melt or brine rejection (Fig. 6.1.5c). The surface water was influenced largely by se ice melt (f_{SIM} > 0), especially at 67–69°N and over the shelf slope. On the other hand, the bottom waters at ~68 and 72°N and the BWW (73–74°N) were associated with brine rejection (f_{SIM} < 0).

The DO distribution (Fig. 6.1.5d) showed a subsurface DO maximum over the shelf slope, which was almost coincident with a subsurface Chl *a* maximum and associated with the photosynthesis in this maximum layers as described in previous studies (e.g., Martin et al., 2010). A notable feature in this section was the lowest DO in the bottom water at ~68°N. Nitrate (Fig. 6.1.5e) was depleted at the surface, except for the Bering Strait, and high

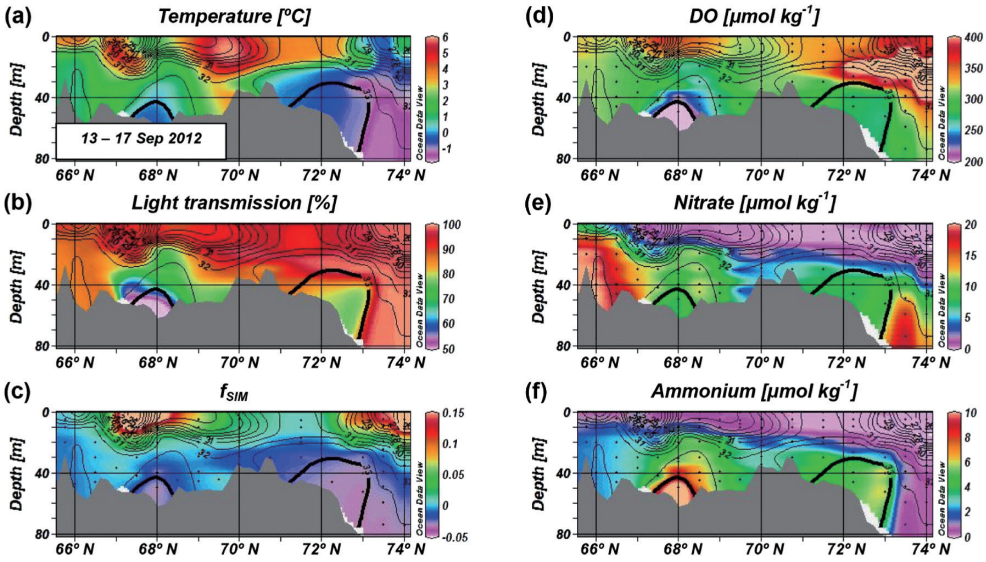

Fig. 6. 1. 5 Vertical sections of (a) temperature (°C), (b) light transmission (%), (c) fraction of sea ice meltwater (fSIM), (d) dissolved oxygen (DO, m mol kg^{-1}), (e) nitrate (m mol kg^{-1}) and (f) ammonium (m mol kg^{-1}) along the 168°45' W meridian near the US-Russia border obtained during the 13–17 September 2012 R/V Mirai cruise. The water sampling level at each station is indicated by a black dot. Salinity contours are superiposed on each section with a 0.5 contour interval. The thick contour in each section indicates a salinity of 33 (Nishino et al., 2016).

concentrations (~20 μ mol kg^{-1}) were found in the bottom water of the strait and BWW. The nitrate concentration in the bottom water at ~68°N was relatively low (~7 μ mol kg^{-1}). Ammonium (Fig. 6.1.5f) was also depleted at the surface, and in contrast to the nitrate, the concentrations were low in the bottom water of the Bering Strait (~2 μ mol kg^{-1}) and BWW (< 0.5 μ mol kg^{-1}) and highest in the bottom water at ~68°N (~12 μ mol kg^{-1}).

The biological hotspot in the southern Chukchi Sea was revisited and hydrographic and biogeochemical surveys were conducted on 3–4 October 2012. Similar to the previous survey in mid-September, a dome like structure of bottom water was found at ~68°N with lower *T*, higher *S*, and lower light transmission than those of the surrounding water. However, bottom water *T* was higher, *S* was lower and light transmission was lower than the values from the previous survey. In 2013, hydrographic and biogeochemical surveys was conducted again from the Bering Strait to the shelf slope of the Chukchi Sea along 168°45' W from 27 September to 4 October. The T and S distribution indicated that BSAW was dominant in this region, except for the upper layer (< ~20 m) where ACW was found at around 67 and 69°N. The cold water north of 72°N below a depth of ~40 m was a mixture of BSAW and BWW, as was the case in 2012. Although a dome-like structure of bottom water was found again at ~68°N with higher S than surroundings, T was similar to the surroundings and higher than that in 2012. Light transmission there was extremely low compared to the surroundings, but higher than that in 2012.

The Chl *a* mooring data captured phytoplankton blooms, as indicated by the high Chl *a* concentration in spring to early summer and in autumn (Fig. 6.1.4c). The first bloom in May was likely a spring bloom including a bloom of ice algae. At the onset of the spring bloom in May, both the DO concentration and the turbidity increased sharply (blue and red lines in Fig. 6.1.4b, respectively), which is consistent with the oxygen production accompanying phytoplankton photosynthetic activity and the resultant increase in phytoplankton particles.

The second bloom (Chl a > 1 mg m^{-3}), which occurred in September-October 2012 and August-October 2013, was an autumn bloom. Before the autumn bloom, the DO concentration decreased and the turbidity increased from the end of July to the beginning of August in 2012 and 2013. The annual DO minimum and turbidity maximum occurred during the bloom. The high turbisity in autumn suggests that the turbid water contained not only phytoplankton particles but also other biogenic and lithogenic particles. The DO minimum in this period suggests decomposition of organic matter that was transported to the bottom with the particles, the amount of which were largest in autumn in the annual cycle.

The above mentioned mooring data revealed two novel results regarding the annual cycle of water characteristics related to the autumn bloom. A large decrease in bottom water DO occurred just before the autumn bloom but not during the spring bloom (Fig. 6.1.4b and c). The decreas in DO was accompanied by an increase in bottom water turbidity, and DO (turbidity) had minimum (maximum) values during the autumn bloom.

Dome-like structure of dense and turbid bottom water in the biological hotspot of the southern Chukchi Sea was found based on hydrographic surveys during autumn blooms. The dome-like structure would have been associated with the Hope Valley topographic depression where dense water may converge and particles likely accumulate. The bottom water characteristics there (at ~68°N) depend on the influences of the BSAW and BWW. The BWW, which is generally influenced by brine rejection in winter, has negative and low f_{SIM} values.

Although the mooring in this study was deployed only at the biological hotspot site in the southern Chukchi Sea, the data show a temporal change in phytoplankton biomass and related parameters for the first time. Spring and autumn blooms were observed associated with high Chl a concentrations. At the onset of the spring bloom, both DO and turbidity increased sharply, which is consistent with the oxygen production accompanying phytoplankton photosynthetic activity and the resultant increase in phytoplankton particles. On the other hand, before the autumn bloom, turbidity increased but DO decresed, suggesting accumulation and decomposition of particulate organic matter (POM; nutrient regeneration) on the bottom. This may have been a trigger for the autumn bloom at this site.

6. 2. Variation of primary production

Sea ice retreat in the Arctic Ocean affects the blooming at the ice edge during spring and summer.

Ocean color remote sensing has been utilized for studying primary productivity in the Arctic Ocean. However, phytoplankton chlorophyll *a* (Chl *a*) is not predicted accurately because of the interference of colored dissolved organic matter (CDOM) and non-algal particles (NAP). To enhance the estimation accuracy, Hirawake et al. (2012) applied a phytoplankton absorption-based primary productivity model (ABPM) to the Bering and Chukchi Seas. The phytoplankton absorption coefficient was determined correctly from sea surface remote sensing reflectance (R_{rs}) and reduced the effect of CDOM and NAP in primary productivity (PP_{eu}) estimates. PP_{eu} retrieved from in situ R_{rs} using ABPM satisfied a factor of 2 measured values. PP_{eu} estimated from the Moderate Resolution Imaging Spectroradiometer (MODIS) R_{rs} data were within the range of historical values. These estimated PP_{eu} values were less than half of those of the model based on Chl *a*, and the difference between the two models reflected the influence of CDOM and NAP absorptions.

Estimated daily primary productivity using the ABPM (Fig. 6.2.1a) represents quite different features from the result using the vertically generalized production model (VGPM) (Fig. 6.2.1b). The level of primary productivity obtained using the new approach is less than half that of the VGPM estimation. Extremely high productivity was not widely distributed around the coastal region of Alaska in the ABPM estimation (Fig. 6.2.1a). Although the primary productivity > 10,000 mg C m^{-2} d^{-1} was frequently found in the VGPM, productivity > 1,500 mg C m^{-2} d^{-1} using the new model was found only at the Yukon River mouth, and in the Kotzebue and Mackenzie River estuaries, where an effect of high CDOM and NAO was likely to remain because the *in situ* spectroradiometer and the quantitative filter technique (QFT) data used to validate a_{ph} (443, 0-) were not collected in these very high CDOM and NAP regions.

The large difference in the PP_{eu} estimations between the ABPM (Fig. 6.2.1a) and the VGPM (Fig. 6.2.1b) might be caused by the overestimation of the Chl *a* concentration attributed to high absorption by CDOM and NAP at the blue wavelengths. To investigate the effect of CDOM and NAP on the differences in the PP_{eu} estimations, the difference between the two models (VGPM/ ABPM; Fig. 6.2.1c) was compared with the relative abundance of absorption by CDOM and NAP to phytoplankton absorption at 443 nm [a_{dg} (433, 0-)/ a_{ph} (443, 0-); Fig. 6.2.1d]. The relationship a_{dg} (443, 0-)/ a_{ph} (443, 0-) was used as an index of interference by CDOM and NAP absrptions. The VGPM estimation was 1.5–5 times larger than ABPM retrieval (Fig. 6.2.1c), and overall, the high VGPM/ ABPM region corresponded to a high a_{dg} (443, 0-)/ a_{ph} (443, 0-). Note that the Russian side of the Bering Strait and western Bering Sea (55–60°N, 170°E–180°E) had relatively low a_{dg} (443, 0-)/ a_{ph} (443, 0-) and VGPM/ ABPM. Althoug the Chukchi Shelf region had higher values of a_{dg} (443, 0-)/ a_{ph} (443, 0-) > 4.0, the VGPM/ ABPM ratio was ~2.5–3.5 and not as high as the coastal region of the Bering Sea.

Interannual variation in PP_{eu} between 2002 and 2010

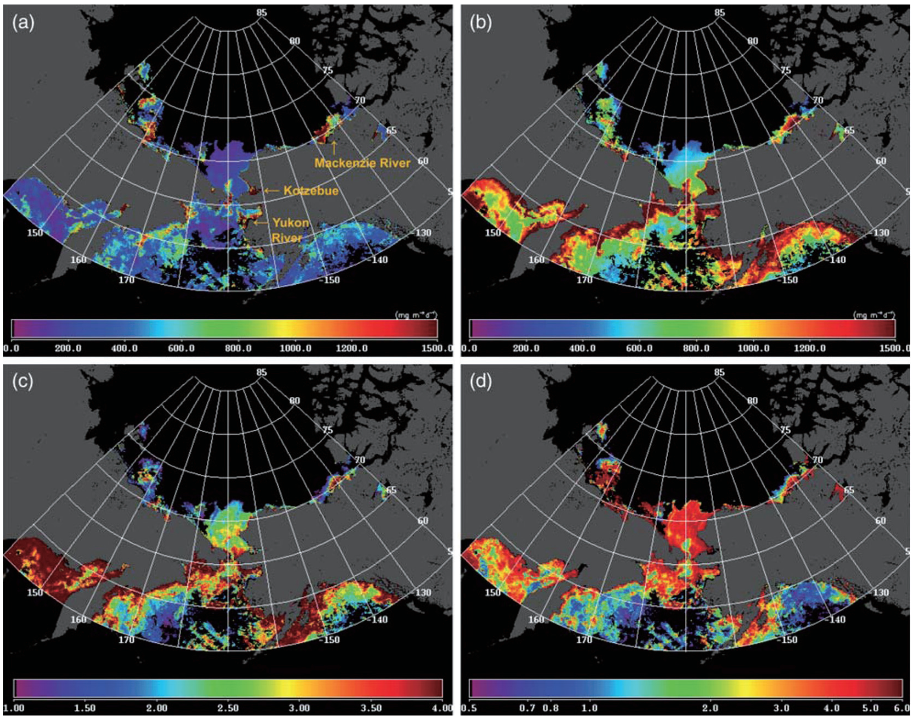

Fig. 6. 2. 1 Distribution of daily primary productivity (PP_{eu}; mg C m^{-2} d^{-1}) from MODIS data for Bering and Chukchi Seas. For July 2002, estimation using (a) the absorption-based productivity model (ABPM, this study) and (b) the VGPM. The ration of the VGPM estimation to the ABPM estimation in (c). The ratio of the absorption coefficient of CDOM + NAP, a_{dg} (443), to that of phytoplankton, a_{ph} (443) in July 2001 is shown in (d) (Hirawake et al., 2012).

derived from satellite data is shown in Fig. 6.2.2. The PP_{eu} derived using the new approach (Fig. 6.2.2a and b) increased significantly over the 9-year period in all categories in both August (r^2 = 0.65–0.85, $p < 0.01$) and September (r^2 = 0.74–0.79, $p < 0.005$). The increments of PP_{eu} from 2006 to 2007 in the Bering Strait and over the Chukchi Shelf increased by a factor of 1.51–1.80 in August and 1.66–2.46 in September. In addition, productivity for 2006–2007 increased by 2.71 times in September at the shelf break. Peaks of primary productivity were found in 2009 and 2010, and the value in the Bering Strait reached 983.9 mg C m^{-2} d^{-1}. These trends are quite different from the results of VGPM (Fig. 6.2.2c and d). Productivity estimated by the VGPM in the northern Bering Sea, Bering Strait and Chukuchi shelf had a higher range, from 500 to 1900 mg C m^{-2} d^{-1}, an increasing trend was not found, and productivity in the northern Bering Sea declined in August.

The new productivity model using a phytoplankton absorption coefficient developed in this study reduced the effect of CDOM in the estimation of Arctic productivity. The reliability of absorption estimation from in situ remote sensing reflectance data was also confirmed. Using the new model, an increasing trend in primary productivity during August and September of 2002–2010 was revealed.

Phytoplankton in coastal and RIKUDANA area

Typical examples in the GRENE Arctic using this remote sensing technique was made by Fujiwara et al. (2016). They focused on the timing of the sea ice retreat (TSR) and the phytoplankton size composition in the marginal ice zone (MIZ), which is the area where ice melt has just recently occurred. They used satellite data from SeaWiFS (reflectance R_{rs} (λ), λ = 412, 443, 490, 555 and 670 nm) and Aqua-MODIS (R_{rs} (λ), λ = 412, 443, 488, 555 and 667 nm). Also euphotic depth Z_{eu} and photosynthetic available radiation (PAR) were derived. The R_{rs} (λ) values from SeaWiFS were converted to R_{rs} (λ) values for MODIS using conversion factors that removed the biases between them.

An index for the phytoplankton community size composition (F_L) was defiend as the ratio of the Chl *a* attributed to cells larger than 5 μm (Chl $a_{>5\mu m}$) to the toatal Chl *a* (Chl a_{total}):

$$F_L = \text{Chl } a_{>5\mu m} / \text{Chl } a_{total} * 100\ (\%). \quad (6.2.1)$$

The satellite F_L values was estimated using the phytoplankton size derivation model (SDM) proposed in Fuji-

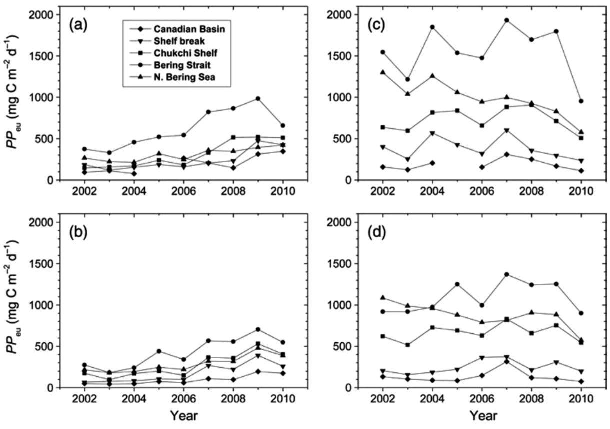

Fig. 6. 2. 2 Interannual variation of column-integrated daily primary productivity (PPeu) from 2002 to 2010 n the northern Bering Sea, the Bering Strait, the Chukchi shelf break and the Canada Basin. Monthly averaged data during (a) August and (b) September were input to the absorption-based productivity model (ABPM, this study). (c and d) Results for August and September using the VGPM (Hirawake et al., 2012).

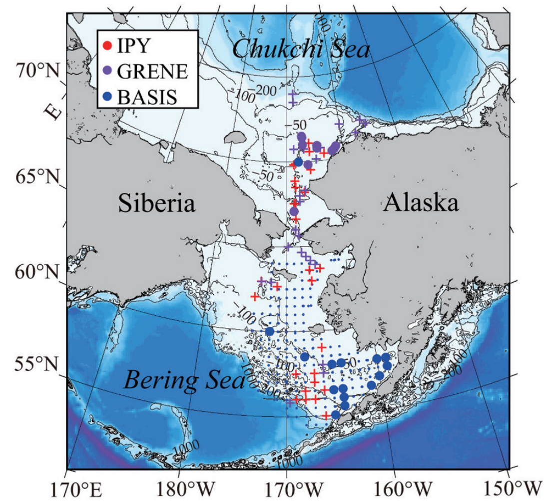

Fig. 6. 2. 3 Location of in situ sampling statins for the IPY cruises (red), GRENE cruises (violet) and BASIS cruises (blue). Note that the stations of the daily matches between the in situ FL measurements and MODIS level-2-derived FL values are shown in large circles, and crosses represent the sites where primary productivity measurements were conducted. Contours indicate the 100 m, 200 m and 1000 m bathymetry lines, based on ETOPO-2 (Fujiwara et al., 2016).

wara et al. (2011), which was optimized for the phytoplankton communities and optical properties in the Bering and Chukchi seas. Then, F_L could be derived using Eq. (6.2.2):

$$F_L = 1 / \{1 + \exp[-(X_0 + X_1\, a_{ph}(\lambda_1)/ a_{ph}(\lambda_2) + X_2\, \gamma)]\} * 100\ (\%), \quad (6.2.2)$$

where $X_0 = 3.175$, $X_1 = -0.570$ and $X_2 = -0.565$, $\lambda_1 = 488$ and $\lambda_2 = 555$, and γ (spectral slope of the particle backscattering coefficient) was empirically quantified using the R_{rs} (γ) ratio (Fujiwara et al., 2011). PP_{eu} was derived using the absorption-based productivity model (ABPM) proposed in Hirawake et al. (2011, 2012). Then, the annual net primary production (APP) was regressed using the annual median F_L, SST, and length of the open water period (OWP) for every one-by-one pixel:

$$\mathrm{APP} = A_1 * \mathrm{OWP} + A_2 * F_L + A_3 * \mathrm{SST}, \quad (6.2.3)$$

where A_1, A_2 and A_3 indicate the partial regression coefficients.

The in situ total and size-fractionated Chl *a* samples were obtained during the cruises of the Bering Arctic Subarctic Integrated Study (BASIS) program conducted in late summer to autumn (August to October) of 2005, 2006 and 2007, and the cruises of the GRENE Arctic Climate Change Research Project conducted in late summer to autumn of 2012 (September to October) and early summer of 2013 (June to July) on the Bering and Chukchi shelves (Fig. 6.2.3). The in situ primary productivity (PP) data, as well as the Chl *a* data, were also used to assess the influence of the subsurface Chl *a* maximum (SCM) on the remotely estimated PP_{eu}. PP samples were collected during the TR/S *Oshoro-maru* (Hokkaido University, IPY and GRENE cruise) and R/V *Mirai* (JAMSTEC, GRENE cruise) cruises in the same region, along with Chl *a* samples (Fig. 6.2.3).

The accuracy of the SDM derived F_L was evaluated by comparing the F_L values from the in situ measurements and daily matched MODIS level-2 data set. The SDM successfully retrieved the F_L values for 17 of the 25 data points (68% of the data) within a ±20% F_L range. The RMSE was 25%. However, it should be taken into account that there was a slight overestimation in the low F_L range and relatively large underestimation in the high F_L range (slope = 0.48 and intercept = 0.18). We found that the MODIS significantly underestimates $R_{rs}(\lambda)$ at every wavelength (the slopes ranged from ~0.34 to ~0.46). It can be said that the underestimations of $R_{rs}(\lambda)$ significantly caused the underestimation of F_L especially in the middle to high range of F_L.

To confirm how the satellite derived F_L and PP_{eu} represent a water column's phytoplankton size structure and productivity, the surface abd vertically integrated F_L values (calculated using Eq. (6.2.1) with water-column-inte-

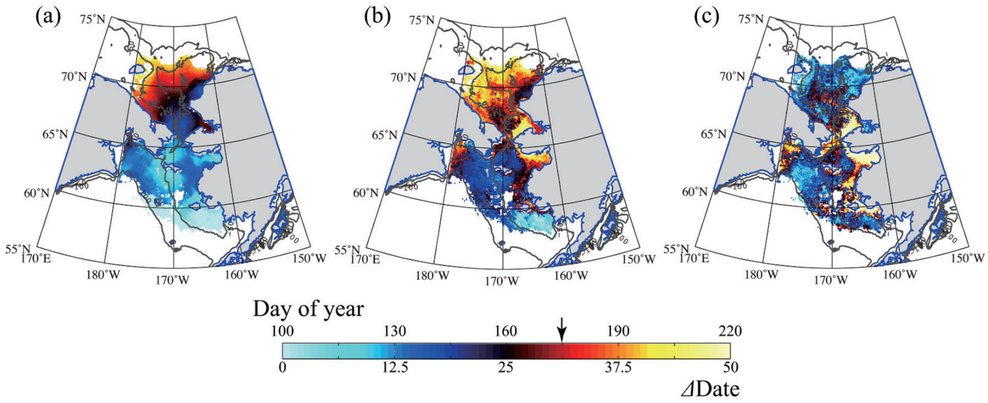

Fig. 6. 2. 4 Distribution of 16-year median of (a) TSR, (b) date of CMAX and (c) date difference between CMAX and TSR. Note that the color scales of (a) and (b) are indicated on the upper tick marks of the color bar, and the scale of (c) is indicated on the lower tick marks. The arrow on the color bar denotes the date of the summer solstice (day of year: 174). Contours indicate 50 m and 100 m bathymetry lines (Fujiwara et al., 2016).

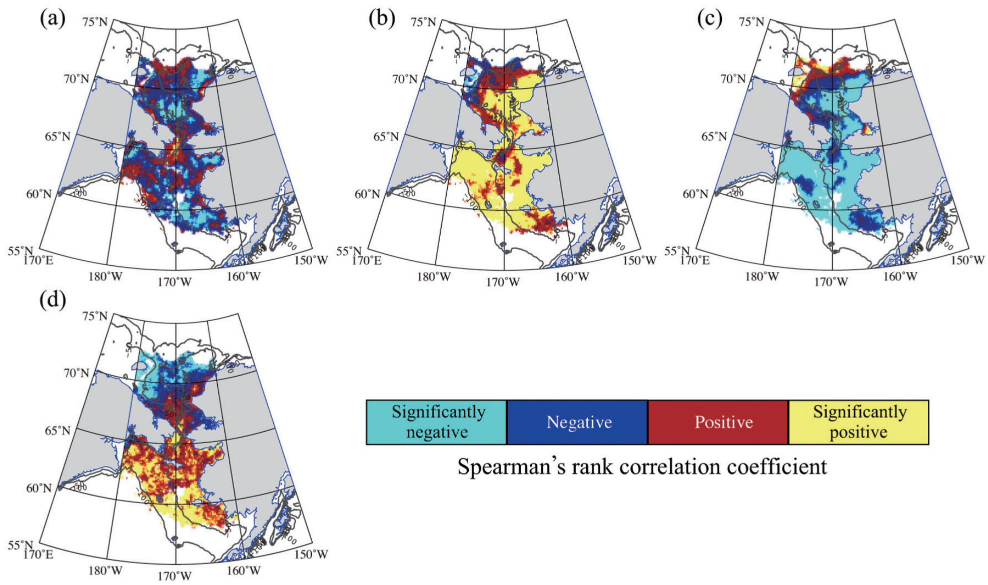

Fig. 6. 2. 5 Spatial distributions of Sperman's rank correlation (ρ) between (a) F_L during MIZ period and TSR, (b) SST during MIZ period and TSR, (c) ΔOHC during MIZ period and TSR, and (d) PAR during MIZ period and TSR. Yellow indicates a significantly positive ρ ($p < 0.05$). Contours indicate 50 m and 100 m bathymetry lines (Fujiwara et al., 2016).

grated Chl a_{total} and $a_{>5\mu m}$) was compared using in situ data set. The vertically integrated F_L showed a significant relationship with the surface F_L in spite of the presence of the subsurface F_L maximum at the many of the sampling sites, especially in low and middle range of the surface F_L were observed.

In order to determine the timing of the spring phytoplankton bloom, the relationship between the timing of the sea ice retreat (TSR) and date of occurrence of the yearly Chl *a* maximum (CMAX) was investigated. Fig. 6.2.4a shows the climatological median of TSR from 1998 to 2013. Then influence of TSR on phytoplankton size composition during MIZ blooms was investigated. Sperman's rank correlation coefficient (ρ) was calculated for every one-by-one pixel between F_L and TSR, SST and TSR, ΔOHC (change in ocean heat content) and TSR, and PAR and TSR (Fig. 6.2.5a-d). It was found that during the MIZ period, F_L was negatively associated with TSR in 68% of the shelf area, with a significant correlation in 15% of the area ($p < 0.05$). A significantly positive ($p < 0.05$) relationship was found for the western side of the Bering Strait and western coast of Alaska; this area accounted for 2% of the whole study area. During the MIZ period, SST was tightly and positively correlated with TSR over most (92%) of the region (Fig. 6.2.5b), with a significant correlation in 65% of the area. This spatial pattern of ΔOHC was also similar to the SST pattern though it was inverse, with a statistically significant negative relationship for more than 61% of the area (Fig. 6.2.5c). These results reveal that an earlier sea ice retreat is associated with a cold surface temperature and relatively large amount of heat release from the sea surface during the MIZ period. However, on the northwestern edge of the Chukchi Sea, the opposite correlations were found, with a significantly positive ρ between SST and TSR, and significantly negative ρ between ΔOHC and TSR (Fig. 6.2.5b and c). PAR was strongly and positively correlated with TSR in the northern Bering Sea up to and through the Bering Strait, but became negative in the northern part of the Chukchi Sea shelf (Fig. 6.2.3d). The highest positive ρ between PAR and TSR was found in the area where the sea ice normally retreats before the summer solstice, at the time when the latest daily PAR would be observed (Fig. 6.2.4a).

Factors controlling annual net primary production (APP) were examined. A standardized multiple regression analysis was used to determine the contribution of the controlling factors for the APP. This analysis revealed that longer growing season, larger proportions of large-sized phytoplankton assemblages, and higher SSTs generally enhanced the APP. However, the magnitude of the contribution changed regionally. Larger partial regression coefficients for the length of the open water period (> 0.7) were found mainly in the northern shelf area of the Chukchi Sea. Larger partial regression coefficients for F_L (> 0.7) were mainly found on the Bering Sea shelf and part of the central Chukchi Sea shelf (67–70°N, 170–175°W), where other variables showed relatively lower contributions. Conversely, the partial regression coefficients for the SST were negative on the southern edge of the Bering Sea shelf study area. Based on the results of the standardized multiple regression analysis, in regions with seasonal ice cover, a large amount of phytoplankton positively contributed to the APP on the northern Bering Sea shelf, and a longer open water period was a major factor for the APP in the Chukchi Sea shelf.

Hence, the ocean color remote sensing is believed to be applicable to discuss the temporal and spatial relationships between the distribution of sea ice and phytoplankton variables (i.e., F_L, PP_{eu}, and Chl a), at least in the study area.

Phytoplankton in basin area

Since we have seen the enrichment of phytoplankton in the shelf region in the above section (Fujiwara et al., 2016), we would like to look at basin area where primary production is basically weak.

The study by Fujiwara et al. (2014) assesses the response of phytoplankton assemblages to recent climate change, especially with regard to the shrinking of sea ice in the northern Chukchi Sea of the western Arctic Ocean. It is important to understand the influence of sea ice reduction on phytoplankton community composition because different phytoplankton functional types such as large diatoms and small flagellates play important but different roles in biogeochemical cycles and ecosystems. Therefore, surface distribution patterns of phytoplankton assemblages were examined as derived from algal pigment data collected from western Arctic Ocean during the late summers of 2008–2010. Data were collected during cruises of the R/V Mirai, primarily in September of 2008 (28 August–6 October), 2009 (11 September–10 October) and 2010 (4 September–13 October).

Multiple regression analysis (MRA) was applied to the phytoplankton pigment data to determine the most predominant phytoplankton group at each sampling station. MRA can access the contributions of accessory pigment to chl a levels and does not require any assumptions about the pigment ratios of each algal group, as does Chemical Taxonomy (CHEMTAX). On the other hand, cluster analysis (CA) was performed to divide sampling sites into groups that have similar pigment composition, with Ward's linkage method using Euclidean distance. The same pigments used for CHEMTAX analysis for Baffin Bay, in the Arctic Ocean, by Vidussei et al. (2004) were chosem for CA because similar algal groups are expected to appear in the study region – chl $c3$, peri, but, fuco, prasi, hex, allo, zea, lut and chl b. Surface chl a concentration of the three cruises were successfully expressed from MRA (Eq. 6.2.4), which included six accessory pigments:

$$\text{chl } a = 1.49\,[\text{peri}] + 1.85\,[\text{fuco}] + 1.74\,[\text{hex}] + 5.88\,[\text{allo}] + 3.54\,[\text{zea}] + 1.31\,[\text{chl } b] + 0.02, \tag{6.2.4}$$

where the adjusted R^2 was 0.99, and all regression coefficients of Eq. (6.2.4) were statistically significant. Surface phytoplankton groups were divided into 4 clusters using CA and their pigment compositions. Using CA, 45, 10, 13 and 8 samples were grouped into cluster 1, 2, 3 and 4, respectively. To determine the dominant phytoplankton group in each cluster, the average pigment/chl a ratio and the average contribution to chl a of the major pigments were confirmed, which was derived by MRA

(Fig. 6.2.6).

Fig. 6.2.7a-c indicate the distributions of sea ice concentration (SIC) and sea surface temperature (SST) as monitored by a satellite on 1 September 2008–2010, along with the dominant phytoplankton groups at the sea surface during the cruises in each year. The ice edge retreated to ~78°N throughout the study area in 2008, except the area of 170–175°W (Fig. 6.2.7a). However, in 2009 and 2010, the northernmost ice edge was located at a similar latitude as in 2008, though the sea ice retreat at such a high latitude was observed only in the narrow areas of 150–155°W in 2009 and 160–165°W in 2010 (Fig. 6.2.7b and c). The distribution of sea surface temperature (SST) also showed spatial variation. A relatively high SST (> 3°C) was common in the southern Chukchi Sea (~72°N), where open water area commonly spread during the three years, and extended to ~75°N in the eastern Cuukchi Sea in 2008 (Fig. 6.2.7a), where ice cover was observed in 2009 and 2010 (Fig. 6.2.7b and c).

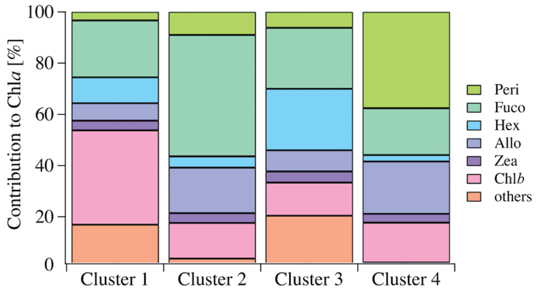

Fig. 6. 2. 6 Average percent contribution to chl *a* of major algal accessory pigments for each cluster. These contributions were determined by multiple regression analysis (Fujiwara et al., 2014).

The interannual variability of SIC from 2008 to 2010 was analyzed, assuming that sea ice distribution was one of the determining factors of algal taxonomic distribution. Fig. 6.2.8a-c show the distribution of sea ice on the dates that SIC became < 10%, the criteria that defined the onset date of open water area. In the study area, sea ice retreat generally begins in May or June in the shelf, and

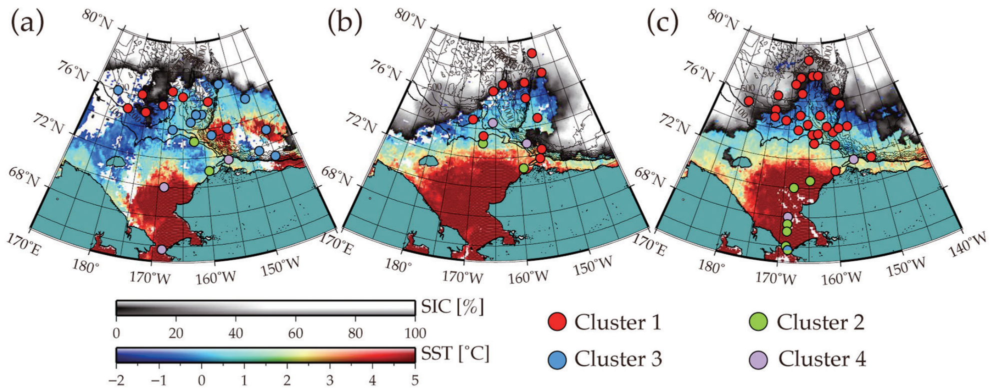

Fig. 6. 2. 7 Distribution of dominant phytoplankton groups at the surface layer in (a) 2008, (b) 2009 and (c) 2010. Clusters were identified by cluster analysis. SIC data were collected by AMSR-E on September 1: SST data were collected by MODIS and composited to 9-day average centered on 1 September of each year. Depth contours indicate 100-, 200-, 500-, 1500- and 2000-m intervals, respectively (Fujiwara et al., 2014).

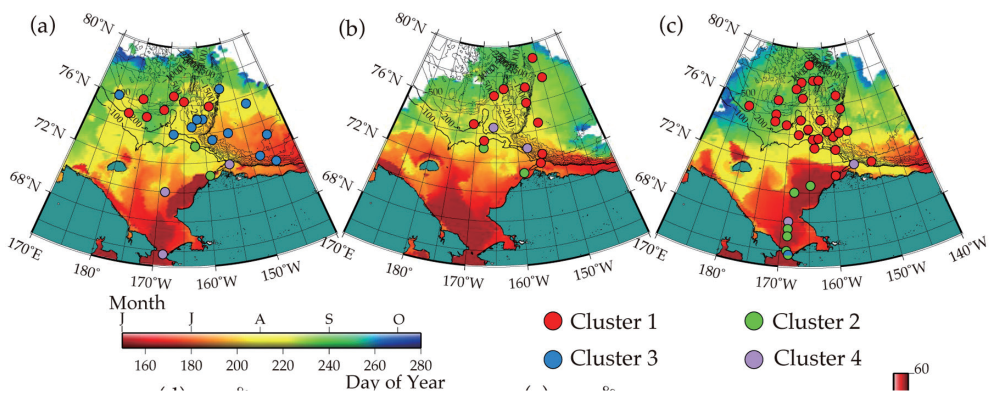

Fig. 6. 2. 8 Distribution of the clusters across Julian day when the area became open water in (a) 2008, (b) 2009 and (c) 2010. Clusters were identified by cluster analysis. White indicates area where no open water appeared during the entire year (Fujiwara et al., 2014).

the shrinking continues until August or September, when the ice edge reaches the basin. However, there was temporal and spatial variability in the onset date of sea ice retreat, especially in the eastern Chukchi Sea (140–160°W), where the algal assemblages of cluster 3 were observed. The onset date in that area occurred in July in 2008 (Fig. 6.2.8a); however, sea ice retreat occurred in July and August in 2009 and 2010, respectively (Fig. 6.2.8b and c). In short, 1 to 2 months earlier sea ice retreat observed in 2008 than in 2009 and 2010 in the deep basin (Fig. 6.2.8b and c).

Cluster 3 dominated by haptophytes was observed only in 2008 in the eastern Chukchi Sea, where prasinophytes were dominant in the other two years. To understand the reason for this difference among the years, the interannual variability of open water area and the temporal variability of the onset of sea ice melt were focused on. As indicated in Fig. 6.2.8a-c, there were significant differences in the onset date among the three years. In particular, an earlier onset of 1 to 2 months was observed in the eastern Chukchi Sea in 2008. It is hypothesized that this earlier sea ice melt and longer ice free periods reduced the ice albedo in 2008, and warm water (~5°C) consequently distributed in the eastern Chukchi Sea. The locations of haptophyte dominated samples showed good agreement with early open water and warm water (Fig. 6.2.7a and Fig. 6.2.8a). Such relatively warm and oligotrophic water conditions should be favorable for haptophytes. In addition, an earlier sea ice retreat might release phytoplankton from light limitation. Under light limited conditions, phytoplankton tends to synthesize chl *b* and chl *a* to increase their photosynthesis efficiency. In the Arctic Ocean, phytoplankton often experiences light limitations due to the presence of sea ice. Therefore, prasinophytes, which contain more chl *b* due to low light acclimation, are distributed widely in the Arctic. However, the longer ice free period of 2008 may have triggered the appearance of unusual phytoplankton community that dominated by haptophytes due to improved light conditions. Thus, it is suggested that the dominance of haptophytes observed only in 2008 was due to the spread of warm, nutrient-depleted water and/or changing light conditions, all of which likely follow early sea ice retreat.

Although the impact of phytoplankton community shift on biogeochemical cycles and food webs might be small, the longer ice free periods and larger open water areas predicted for the future may amplify the spatial and temporal influence of algal community shifts. Therefore, the spatiotemporal patterns and changes in phytoplankton community structure should be taken into account when assessing biogeochemical cycles and food webs in the western Arctic Ocean.

6. 3. Changes and shifts in the dominant group due to warming and sea ice retreat in the Arctic Ocean

To evaluate the effect of sea ice reduction on zooplankton, Matsuno et al. (2011) studied year-to-year changes of zooplankton community structure in the Chukchi Sea during summers of 1991, 1992 (when sea ice extended), 2007 and 2008 (when sea ice reduced). Zooplanktons are secondary producers of the marine ecosystem and comprise a vital link between primary production (explained in Section 6.2) and fishes (Section 6.4) or marine mammals (6.5) in the western Arctic Ocean. In the southern Chukchi Sea, since Pacific water flows into the sea through the Bering Strait, not only Arctic copepods but also large-sized Pacific copepods are dominant taxa. The zooplankton community in the western Arctic Ocean is expected to be changed after 2007 when the drastic decrease of sea ice area was observed, but no study has contrasted zooplankton community structure between 1990s and recent years.

A total of 120 zooplankton samplings were conducted by T/S. *Oshoro-Maru* in the Chukchi Sea (66°00’–71°11’ N, 162°02’–168°58’ W) during 24–31 July 1991 (n = 27), 24–31 July 1992 (n = 34), 5–13 August 2007 (n = 31) and 7–13 July 2008 (n = 28). Zooplankton samples were collected at day and night by vertical tows with a NORPAC net from 5 m above the surface.

Zooplankton abundance ranged from 4,000 to 316,000 ind. m^{-2} (mean: 70,000) (Fig. 6.3.1a). Abundance in 1991, 1992 and 2008 was greater north of Lisburne Peninsula, while in 2007 abundance was greater south of Lisbrune Peninsula (Fig. 6.3.1a). Zooplankton biomass ranged from 0.07 to 286 g WM m^{-2} (mean: 36). The geographic distribution of biomass was not parallel with abundance except for the south of Lisbrune Peninsula in 2007 (Fig. 6.3.1b).

Copepods composed 2–86% (mean: 31) of zooplankton abundance, and barnacle nauplii and cypris larvae (*Balanus crenatus* Brugiere) were also dominant in the northern area (Fig. 6.3.2). Within the copepods, proportions of C. *glacialis* and *Pseudocalanus* spp. were relatively high, especially in 1991 and 1992. In 2007, pro-

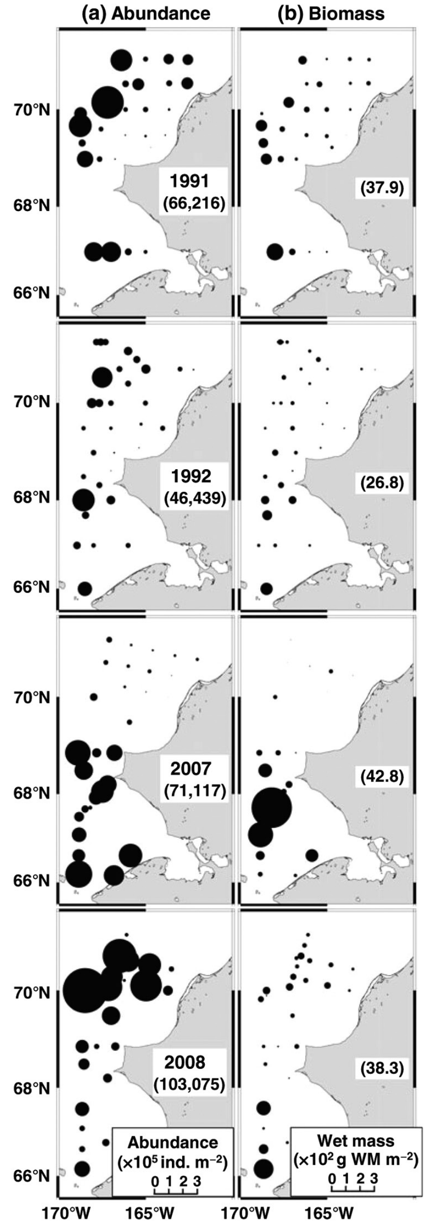

Fig. 6. 3. 1 Geographic distribution of the zooplankton abundance (a) and biomass (b) in the Chukchi Sea during July–August of 1991, 1992, 2007 and 2008. Values in the parenthese indicate mean values of each year (Matsuno et al., 2011).

portions of Pacific copepods (*E. bungii* and *M. pacifica*) were high, while the proportion of barnacle larvae was low (Fig. 6.3.2). Barnacle larvae predominated in 2008. Through the 4 years of analysis, 22 species of calanoid copepods belonging to 13 genera were identified. Within these species, 6 species belonging to 4 genera were Pacific copepods. Since Pacific copepods were dominant in 2007, total copepod abundance was the greatest in 2007. When barnacle larvae were dominant in 2008, total zooplankton abundance was the highest in 2008.

Based on the taxon abundance, zooplankton communities were classified into six groups (A-F) by cluster analysis. Environmental parameters significantly affecting cluster analysis were latitude, longtitude, sea surface temperature, sea surface salinity and bottom salinity, with 24–37% coefficient of determinations (r^2). Mean abundances of groups A, B and D ranged from 76,800 to 101,030 ind. m^{-2}, but those of groups C, E and F were lower and ranged from 5,744 to 30,283 ind. m^{-2}. For groups B, C and E, barnacle larvae dominated and species diversities were low. Groups A, D and F were characterized by few barnacle larvae and dominance of Pacific copepods (groups A, D) or Arctic copepods (group F). Species diversity of groups A and D was high because of the occurrence of both Pacific and Arctic copepods. Distribution of each group was well separated both geographically and interannually (Fig. 6.3.3). Group B was bserved offshore north of Lisburne Peninsula in 1991 and 1992, and north of Lisbrune Peninsula in 2007 and 2008. Group D, characterized by the high abundance and dominance of Pacific copepods, was observed only south of Lisburne Peninsla in 2007. Concerning interannual variability in the zooplankton community, geographic distribution was similar for 1991 and 1992 (Fig. 6.3.3). In 2007, the whole distribution area was shifted northward compared to 1991 and 1992 and group D, characterized by dominance of Pacific copepods, was observed south of Lisburne Peninsula. In 2008, geographic distribution of groups was similar to 1991 and 1992, but distribution of group A, which was observed south of Lisburne Peninsula in 1991 and 1992, also penetrated to the north of Peninsula (Fig. 6.3.3).

Comparison between 1991/1992 (sea ice extent) and 2007/2008 (sea ice reduced) showed a remarkable northward shift in geographic distribution of zooplankton communities (Fig. 6.3.3). This northward shift in zooplankton community in 2007/2008 may be related to the differences in formation of water masses. The greatest differences in the hydrographic environment between 1991/1992 and 2007/2008 were in the presence (1991/1992) or absence (2007/2008) of sea ice meltwater and were also evident in the salinity of the surface layer, which was low for 1991/1992 and high for 2007/2008.

Concerning the zooplankton community, the Arctic copepod C. glacialis was relatively abundant in 1991/1992, and less so in 2007/2008. The zooplankton community in 2007 was characterized by the dominance of Pacific copepods, and in 2008 was dominated by barnacle larvae (Fig. 6.3.2). The dominance of barnacle larvae in 2008 suggests an earlier release of the larvae from their benthic adult form than in 1991/1992. Concerning

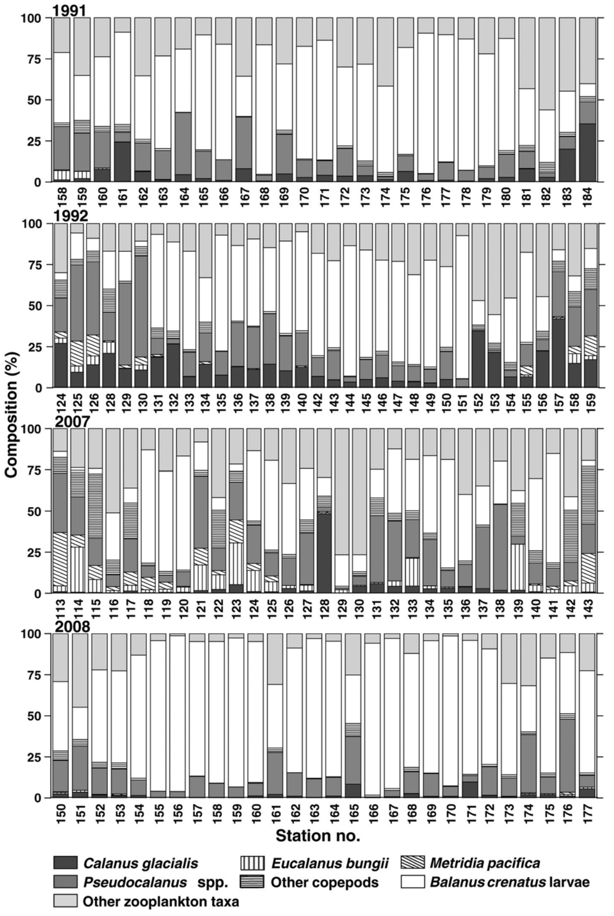

Fig. 6. 3. 2 Taxonomic composition in total zooplankton abundance of the Chukchi Sea during July–August of 1991, 1992, 2007 and 2008 (Matsuno et al., 2011).

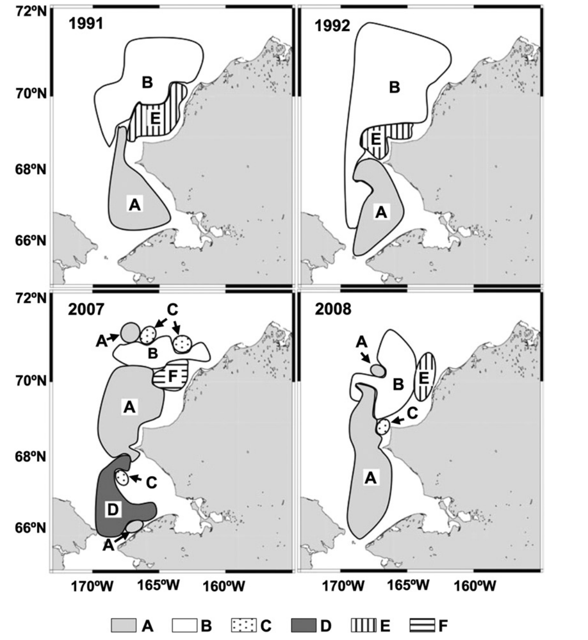

Fig. 6. 3. 3 Geographic distributions of the six groups (A–F) identified from Bray-Curtis similarity based on zooplankton abundances in the Chukchi Sea during July-August of 1991, 1992, 2007 and 2008 (Matsuno et al., 2011).

the release timing of barnacle larvae from benthic adults, laboratory rearing studies show that the amount of food concentration (phytoplankton) is a key factor for release timing. Field studies also indicate that onset of the phytoplankton bloom is a key factor stimulating the release of barnacle larvae. Because the sea surface salinity was higher in 2007/2008 than in 1991/1992, the timing of sea ice reduction was considered to be earlier in 2007/2008. This earlier sea ice reduction in 2007/2008 may induce that earlier phytoplankton bloom for these years because of the earlier release from the light limitation on the photosynthesis. The earlier onset of the phytoplankton bloom in 2008 is considered to be a cause of the dominance of the barnacle larvae in that year. The earlier sea ice reduction and onset of phytoplankton bloom was also the case of 2007. However, the greater inflow of Pacific summer water (PSW) in 2007 forced the barnacle distribution area north (Fig. 6.3.3), leading to a lower abundance of barnacle larvae in 2007 than 2008.

From the viewpoint of zooplankton production, increased inflow of PSW induced the dominance of the large sized Pacific copepods, and thus may have positively affected productivity. However, increased inflow of PSW caused changes in the marine ecosystem structure in the Chukchi Sea (loss of characteristic Arctic species in part of the region), which is considered as a negative effect of global warming.

Larger zooplankton, copepods

Matsuno et al. (2014) investigated seasonal changes in mesozooplankton swimmers, copepods. Zooplankton swimmers collected by sediment trap sampling at 13–15 day intervals moored at 184 m on the Northwind Abyssal Plain (75°00’ N, 162°00’ W, bottom depth 1975 m; NAPt) during October 2010–September 2011 were analyzed (Fig. 6.3.4). This station is seasonally affected by inflow of Bering Shelf Water from the Bering Strait. Through this analysis, seasonal changes in swimmer community structure and population structure of the four dominant copepods (*Calanus hyperboreus, Metridia longa, Paraeucaeta glacialis and Heterorhabdus norvegicus*) were evaluated. For zooplankton swimmer samples (> 1 mm), identification and enumeration of zooplankton were made under a dissecting microscope. In this study, swimmers were defined as zooplankton > 1 mm samples that swam actively into the trap.

The trap depth varied between 181 and 218 m, and was mostly stable around 184 m then temporally deep-

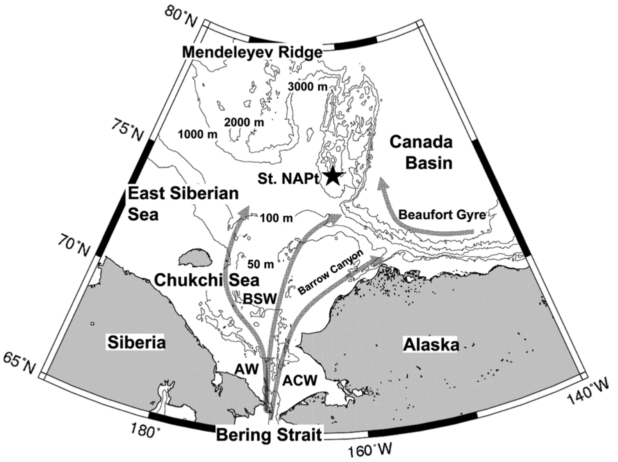

Fig. 6. 3. 4 Location of St NAPt (Northwind Abyssal Plain trap) in the western Arctic Ocean where the sediment trap was moored at 184 m during October 2010–September 2011. ACW, Alaskan Coastal Water; AW, Anadyr Water; BSW, Bering Shelf Water (Matsuno et al., 2014).

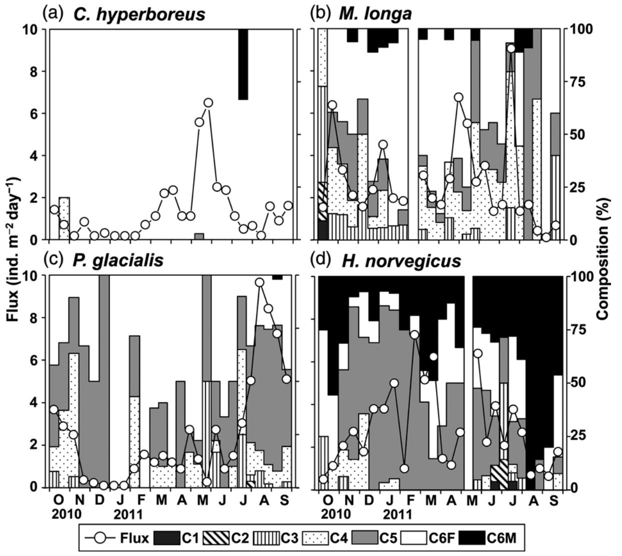

Fig. 6. 3. 5 Seasonal changes in flux and copepodid stage composition of the four dominant copepods: *Calanus hyperboreus* (**a**), *Metridia longa* (**b**), *Paraeuchaeta glacialis* (**c**), *Heterorhabdus norvegicus* (**d**), at 184 m at St NAPt during 4 October 2010–28 September 2011(Matsuno et al., 2014).

ened within a short period. Temperature at the sediment trap ranged from −1.6 to −0.6°C. The 5-day mean of current velocity showed a slow subsurface current (< 11.3 cm s^{-1} at 45 m and < 2.7 cm s^{-1} at 188 m water depths) at St NAPt. Sea ice around the sediment trap site showed clear seasonal changes, with a decrease from early July, complete melting (sea ice concentration: 0%) in September, a rapid increase during October and 100% coverage during November to June. The total mass flux (< 1 mm size range) ranged from 19.3 to 215.9 mg DM m^{-2} day^{-1} and peaked during November–December. High chl *a* was observed during August–September. At St NAPt, the midnight sun occurred during early May to early August, and the polar night was from early November to early February.

The population structure of the four dominant copepods varied with species. Throughout the year, *C. hyperbpreus* was predominated by C6F. The population structure of *M. longa* and *P. glacialis* showed seasonal change; both were dominated by C6F from January to May, and early copepodic stages (C1–C4) occurred during June–October. *Heterorhabdus norvegicus* showed a different seasonal pattern; it was dominated by C5 during November–February, the contribution of C6F/M increased during March–October and C1 and C2 stages occurred in June–July.

Lipid accumulation in C6Fs of the dominant copepods (excluding *H. norvegicus*) also showed species-specific seasonal patterns. Most *C. hyperboreus* contained more lipids (stage III) during December–January (83%) than during February–October (56%). For *M. longa*, stage III individuals dominated during October–December, their lipid levels gradually decreased during March–June and all specimens had no oil sacs in July. The lipid accumulation of *P. glacialis* showed fluctuating seasonal change. Gonad maturation of C6Fs of the dominant copepods (excluding *H. norvegicus*) showed more distinct seasonality. For *C. hyperboreus*, mature individuals were observed only during February–April. Mature M. longa were seen during March–July, although only one specimen was observed in September, and lipid accumulation decreased. Most *P. glacialis* (47%) matured during August–January, when egg carrying adult females also seen.

The Pacific copepod *Neocalanus cristatus* occurred (0–0.92 ind. m^{-2} day^{-1}) throughout the year, and was more abundant during August–September when the sea ice was reduced. All *N. cristatus* were stage C5, and lipid accumulation varied.

Throughout the previous studies, copepods are the most dominant taxa, followed by amphipods or pteropods consistent with the present study. Dominant copepods in this study were *H. norvegicus* followed by *M. longa*, unique because of the dominance of mesopelagic copepods (Yamaguchi and Ikeda, 2000). *Heterorhabdus norvegicus* is reported to be the second most dominant copepod in the zooplankton swimmer fauna of the eastern Greenland Sea (Seiler and Brandt, 1997); thus this species may be a dominant copepod throughout the mesopelagic layer of the Arctic Ocean. Additional to these

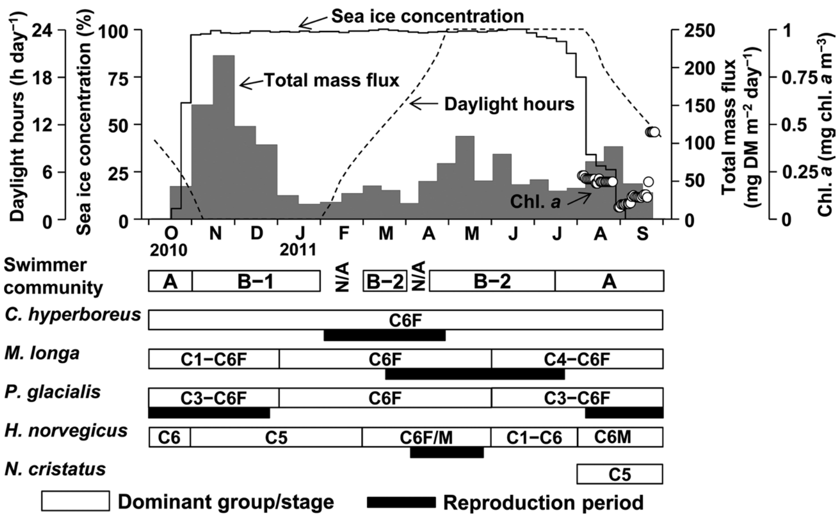

Fig. 6. 3. 6 Schematic diagram of seasonal changes in daylight hours, sea ice concentration, chl *a*, total mass flux (upper panel), swimmer community, population structure and reproduction period of copepods (*C. hyperboreus, M. longa, P. glacialis* and *H. norvegicus*), and occurrences of the Pacific *N. cristatus* collected by sediment trap at 184 m of St NAPt during 4 October 2010–28 September 2011 (lower panel). For *C. hyperboreus, M. longa* and *P. glacialis*, the reproduction period was evaluated by C6F gonad maturation. For *H. norvegicus*, their reproduction period was estimated by the occurrence of early copepodid stages (Fig. 5d) (Matsuno et al., 2014).

copepods, the occurrence of a small number of Pacific copepods is a special feature of this study. Since the zooplankton swimmer community showed clear seasonal changes (groups A, B-1 and B-2), in the following, the characteristic of each swimmer group were discussed.

The group A, corresponded with the open water period (July–October), dominated by the carnivorous *P. glacialis*. Thus, if *P. glacialis* exhibits similar DVM to *P. norvegica*, the dominance of *P. glacialis* in group A (July–October) was caused by *P. glacialis* diel vertical migration (DVM) during this period. Changes in the zooplankton swimmer community from groups A to B-1 corresponded to the timing of ice coverage and entry into polar night. The group B-1 was characterized by the dominance of mesopelagic *M. longa* and *H. norvegicus*. While their flux showed little seasonal change (Fig. 6.3.5b and d), the other two species showed clear seasonality: peaked in May–June for *C. hyperboreus* (Fig. 6.3.5a) and July–October for *P. glacialis* (Fig. 6.3.5c). Thus, group B-1 was composed mainly of mesopelagic copepods (*M. longa* and *H. norvegicus*) in the mesopelagic layer. For the other two species (*C. hyperboreus* and *P. glacialis*), seasonal vertical migration (SVM) and presence/absence of DVM is considered to be a key mechanism governing the seasonal changes in the swimmer community.

During the ice coverage period (November–June), the swimmer community changed from groups B-1 to B-2 in February due to the drastic increase (ca. 10 times) of *C. hyperboreus*. Since daylight hours changed greatly from 0 (polar night) to 24 h (midnight sun) during February to April, this change in day–night cycle may affect the arousal from diapause for *C. hyperboreus*. As a specialized seasonal event in this study, the occurrence of Pacific copepods was observed. The Pacific copepod *N. cristatus* C5 was abundant during August–September when sea ice coverage decreased (Fig. 6.3.6). This seasonal pattern suggests that the amount of Pacific Water inflow may increase when the sea ice coverage decreases. While *N. cristatus* C5 are known to perform SVM to deep layers to diapause during late summer (Miller et al., 1984), the greater flux of *N. cristatus* C5 in August–September may also be caused by their SVM. Since their reproduction occurs > 1000 m depth (Miller et al., 1984), the possibility of their reproduction in the Arctic Ocean could not be evaluated in this study.

Thus, the reproduction seasons of the dominant four copepods differed (Fig. 6.3.6), and possible causes of these differences include species-specific feeding modes, seasonal changes in food availability and the presence/absence of ontogenetic vertical migration. In summary, while the limitation of sampling design, through the analysis of zooplankton swimmers collected by the sediment trap, zooplankton communities were clearly separated into three seasons (Fig. 6.3.6). The season when each copepod dominated corresponded with the active vertical migration timing of each species. For the four dominant copepods, their reproduction timings varied with species, which may be related to the feeding modes. In addition, the occurrence of Pacific copepods was observed. Since their peak period (August–September) corresponded with timing of their SVM, they may have entered the sediment trap while performing descent SVM.

Reproductive success

The species composition of Arctic zooplankton differs greatly from that of the zooplankton of the North Pacific and Bering Sea. Particularly with greater warming from sea-ice retreat, the reproduction of North Pacific species transported into the Chukchi Sea and beyond may lead to changes in the Arctic pelagic ecosystem. Matsuno et al. (2015) reported the egg production and hatching of the Pacific copepod *Neocalanus flemingeri* in the Chukchi Sea based on shipboard experiments performed in September 2013. The reproductive capability of *N. flemingeri* observed in the Chukchi Sea resembled that reported in the Pacific, with the exception of a lower hatching success. Only 7.5% of *N. flemingeri* eggs hatched compared with 93% in Pacific experiments (Saito and Tsuda, 2000). This large discrepancy may be the results of differences in the fraction of eggs successfully fertilized. Adult males of N. flemingeri were not observed in this study. The extremely low hatching success in the Arctic Ocean (7.5%) is considered to be caused by failures of fertilization. The potential recruitment number for *N. flemingeri* suggests that it is unlikely to establish expatriate Arctic populations in the near future.

6. 4. Distribution patterns of fish species

From the long term survey by T/S *Oshoro-Maru* from Hokkaido University, polar cod was found to be a dominant species in northern Bering Sea and Chukchi Sea, while suketo cod was in shelf region of Bering Sea.

Diets and body conditions

Polar cod, *Boreogadus saida*, is an abundant epipelagic fish found throughout the Arctic Ocean, an important food for other fish, marine mammals and seabirds, and thus a key species in the Arctic Ocean ecosystem. To understand how changes in Arctic marine food webs may impact polar cod, a study of their trophic responses (changes in diet and energy stores) to differences in zooplankton and benthic invertebrate communities across regions with different environments was conducted (Nakano et al., 2016). The stomach contents and body

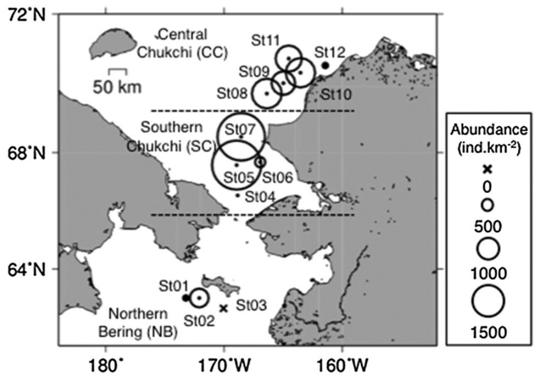

Fig. 6. 4. 1 Sampling stations (St) and abundance of polar cod (catch per unit effort as number of fish per km^2 of area swept by bottom trawl) in the northern Bering Sea (NB), southern Chukchi Sea (SC) and central Chukchi Sea (CC). No fish were collected at St03 (Nakano et al., 2016).

condition of polar cod were compared between three regions with different environments: the northern Bering Sea (NB), southern Chukchi Sea (SC) and central Chukchi Sea (CC).

Sampling was conducted aboard the T/S *Oshoro-Maru* at 12 stations (St; Fig. 6. 4. 1) at depths between 34 and 68 m during July 4–17, 2013. The density of polar cod was calsulated as the number of fish per unit survey area. Polar cod were most abundant at St05 (Fig. 6.4.1). No fish were collected at St03, and a single fish was collected at St04. Polar Cod collected in the NB and the SC were larger than those collected in the CC. The stomach fullness indices were higher in the NB and SC than in the CC, while body condition indices did not differ between the regions.

Prey items were found in 211 stomachs out of 238 fish collected. Although the percentage index of relative importance (IRI) of each prey type varied between the stations (Fig. 6.4.2), the average IRI across stations within the region showed that appendicularians were the most dominant prey found in the polar cod stomachs collected in the NB (47%) and SC (50%), while in the CC appendicularians were completely absent (Fig. 6. 4. 2).

The stomach fullness index of polar cod collected in the NB and SC was greater than in the CC, possibly reflecting the higher biomass of zooplankton in the water column in the SC and NB than CC. Inflow of nutrient-rich water from the Pacific induces higher primary production in the SC than CC, which presumably explains higher zooplankton abundance. This high primary production, seasonal ice cover, and shallow water depth may also support a large biomass of benthic communities in the NB and SC. In addition to the availability of prey,

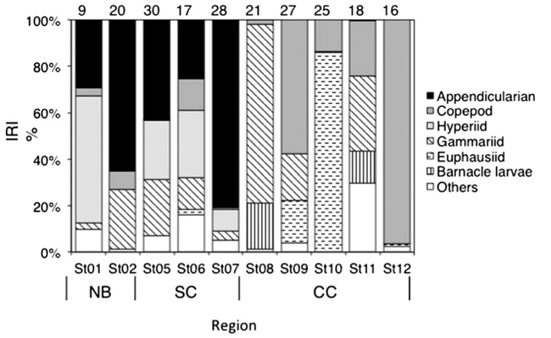

Fig. 6. 4. 2 The percentage composition of prey taxa, shown by the index of relative importance (IRI), found in the stomachs of polar cod collected in the northern Bering Sea (NB), southern Chukchi Sea (SC) and central Chukchi Sea (CC). Sample sizes (number of stomachs) are shown at the top of *bars* (Nakano et al., 2016).

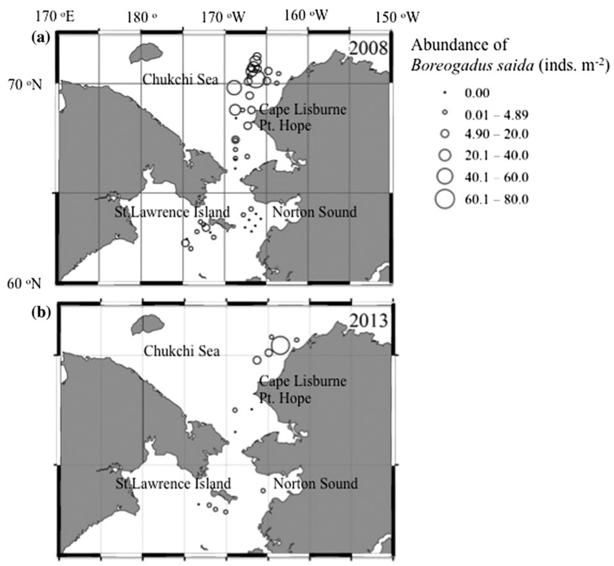

Fig. 6. 4. 3 The distribution and abundance of *Boreogadus saida* in (**a**) 2008 and (**b**) 2013 (Kono et al., 2016).

water temperature might influence foraging activities and hence stomach fullness. Water tempearature at the seafloor in our study, however, were highest in the SC (0.8–1.3°C), followed by the CC (−1.7 to −0.8°C) and then the NB (−1.7 to −1.6°C); indicating that ambient temperature might not explain observed differences in stomach fullness.

The reduced sea ice coverage has been proposed to favor a phytoplankton-/zooplankton-dominated ecosystems over a sea ice algae/benthos ecosystem (Grebmeier, 2012), while the expansion of warmer Pacific water into the southern Arctic Ocean induced the dominance of warm water copepod species (Matsuno et al., 2011). Climate change may also influence the distribution and abundance of gelatinous zooplankton. These expected climate-induced changes in pelagic zooplankton and benthic invertebrate communities either to the gelatinous zooplankton or to warm water living copepods may influence the diet and body condition of polar cod, and hence, their recruitment has been found in Atlantic cod.

Distribution patterns

Kono et al. (2016) examined the distribution pattern of Polar cod (*Boreogadus saida*) and other fish larvae in relation to oceanographic parameters, including sea surface temperature and salinity (SST and SSS), the mode of temperature and salinity within the water column (F_{temp} and F_{sal}), and the temporal duration between the date of sea ice retreat and the date of field surveys (dSRT) in the northern Bering and Chukchi Seas during the summers of 2008 and 2013.

Changes in sea ice extent and timing of sea ice retreat affect the physical and biological environment in the northern Bering Sea and the Chukchi Sea, including water temperatures, timing of phytoplankton blooms and zooplankton reproduction in spring and summer, as well as fish and broader ecological system (Grebmeier et al., 2006). The composition and distribution of fish assemblages also would be affected by sea ice reduction via environmental change because demersal fish assemblages are known to be governed by water temperature and habitats are structured by water masses. Because the fish larvae studied here have a lower swimming ability and are smaller than adult fish, they are easily preyed upon by other carnivorous fish and cannot escape from unfavorable environmental conditions. Therefore, the analysis of fish larval assemblages may facilitate the prediction of ecosystem responses to a changing climate.

Fish larvae were collected at 57 sampling stations in 2008 and 2013. The total number of fish larvae collected by bongo net was 1186, and the average abundances of fish larvae was 23.53 inds. m^{-2} comprised of 7 families and 17 taxa in 2 years. Abundances were numerically dominated by *B. saida* (35%), *A. hexapterus* (27%) and Pleuronectidate (17%). Results of the analysis showed that the main indicator species for group A, B, C and D were Pleuronectidate (87.95% of total abundance in group A), *B. saida* (85.33% in group B), *A. hexapterus* (51.12% in group C) and *A. hexapterus* (32.53% in group D), respectively.

Kono et al. focused on the marine environment where *B. saida* larvae were distributed. The abundance of *B. saida* varied greatly across sampling stations with a median of 4.9 inds. m^{-2}. The high abundance regions were

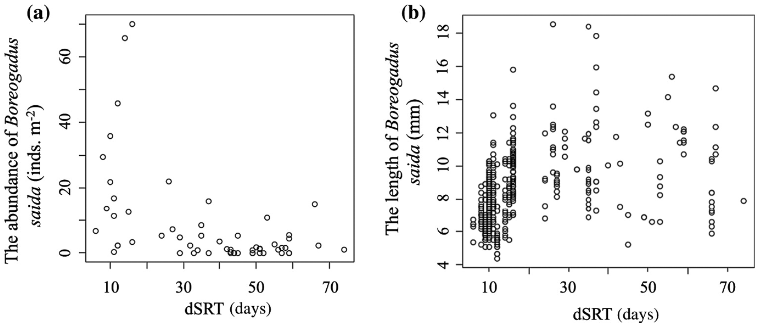

Fig. 6. 4. 4 Scatter plots of the duration from sea ice retreat timing (dSRT) against (**a**) abundance of *Boreogadus saida* and (**b**) size of *B. saida* (Kono et al., 2016).

predominantly in the northeastern Chukchi Sea (Fig. 6. 4. 3) where SST ranged from 0.31 to 5.89°C, F_{temp} ranged from −1.75 to 5.75°C, F_{sal} ranged from 31.3 to 32.8, SSS ranged from 29.0 to 32.5 and dSRT ranged from 6 to 66 days. The low abundance regions were predominantly in the northern Bering Sea and in the southern Chukchi Sea (Fig. 6.4. 3), where SST ranged from 0.66 to 9.7°C, F_{temp} ranged from −1.75 to 6.25°C, F_{sal} ranged from 30.8 to 32.8, SSS ranged from 26.3 to 32.6 and dSRT ranged from 11 to 74 days. Sea surface environment (SST and SSS) and dSRT were significantly different between station with low and high abundance. Although not statistically significant, F_{temp} of high abundance stations was lower than that of low abundance station. Further, the abundance of *B. saida* was weakly and negatively correlated with dSRT ($r = -0.49$, $p < 0.01$, Fig. 6. 4. 4).

The total length of *B. saida* varied among areas. Larval *B. saida* captured south of St. Lawrence Island were larger (range 6.6–14.2 mm, mean 10.6 mm) compared with those captured in the Chukchi Sea (4.4–18.5 mm, 8.4 mm). The size of *B. saida* was positively and negatively correlated with F_{temp} and F_{sal}, respectively, but was not correlated with SST and SSS. Finally, smaller lengths of *B. saida* were associated with stations with a shorter dSRT and vice versa (Fig. 6. 4. 4).

The northern Bering Sea and Chukchi Sea are an area of high productivity with a short food web that supports a high benthic biomass, fishes, sea birds and marine mammals. Among the four groups of stations identified in this study, B. saida was the dominant indicator species only in group B, which was characterizes by cold/saline waters and occurred both south of St. Lawrence Island and to the north of 70°N. South of St. Lawrence Island, these properties reflect the presence of Anadyr waters with temperatures between −1.0 and 1.5°C and subsurface salinities between 32.5 and 33.5, which likely formed during the previous winter as a result of a polynya. North of 70°N, these water properties reflect the presence of Winter Water, which formed during the previous winter under the sea ice, with temperature < −1.4°C and salinities between 32.5 and 33.5. Conditions in both of these areas, characterized by polynya wate and WW, respectively, appear to provide a suitable environment for the growth of B. saida and supported high abundance of this species.

In the present study, B. saida were more abundant and smaller in the Chukchi Sea, where the sea ice retreated more recently (shorter dSRT). B. saida typically spawn under the sea ice, beginning under the ice cover and ending near the surface in ice-free areas after the ice cover has melted, and larvae hatch in areas recently cleared of ice. We conclude that spatial differences observed across the study region reflect the temporal changes in abundance and size at a given location following ice retreat. Also, the potential presence of two separate spawning area in the northern Bering and Chukchi Seas were suggested.

6. 5. Examinations of sea birds and sea mammals

Among the Arctic ecosystems, examinations of sea birds and mammals clarify not only their own ecosystem but also could assume distributions of feeding species such as zooplankton, bottom livings and fishes. The marine ecosystems of the Bering Sea and adjacent southern Chukchi Sea are experiencing rapid changes due to recent reduction in sea ice.

Migrating sea birds

Short-tailed shearwaters *Puffinus tenuirostris* is a trans-equatorial migrant, which breeds in southern Australia from October to March and visit this region in huge

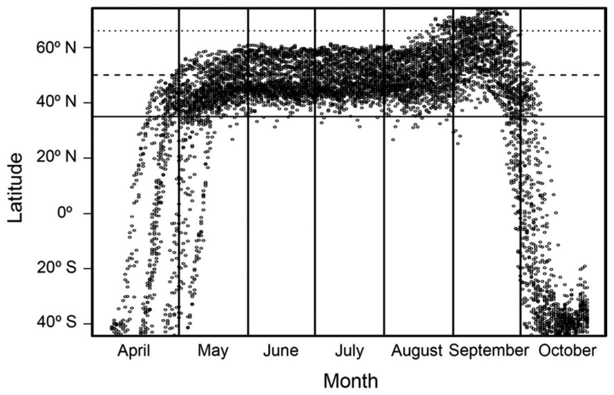

Fig. 6. 5. 1 Latitudinal movements of short-tailed shearwaters between the breeding colony (40°15'S) and the North Pacific during the non-breeding period (April–October) (Yamamoto et al., 2015).

number between boreal summer and autumn during non-breeding season, and represent one of the dominant top predators. To understand the implications for this species of ongoing environmental change in the Pacific sub-Arctic and Arctic seas, Yamamoto et al. (2015) tracked the migratory movements of 19 and 24 birds in 2010 and 2011, respectively, using light-level geolocators. Fieldwork was carried out on Great Dog Island (40°15'S, 148°15'E), Tasmania, Australia. 50 and 46 incubating short-tailed shearwaters in early December 2009 and 2010, respectively were captured and fitted Mk15 geolocation-immersion loggers (British Antarctic Survey, Cambridge, UK).

In both years, tracked birds occupied North Pacific, southeast Bering Sea, from May to July (Fig. 6. 5. 1). In August-September of 2010, but not 2011, a substantial portion (68% of the tracked individuals in 2010 compared to 38% in 2011) moved through the Bering Strait to feed in the Chukchi Sea. Based on the correlation with oceanographic variables, the probability of shearwater occurrence was highest in waters with sea surface temperatures (SSTs) of 8–10°C over shallow depths. Furthermore, shearwaters spent more time flying when SST was warmer than 9°C, suggesting increased search effort for prey.

We hypothesized that the northward shift in the distribution of shearwaters might have been related to temperature-driven changes in the abundance of their dominant prey, krill (*Euphasusacea*), as the timing of krill spawning coincides with the seasonal increase in water temperature. Hence, the expected future reduction in sea ice will possibly shift the distribution of shearwaters northwards. The movements of this species may therefore provide a useful indicator of wider ecosystem changes, especially in krill availability, in this region, unless other environmental changes associated with reduced sea ice result in a shift in diet or short-tailed shearwaters from krill to other types of prey. Given the huge numbers of shearwaters that migrate to this region, changes in the size or species composition of their diet, as well as in their foraging locations, may have a top-down influence on the abundance or distribution of their prey, with potentially major effects on energy transfer pathways in local marine ecosystems and on food web structure in general.

Diving sea birds

Subarctic environmental changes are expected to affect the foraging ecology of marine top predators, but the response to such changes may vary among species if they use food resources differently. Kokubun et al. (2016) examined the characteristics of foraging behavior of two sympatric congeneric diving sea bird: common murres (*Uria aalge*: hereafter COMUs) and thick-billed murres (*U. lomvia*: hereafter TBMUs) breeding on St. George Island, located in the seasonal sea ice region of the Bering Sea. They investigated their foraging trip and flight durations, diel patterns of dive depth, and underwater wing strokes, along with wing morphology and blood stable isotopic signatures and stress hormones.

Acceleration-temperature-depth loggers (ORI-380D3GT: housed in a cylindrical container, 12 mm diameter, 45 mm length, mass 10 g, Little Leonard, Tokyo, Japan) were attached to chick-guarding birds, and data were obtained from 7 COMUs and 12 TBMUs. Stable isotopic analyses, observation of prey delivered to chicks, and stress hormone analyses were used to examine interspecific differences in diet and consequent nutritional stress. We combine detailed foraging behavior, diet, and morphology to discuss how interspecific differences in the foraging behavior may affect the responses of two murre species to environmental change in the southeastern Bering Sea.

The data covered 14 and 21 foraging trips that included 64 and 79 dive bouts for COMUs and TBMUs, respectively. COMUs had smaller body mass (COMUs: 946±45 g; TBMUs: 1023±64 g), smaller wind area (COMUs: 0.053±0.007 m^2; TBMUs: 0.067±0.007 m^2), and greater wing loading than TBMUs (COMUs: 176±26 N m^{-2}; TBMUs: 151±20 N m^{-2}). There were no significant differences in these morphological parameters between

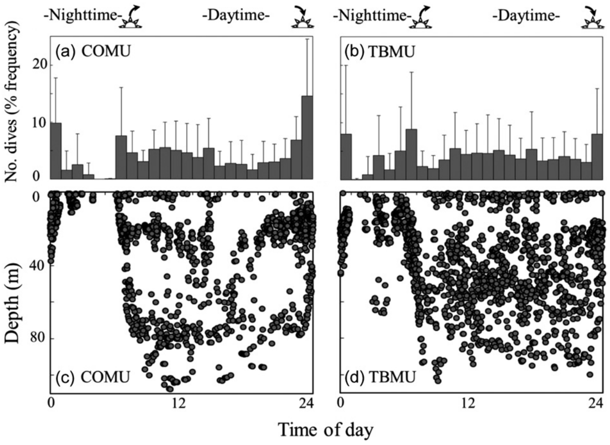

Fig. 6. 5. 2 (a, b) Frequency distribution and (c, d) depth distribution pattern of dives in relation to time of day. Left panels represent data for common murres (COMU) and right panels represent data of thick-billed murres (TNMU). Mean±standard deviation (SD) are shown in (a) and (b), calculated by individual bird data. The timing of sunrise and sunset is shown by marks on the top horizontal axis (Kokubun et al., 2016).

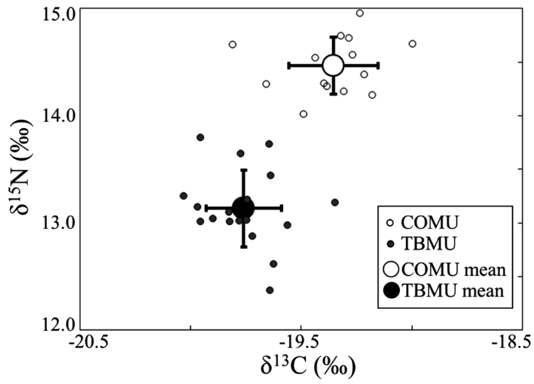

Fig. 6. 5. 3 Carbon (d13C) and nitrogen (d15N) stable isotope ration values of common murres (COMU: open circles) and thick-billed murres (TBMU: closed circles) measured in red blood cells. Smaller circles show individual data, and larger circles with error bars show means±standard deviation (SD) (Kokubun et al., 2016).

the sexes in either COMUs or TBMUs. Foraging duration, total flight duration and dive bout duration did not differ between COMUs and TBMUs. The maximum distance from the colony during foraging trips estimated by total flight duration was 42.6±21.1 km for COMUs and 38.1±21.9 km for TBMUs, respectively. With these small foraging ranges, both COMUs and TBMUs probably foraged on the continental shelf. The sea surface temperature (SST), where the dive bouts occurred, did not differ between COMUs and TBMUs. The temperature at depth (> 40 m) did not differ between COMUs and TBMUs. The thermocline depth and thermocline intensity did not differ between the species.

Both COMUs and TBMUs showed a diel diving pattern that indicated more dives with divergent depths in the daytime and fewer dives with shallow depths in the nighttime (Fig. 6. 5. 2). The portion of the daytime and nighttime dives did not differ between the species. During the daytime, birds dove to both shallow (< 40 m) and deep (> 40 m) depths in regard to the maximum thermocline depth. In the nighttime, both COMUs and TBMUs dove almost exclusively to shallow (< 40 m) depths. During the daytime, the shallow diving depth did not differ between the species. However, the deep diving depth was deeper for COMUs (74.2±8.7 m) compared to TBMUs (59.7±7.9 m). In the nighttime, the depth of shallow dives did not differ between the species. There were no significant differences between the sexes in either COMUs or TBMUs dive depths. The number of wing strokes during the bottom phase of day and night dives was higher in COMUs than TBMUs. The number of wing strokes during the dive descent phase did not differ between the species either in the daytime or the nighttime.

20 and 39 prey items were observed delivered by parent COMUs and TBMUs, respectively, to feed their chicks. The proportion of fishes was higher for COMUs compared to TBMUs. Conversely, the proportion of invertebrates for COMUs, was higher for TBMUs compared to COMUs.

The stable isotope analysis for red blood cells showed differences in the potential adult diet between the species. δ^{15}N was higher in COMUs than TBMUs (Fig. 6. 5. 3). δ^{13}C was also slightly higher for COMUs compared to TBMUs (Fig. 6. 5. 3). Based on the Bayesian mixing analysis for estimating potential food sources, COMUs were inferred to have fed on more fishes such as age-1 walleye Pollock and age-0 flounder, whereas TBMUs were inferred to have fed on more invertebrates such as euphausiids and squids.

The study investigated the fine-scale differences in foraging behavior between two closely related seabirds: common and thick-billed murres. Both species showed similar foraging ranges and diel patterns of diving (Fig. 6. 5. 3). Both species used similar thermal environments at sea, with no significant interspecific differences in SST, temperature at depth, thermocline depth and intensity. Thus the two species appeared to forage in similar stratified water masses, presumably in the middle- or outer-shelf domains around ST. George Island. However, despite similarities in geographic location, COMUs dove to deeper depths in the daytime and showed more frequent underwater wing strokes during dive bottom time, compared to TBMUs. In addition, COMUs used higher-trophic-level prey, presumably consisting of larger fishes such as age-1 walley Pollock, as estimated from SIAR models, whereas TBMUs used lower-trophic-level prey, which possibly includes squids and meso-zooplankton. Red blood cells reflect adult diet during incubation and early chick rearing.

This study was conducted during the chick-rearing period of both species, when the energy demands of parents are highest. High energy demand may force both COMUs and TBMUs to forage closer to the colony, compared to during incubation and post or pre-breeding periods. Potential foraging range and the diel patterns of diving were similar between COMUs and TBMUs at the study colony, which may reflect the necessity to guard chicks, along with the similar nest attendance patterns.

Reproductive success was similar between the species at the study colony in 2014 and it was higher than long-term averages (Mudge et al., 2015). This is supported by the relatively low level of stress hormones measured in our study birds, which suggests that the behavioral data shown in this study represent a year with favorable feeding conditions for both COMUs and TBMUs. In order for a clear prediction to be made regarding how these two species will respond to environmental change it would be necessary to determine whether the segregation patterns observed in this study persist in years with relatively unfavorable foraging conditions.

In conclusion, interspecific comparison of foraging behavior between closely related common and thick-billed murres in the Bering Sea showed both species foraged in similar foraging ranges with similar diel pattern of diving frequency. However, common murres dove to deeper depths below the thermocline (> 40 m) in the daytime, showed more frequent underwater wing strokes during the bottom phase of dives, and used higher-trophic-level prey, compared to thick-billed murres. Common murres have smaller wings, which potentially enable the pursuit of more mobile prey. These results suggest that common and thick-billed murres segregated prey species in relation to differences in their morphology. These differences in food resource use may lead to the differential responses of the two murre species to marine environmental changes in the Bering Sea.

References:

Bates, N. R., Mathis, J. T. and Cooper. L. W., 2009. Ocean acidification and biologically induced seasonality of carbonate mineral saturation states in the western Arctic Ocean. J. Geophys. Res., 114, C1107, doi: 10.1029/2008JC004862.

Fujiwara, A., Hirawake, T., Suzuki, K. and Saitoh, S.-I., 2011. Remote sensing of size structure of phytoplankton communities using optical properties of the Chukchi and Bering Sea shelf region. Biogeosciences, 8, 3567–3580, doi: 10.5194/bg-8-3567-2011.

Fujiwara, A., Hirawake, T., Suzuki, L., Imai and Saitoh, S.-I., 2014. Timing of sea ice retreat can alter phytoplankton community structure in the western Arctic Ocea. Biogeosciences, 11, 1705–1716, doi: 10.5194/bg-11-1705-2014.

Fujiwara, A., Hirawake, T., Suzuki, K., Eisner, L., Imai, I., Nishino, S., Kikuchi, T. and Saitoh, S.-I., 2016. Influence of timing of sea ice retreat on phytoplankton size during marginal ice zone bloom period on the Chukchi and Bering shelves. Biogeoscies, 13, 115–131, doi: 10.5194/bg-13-115-2016.

Grebmeier, J. M., Overland, J. E., Moore, S. E., Farley, E. V., Carmack. E. C., Cooper, L. W., Frey, K. E., Helle, J. H., McLaughlin, F. A. and McNutt, S. L., 2006. A major ecosystem shift in the northern Bering Sea. Science, 311, 1461–1464. Doi: 10.1126/science.1121365.

Grebmeier, J. M., 2012. Shifting patterns of life in the Pacific Arctic and Sub-Arctic Seas. Ann. Rev. Mar. Sci., 4, 63–78.

Hirawake, T., 2013. Cruise Report, Training Ship Oshoro Maru Cruise No. 255, Hokkaido University, Japan.

Hirawake, T., Takano. S., Horimoto, N., Ishimaru, T., Yamaguchi, Y. and Fukuchi, M., 2011. A phytoplankton absorption-based primary productivity absorption-based primary productivity model for remote sensing in the Southern Ocean. Polar Biol., 34, 291–302. Doi: 10.1007/s00300-010-0949-y.

Hirawake, T., Shinmyo, K., Fujiwara, A. and Saitoh, S., 2012. Satellite remote sensing of primary productivity in the Bering and Chukchi Seas using an absorption-based approach. ICES J. Marine Sci., 69, 1194–1204.

IPCC, 2013. Climate Change 2013: The Physical Science Basis, in Contribution of Working Group I to the Fifth Assessment Report of the Intergovernmental Panel on Climate Change.

Kikuchi, T., 2012. R/V Mirai Cruise Report MR 12-E03, JAMSTEC, Yokoska, Japan, http://www.jamstec.go.jp/darwin/e.

Kokubun, N., Yamaoto, T., Sato, N., Watanuki, Y., Will, A., Kitayasky, A. S. and Takahashi, A., 2016. Foraging segregation of two congeneric diving seabird species breeding on St. George Island, Bering Sea. Biogeosciences, 13, 2579–2591, doi: 10.5194/bg-13-2579-2016.

Kono, Y., Sasaki, H., Kurihara, Y., Fujiwara, A., Yamamoto, J. and Sakurai, Y., 2016. Distribution pattern of Polar cod (*Boreogadus saida*) larvae and larval fish assemblages in relation to oceanographic parameters in the northern Bering Sea and Chukchi Sea. Polar Biol., 39, 1039–1048. DOI 10.1007/s00300-016-1961-7.

Martin, J. et al., 2010. Prevalence, structure and properties of subsurface chlorophyll maxima in Canadian Arctic waters.

Mar. Ecol. –Prog. Ser., 412, 69–84, doi: 10.3354/meps08666.
Matsuno, K., Yamaguchi, A., Hirawake, T. and Imai, I., 2011. Year-to year changes of the mesozooplankton community in the Chukchi Sea during summers of 1991, 1992 and 2007, 2008. Polar Biol., 34, 1349–1360, doi: 10.1007/s00300-011-0988-z.
Matsuno, K., Yamaguchi, A., Fujiwara, A., Onodera, J., Watanabe, E., Imai, I., Chiba, S., Harada, N. and Kikuchi, T., 2014. Seasonal changes in mesozooplankton swimmers collected by sediment tap moored at a single station on the Northwind Abyssal Plain in the western Arctic Ocean. J. Plankton Res., 36, 490–502.
Matsuno, K., Yamaguchi, A., Hirawake, T., Nishino, S., Inoue, J. and Kikuchi, T., 2015. Reproductive success of Pacific copepods in the Arctic Ocean and the possibility of changes in the Arctic ecosystem. Polar Biol., 38, 1075–1079, DOI 10.1007/s00300-015-1658-3.
Miller, C. B., Frost, B. W., Batchelder, H. P. et al., 1984. Life histories of large, grazing copepods in the subarctic ocean gyre: *Neocalanus plumchrus*, *Neocalanus cristatus* and *Eucalanus bungii* in the Northeast Pacific. Prog. Oceanogr., 13, 201–243.
Mudge, M. L., Pietrzak, K. W., Drummond, B. A. and Romano, M. D., 2015. Biological monitoring at St. George Island, Alaska, in 2014. US Fish and Wildl. Ser. Rep., AMNWR 2015/02. Homer, Alaska.
Nakano, T., Matsuno, K., Nishizawa, B., Iwahara, Y., Mitani, Y., Yamamoto, J., Sakurai, Y. and Watanuki, Y., 2016. Diets and body condition of polar cod (*Boreogadus saida*) in the northern Bering Sea and Chukchi Sea. Polar Biol., 39, 1081–1086, DOI 10.1007/s00300-015-1769-x.
Nishino, S., Kikuchi, T., Fujiwara, A., Hirawake, T. and Aoyama, M., 2016. Water mass characteristics and their temporal changes in a biological hotspot in the southern Chukchi Sea. Biogeosci., 13, 2563–2578, doi: 10.5194/bg-13-2563-2016.
Orr, J. X., Fabry, V. J., Aumont et al., 2005. Anthropogenic ocean acidification over the twenty-first centry and its impact on calcifying organisms. Nature, 437, 681–686.
Saito, H., Tsuda, A., 2000. Egg production and early development of the subarctic copepods *Neocalanus cristatus*, *N. plumchrus* and *N. flemingeri*. Deep-Sea Res I 47, 2141–2158.
Seiler, D. and Brandt, A., 1997. Seasonal occurrence of plankton Crustacea in sediment trap samples at three depth horizons in the Greenland Sea. Polar Biol., 17, 337–349.
Vidussi, F., Roy, S., Lovejoy, C., Gammelgaard, M., Thomesen, H. a., Booth, B., Tremblay, J. -E. and Mostajir, B., 2004. Spatial and temporal variability of the phytoplankton community structure in the North Water Polynya, investigated using pigment biomarkers. Can. J. Fish. Aquat. Sci., 61, 2038–2052.
Yamaguchi, A. and Ikeda, T., 2000. Vertical distribution, life cycle, and body allometry of two oceanic calanoid copepods (*Pleuromamma scutullata* and *Heterorhabdus tanneri*) in the Oyashio region, western North Pacific Ocean. J. Plankton Res., 22, 29–46.
Yamamoto, T., Hoshina, K., Nishizawa, B., Meathrel, C. E., Phillips, R. A. and Watanuki, Y., 2015. Annual and seasonal movements of migrating short-tailed shearwaters reflect environmental variation in sub-Arctic and Arctic waters. Mar. Biol., 162, 413–424, DOI 10.1007/s00227-014-2589-1.
Yamamoto-Kawai, M., McLaughlin, F. A., Carmack, E. C., Nishimo, S. and Shimada, K., 2009. Aragonite undessaturation in the Arctic Ocean: effects of oceanic acidification and sea ice melt. Science, 326, 1098–1100.
Yamamoto-Kawai, M., McLaughlin, F. A. and Carmack, E. C., 2011. Effects of ocean acidification of the Canada Basin surface water. Geophys. Res. Lett., 38, L03601, doi: 10.1029/2010GL045501.
Yamamoto-Kawai, M., McLaughlin, F. and Carmack, E., 2013. Ocean acidification in the three oceans surrounding northern North America. J. Geophys. Res., 118, 6274–6284, doi: 10.1002/2013JC009157.
Yamamoto-Kawai, M., Mifune, T. Kikuchi, T. and Nishino, S., 2016. Seasonal variation of CaCO3 saturation state in bottom water of a biological hotspot in the Chukchi Sea, Arctic Ocean. Biogeosci. 13, 6155–6169, doi: 10.5194/bg-13-6155-2016.

7. Global Influences

As for the strategic target 2, Modeling Theme, Terrestrial Theme, Atmosphere Theme, Glaciology Theme, Greenhouse Gas Theme and Sea Ice Theme joined together to work on the aim of "understanding the Arctic system for global climate and future change".

7. 1. Greenhouse gas cycle and its climatic response

In order to clarify global influences of Arctic change, it is indispensable to improve the prediction of future greenhouse gas (GHG) concentrations. In this direction, it is needed to understand variation of sink and source of greenhouse gases depending on climate and environmental change. To this objective, behaviors of GHGs were observed in the network shown in Fig. 7.1.1, through ground surface, airborne and ship based measurements. Based on these observation data, source and sink of GHG in the Arctic were analyzed using high resolution atmospheric chemistry transport models. Discussions of carbon cycles together with biospheric changes are reported in Section a. Additionally, temporal variation of sink and source of GHG and climatic response of GHG sources were discovered from the shallow ice core and firn air analysis.

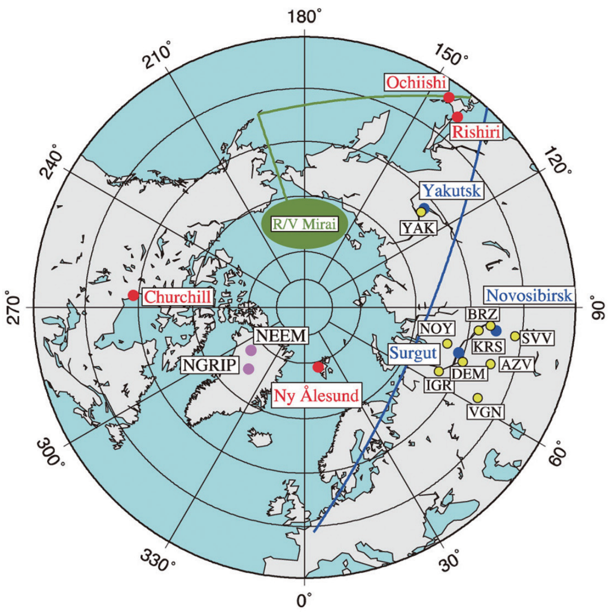

Fig. 7. 1. 1 Pan Arctic observation network for GHGs constructed in this project. Red dots are surface based stations, yellow dots tower site, and blue dots small airplane sites. Blue line shows line of commercial flight with GHG observations, green line and green area is of Mirai cruise, and purple dots for ice core drilling and firn air sampling sites, all referred in this section.

Surface based observations of CO_2

Several species of GHGs already have been measured for a long term. At the main Japanese Arctic observatory, Ny-Ålesund, Svalbard, atmospheric concentrations of CO_2, CH_4 and stable isotopes have been continuously measured by flask sampling since early 1990s (Yamanouchi et al., 1996; Morimot et al., 2006). During the GRENE Arctic, also the continuous measurements of CO_2 and oxygen (O_2), $\delta(O_2/N_2)$, has been started.

O_2 and CO_2 exchange at photosynthesis or respiration, but they are exchanged independently at the sea surface. From these relations, we could obtain information as for the ocean and terrestrial biosphere sinks, respectively. From the concentration changes of CO_2 (ΔCO_2) and O_2 (ΔO_2), absorption of CO_2 by terrestrial biosphere (B) and ocean uptake (O) are shown with exhaust from fossil fuel, F,

$$\Delta CO_2 = F - B - O \quad (7.1.1)$$
$$\Delta O_2 = -1.4\,F + 1.1\,B - Z, \quad (7.1.2)$$

here Z is a net release of O_2 from the ocean. From both equations, absorption by terrestrial biosphere B and ocean uptake O could be calculated as follows,

$$O = (-0.3F - \Delta O_2 - 1.1\Delta CO_2 - Z) \quad (7.1.3)$$
$$B = F - \Delta CO_2 - O. \quad (7.1.4)$$

Manning and Keeling (2006) defined the atmospheric potential oxygen APO as eq. (7.1.5), then O could be shown as eq. (7.1.6).

$$APO = [O_2] + 1.1[CO_2], \quad (7.1.5)$$
$$O = (-1.3F - \Delta APO - Z)/\,1.1 \quad (7.1.6)$$

From the observations at Ny-Ålesund and Syowa station, Antarctica, Ishidoya et al. (2012) estimated the average CO_2 uptake during the period 2001–2009, as shown in Fig. 7.1.2, to be 2.9±0.7 and 0.8±0.9 Gt C yr^{-1} for the ocean and terrestrial biosphere, respectively. By excluding the influence of El Nino around 2002–2003, the terrestrial biospheric uptake for the period 2004–2009 increased to 1.5±0.9 Gt C yr^{-1}, while the oceanic uptake decreased slightly to 2.8±0.8 Gt C yr^{-1}.

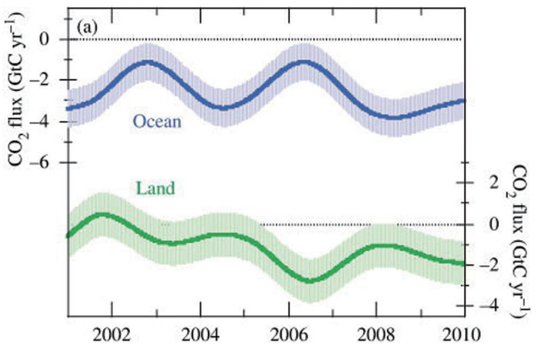

Fig. 7. 1. 2 Interannual variations of the oceanic and terrestrial biospheric CO_2 uptake estimated using the average increase rate of APO observed at Ny-Ålesund and Syowa. Shades around solid lines with Ocean and Land represent uncertainties of their values (Ishidoya et al., 2012).

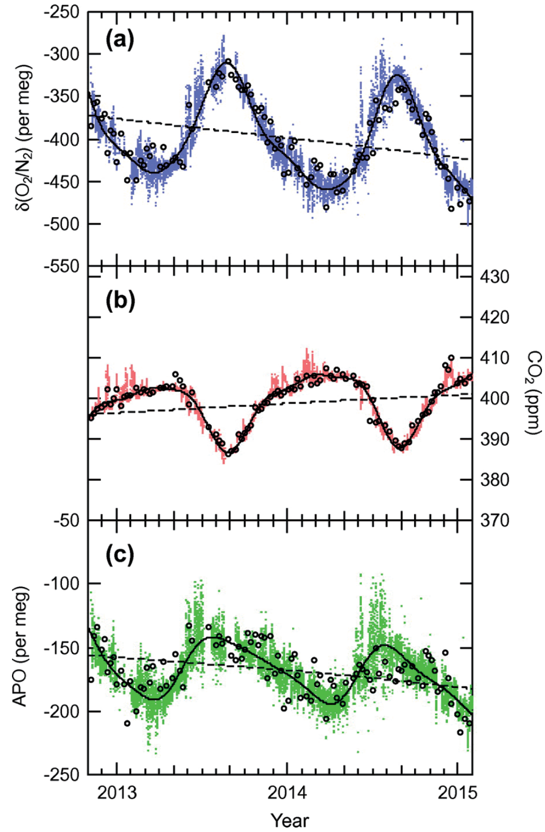

Fig. 7. 1. 3 Temporal variations in (a) $\delta(O_2/N_2)$, (b) CO_2 and (c) APO observed at Ny-Ålesund from November 2012 to January 2015. Cots, solid lines and dashed lines represent hourly mean values, the best fit curve, and the long-term trend, respectively. The results obtained from discrete flasksampling measurements (Ishidoya et al., 2012) are shown by an open circles, The vertical axis of APO is scaled 1.5 times compared to that of $\delta(O_2/N_2)$ (Goto et al., 2017a).

In order to contribute to a better understanding of the global carbon cycle, Goto et al. (2013a) developed a high precision continuous measurement system for atmospheric O_2/N_2 ratio using a fuel cell oxygen analyzer. To obtain highly precise values of the atmospheric O_2/N_2 ratio, pressure fluctuations of the sample and standard air were reduced to within ±0.005 Pa, with temperatures stabilized to 32±0.1°C. The analytical precision of the system was estimated to be 1.4 per meg for 24-minutes measurement as the standard deviation of replicate analyses of the same sample air. Using the new system, they initiated a systematic observation of the atmospheric O_2/N_2 ratio as a test case, and the measurements clearly showed seasonal and diurnal cycles, along with short-term variations on time scales of several hours to several days, caused by terrestrial biospheric and human activities.

Goto et al. (2013b) installed a similar system with a consideration of remote measurements, at Ny-Ålesund, Svalbard and started systematic observation on November 2012. From the continuous observations of CO_2 and $\delta(O_2/N_2)$ conducted using the system, two year data were obtained and discussed by Goto et al. (2017a). Fig. 7.1.3 shows hourly mean values of atmospheric $\delta(O_2/N_2)$, CO_2 mole fraction and APO. The best-fit curves and long-term trends were obtained by applying digital filtering technique to the daily mean values. The $\delta(O_2/N_2)$ and CO_2 mole fraction decreased and increased secularly, and varied seasonally in opposite phase each other. The APO showed not only a secular decrease, but also a seasonal cycle that was almost in phase with that of $\delta(O_2/N_2)$. The results reported by Ishidoya et al. (2012) from mass spectrometry analyses of weekly flask air samples are also presented in Fig. 7.1.3. The daily mean values of $\delta(O_2/N_2)$ calculated from this observation were compared with values reported by Ishidoya et al. (2012), and found that continuous measured data were slightly higher than flask sampling data by 0.27±14.48 per meg, and both were correlated (correlation coefficient was 0.95).

The continuous measurements revealed short-term fluctuations, which were not detected by discrete flask sampling (Goto et al., 2017a). During May–June 2013, large irregular variation in APO was seen. If these fluctuations occurred in association with terrestrial biospheric activity, the amplitudes of $\delta(O_2/N_2)$ and CO_2 fluctuations were expected to be nearly equal, since the exchange ratio, $-O_2/CO_2$, is 1.1 (Keeling and Manning, 2014). However, the observational results indicated that the CO_2 mole fraction showed much smaller amplitudes (Fig. 7.1.3), suggesting that the fluctuations were more likely to be affected by oceanic process than by terrestrial biosphere process. From trajectory analysis to determine the origin of short-term APO variations, it was shown that the high APO values are observed when air masses

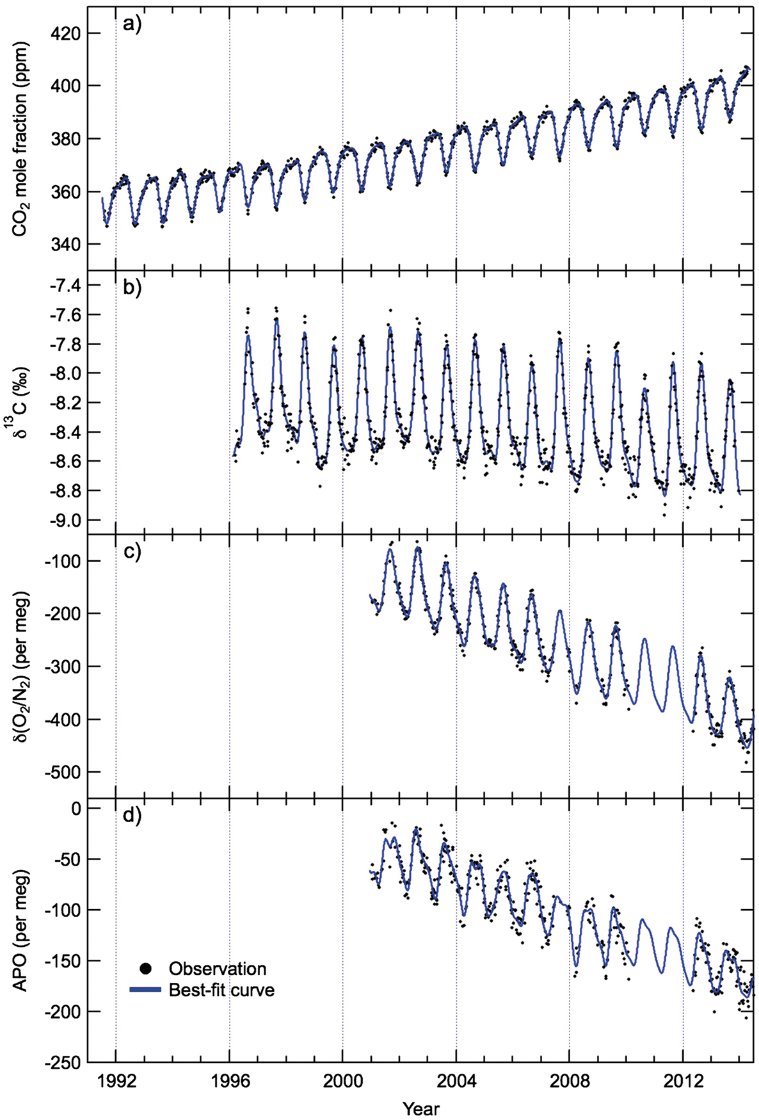

Fig. 7. 1. 4 Temporal variations of the atmospheric (a) CO_2 mole fraction, (b) d13C, (c) $\delta(O_2/N_2)$, and (d) APO observed at Ny-Ålesund, Svalbard. The dots and solid lines represent the observed values and their best fit curves, respectively (Goto et al., 2017b).

arrived at Ny-Ålesund after passing over the seas on the south side of the Svalbard Islands, while most of low or stable APO values are observed when the air arrived from the ice-covered Arctic Ocean. Moreover, the south side ocean area was of high marine net primary production (NPP). These continuous observations of atmospheric $\delta(O_2/N_2)$ and CO_2 mole fraction could play an important role in detecting possible changes in the carbon cycle in the near future.

Systematic observations of CO_2 mole fraction (Yamanouchi et al., 1996), the isotopic ratio $\delta^{13}C$ of CO_2 (Morimoto et al., 2001), and oxygen to nitrogen ratio ($\delta(O_2/N_2)$) in the atmosphere (Ishidoya et al., 2012) have been carried out at Ny-Ålesund, Svalbard since 1991, 1996 and 2001, respectively. Fig. 7.1.4 shows temporal variations of the observed CO_2 mole fraction, $\delta^{13}C$, $\delta(O_2/N_2)$ and APO. The CO_2 mole fraction shows a clear seasonal cycle superimposed on a secular increase with an average rate of 2.0 ppm yr^{-1} for the period of 1996–2013. On the other hand, $\delta^{13}C$ and $\delta(O_2/N_2)$ decrease secularly at an average rate of –0.020‰ yr^{-1} for 1996–2013 and –19.9 per meg yr^{-1} for 2001–2013, respectively. Secular trends and rates of increase of the CO_2 mole fraction, $\delta^{13}C$, $\delta(O_2/N_2)$, and APO are shown in Fig. 7.1.5. The CO_2 mole fraction and d13C were also observed at Alert (82.45°N, 62.51°E), Mauna Loa (19.54°N, 155.58°W), and the South Pole (89.98°S, 24.80°W) by NOAA/ESRL GMD (Dulgokencky et al., 2016; White et al., 2015). Measurements of $\delta(O_2/N_2)$ and CO_2 were also conducted by the Scripps O_2 program (http://scrippso2.ucsd.edu) (Keeling and Manning, 2014) at the three sites. The rates of increase obtained from these observations are compared in Table 7.1.1 with these results. The rates of increase of CO_2 and APO are very close to the values at Ny-Ålesund.

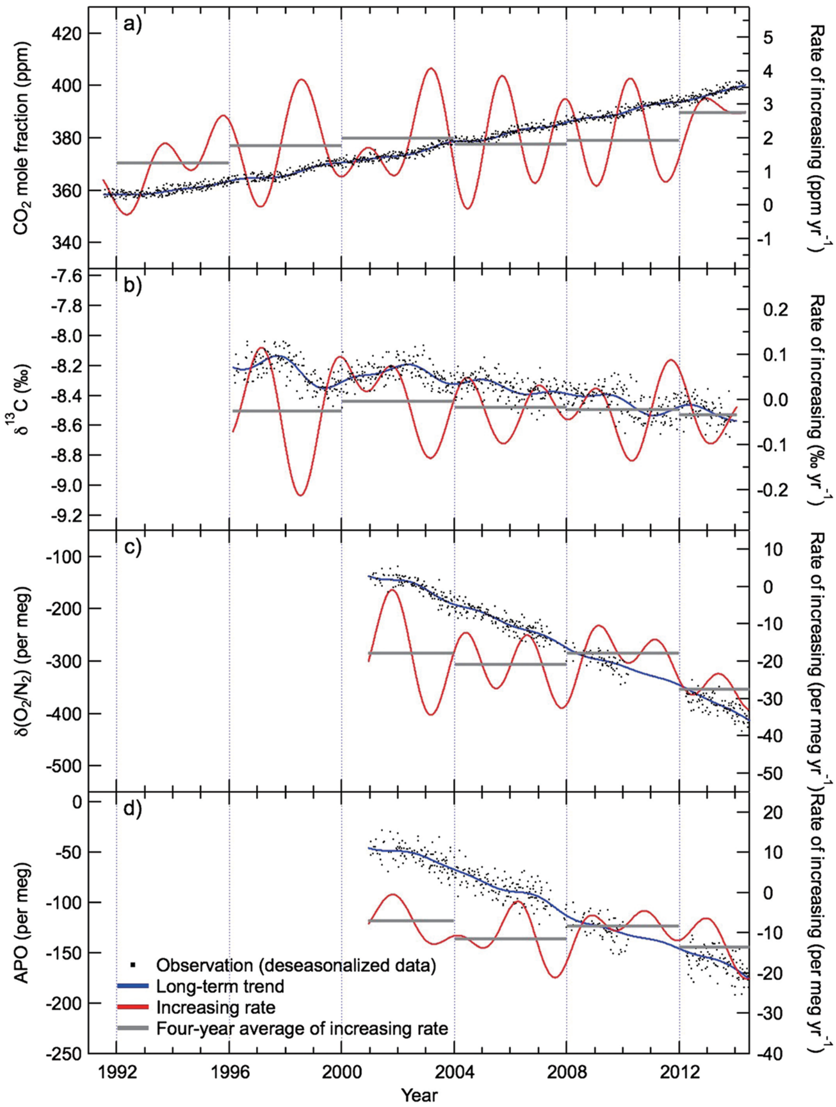

Fig. 7. 1. 5 Secular trends and rates of increase of (a) the atmospheric CO_2 mole fraction, (b) d13C, (c) $\delta(O_2/N_2)$, and (d) APO observed at Ny-Ålesund. The dots, blue solid lines, and red solid lines represent seasonally adjusted observed values, long-term trends, and rates of increase, respectively. Four-year mean values of the respective rates of increase are also shown as gray solid horizontal bars (Goto et al., 2017b).

Table 7. 1. 1 Average rates of increase of the atmospheric CO_2 mole fraction, $\delta^{13}C$, $\delta(O_2/N_2)$, and APO observed at Ny-Ålesund, Alert, Mauna Loa, and the South Pole for the respective periods (Goto et al., 2017b).

			Average Rates of Increase		
Site	Location	CO_2 (ppm yr^{-1}) 1996–2013	$\delta^{13}C$ (ppm yr^{-1}) 1996–2013	$\delta(O_2/N_2)$ (per meg yr^{-1}) 2001–2013	APO (per meg yr^{-1}) 2001–2013
Ny-Ålesund	78.92°N, 11.93°E	1.99 ± 0.02[a]	−0.020 ± 0.002[a]	−19.9 ± 0.3[a]	−10.1 ± 0.3[a]
Alert	82.45°N, 62.51°E	1.95 ± 0.01[b]	−0.024 ± 0.001[c]	−20.2 ± 0.2[d]	−10.6 ± 0.2[d]
Mauna Loa	19.54°N, 155.58°W	1.97 ± 0.01[b]	−0.025 ± 0.001[c]	−20.5 ± 0.2[d]	−10.9 ± 0.2[d]
South Pole	89.98°S, 24.80°W	2.01 ± 0.01[b]	−0.024 ± 0.001[c]	−20.7 ± 0.2[d]	−10.7 ± 0.2[d]

[a]Values obtained in this study.
[b]Based on the NOAA/ESRL GMD data [*Dlugokencky et al.*, 2016].
[c]Based on the NOAA/ESRL GMD data [*White et al.*, 2015].
[d]Based on the Scripps O_2 program data (http://scrippso2.ucsd.edu) [*Keeling and Manning*, 2014].

This suggests that their secular trends observed at Ny-Ålesund for the respective variables are representative of the global averages. On the other hand, the rate of increase in $\delta^{13}C$ observed at Ny-Ålesund is clearly larger than those obtained by NOAA/ESRL GMD. The reason why such a discrepancy exists is not clear at the moment.

Goto et al. (2017b) also estimated globally averaged terrestrial biospheric and oceanic CO_2 uptakes employing two kinds of approach, one using APO and the CO_2 mole fraction (the APO method) and the other using $\delta^{13}C$ and

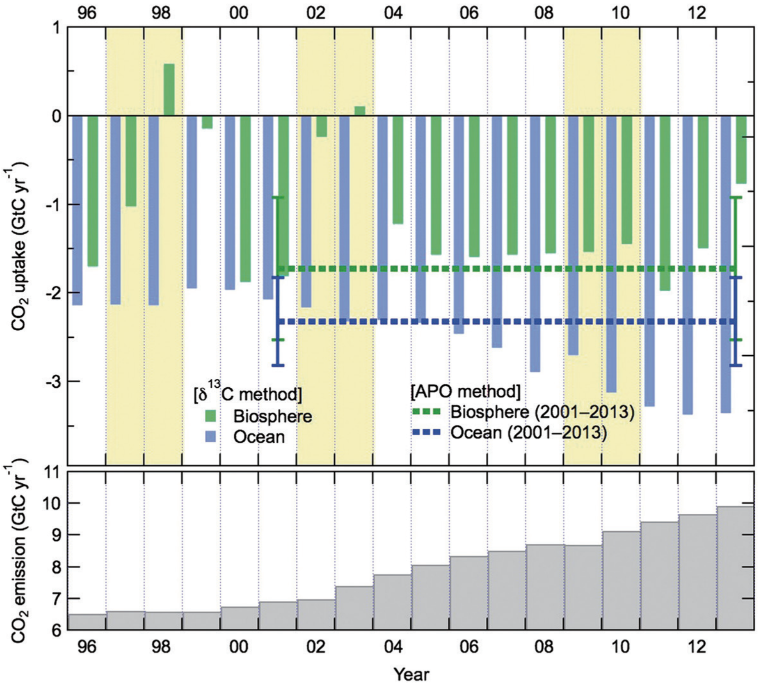

Fig. 7. 1. 6 (top) Terrestrial biospheric and oceanic CO_2 uptakes estimated using δ^{13}C method and the APO method for the respective periods of 1996–2013 and 2001–13. The yellow shaded periods represent El Nino years. (bottom) Annual CO_2 emissions from 1996 to 2013, taken from the statistical data of the Carbon Dioxide Information Analysis Center (CDIAC) (Boden et al., 2016), are slso shown (Goto et al., 2017b).

CO_2 (the δ^{13}C method), under the assumption that the secular trends and the interannual variations of the related variables at Ny-Ålesund are representative of their global averages, as indicated in the previous section. The average terrestrial biospheric and oceanic CO_2 uptakes were estimated to be 1.6±0.8 and 2.3±0.5 GtC yr^{-1} for the period of 2001–2013. As seen in Fig. 7.1.6, the terrestrial biosphere shows larger year-to-year variations in the CO_2 uptake than the ocean does. For example, the biospheric CO_2 uptake is close to zero for the periods of 1997–98 and 2002–03 when the El Nino event occurred. However, the terrestrial biospheric CO_2 uptake in 2009/10 is not so different from the values in adjacent years, though the El Nino event occurred in this period. To better understand the relationship between climate change and the CO_2 budget on the Earth's surface, further studies are needed. As seen in Fig. 7.1.6, the interannual variation in the oceanic CO_2 uptake is relatively small, but the CO_2 uptake increases gradually with time for the period covered by tis study. Since a rapid growth of the atmospheric CO_2 mole fraction by anthropogenic CO_2 emissions increases the CO_2 partial pressure difference (pCO_2) between the atmosphere and the ocean, it is expected that the oceanic CO_2 uptake is steadily enhanced. Some precious studies also reported that the oceanic CO_2 uptake had been increasing in recent years (Iida et al., 2015; Le Quere et al., 2016). To better understand the impact of climate change on the global carbon cycle, it is crucial to monitor changes in the terrestrial biospheric and oceanic uptake of anthropogenic CO_2 for a long time.

Surface based observations of methane

Atmospheric CH_4 is one of the most important gases for the atmospheric greenhouse effect and the atmospheric chemistry. To predict future climate change more precisely, characterizing variations in the CH_4 sources and sinks and their response to climate variability is indispensable. Systematic observations of the CH_4 mole fraction and its carbon isotope ratio (δ^{13}C) has been conducted at Ny-Ålesund, Svalbard using air samples collected weekly since 1991 and 1996, respectively (Morimoto et al., 2006, 2009). Here, Morimoto et al. (2017) presented long-term variations of the CH_4 mole fraction and δ^{13}C at Ny-Ålesund until the end of 2013 and discussed the causes of the atmospheric CH_4 variations based on the δ^{13}C data. Fig. 7.1.7a and b show the CH_4 mole fractions and δ^{13}C values observed at Ny-Ålesund, respectively, along with their best-fit curves and long-term trends, obtained by using a digital filtering technique. In the curve fitting procedure, the cut-off period of the low-pass filter was set to four months to derive the best-fit curves to the data and to five years to extract the long-term trends. As seen

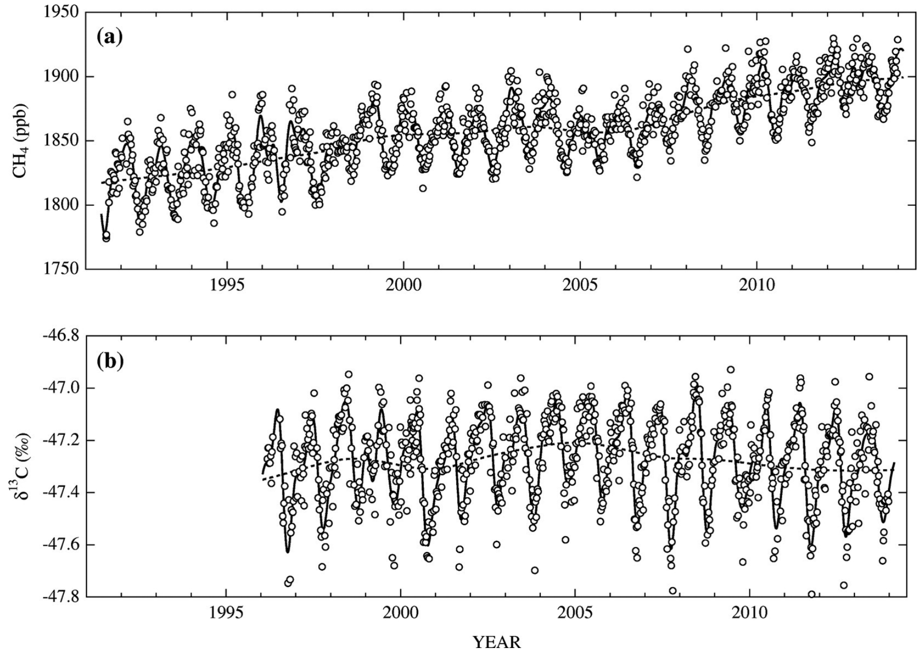

Fig. 7. 1. 7 Temporal variations of the CH_4 mole fraction (a) and $\delta^{13}C$ of CH_4 (b) observed at Ny-Ålesund, Svalbard. Also shown are their best-fit curves (solid lines) and long-term trends (broken lines) (Morimoto et al., 2017).

in the figures, the CH_4 mole fraction and $\delta^{13}C$ showed clear seasonal cycles superimposed on the long-term trends. Average peak-to-peak amplitudes of the CH_4 and $\delta^{13}C$ seasonal cycles were 45 ppb and 0.44‰, respectively. The amplitudes and seasonal phase are similar to those previously reported (Morimoto et al., 2006). The CH_4 mole fraction increased from 1991 to 2000, stagnated until around 2006, and then resumed increasing at a similar rate as the 1990s after 2006. Such a stepwise CH_4 increase has also been observed around the world (Rigby et al., 2008; Dlugokencky et al., 2009). On the other hand, $\delta^{13}C$ observed at Ny-Ålesund showed a continuous increase from 1996 to around 2006 and a decrease afterwards, with smaller temporal variability than at Alert (White et al., 2015). By comparing the rates of change in the CH_4 mole fraction and $\delta^{13}C$ under the assumption that the atmospheric CH_4 lifetime is constant, it is suggested that the temporal pause of the CH_4 mole fraction observed at Ny-Ålesund is attributed to reductions of CH_4 release from the microbial and fossil fuel sectors. On the other hand, the increase in CH_4 after 2006 could be ascribed to an increase in microbial CH_4 release. The CH_4 and $\delta^{13}C$ data presented in this paper would be useful for clarifying their temporal variations in the Arctic atmosphere, as well as providing additional constraints on the global CH_4 budget.

Fujita et al. (2018) conducted simultaneous measurements of the mole fraction and carbon and hydrogen isotope ratios ($\delta^{13}C$ and δD) of atmospheric methane (CH_4) at Churchill (58°44’N, 93°49’W) in the northern part of the Hudson Bay Lowlands (HBL), Canada, since 2007, under the cooperation between National Institute of Polar Research (NIPR), Tohoku University (TU) and Environment and Climate Change Canada (ECCC). HBL, the second largest continuous wetland in the world, is an important natural CH_4 source region in northern latitudes. Nevertheless, there still remains a large uncertainty in magnitude, seasonality, and spatial distribution of CH_4 emissions in the HBL. In addition to the regional influence, the HBL area is also affected to some extent by anthropogenic CH_4 released in Europe and boreal Asia due to long-range air transport, especially in winter. There may also be large anthropogenic CH_4 sources in Alberta located to the west of the HBL in association with natural gas production. Churchill is a small port city on the western shore of Hudson Bay with a population of about 900. The land cover around Churchill is mainly characterized by the Arctic tundra and the boreal forest. Air samples were taken from an intake mounted at the top of a 60-m high tower in the Churchill Northern Studies Centre (https://www.churchillscience.ca/), located 23 km east of the town of Churchill. Each air sample was automatically collected twice a week into a 2-L Pyrex glass flask. The collected samples with a dew point of around −60°C were first analyzed at ECCC for mole fractions of various trace gases such as CO_2, CH_4, CO, N_2O, and SF_6

and then transported to NIPR, Japan, for isotope analyses of atmospheric CH_4. At NIPR, each sample was divided into four glass flasks, two for the analysis of $\delta^{13}C$ at NIPR and two for δD at TU. To interpret temporal variations of CH_4 in the atmosphere at Churchill and to estimate CH_4 emissions from the HBL, forward simulations of atmospheric CH_4 mole fraction were conducted for 2007–2013 using the CCSR/NIES/FRCGC (Center for Climate System Research/National Institute for Environmental Studies/Frontier Research Center for Global Change) AGCM-based Chemistry Transport Model (ACTM) developed at JAMSTEC (Japan Agency for Marine-Earth Science and Technology), with the setup described in Patra et al. (2016).

Compared with the measurements at an Arctic baseline monitoring station, Ny-Ålesund, Svalbard, CH_4 mole fraction is generally higher and $\delta^{13}C$ and δD are lower at Churchill due to regional biogenic CH_4 emissions. As seen in Fig. 7.1.8, the CH_4 mole fraction at Churchill shows a clear seasonal cycle with a prominent minimum in June–July and a broad maximum in late winter. Similar characteristics are also observed at Ny-Ålesund. However, there are noticeable differences between the CH4 variations at Churchill and Ny-Ålesund: (1) the annual mean CH_4 mole fraction is higher by 3–16 ppb at Churchill than at Ny-Ålesund for 2007–2013, and (2) the timing of the seasonal CH_4 minimum is earlier by about 1 week, on average, at Churchill than at Ny-Ålesund (Fig. 7.1.8a). A clear seasonal cycle is also observed in $\delta^{13}C$ and δD at Churchill and Ny-Ålesund, showing the maximum in early summer and the minimum in autumn. From inspection of the observation data at the two sites, it is obvious that (1) the annual means are lower by 0.1–0.2‰ for $\delta^{13}C$ and 1–4‰ for δD at Churchill than at Ny-Ålesund, and (2) the average seasonal maxima of $\delta^{13}C$ and δD at Churchill precede those at Ny-Ålesund by about 2–3 weeks (Fig. 7.1.8b and c). The differences in annual mean CH_4, $\delta^{13}C$, and δD between the two sites suggest that Churchill is more strongly affected by biogenic CH_4 sources with low $\delta^{13}C$ and δD than Ny-Ålesund.

To examine the contributions of biogenic, fossil fuel, and biomass burning CH_4 sources to the observed seasonal CH_4 cycle at Churchill and NyÅlesund, a simple one-box model was employed. The respective isotopic signatures of biogenic (BIO), fossil fuel (FF), and biomass burning (BB) sources were assumed to be −61.7 ±6.2 (±1σ), −44.8±10.7, and −26.2±4.8‰ for $\delta^{13}C$ and

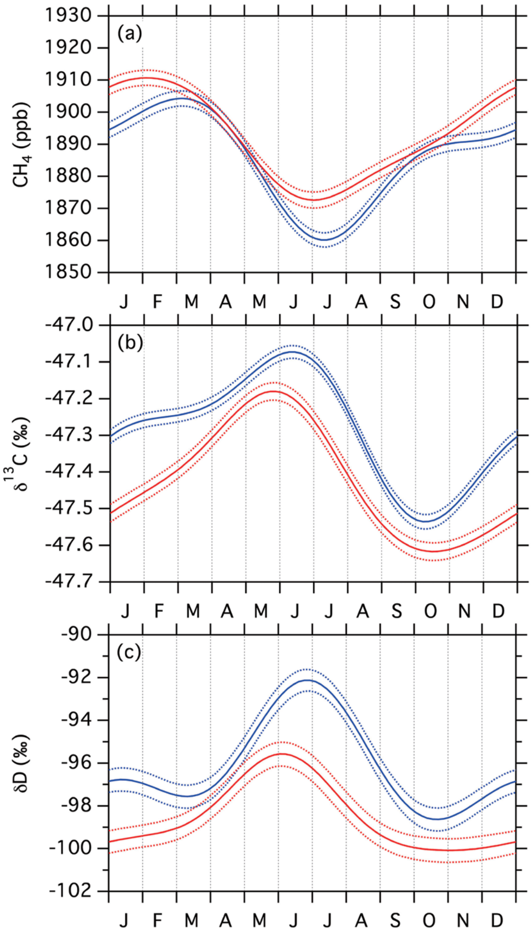

Fig. 7. 1. 8 Average seasonal cycles of (a) the CH_4 mole fraction, (b) $\delta^{13}C$, and (c) δD observed at Churchill (red lines) and Ny-Ålesund (blue lines) for 2007–2013. Dotted lines represent the 95 percentile bootstrap confidence intervals (see text). Each average seasonal cycle is plotted after adding its average value for 2007–2013 (Fujita et al., 2018).

−317±33, −197±51, and −211±15‰ for δD (Sherwood et al., 2017). Fig. 7.1.9a and b show the calculated monthly contributions of individual CH_4 sources (S_{BIO}, S_{FF}, S_{BB}) for Churchill and Ny-Ålesund, respectively, together with those of CH_4 destruction by OH. As seen in Fig. 7.1.9, biogenic sources of CH_4 are the most dominant ones for the seasonal cycle of atmospheric CH_4 observed at Churchill and NyÅlesund, with large contributions in summer. This source would be boreal wetlands, since there is a vast amount of wetlands (e.g., bogs, fens, and tundra) in northern high latitudes from which a large quantity of CH_4 is released, showing a strong seasonal variation unlike anthropogenic biogenic CH_4 (e.g., ruminants, landfills, and waste). The biogenic CH_4 contribution at Churchill begins in May, reaches a maximum in July, and then ceases in November (Fig. 7.1.9a). This seasonality is probably associated with soil temperature rise and snow melting, the highest soil temperature, and

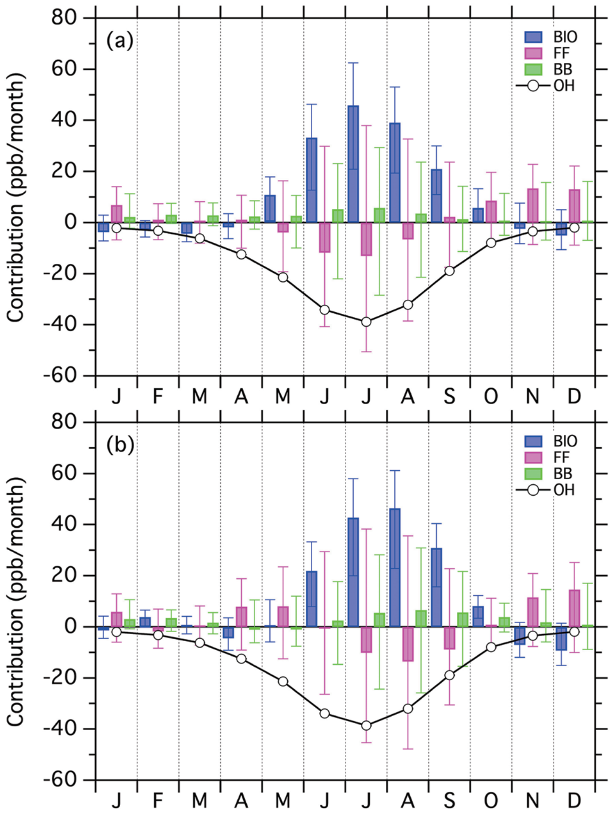

Fig.7. 1. 9 Monthly contributions of biogenic (BIO), fossil fuel (FF), and biomass burning (BB) CH_4 sources to the seasonal CH_4 cycle estimated using the one-box model for (a) Churchill and (b) Ny-Ålesund. Error bars denote the 68 percentile confidence intervals derived by the Monte Carlo method with 5000 pseudo time series. Open circles connected with line are the monthly values of CH_4 destruction by OH (Fujita et al., 2018).

low surface temperatures and snow cover in the respective months. Seasonal variations of the contribution of biogenic CH_4 estimated for Churchill and Ny-Ålesund are slightly different from each other (Fig. 7.1.9a and b). For example, the biogenic CH_4 is discernible at Churchill in May, but there is no appearance of such a contribution at Ny-Ålesund. Moreover, the seasonal maximum of the biogenic CH_4 contribution appears in July at Churchill and in August at Ny-Ålesund. This difference is presumably attributable to the influence of local/regional wetland CH4 emissions on Churchill and to different latitudes of the two sites. Churchill is located on the northern perimeter of the HBL; thus, CH_4 emitted from HBL wetlands could directly affect the CH_4 mole fraction at Churchill. On the other hand, since Ny-Ålesund is far from strong CH_4 sources, seasonal signals of CH_4 emissions from boreal wetlands may reach the site with a time lag. It is also noteworthy that the onset of wetland CH_4 emissions is earlier at lower latitudes due to the latitude-dependent seasonal temperature pattern.

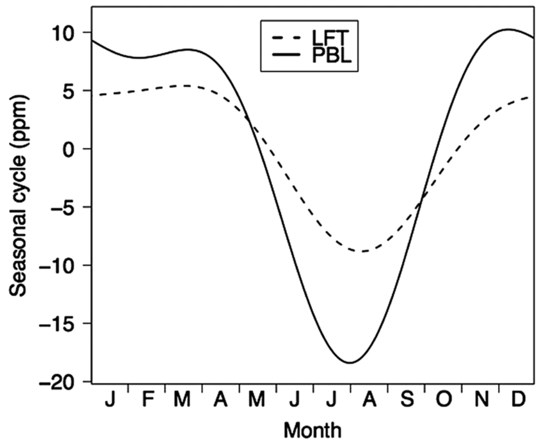

Fig. 7. 1. 10 Seasonal cycle in mean CO_2 concentrations in the PBL (solid line) and LFT (dashed line) from aircraft observations (Sasakawa et al., 2013).

Airborne observations of GHGs in the atmosphere

Siberia, in northern Eurasia, contains large quantities of plant biomass and soil organic carbon, making it one of the largest carbon reservoirs in the world. Accurate estimates of carbon fluxes in Siberia are therefore essential both for understanding global and regional carbon cycles and for predicting future changes in the Siberian carbon cycle. Inverse modeling using atmospheric transport models and atmospheric CO_2 observations can be effective for estimating regional and global carbon fluxes from limited atmospheric observations, and this approach has been successful in deriving reasonable carbon fluxes for most land and ocean areas. However, the available CO_2 observations remain too sparse to fully constrain carbon fluxes in Siberia with inversion modeling. To overcome this problem, the National Institute for Environmental Studies (NIES), with the cooperation of the Russian Academy of Science (RAS), began periodic flask sampling for GHG measurements from aircraft over three sites in Siberia in 1993. In addition, in 2001, NIES and RAS began establishing the Siberian tower network, which at present consist of nine towers, to obtain regional and short-term variations of GHGs and to produce data for inverse modeling to obtain regional carbon estimates. Sasakawa et al. (2013) evaluated the temporal variation of CO_2 concentration in the planetary boundary layer (PBL) and the lower free troposphere (LFT) using measurements carried out by light aircraft on and above the tower at Berezorechka (56°08’45”N, 84°19’49”E) in the taiga region of West Siberia from 2001 to 2011. Fig. 7.1.10 shows the average seasonal cycle for the PBL characterized by a minimum in late July and a maximum in November–December, yielding a seasonal amplitude of 29 ppm. This amplitude was about twice the minimum in the LFT (14 ppm), and the seasonal minimum in the PBL occurred about half a month earlier than the minimum in the LFT, demonstrating the strong CO_2 source-sink forcing by the tiga ecosystem.

Under the NIES program, collection of air samples over western Siberia had been carried out vertically at altitudinal levels ranging from 0.5 to 7.9 km upwind of Surgut (61°N, 73°E) within about 100-km distance once a month since July 1993 using a chartered aircraft (AN-24). Umezawa et al. (2012) analyzed the time series of the CH_4 concentration, $\delta^{13}CH_4$ and δD-CH_4 observed at 1 and 2 km altitudes over Surgut during 2006–09. $\delta^{13}CH_4$ showed a clear seasonal minimum in the late summer, while seasonality of CH_4 and δD-CH_4 was ambiguous due to the local disturbances. By inspecting the relationships between the CH_4 concentration and isotopes, we found that isotopic source signatures in the winter (December–April) are −41.2±1.8 and −187±18‰ for $\delta^{13}CH_4$ and δD-CH_4, respectively, and the corresponding values in the summer (June–October) are −65.0±2.5 and −282 ±25‰. These values indicate predominant CH_4 emissions from fossil fuel facilities in the winter and wetlands in the summer. It was also found that the shorter-term CH_4 variations are more influenced by fossil CH_4 than that from wetlands. The finding presumably reflects the fact that the former is released from limited areas such as leakage from fossil fuel facilities, while the latter is released from a vast expanse of wetland. By employing a CH_4 emission data set used in an atmospheric chemistry transport model (Patra et al., 2009), they calculated seasonal isotopic changes of CH_4 sources in western Siberia and compared them to the estimates obtained in this study. The results, Fig. 7.1.11 indicated that the seasonal change in the CH_4 emission data set is reasonable at least in terms of a ratio of fossil to biogenic emissions.

To increase the spatiotemporal data coverage, aircraft observation campaigns have been conducted; however, up to now regular aircraft observations are still limited over Siberia. Commercial airlines constitute a very powerful platform for observing spatiotemporal variations of trace gases, and the commercial airliner project named Comprihensive Observation Network for Trace gases by AirLiners (CONTRAIL) with Japan Airlines (JAL) has been conducting flask sampling at low latitudes, mainly between Australia and Japan, since 1993 (Matsueda and

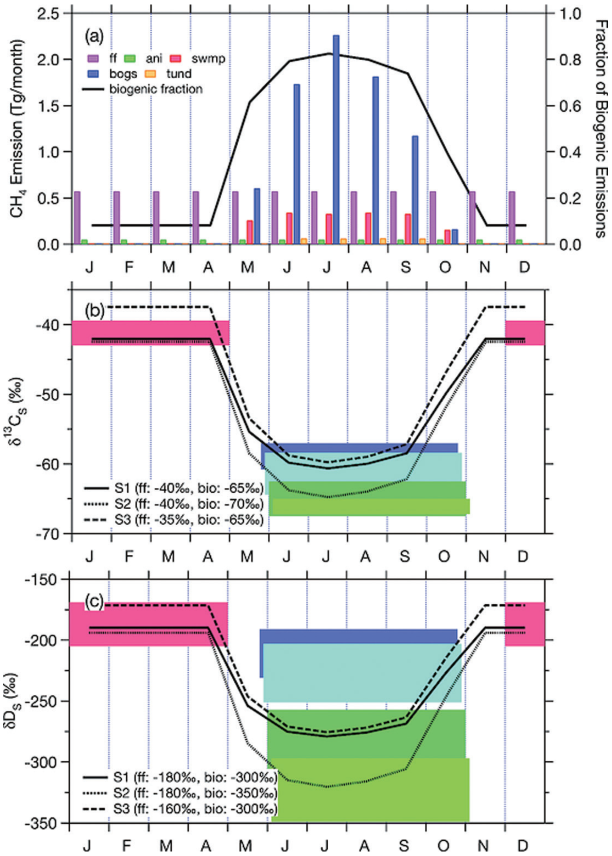

Fig. 7. 1. 11 (a) Monthly CH_4 emissions from an area including Surgut employed by Patra et al. (2009). Abbreviations are as follows: ff, fossil fuel; ani, animals; swmp, swamps; bogs, bogs; and tund, tundra. Also shown is the monthly fraction of biogenic CH_4 emissions (=(ani + swmp + bogs + tund)/all). (b) Monthly flux-weighted $\delta^{13}CH_4$ of the source based on the CH_4 emissions shown in Fig. 7.1.11a. (c) Same as Fig. 7.1.11b but for δD-CH_4. $\delta^{13}CH_4$ and δD-CH_4 for fossil and biogenic emissions are assumed to have three cases (S1, S2 and S3) shown in the respective panels. In Figs 7.1.11b and c, shaded bands show the source values estimated from Miller/Tans plot for each season: wintertime raw data estimates (red); summertime raw data estimates (dark green); estimates by residuals from the trends (light blue), from the best fit curves (blue) and from the data at 2 km (light green) (Umezawa et al., 2012).

Inoue, 1996; Machida et al., 2008). Sawa et al. (2015) reported a new program launched in April 2012 to conduct a flask sampling on commercial aircraft flights between Europe and Japan, as part of the GRENE Arctic. Objective of these midlatitude and Arctic observations are (i) to reveal seasonal changes and differences in GHG distributions on a wider latitudinal band from the equator to 70°N with the CONTRAIL project and (ii) to derive the seasonal transport/mixing of GHGs inferred from observed north-south or vertical gradients in the upper troposphere (UT)/lower stratosphere (LS). Air samples have been collected once a month by the Automatic air

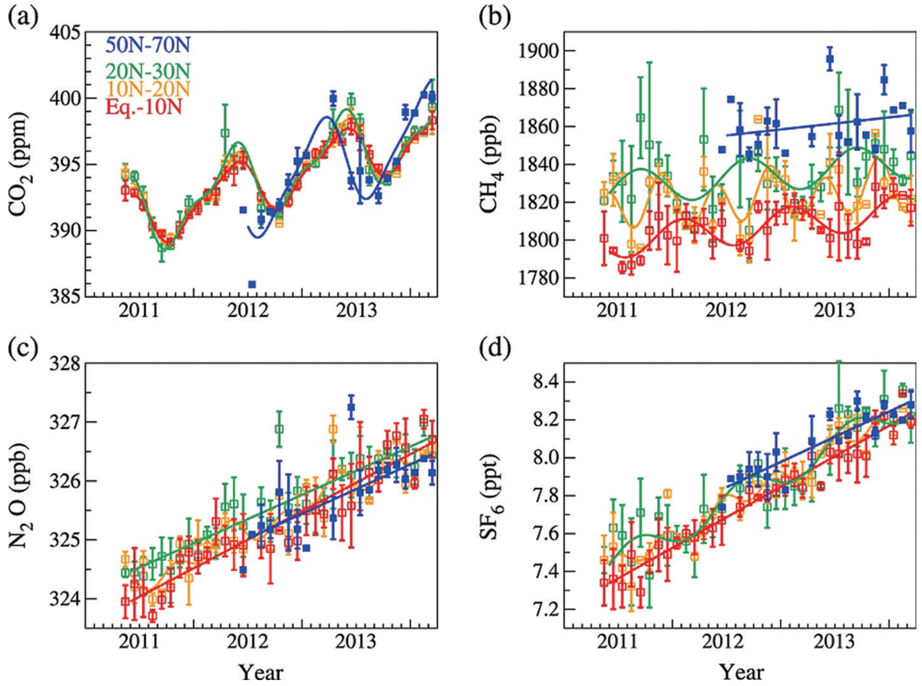

Fig. 7. 1. 12 Time series of greenhouse gases observed in the upper troposphere since April 2012. Monthly means and standard deviations for (a) CO_2, (b) CH_4, (c) N_2O, and (d) SF_6. Blue color represents the mole fractions observed over the Eurasian continent in the 50–70°N latitudinal band. Red, orange, and green colors represent those observed over the western North Pacific in the 0–10°N, 10–20°N, and 20–30°N latitudinal bands, respectively. The lines are the fitted curves to the data, each composed of a linear trend with or without harmonics based on Akaike information criteria (AIC) (Sawa et al., 2015).

Sampling Equipment (ASE) between Europe and Japan aboard a commercial airliner JAL, Boeing 777-200ER at cruising altitudes of 9–12 km, since April 2012 (Machida et al., 2008). GHG distributions at about 9–12 km altitudes in the etratropics are largerly determined by the tropopause height. In order to derive vertical profiles and their variations relative to the tropopause, they used the difference in the potential temperature at flight level (Θ) and the dynamical tropopause (Θ_{TP} indicated by the 2 PVU (potential vorticity unit, 1 PVU = 106 m^2 s^{-1} K kg^{-1}) surface, $\Delta\Theta_{TP} = \Theta - \Theta_{TP}$.

Fig. 7.1.12 shows the time series of CO_2, CH_4, N_2O, and SF_6 in the upper troposphere between 50° and 70°N over Siberia, as well as those observed between the equator and 30°N over the western North Pacific between May 2011 and March 2014. The depicted monthly means are based on the average values observed between 7 km altitude and the tropopause (Θ_{TP}) in each latitudinal band. N_2O did not show a significant latitudinal gradient from the equator to 70°N (Fig. 7.1.12c). Compared to low latitudes, the seasonal variation of CO_2 at northern high latitudes showed somewhat large seasonal peak-to-peak amplitude (with ~9 ppm) with a phase shift of ~2 months. Earlier decrease in CO_2 in the UT over Siberia compared to regions in the North Pacific was reported by Sawa et al. (2012), suggesting strong influence of photosynthesis activity by land biosphere at higher latitudes. CH_4 showed ~20 ppb higher mole fractions over Siberia (50–70°N) than those in the low latitudes (0–30°N) over the western North Pacific, and the difference was found to be statistically significant at 95% confidence level using the Student t test. The higher mixing ratios of CH_4 at higher latitudes suggest larger emissions at high latitudes and a transport and mixing from the surface to the upper troposphere. CH_4 showed opposite phase in the seasonal cycle between 0–10°N and 20–30°N. While CH_4 showed lower mole fractions and a summer minimum in 0–10°N due to reactions with OH as observed at surface stations, the summer maximum of CH_4 in 20–30°N could be influenced by emissions in South and East Asia and the subsequent transport to the upper troposphere over the western Pacific. In addition, suppression of vertical transport in winter could contribute to the CH_4 minimum around March in 20–30°N. Slightly higher SF_6 in the high latitudes was found than that in the low latitudes, suggesting stronger anthropogenic emissions at high latitudes. However, the differences in SF_6 between 50–70°N and 20–30°N bands were not statistically significant due to large variability.

The observed seasonal cycles of CO_2, CH_4, N_2O, and

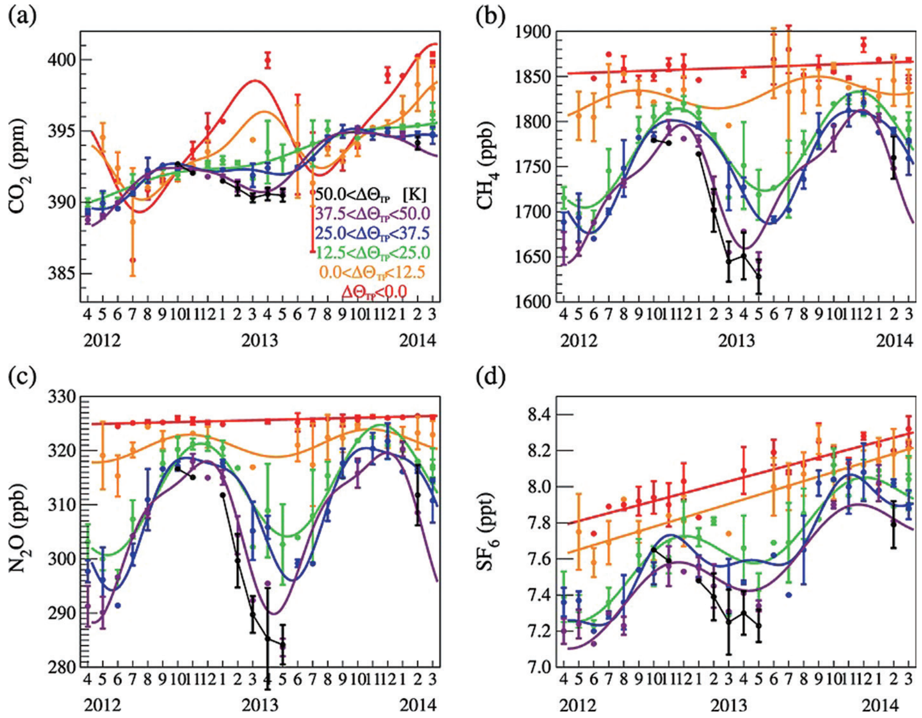

Fig. 7. 1. 13 Time series of greenhouse gases observed in the upper troposphere and the lower stratosphere between April 2012 and March 2014. Monthly means and standard deviations for (a) CO_2, (b) CH_4, (c) N_2O, and (d) SF_6. The colors represent the mole fractions observed at every 12.5 K bin from the local tropopause along the flight route over the Eurasian continent. The lines are the fitted curves to the data, each composed of a linear trend with or without harmonics based on AIC (Sawa et al., 2015).

SF_6 in the lower stratosphere and the upper troposphere in the high latitudes are shown in Fig. 7.1.13. The observed values are binned into layers of 12.5 K thickness each, beginning with $0 < \Delta\Theta < 12.5$ K up to $37.5 < \Delta\Theta < 50$ K. The tropospheric data, the same values for 50–70°N shown in Fig. 7.1.12, are also shown in Fig. 7.1.13 for comparison. Stratospheric CO_2 showed a weak seasonal cycle with amplitudes of about 1–2 ppm, with a slow decrease from autumn to spring, followed by a rapid increase from June to September. On the contrary, tropospheric CO_2 showed a large opposite seasonal variations. Stratospheric CH_4 and N_2O, due to chemical destruction in the LS, have a large difference to their concentrations in the troposphere, and also have a large vertical gradient. Atmospheric concentrations of CH_4 and N_2O in the UT does not show distinct seasonal variation, but showed a gradual secular increases similar to the surface values. Tropospheric CH_4 near the ground surface shows a clear seasonal variation with a low value in summer due to destruction by OH radicals; however, in the low pressure layer such as UT, reaction with OH radicals become weak and less seasonal variation. Also, as in the continental inland area such as Siberia, vertical transport of high concentration CH_4 becomes active in summer and this also makes the seasonal variation smaller. Tropospheric N_2O has a long life time in the troposphere, and shows only small seasonal variation. On the other hand, stratospheric CH_4 and N_2O showed a strong seasonal variation. The major mechanisms to derive this seasonal variation is, as similar to CO_2, intrusion of tropospheric air in summer and subsidence of upper atmosphere in winter. Due to a large difference between LS and UT and larger vertical gradients in the stratosphere compared to CO_2 make this large seasonal variations in LS. SF_6 has a long life time in the UT as N_2O, shows little seasonal variation, but in LS, clear seasonal variation is made by the transport in summer and winter due to the difference in concentration in the UT and LS, and large gradient.

Since SF_6 is stable in the atmosphere, we could derive an average time (age) of the air parcel in the stratosphere after its leaving from the troposphere. At potential temperatures of 37.5–50 K above the tropopause, SF_6 age was estimated to be about 22 months in May and 9 months in November. This strong seasonal variation is explained by the subsidence of high-stratospheric air in spring and the effective flushing of the lowermost stratospheric air with tropospheric air in autumn.

Shipborne observations

Atmospheric potential oxygen (APO) is a useful pa-

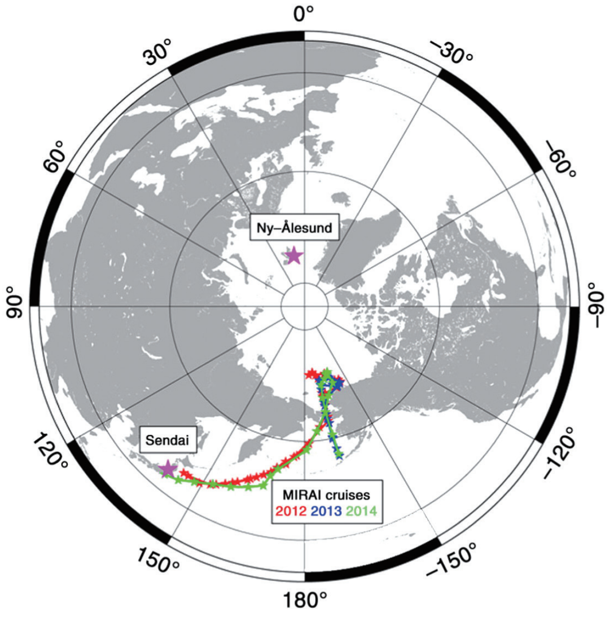

Fig. 7. 1. 14 Locations where air samples were collected (small stars) onboard MIRAI for the period 5 September–15 October 2012 (red) 29 August–6 October 2013 (blue), and 1 September–9 October 2014 (green). Locations of NyÅlesund, Svalbard, and Sendai, Japan, are also shown (large purple stars) (Ishidoya et a., 2016).

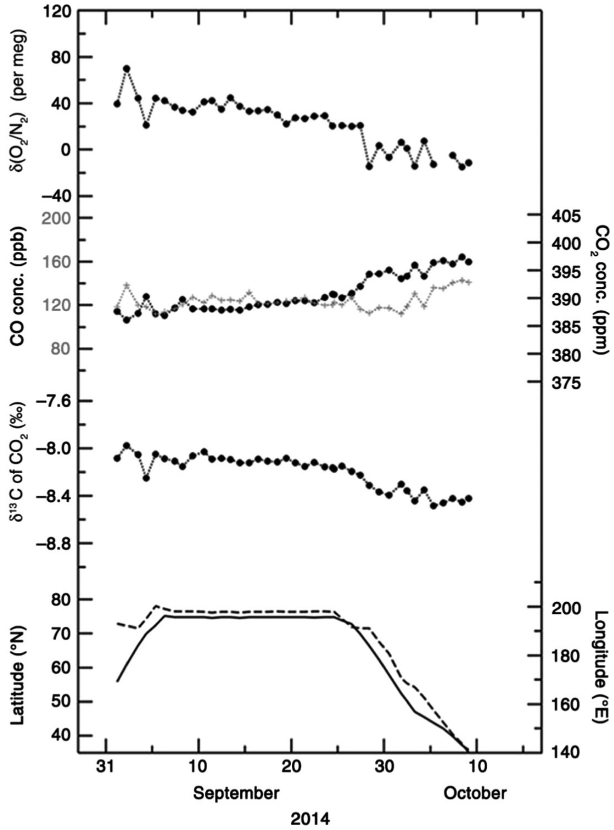

Fig. 7. 1. 15 Temporal variations in $\delta(O_2/N_2)$, CO_2 concentration and $\delta^{13}C$ of CO_2 observed onboard MIRAI for the period 1 September–9 October 2014 (black filled circles). Temporal variation in CO concentration (grey crosses), latitude and longitude of the cruise are also shown (Ishidoya et a., 2016).

rameter to discuss the marine biological and physical processes. In order to increase our understanding of the relationship between the local air-sea O_2 flux variation and APO, we need to observe APO just above the sea surface. Simultaneous observations of atmospheric potential oxygen (APO = O_2 + 1.1 × CO_2) and air-sea O_2 flux, derived from dissolved oxygen in surface seawater, were carried out by Ishidoya et al. (2016) onboard the research vessel *Mirai* in the northern North Pacific and the Arctic Ocean in the autumns of 2012–2014 as shown in Fig. 7.1.14. A simulation of the APO was also carried out using a three-dimensional atmospheric transport model that incorporated a monthly air-sea O_2 flux climatology. Fig. 7.1.15 shows the temporal variations in $\delta(O_2/N_2)$, CO_2 concentration and $\delta^{13}C$ of CO_2 observed onboard MIRAI for the period 1 September–9 October 2014. Sampling locations (in latitude and longitude) are also shown at the bottom of the graph. As seen in Figs. 7.1.15, $\delta(O_2/N_2)$ and $\delta^{13}C$ show a gradual decrease with time, while CO_2 shows a gradual increase. Negative correlations of $\delta(O_2/N_2)$ and $\delta^{13}C$ with CO_2 were also observed in the day-to-day variations. It is known that $\delta(O_2/N_2)$ and $\delta^{13}C$ are negatively correlated with CO_2 due to fossil fuel combustion and terrestrial biospheric processes (e.g. Keeling et al., 1993; Nakazawa et al., 1997). Furthermore, while seasonal and subseasonal variations in $\delta(O_2/N_2)$ are also affected significantly by the air-sea exchanges of O_2 and N_2, similar variations in CO_2 are less affected by the air-sea exchange of CO_2 because of the bicarbonate equilibrium (e.g. Keeling et al., 1993).

Following the discussion in last paragraph, we can extract the oceanic component from the measured values of $\delta(O_2/N_2)$ by using APO [defined by eq. (3)]. The APO values for the period 1 September–9 October 2014 are shown in Fig. 7.1.16 (black filled circles). The APO values are also plotted, calculated from the STAG model driven by F_{O2_cli} and F_{N2_cli} (blue crosses). The average value of the simulated APO for each cruise was adjusted as a function of the differences between F_{O2_obs} and F_{O2_cli}. It is seen from Fig. 7.1.16 that the observed APO values decrease gradually with time for each cruise. This decrease from September to October was widely observed in the Northern Hemisphere in other studies (e.g. Keeling et al., 1998; Tohjima et al., 2012), and reflected seasonal changes in the air-sea O_2 flux. While the simulated APO values showed similar seasonal decreasing trend in APO for each cruise, the observed day-to-day variation was significantly under estimated by the model. This under-

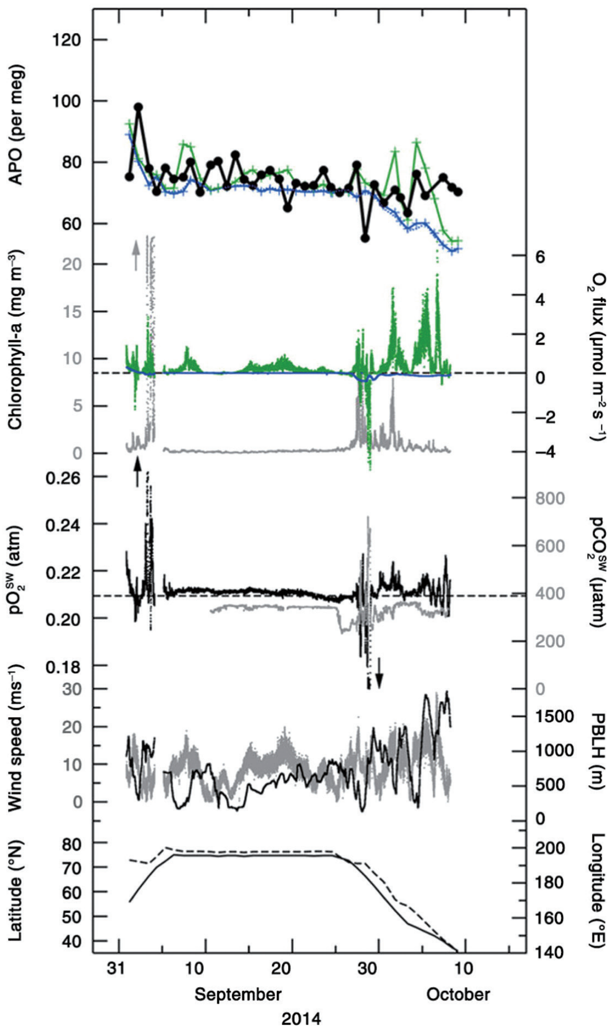

Fig. 7. 1. 16 Temporal variations in APO (filled black circles) and air-sea O_2 flux observed onboard MIRAI (F_{O2_obs}; green dots, positive value denotes flux emitted from the ocean to the atmosphere) for the period 1 September–9 October 2014. Corresponding APO values simulated using the STAG model that incorporated the monthly air-sea O_2 (N_2) flux climatology (blue crosses), and the climatological air-sea O_2 flux along the observation route (F_{O2_cli}; blue dots) are also plotted. Simulated APO values calculated by including the contribution of air-sea CO_2 flux are also shown by the blue dotted line (see text). Green crosses denote temporal variations in APO calculated by using F_{O2_obs} (see text). Chlorophyll-a concentration, partial pressure of O_2 and CO_2 in surface water, heights of planetary boundary layer (PBLH), wind speed at 25 m heights, latitude and longitude of the cruise are also shown (Ishidoya et a., 2016).

estimation could be due to the difference between F_{O2_cli} used to drive the model and the actual air-sea O_2 flux used to calculate the observed APO, and the average value of the observed air-sea O_2 fluxes was systematically higher than that of the climatological O_2 flux. In order to show this to be the case, we also plotted in Fig. 7.1.16, F_{O2_obs} and F_{O2_cli} for each cruise. This could explain the discrepancy between the observed and simulated seasonal APO cycles widely seen at various northern hemispheric observational sites in the fall season, and the importance of knowing the variation of air-sea O_2 fluxes due to the marine biological productivities.

The extent and thickness of sea ice in the Arctic Ocean have been declining in recent decades, and because of this decline in the extent of sea ice, the air-sea CO_2 flux is also thought to be dramatically changing.

In late summer 2013, Kosugi et al. (2017) made shipboard observations in the Chukchi Sea and in the Canadian Basin of the western Arctic Ocean. As shown in Fig. 7.1.17, an expanse of surface water was observed with low CO_2 partial pressure (pCO_2^{sea}) (< 200 μatm) in the Chukchi Sea of the western Arctic Ocean. The large undersaturation of CO_2 in this region was the result of massive primary production after the sea-ice retreat in June and July. In the surface of the Canada Basin, salinity was low (< 27) and pCO_2^{sea} was closer to the air–sea CO_2 equilibrium (~360 μatm). From the relationships between salinity and total alkalinity, it was confirmed that the low salinity in the Canada Basin was due to the larger fraction of meltwater input (~0.16) rather than the riverine discharge (~0.1). Such an increase in pCO_2^{sea} was not so clear in the coastal region near Point Barrow, where the fraction of riverine discharge was larger than that of sea-ice melt. Low pCO_2^{sea} (< 250 μatm) in the depth of 30–50 m was also identified under the halocline of the Canada Basin. This subsurface low pCO_2^{sea} was attributed to the advection of Pacific-origin water, in which dissolved inorganic carbon was relatively low, through the Chukchi Sea where net primary production was high. Oxygen supersaturation (> 20 μmol kg^{-1}) in the subsurface low pCO_2^{sea} layer in the Canada Basin indicated significant net primary production undersea and/or in preformed condition. If these low pCO_2^{sea} layers surface by wind mixing, they will act as additional CO_2 sinks; however, this is unlikely because intensification of stratification by sea-ice melt inhibits mixing across the halocline.

Yasunaka et al. (2016) produced 204 monthly maps of the air-sea CO_2 flux in the Arctic north of 60°N, including the Arctic Ocean and its adjacent seas, from January 1997 to December 2013 by using a self-organizing map (SOM) technique. The partial pressure of CO_2 (pCO_2) in surface water data were obtained by shipboard underway measurements or calculated from alkalinity and total inorganic carbon of surface water samples. Subsequently, we investigated the basin-wide distribution and seasonal to interannual variability of the CO_2 fluxes. They used

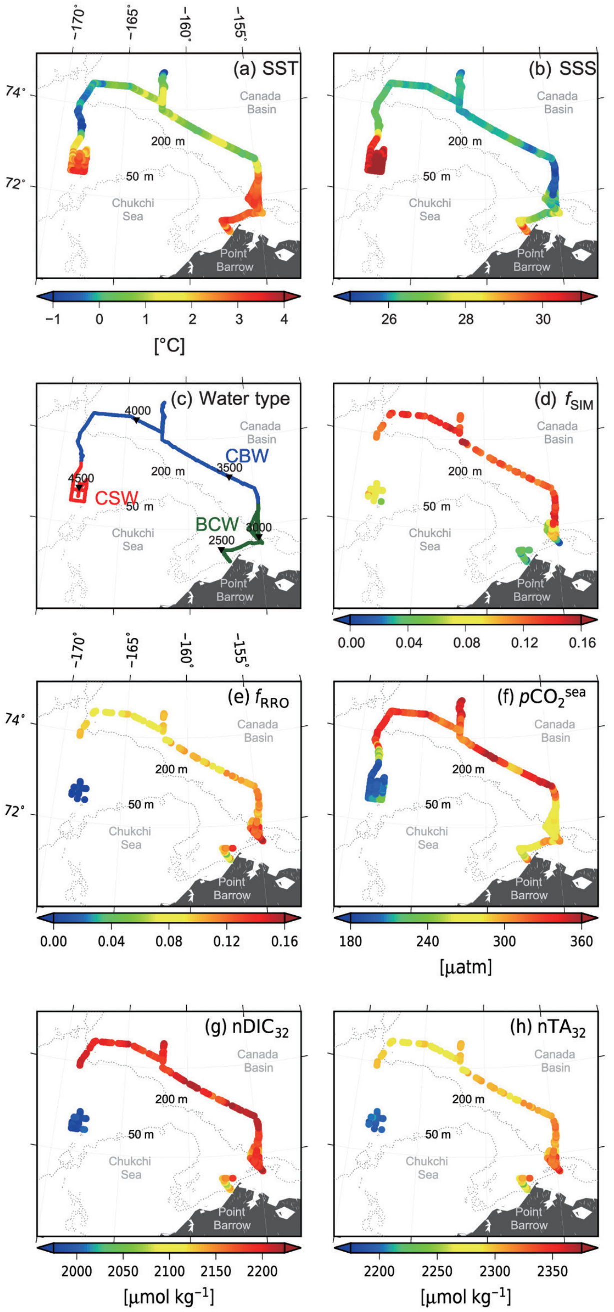

Fig. 7. 1. 17 Surface water properties along the track of cruise MR13-06 from 4 to 11 September 2013. **(a)** Sea surface temperature (SST); **(b)** sea surface salinity (SSS); **(c)** BCW (Barrow coastal water), CSW (Chukchi Sea water), and CBW (Canada Basin water) water types according to SST and SSS. The numbers over triangles indicate distance sailed from Dutch harbor, Alaska, USA (km). **(d)** Fraction of sea ice melt (f_{SIM}), **(e)** fraction of riverine outflow (f_{RRO}) and **(f)** pCO_2^{sea} (Kosugi et al., 2017).

pCO_{2w} observations (converted from the fugacity of CO_2 values) from the Surface Ocean CO_2 Atlas (SOCAT) version 3 (Pfeil et al., 2013; Bakker et al., 2014, 2016; http://www.socat.info/), and the Global surface pCO_2 (LDEO) database version 2014 (Takahashi et al., 2015; http://cdiac.ornl.gov/oceans/LDEO_ Underway_Database/). They

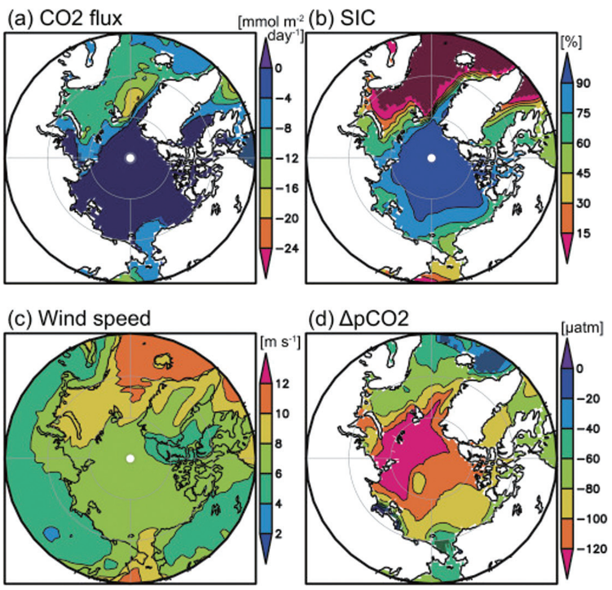

Fig. 7. 1. 18 Seventeen-year annual means of (a) CO_2 flux (m mol m^{-2} day^{-1}) (negative values indicate influx into the ocean), (b) SIC (%), (c) wind speed (m s^{-1}), and (d) ΔpCO_2 (= pCO_{2w} – pCO_{2a}) (m atm). Darker shades show values in grids where values were smaller than the uncertainty (Yasunaka et al., 2016).

also used shipboard pCO_{2w} measurements obtained during cruises of the R/V *Mirai* that have not yet been archived in the SOCAT and LDEO databases (cruises MR09_03, MR10_05, MR12_E03, and MR13_06; http://www.godac.jamstec.go.jp/darwin/e).

pCO_{2w} was estimated by a SOM technique similar to that used by Telszewski et al. (2009) and Nakaoka et al. (2013). In their estimation, they used SST, SSS, SIC, and pCO_{2a} as training parameters. Among those variables representing the spatial distribution and temporal variation of surface water properties in the Arctic, SST, SSS, and SIC are basic parameters and their gridded products are readily available. Monthly air-sea CO_2 flux (F) values was calculated from the pCO_{2w} values estimated as described above by using the bulk formula of Wanninkhof (1992):

$$F = kL\,(pCO_{2w} - pCO_{2a}), \qquad (7.1.7)$$

where k is the gas transfer velocity (calculated from wind speed) and L is the solubility of CO_2. The 17-year annual mean CO_2 flux distribution shows that all areas of the Arctic Ocean and its adjacent seas were net CO_2 sinks (Fig. 7.1.18a). The annual CO_2 influx to the ocean was strong in the Greenland/Norwegian Seas (>10 m mol m^{-2} day^{-1}), the Barents Sea (~10 m mol m^{-2} day^{-1}), and the Chukchi Sea (~4 m mol m^{-2} day^{-1}). In contrast, it was

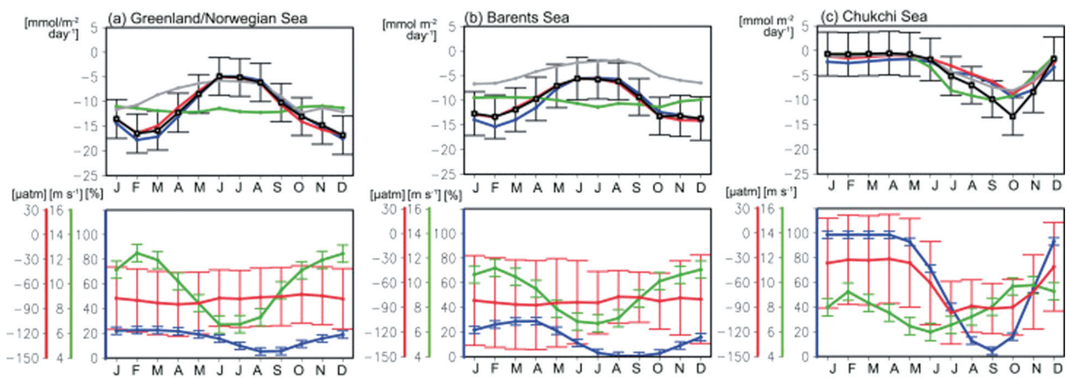

Fig. 7. 1. 19 Area-mean seasonal variations in (a) the Greenland/Norwegian Seas (65°–80°N, 45°W–15°E), (b) the Barents Sea (65°–80°N, 15°–50°E), and (c) the Chukchi Sea (65°–75°N, 180°–160°W). The upper panels show seasonal variations in the CO_2 flux (black, standard; blue, SIC constant; green, wind constant; red, $\Delta p CO_2$ constant; gray, from Takahashi et al., 2009) in each region (m mol m^{-2} day^{-1}), and the lower panels show seasonal variations in SIC (%) (blue), wind speed (m s^{-1}) (green), and $\Delta p CO_2$ (m atm) (red). Error bars indicate the uncertainty (Yasunaka et al., 2016).

weak within the uncertainty in the Eurasian and Canada Basins, as well as in the Laptev and East Siberian Seas (<4 m mol m^{-2} day^{-1}). Our annual CO_2 flux estimates averaged in the Greenland/Norwegian Seas and the Barents Sea are consistent with those reported by most previous studies (e.g., Aoki et al., 1996; Nakaoka et al., 2006).

Next, they examined the relationship between the CO_2 flux and SIC, wind speed, and $\Delta p CO_2$, parameters that directly relate to the CO_2 flux. The annual mean CO_2 flux distribution showed strong similarities to the SIC and wind distributions (Fig. 7.1.18b and c). The 75% SIC contour mostly corresponds to the −4 m mol mol m^{-2} day^{-1} contour of the CO_2 flux, indicating that in the area with an average sea ice cover of more than 75%, the CO_2 influx was less than 4 m mol mol m^{-2} day^{-1}. Strong fluxes into the Greenland/Norwegian Seas, the Barents Sea, and the Chukchi Sea were associated with high winds and large areas of open water in those regions. In the Eurasian Basin, the CO_2 influx was relatively small because of the large SIC (>75%), even though $\Delta p CO_2$ was highly negative (Fig. 7.1.18d). Here they defined the Arctic Ocean as the ocean area north of 65°N excluding the Greenland/Norwegian Seas and Baffin Bay, the estimated 17-year average influx to the Arctic Ocean was 4 m mol m^{-2} day^{-1}, equivalent to an uptake of 180 TgC yr^{-1}. The formal uncertainty is large (210 TgC yr^{-1}), however, mainly because of the poor coverage of pCO_2 observations and the uncertainty of the SIC effect on gas exchange. 17-year monthly mean CO_2 fluxes and related variables were shown in Fig. 7.1.19.

Interannual variation of the CO_2 flux was larger than uncertainty in the Greenland/Norwegian Seas and the Barents Sea in early winter, and in the Chukchi Sea in late summer. The amplitudes of the interannual variation in these regions were about 10 m mol m^{-2} day^{-1}. The $\Delta p CO_2$ contribution to the interannual variation was thus much larger than its contribution to the seasonal variation of the CO_2 fluxes. About 80% of the $\Delta p CO_2$ interannual variation arose from the interannual variation of pCO_{2w}. The 17-year trend in the CO_2 flux was negative (i.e., uptake by the ocean was increasing) in the Greenland/Norwegian Seas and northern Barents Sea, and positive (i.e., uptake was decreasing) in the southern Barents Sea. The 17-year trends were larger than the uncertainty in these regions. The $\Delta p CO_2$ trend in all of these regions corresponded well to the SST trend. This result showed that whether pCO_{2w} increased faster or slower than the increasing pCO_{2a} depended on the thermodynamic relationships. Cai et al. (2010) also reported a rise in pCO_{2w} with increasing SST in the Canada Basin. Simultaneous trends toward positive $\Delta p CO_2$ and decreased SIC suggest that the CO_2 uptake can be expected to decrease once the ocean becomes free of sea ice, as suggested by Cai et al. (2010). Retreating sea ice has two opposite effects on pCO_{2w} and the CO_2 flux; on the one hand, it leads to increased pCO_{2w} due to increased SST, while on the other hand, it leads to decreased pCO_{2w} due to active biological production.

After GRENE Arctic, Yasunaka et al. (2018) again estimated monthly air–sea CO_2 fluxes in the Arctic Ocean and its adjacent seas north of 60°N from 1997 to 2014, using similar SOM technique, but with incorporating chlorophyll *a* (Chl *a*) concentration. This was because one possible reason for the large uncertainties of the estimated CO_2 uptake by Yasunaka et al. (2016) (180±210 Tg C y^{-1}) was that no direct proxies for the effect of biological processes on pCO_{2w} were used in that study, leading to an underestimation of the seasonal amplitude of pCO_{2w}. The addition of Chl *a* as a parameter in the SOM process enabled us to improve the estimate of pCO_{2w}, particularly via better representation of its decline in spring, which resulted from biologically mediated pCO_{2w} reduction. As a result of the inclusion of Chl *a*, the uncertainty in the CO_2 flux estimate was reduced, with a net annual Arctic Ocean CO_2 uptake of 180±130 Tg C yr^{-1}.

7. 2. Terrestrial ecosystem and carbon cycle

Carbon cycle has a crucial role in the earth system and its changes have substantial effects on climate change. Terrestrial ecosystems have both positive and negative feedback to the carbon cycle. It is urgent to better understand mechanisms of the carbon cycles and their interactions with the earth system.

The boreal forests in the Northern Hemisphere currently fix CO_2 in the atmosphere, but their changes associated with climate change due to increased CO_2 are highly uncertain (IPCC, 2013). This is because boreal forests have the potential to enhance CO_2 fixation through fertilization effects of increased CO_2 and to expand its coverage northward due to global warming (i.e., negative feedback), while they also have the potential to increase CO_2 emission due to increased respiration caused by the warming and due to declining their biomass resulted from their vulnerability to climate change (i.e., positive feedback).

It has been confirmed, from ground-based and atmospheric observations of CO_2 concentration, that the northern terrestrial ecosystems have been functioning as sinks for CO_2 and that seasonal amplitude of CO_2 absorption over land has been increasing in the recent years (Gvaven et al., 2013). The current conditions and future projections of the CO_2-flux balances are described, in this section, from various observations and modeling on the terrestrial area and comparison of the estimated values by multiple methods.

Changes in CO_2 balance observed on land

Observations of energy, water and CO_2 fluxes on land used to be performed in various ways in various places. Since the 1990s, they have been carried out by the common methods for the common variables. A global observation network FLUXNET (see https://fluxnet.fluxdata.org/, viewed on 25 January 2020) was started in 1997, and the global database has been established that enable us to mutually use the data.

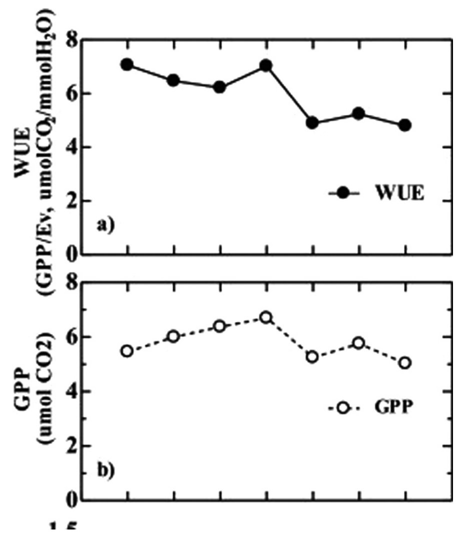

Fig. 7. 2. 1 Time series of annual water use efficiency in Spasskaya Pad during 2004–2010. Water use efficiency in 2004–2007 was increased by evapotranspiration, and that in 2008–2010 was increased by gross primary production (Ohta et al., 2014).

In the pan-Arctic region, observations of energy, water and CO_2 fluxes have been conducted for more than 10 years at a few sites (e.g., Yakutsk, Fairbanks, etc.). Ohta et al. (2014) analyzed the observation data at larch forests from 1998 to 2011 at Yakutsk, in an Eastern Siberian, to understand the relationship of the interannual variations of climate changes and forest changes. They found that in the wet years from 2005 to 2008 the larch forest had been damaged by the wet stress, resulted in the decrease of gross primary production and water use efficiency (Fig. 7.2.1).

It is widely known that the below-ground biomass is large in comparison to the above-ground biomass in permafrost regions. The field measurements of above-ground and below-ground biomass of trees and understory plants in the black spruce forests in Fairbanks, Alaska, showed that the ratio of below-ground biomass was higher especially for fine roots on shallower permafrost table. It is also revealed that understory plants would have significant contribution to below-ground carbon dynamics in forest on permafrost (Noguchi et al, 2016; Fig. 7.2.2). In addition, the relationships between tree growth and the effects of mycorrhizae on N uptake using isotope ratios of nitrogen (N) in foliage and root were investigated along a slope. It has shown that tree growth depends less on mycorrhizae for N uptake on the N-rich upper slope, while it depends more on the lower slope with the shal-

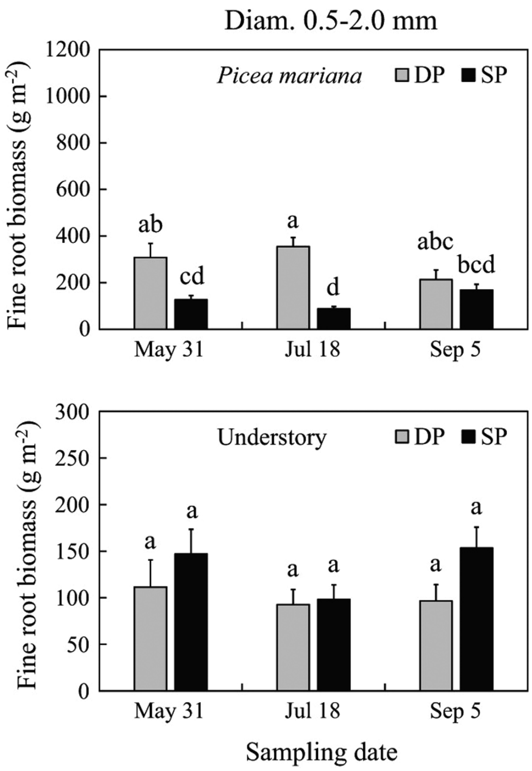

Fig. 7. 2. 2 Fine root biomass of black spruce (*Picea mariana*; top) and understory plants (bottom) at each sampling date. Figures show results on fine roots 0.5–2.0 mm in diameter. Gray and black columns represent data from DP and SP plots, respectively. Data shown are mean + SE (N = 9). Different letters above the columns indicate significant difference between the values (Tukey's HSD test, α = 0.05) (Noguchi et al., 2016).

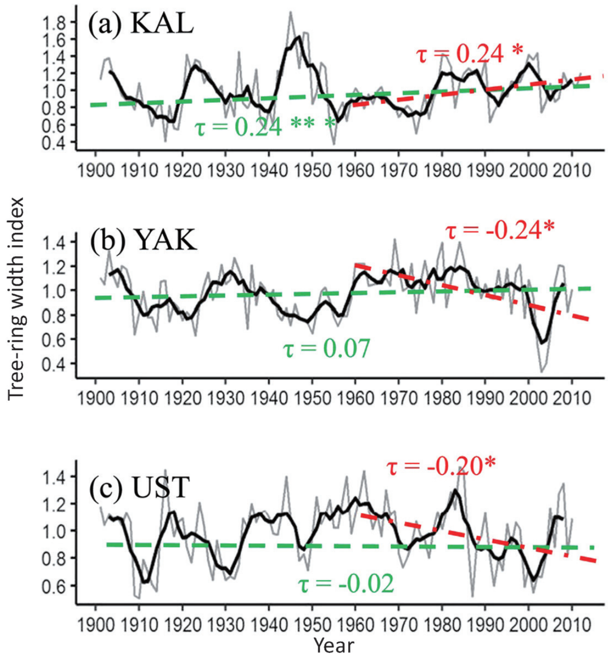

Fig. 7. 2. 3 Tree-ring width index and C_i/C_a in the six circum-Arctic forest sites studied. Ring-width chronologies (gray line) at (a) Kalina (KAL, Estonia), (b) Yakutsk (YAK), (c) Ust'Maya (UST). The smooth curve (bold line) shows the 5 year mean of the chronologies. Trends in chronologies after 1901 (green dotted line) and 1961 (red dotted line) are also shown. We used the rank-based nonparametric Mann Kendall test (Mann Kendall coefficient τ) to evaluate trends' significance. Significant trends are indicated by * ($p < 0.05$), ** ($p < 0.01$), and *** ($p < 0.001$) (Tei et al., 2017).

low permafrost table where tree growth is small (Tanaka-Oda et al., 2016).

Tree ring analysis and carbon isotope analysis are useful for investigating longer-term changes in boreal forests. According to the tree-ring analysis results at Yakutsk and Ustmaya, in the latter half of the 20th century, the annual ring width decreased with increasing temperature, and the carbon isotope ratio showed that the stomatal resistance increased due to water stress and slowed the CO_2 fixation then the tree growth as shown in Fig. 7.2.3 (Tei et al., 2017a). On the other hand, the estimated value of NPP by the dynamic vegetation model (DGVM) showed an increasing trend (Fig. 7.2.4). This is because DGVM is too sensitive to increased precipitation and does not adequately reflect the effects of water stress. This suggests that the future prediction of CO_2 fixation rate by the model may be overestimated (Tei et al., 2017a). In addition, we analyzed long-term and wide-ranging spatio-temporal variability of vegetation using annual tree-ring width index (RWI) and normalized difference vegetation index (NDVI3g) by satellite in the Arctic Circle, and compared it with climate change (Tei and Sugimoto, 2018). As a result, it was found that the change tendency of RWI and NDVI3g differs depending on the region (Fig. 7.2.5), and the relationship with climate change showed different tendencies between the Arctic ecosystems north of 67°N and the boreal forests of 50–67°N (Fig. 7.2.6). After the GRENE Arctic Project term, still some papers are originated related to this topic, such as by Tei et al. (2017b) and Tei et al. (2018a, b).

Many estimates of forest biomass have been made using satellite data. In order to predict future changes in biomass, it is important to understand not only the amount of biomass and its change until now, but also the physical quantities that might be the changing factors. Traditionally, forest-wide biomass and leaf area index (LAI) had been estimated using multiple satellite data (e.g., Myneni et al., 2002; Nagai et al., 2019). Combined with the vegetation canopy radiative transfer model, LAI of canopy could be derived as Fig. 7.2.7 (Kobayashi et al., 2010). In addition, by combining a high-resolution multi-channel visible sensor with in-situ forest phenology observation, it became possible to estimate a wide

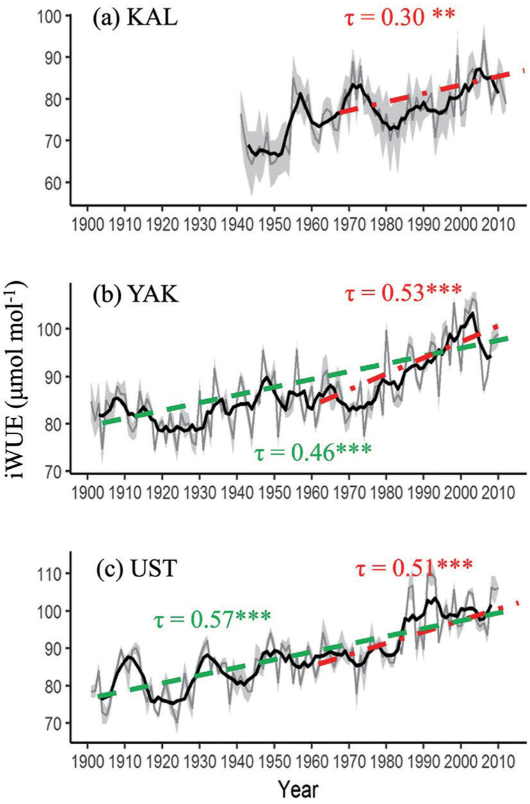

Fig. 7. 2. 4 Yearly variations in intrinsic water use efficiency (iWUE) for the six circum-Arctic forest sites studied. The iWUE (gray line) was calculated from tree-ring $\delta^{13}C$ registered from 1901 to 2012 at (a) Kalina (KAL, Estonia), (b) Yakutsk (YAK), (c) Ust'Maya (UST). The 90% confidence interval is indicated by the gray shade. The smooth curve (black bold line) shows the 5 year mean of the chronologies. Trends in chronologies after 1901 (green dotted line) and 1961 (red dotted line) are also shown. We used the rank-based nonparametric Mann Kendall test (Mann Kendall coefficient τ) to evaluate trends' significance. Significant trends are indicated by * ($p < 0.05$), ** ($p < 0.01$), and *** ($p < 0.001$) (Tei et al., 2017).

distribution of the timing of leaf and leaf litter, start of the growing seaon and end of the growing season (SGS & EGS), throughout East Siberia (Fig. 7.2.8, Nagai et al., 2019).

A method for estimating gross primary production (GPP) and net ecosystem CO_2 exchange (NEE) has been developed by a machine learning algorithm, the support vector regression (SVR), using satellite data (Ichii et al., 2017). This development has enabled data-driven estimation of CO_2 fluxes over a wide area (Fig. 7.2.9).

In High Arctic tundra, Uchida et al. (2016) made sensitivity analysis of ecosystem CO_2 exchange to climate change using an ecological process-based model. Although in situ net ecosystem production (NEP) values over the growing season varied widely among the three study plots, all NEP values were positive (CO_2 sink) within the range 17–110 mgC m^{-2} h^{-1}. Despite the range in NEP values among the three plots owing to their variable cover of *S. polaris*, we found that net primary production for all plants (vascular plants and cryptogams; $P_v + P_c$) and R_h had strong sensitivities to temperature increase as shown in Fig. 7.2.10. The value of $P_v + P_c$ decreased with increasing temperature because respiration of both *S. polaris* and *S. uncinata* increased markedly under warmer temperatures. In contrast, R_h rose with increasing temperature. As a result, NEP ($P_v + P_c - R_h$) responded significantly to temperature (Fig. 7.2.10c). Although all plots were shown to be CO_2 sinks under the present temperature condition, two of the three plots became CO_2 sources for the atmosphere (with a negative NEP) under a 2°C temperature rise. All three plots became carbon sources, under a 4°C temperature increase. In contrast, gross ecosystem production (GEP), calculated as the difference between NEP and ecosystem respiration, gradually decreased with increasing temperature (Fig. 7.2.10d).

Estimation of CO_2 balances by land surface models

There are many studies that estimate the CO_2 balance using a land surface hydrological model. The development of terrestrial hydrological models for climate research was accelerated in the 1980s, with intercomparisons for various purposes (e.g., Henderson-Sellers, 1996), which is extended to the Coupled Climate Carbon Cycle Model Intercomparison (C4MIP) (Arora and Matthews, 2009). However, the Arctic region has not been included in the target area due to the lack of observation data.

Saito, K. et al. (2018) conducted a research project for estimation and comparison (GTMIP) of the developed land model in various fields such as physical processes, biogeochemical processes, and ecosystem processes using the observation data at multiple sites described in the previous section as input values to determine the CO_2 balance in the Arctic land (Fig. 7.2.11). First, we constructed an observation network in which observation items and methods were arranged at multiple points, and conducted intercomparison studies using the observation data as input values. (Miyazaki et al., 2015). Four points, Yakutsk (2005–2011), Fairbanks (2011–2013), Kevo (1995–2012) and Tiksi (1997–2012), from which long-term continuous observation data can be obtained for items required as model inputs are selected and entered.

The output data has been released by Sueyoshi et al. (2016). Using these data, we analyzed the energy and

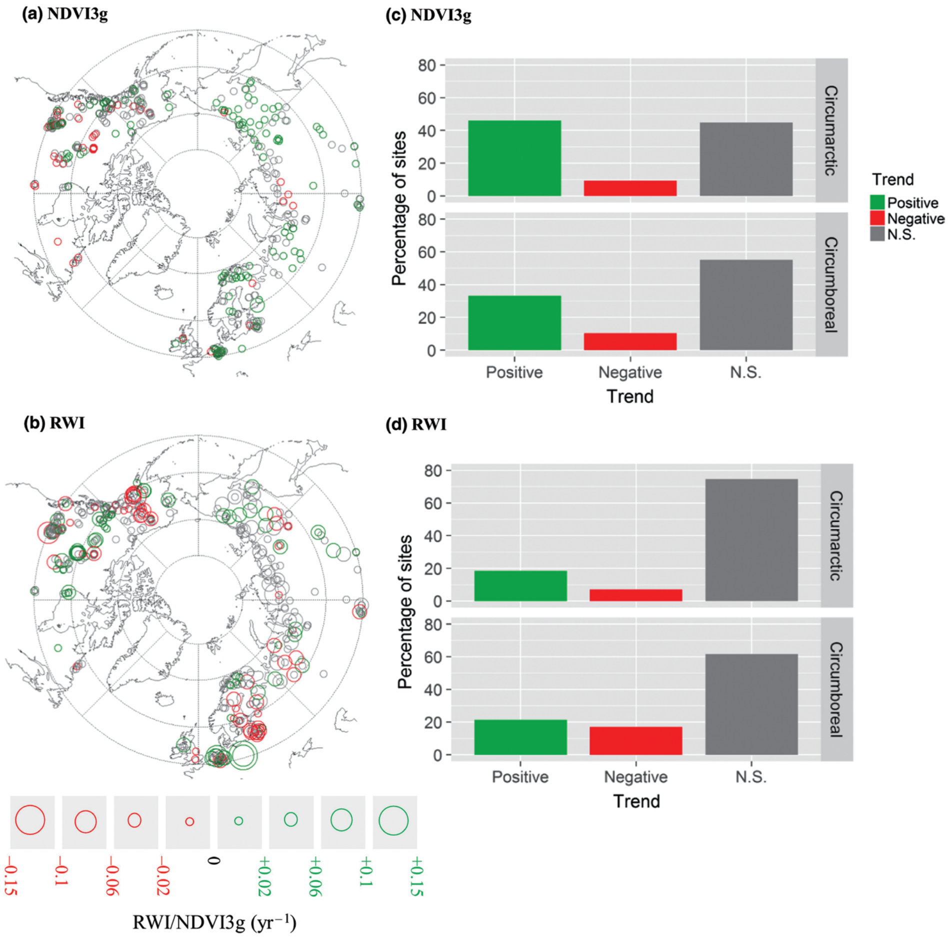

Fig. 7. 2. 5 Trends in NDVI3g and tree radial growth (RWI) over the northern high latitude region. Left panels (a–b): Spatial distribution in linear trends for NDVI3g and RWI. These trends were estimated for the period from 1982 to the last year of each RWI chronology (1990s or 2000s). Green and red circles show significant positive and negative trends ($p < .10$), respectively, and the gray circles show a nonsignificant trend. Right panels (c–d): Percentage of sites showing positive, negative, and nonsignificant trends for NDVI3g and RWI over the circumarctic and circumboreal forest ecosystems (Tei and Sugimoto, 2018).

water balance among the experimental results for 12 models of physical systems and 7 models of ecosystems. The difference between the model systems (physical systems and ecosystems) was not remarkable, and the model median was observed. It was shown that it might be regarded as a representative. It was also suggested that it was important to sufficiently capture the snow and frozen soil peculiar to the cold region as in Fig. 7.2.12 (Saito, K. et al., 2018). In addition to estimating the carbon budget based on site observation data, we are also working on an inter-comparison using global climate model prediction results of future warming. From the preliminary experiment, it was shown the soil respiration to increase overall the Arctic following the soil temperature increase (ref). This suggests that the terrestrial ecosystem in the pan-Arctic could be a source, albeit a weak sink at present. In addition, through this initiative, a coordination system between observation and model research in the Arctic land and an information exchange/ cooperation system between model researchers have been established. The foundation for building a next-generation cold-land model was developed by quantifying the uncertainty of the land model and the variation due to model implementation (Saito, K. et al., 2018).

Inter-comparison of terrestrial CO_2 flux estimated by multi-models with multi-methods

The changes in the processes involved in the CO_2 budget to climate change vary by region and time scale. As mentioned at the beginning of this section, the Arctic terrestrial ecosystem plays an important role in the global carbon budget. It is known that the change in the CO_2 balance during warming is highly uncertain especially on land (IPCC, 2013, Chap.6).

Estimation of land-based CO_2 balance is generally difficult to estimate with high accuracy over a wide area due to uneven surface conditions (land cover, topography, surface conditions, etc.). Among them, the area around

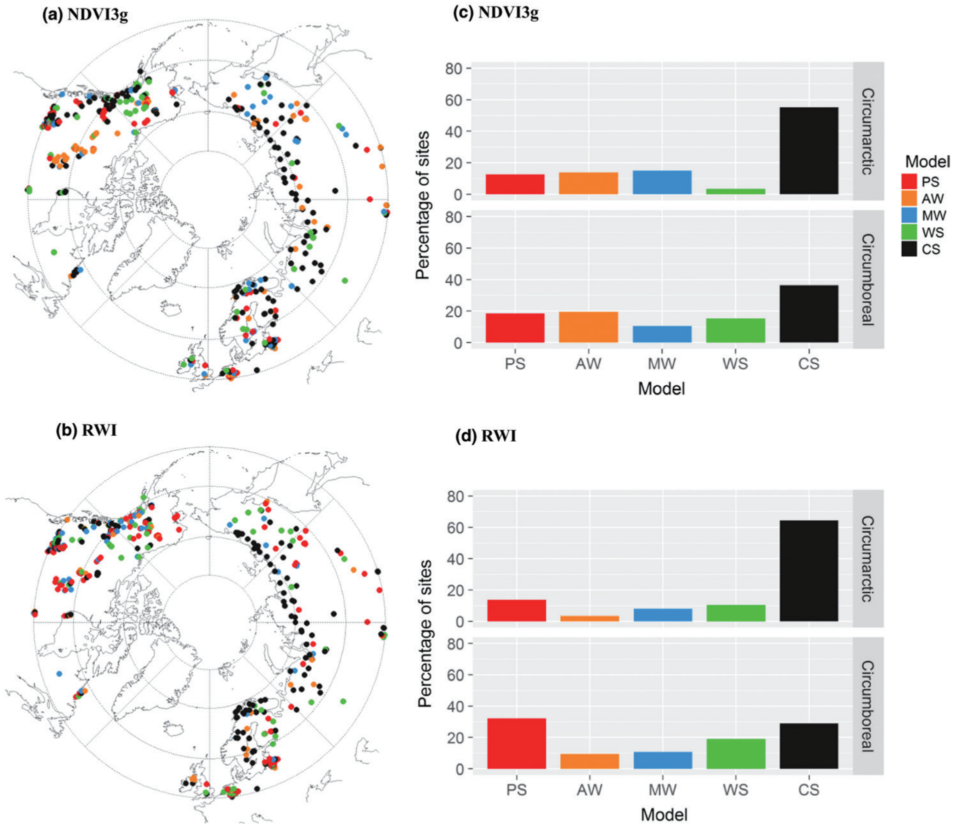

Fig. 7. 2. 6 Optimal multiregression model, with monthly climate variables for NDVI3g and tree radial growth (RWI) over the northern high latitude region. Left panels (a–b): Spatial distribution in the optimal NDVI3g and RWI models. We used the monthly temperature and precipitation in the following months as candidates of independent variables for each seasonal model, namely, (i) June, July, and August in the previous year for the PS (previous summer) model (red circles); (ii) September, October, and November in the previous year for AW (previous autumn and winter) model (orange circles); (iii) December in the previous year and January and February in the current year for the MW (mid-winter) model (blue circles); (iv) March, April, and May in the current year for the WS (winter and spring) model (green circles), and (v) June, July, and August in the current year for the CS (current summer) model (black circles). Optimal models were selected according to the lowest Akaike information criterion (AIC). Right panels (c–d): Percentage of sites showing these optimal models over the circumarctic and circumboreal forest ecosystems (Tei and Sugimoto, 2018).

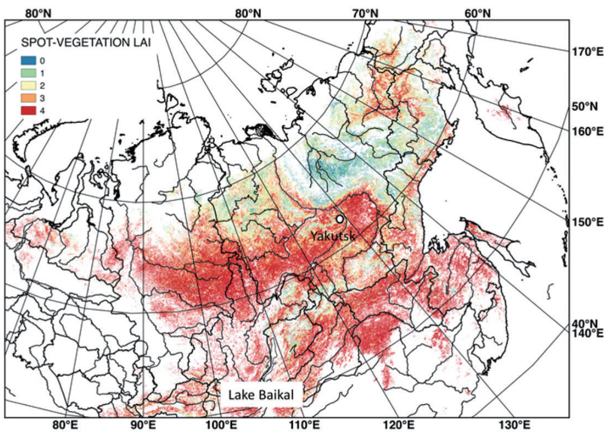

Fig. 7. 2. 7 Larch overstory LAI in eastern Siberia estimated from SPOT-VGT data sets (Nagai et al., 2019).

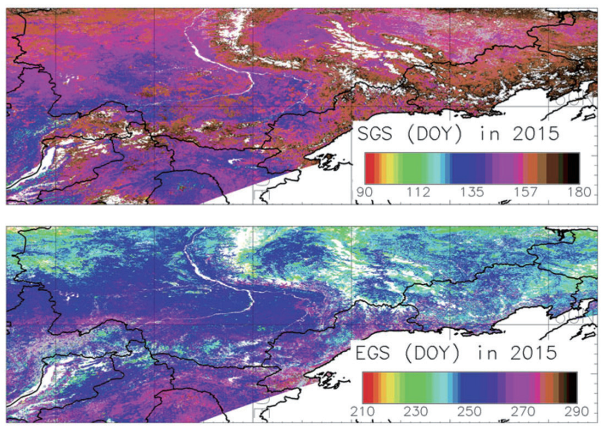

Fig. 7. 2. 8 Spatial distribution of the first date on which GRVIMODIS was more than zero in spring (i.e., SGS; top) and the first date on which GRVIMODIS was less than zero in autumn (i.e., EGS; bottom) in 2015 in eastern Siberia between 70_N and 50_N and 105_E and 165_E. The color scales show day of year (DOY) (Nagai et al., 2019).

Yakutsk, Russia with flat terrain and uniform vegetation is considered to be highly representative of a wide area. Various methods have been used at the area to estimate the CO_2 balance as described above. As bottom-up esti-

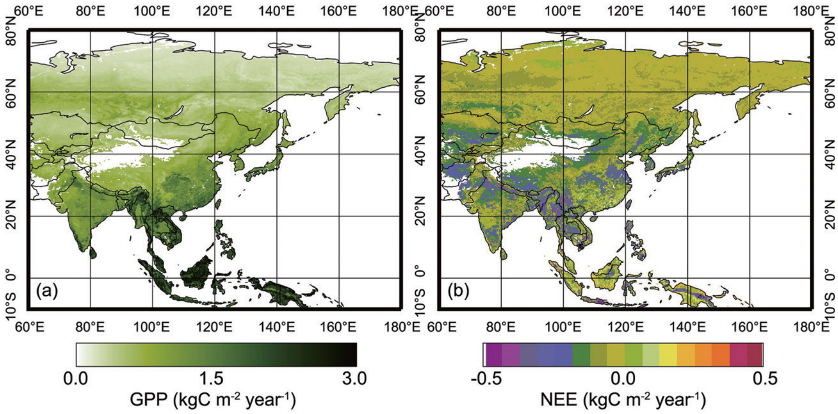

Fig. 7. 2. 9 Spatial distribution of (a) estimated annual gross primary productivity (GPP), (b) estimated annual net ecosystem exchange (NEE). Annual mean values were calculated for the 2000 to 2015 period (Ichii et al., 2017).

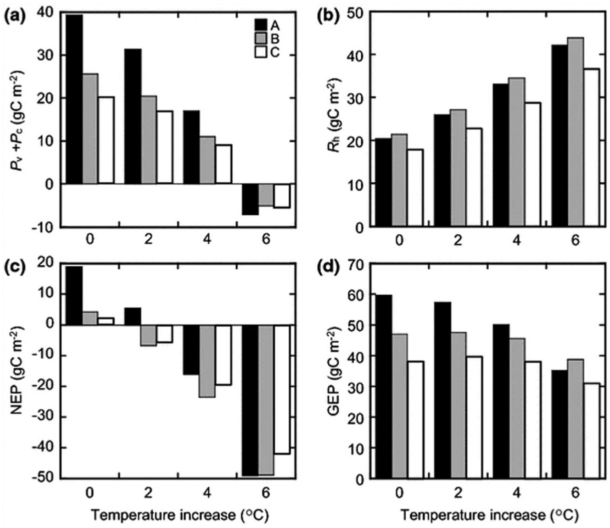

Fig. 7. 2. 10 Effect of temperature increase on **a** net primary production ($P_v + P_c$), **b** heterotrophic respiration (R_h), and **c** net ecosystem production (NEP) and **d** gross ecosystem production (GEP) for the growing season (73 days) at three study plots (*A*, *B*, and *C*) (Uchida et al., 2016).

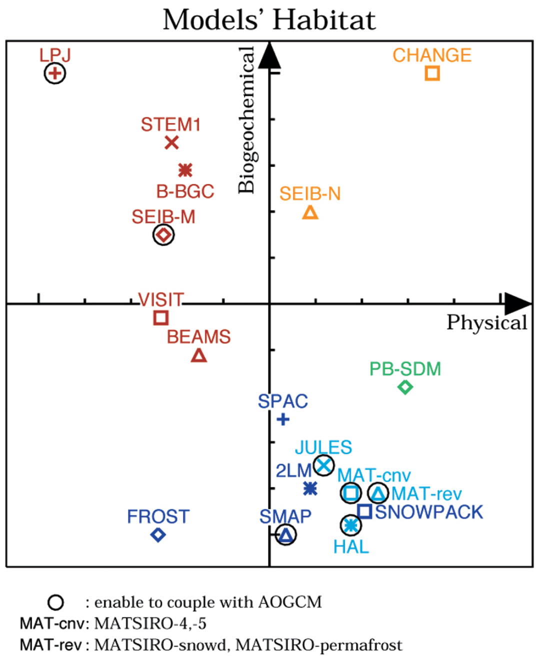

Fig. 7. 2. 11 The habitat of models participating in the GTMIP. The vertical and horizontal axes show the ratio of the incorporation of biogeochemical processes and physical processes, respectively (Miyazaki et al., 2015).

mation methods, there are flux measurements using the eddy correlation method (Ohta et al., 2014), estimation based on terrestrial ecosystem models (Saito, K. et al., 2018), and the statistical method using satellite data. There is an estimate by (Ichii et al., 2017). As a top-down estimation method, there is an estimation value by the atmospheric inversion method (e.g., Niwa et al., 2012; Saeki et al., 2013). Takata et al. (2017) compared the estimated values of CO_2 flux in Yakutsk by these multidisciplinary and multi-methods, and clarified the current state of seasonal and interannual variability. The annual balance of CO_2 was net sink by all methods. Seasonal changes were absorbed in summer and released in winter by all methods, and were consistent within the range of model variation (Fig. 7.2.13). For the year-to-year fluctuations, the top-down estimated values were close to the tower observations, but the bottom-up estimated values varied in individual models, and the model mean fluctuations had become quite small. This might be due to differences in the processes considered. Care should be taken in this point when considering the model average as a representative value (Fig. 7.2.14).

Comparing the multi-method, multi-disciplinary estimates suggested some characteristics of the estimated results by these methods: bottom-up model estimates could not adequately represent the inter-annual variability characteristic. It was confirmed that the results obtained by statistical methods using satellite data differed depending

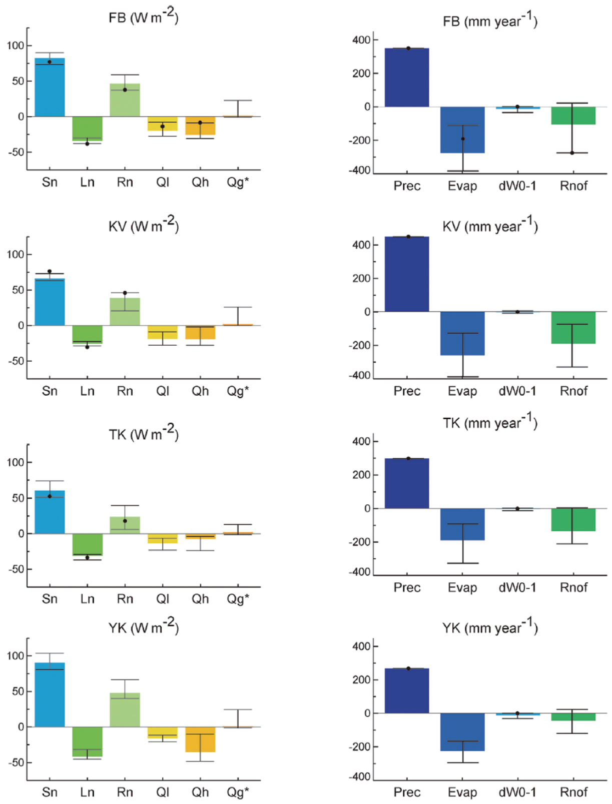

Fig. 7. 2. 12 Heat budget (left) and water budget (right) analyzed for the all term 1980–2013. But annual average of heat budget and water budget for calendar year and hydrology year, respectively. From top to bottom, Fairbanks (FB), Kevo (KV), Tiksi (TK) and Yakutsk (YK). Black dots for observation at the site (Saito, K. et al., 2018).

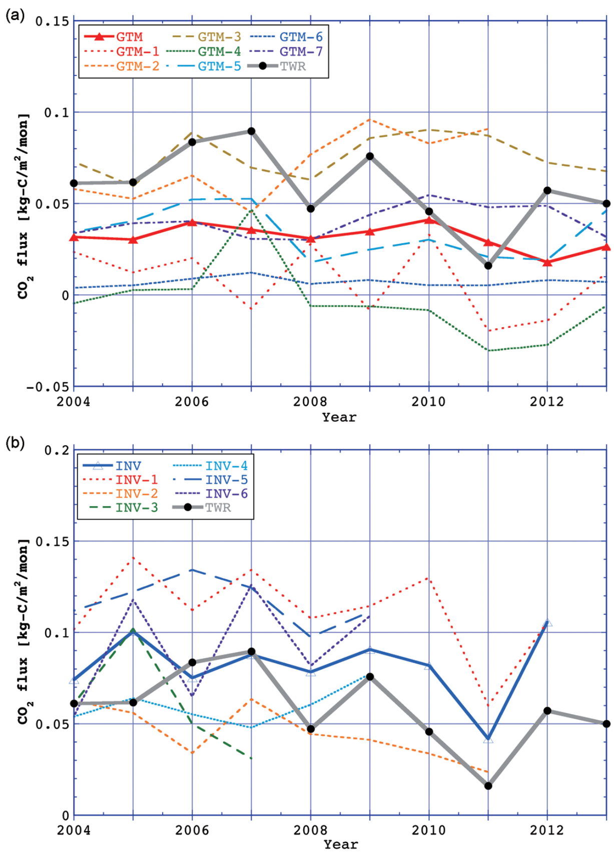

Fig. 7. 2. 14 The interannual variations of atmosphere-to-land CO_2 fluxes in July. (**a**) GTMand TWR, (**b**) INVand TWR. Units are kg Cm^{-2} $month^{-1}$ (Takata et al., 2017).

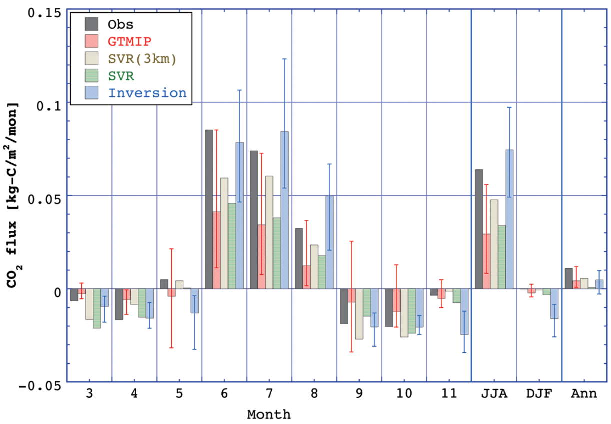

Fig. 7. 2. 13 The annual, seasonal and monthly mean atmosphere-to-land CO_2 fluxes averaged for 2004–2007 by TWR (black), GTM (red), SVR (light and dark green), and INV (blue). Error bars denote the ranges of the inter-model variations. Units are kg Cm^{-2} $month^{-1}$ (Takata et al., 2017).

on the target time scale and horizontal scale. In the future, by conducting a systematic investigation, such as conducting a comparative experiment with a common time scale and horizontal scale, the way to understand the CO_2 balance was shown.

7. 3. Ice mass change and the global sea level

Under the strong warming in the Arctic, small glaciers are going to disappear, and Greenland Ice Sheet will lose its ice mass through melting and discharge at the ice edge and then contribute to the global sea level rise. The Greenland ice sheet was losing mass at a rate accelerating from −121 Gt a^{-1} in 1993–2010 to −229 Gt a^{-1} in 2005–2010 (IPCC, 2013). The mass loss was most significant in southeastern Greenland at the beginning, and since 2005 mass loss has been spreading particularly to northwestern coast. Here, in the GRENE Arctic Climate Change Project, main activities were concentrated to northwestern area of Greenland, where the investigations were limited before hands. Some activities were also done at the mountain glaciers, particularly in the East Siberia glaciers.

Field observations to monitor mass balance and clarify the mechanism of mass balance, Greenland

Coastal regions of Greenland contain a number of glaciers and ice caps (GICs), which are physically separated

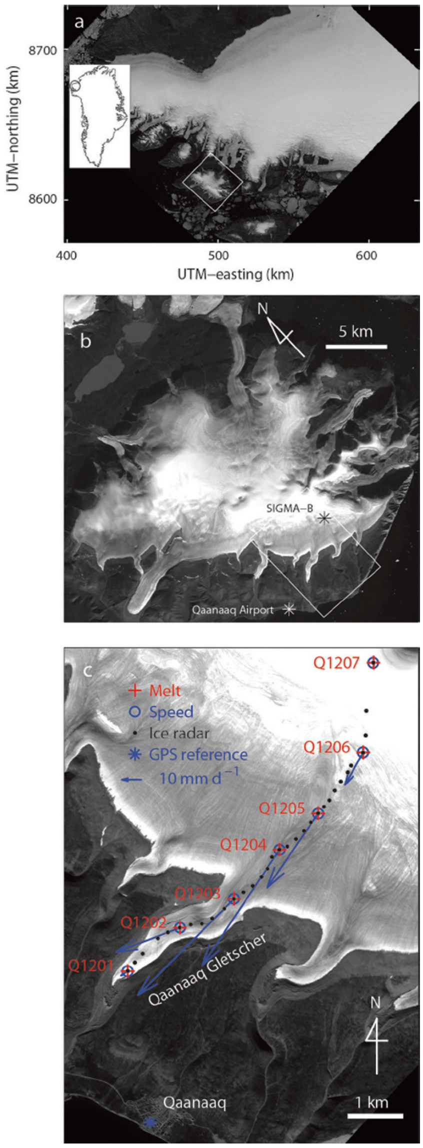

Fig. 7. 3. 1 (a) Satellite image (Landsat, 5 February 1999) showing northwestern Greenland including Qaanaaq. The inset shows the location of the region in Greenland, and the box indicates the area shown in (b). (b) Satellite image of QIC (ALOS PRISM, 25 August 2009). The locations of Qaanaaq Airport and the temperature measurement site on the ice cap (SIGMA-B) are indicated by asterisks. The box indicates the area covered by (c). (c) Satellite image (ALOS PRISM, 25 August 2009) of the study site, showing the locations of the measurement sites for surface melt (+), ice velocity (*), ice radar (*) and the GPS reference station (*). The arrows are horizontal surface flow vectors from 18 to 29 July 2012 (Sugiyama et al., 2014).

from the Greenland ice sheet. The total area of these ice bodies (1.3 × 10^5 km^2) accounts for 7% of the entire ice cover over Greenland, so their volume change has substantial influence on sea-level rise. Because GICs are located at relatively lower elevations, they are susceptible to the recent strong warming trend in Greenland.

Sugiyama et al. (2014) reported melt rates, ice velocity and ice thickness of Qaanaaq ice cap (QIC) as the results

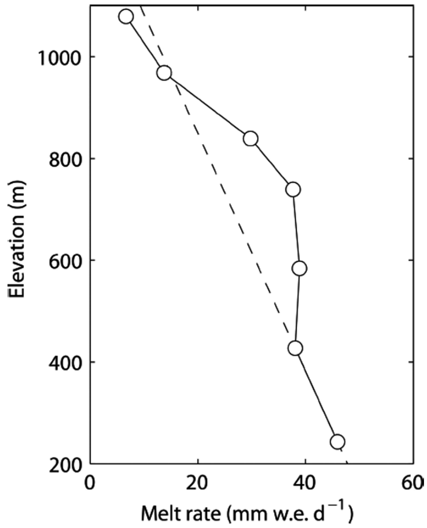

Fig. 7. 3. 2 Mean melt rate at Q1201–Q1207 measured over the periods indicated in Table 1. The dashed line is the extrapolation of the line connecting the data at Q1201 and Q1202 (Sugiyama et al., 2014).

of the initial glaciological investigation on this ice cap in northwestern Greenland. Qaanaaq ice cap (77°28’ N, 69°14’ W) is located in northwestern Greenland, covering an area of 289 km^2 and an elevation range of 30–1110 m a. s. l. over the central part of a peninsula (Fig. 7.3.1). A number of outlet glaciers protrude from the ice cap for distances of 1–10 km. The study site in the 2012 summer field campaign was Qaanaaq Gletscher, which flows southwest from the southern part of the ice cap (Fig. 7.3.1c). The field observations were performed along a survey route, which follows a glacier flow line from one of the highest peaks of the ice cap to the terminus of Qaanaaq Gletscher. Melt rates measured ranged from 7 mm w. e. d^{-1} at the ice-cap summit to 46 mm w. e. d^{-1} at the lowermost site. The mean rate of the seven sites was 30 mm w. e. d^{-1}. The rates were greater down-glacier in general, but the relationship to elevation was not simple as seen in Fig. 7.3.2. The melt rate obtained near the terminus of Qaanaaq Glettscher (46 mm d^{-1}) is comparable to the values reported for mid-latitude glaciers. The observed melt rates represented midsummer melt conditions on QIC over the last several years. This ice surface over the region including Q1203–Q1205 was covered by dark materials, and thus absorbed more solar radiation as a result of low albedo. The spatial variation in surface reflectance was clearly observed by in situ visual observations (Fig. 7.3.3). Darkening of the glacier surface had been reported in many glaciers in the world, including marginal regions of the Greenland ice sheet as already shown in Section 3. 4. Such changes in ice surface con-

Fig. 7. 3. 3 Photographs showing (a) clean and (b) dark ice surface conditions on QIC. Photographs were taken (a) at Q1201 viewing up-glacier on 18 July 2012 and (b) at the middle reach of Q1203 and Q1204 viewing down-glacier on 22 July 2012 (Sugiyama et al., 2014).

ditions resulted in melt increase due to the reduction in albedo, and thus accelerate mass loss of glaciers and ice sheets.

The flow vectors of ice motion are shown in Fig. 7.3.1c. Ice flowed faster in the middle part of the survey route, where ice was expected to be thick. The greatest horizontal velocities were observed at Q1203 (67.5 mm d^{-1}) and Q1204 (69.0 mm d^{-1}), and from that region the velocity progressively decreased down- and up-glacier. Flow velocity was only 4.0 mm d^{-1} at the lowermost site Q1201 ~500 m from the terminus. Vertical ice motion was downward except for Q1201, where ice emerged at a rate of 0.9 mm d^{-1}. The continuous GPS measurement at Q1203 had shown significant ice velocity variations within the range 36–94 mm d^{-1}, equivalent to 50–140% of the mean velocity (Fig. 7.3.4). The variations were diurnal, with minimum and maximum velocities in early morning and late afternoon, respectively. Diurnal flow velocity variations at Q1203 imply that surface meltwater drained to the bed through cold ice and enhanced basal motion. Thus, at least a part of the glacier bed is melting in this region. This observation contradicted the wholly

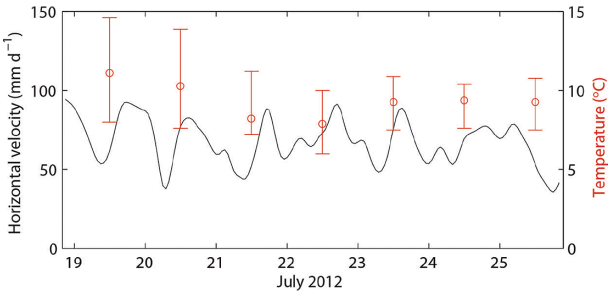

Fig. 7. 3. 4 Horizontal ice velocity variations at Q1203 and daily mean temperature with its variation range measured at Qaanaaq Airport (Sugiyama et al., 2014).

frozen ice temperature computed by the numerical model. Melt water should had been routed through ice to the bed, although surface annual mean air temperature was far below the melting point (below −8°C at the terminus).

To better understand the processes controlling recent mass loss of peripheral glaciers and ice caps in northwestern Greenland, Tsutaki et al. (2017a) measured surface mass balance (SMB), ice velocity and near- surface ice temperature on Qaanaaq Ice Cap in the summers of 2012–16. The measurements were performed along a survey route spanning the terminus of an outlet glacier to the upper reaches (243–968 m a.s.l.). The most negative SMB was observed in 2014/15, whereas the most positive was in 2012/13 (Fig. 7.3.5a). For example, SMB at Q1201 in 2014/15 was 1.8 times more negative than in 2012/13. The ice-cap-wide SMB ranged from −1.10± 0.29 to −0.13±0.26 m w.e. a^{-1} for the years from 2012/13 to 2015/16, and the mean glacier-wide SMB from 2012 to 2016 was −0.22±0.30 m w.e. a^{-1}. Mass balance showed substantially large fluctuations over the study period under the influence of summer temperature and snow accumulation. The equilibrium line altitude was 862±8, 868±19, 1001±12 and 932±9 m a.s.l. for the balance years from 2012/13 to 2015/16. Ice velocity (Fig. 7.3.6) showed seasonal speedup only in the summer of 2012, suggesting an extraordinary amount of meltwater penetrated to the bed and enhanced basal ice motion. Ice temperature at a depth of 13 m was −8.0°C at 944 m a.s.l., which was 2.5°C warmer than that at 243 m a.s.l., suggesting that ice temperature in the upper reaches was elevated by refreezing and percolation of meltwater. Our study provided in situ data from a relatively unstudied region in Greenland, and demonstrated the importance of continued monitoring of these processes for longer timespans in the future.

Kinematic GPS measurements provide in-situ data

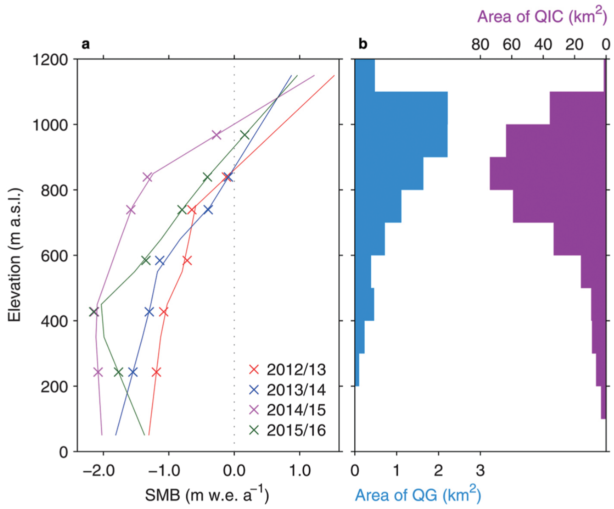

Fig. 7. 3. 5 (a) Measured SMB at Q1201–Q1206 (cross) and the SMB gradient every 100 m bin for the balance years 2012/13–2015/16. (b) Hypsometry of QG (blue) and QIC (purple) with altitude bands of 100 m (Tsutaki et al., 2017a).

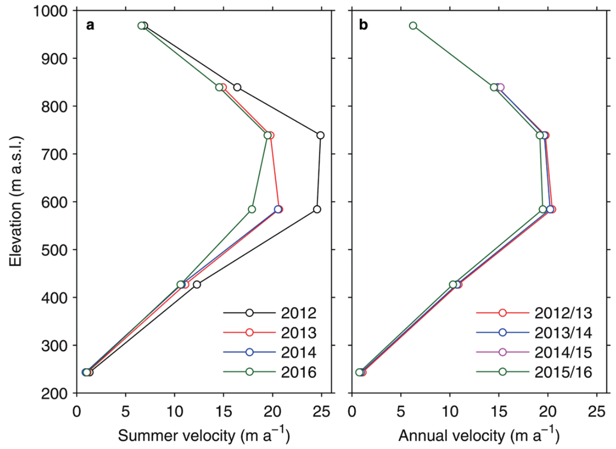

Fig. 7. 3. 6 (a) Summer ice flow velocity measured at Q1201–Q1206 in 2012–16. (b) Annual mean ice flow velocity at Q1201–Q1206 in 2012/ 13–2015/16 (Tsutaki et al., 2017a).

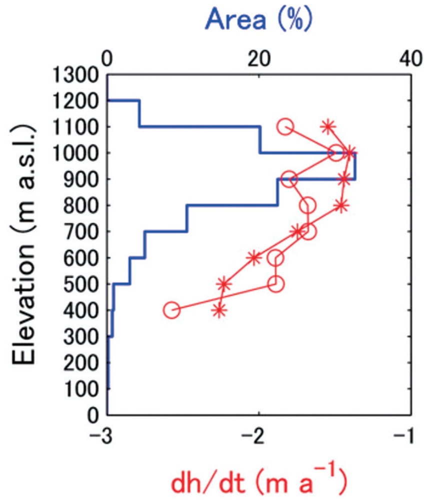

Fig. 7. 3. 7 The mean rate of elevation change on HIC analyzed with a grid resolution of 500 m (○), generated DEMs of 100 m (*). The blue line indicates the hypsometry of the ice cap surface shown in 100 m altitude bins (Saito, J. et al., 2016).

crucial for measuring the surface elevation change of glaciers. Owing to their accuracy, which is generally better than half meter, surface elevations derived from kinematic GPS surveys are useful and essential for generating precise digital elevation models (DEMs) and evaluating geometry changes of glaciers. Tsutaki et al. (2017b) presented a surface elevation data set derived from kinematic GPS measurements covering the lower 5 km of Qaanaaq and Bowdoin Glaciers in northwestern Greenland. The data included elevations over ice-free terrain nearby the glaciers, important for calibrating remote sensing data. More than 600,000 GPS survey data points were processed to produce a 1-m resolution mesh grid of elevation data in a CSV file format. Based on our error analysis, the accuracies of the elevation data were better than 0.2 and 0.3 m in horizontal and vertical directions, respectively. This dataset can be utilized to investigate glacier surface elevation changes by making comparison with DEMs obtained in the past, and from future remote sensing and in-situ observations.

These data were also provided to the International communities (Machguth et al., 2016). Glacier surface mass-balance measurements on Greenland started more than a century ago, but no compilation exists of the observations from the ablation area of the ice sheet and local glaciers. Such data could be used in the evaluation of modeled surface mass balance, or to document changes in glacier melt independently from model output. Here, Machguth et al. (2016) present a comprehensive database of Greenland glacier surface mass-balance observations from the ablation area of the ice sheet and local glaciers. The database spans the 123 a from 1892 to 2015, contains a total of ~3000 measurements from 46 sites, and is openly accessible through the PROMICE web portal (http://www.promice.dk).

Ice loss of Greenland by satellite measurements

Saito, J. et al. (2016) presented the surface elevation changes of six ice caps near Qaanaaq in northwestern Greenland based on DEMs generated from the Advanced Land Observing Satellite, Panchromatic Remote-sensing Instrument for Stereo Mapping (ALOS PRISM) stereo pair images. They quantified volume changes of the ice caps during periods between 2006 and 2010. The magnitude of the elevation change generally decreased from

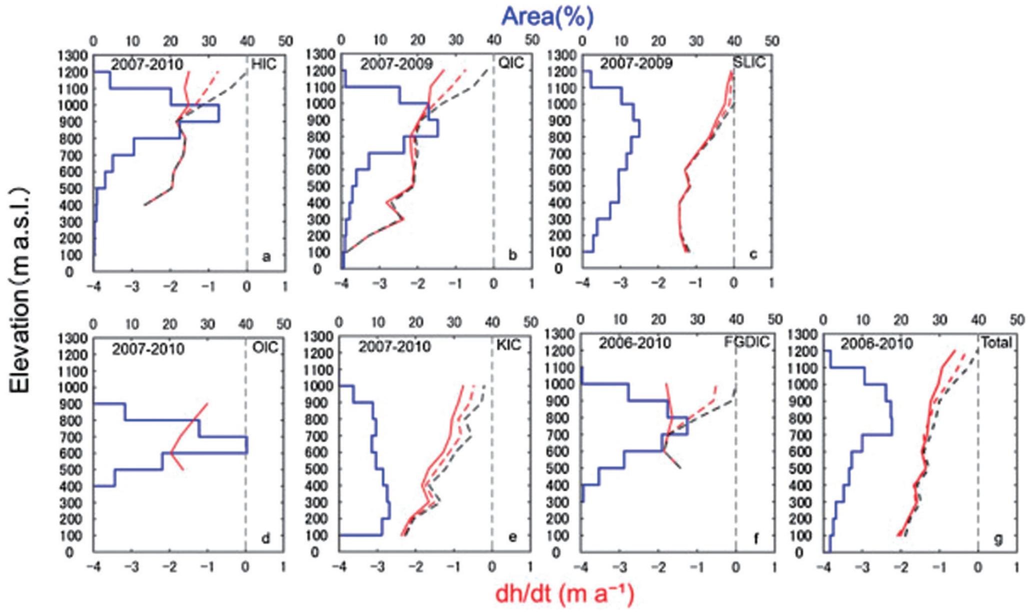

Fig. 7. 3. 8 The rate of elevation change averaged in each elevation band (red and black) and hypsometry (blue) of the studied ice caps as shown in 100 m altitude bins. Results are shown for each individual ice cap (a–f) and the entire study area (g). Elevation change in snow covered high elevation area was assumed as zero (black) or extrapolated from the data in lower elevation (red line). The red dashed line indicates the mean of these two estimates (Saito, J. et al., 2016).

high to lower elevation, and the rates of the change obtained at every 100 m elevation range agreed each other within 4–25% (Fig. 7.3.7). Based on these results, they assumed that their analysis with 500-m-resolution DEMs was sufficient to quantify total mass loss of the ice caps and its dependence on surface elevation. All of the ice caps had lost ice mass during this period, with a mean elevation change rate averaged all over the analyzed ice cap surface area (1215 km^2) of -1.1 ± 0.1 m a^{-1}. The mean rate over each individual ice cap ranged from -1.8 to -0.8 m a^{-1}, with the greatest thinning rate observed on Qaanaaq Ice Cap (QIC). Compared to the other five ice caps, the elevation change on Steensby Land Ice Cap (SLIC) was relatively small. The ice caps had thinned in the entire elevation range, but more significantly in lower elevation areas (Fig. 7.3.8). For example, at QIC, the mean elevation change rate in the area below 100 m a.s.l. was -3.9 m a^{-1}, whereas between 1000 and 1100 m a.s.l. it was -1.7 m a^{-1}. This reduction in surface elevation indicated significant ice cap thinning and mass loss. The rate of the total volume change of the six ice caps was -1369×10^6 m^3 a^{-1}, equivalent to a mass loss of 1.2 ± 0.1 Gt a^{-1}, amounting to a sea-level-rise of 0.0032 ± 0.0002 mm a^{-1}.

The mean rate of elevation change over the six ice caps (1215 km^2) was -1.1 ± 0.1 m a^{-1} for the 2006–2010 period. This rate was 1.8 times greater than that reported for GICs in northwestern Greenland (4340 km^2) for the 2003–2008 period (-0.6 ± 0.1 m a^{-1}) ("North-west sector" in Bolch et al., 2013). Because the mean elevation was higher in this study, the obtained greater thinning rate was not due to enhanced thinning in lower elevation, but likely represented a change in time from 2003–2008 to 2006–2010. This result indicated that the mass loss of GICs in northwestern Greenland was increasing in recent years. This was consistent with the increase in ice mass loss in this region since 2005 (Khan et al., 2010). Moreover, thinning rates obtained in this study were significantly greater than those observed on GICs in other regions at similar latitudes (74°–82°N), in Svalbard (0.12 m a^{-1} for 2003–2008; Moholdt et al., 2012) (0.27 m a^{-1} for 2001–2010; Zemp et al., 2015) and the Canadian Arctic Archipelago (0.27 m a^{-1} for 2003–2009; Nilsson et al., 2015). The recent increase in mass loss agreed with a warming trend in the region studied, which was represented by 10% increase in the summer positive degree-days (PDD) from 2003–2008 to 2006–2010. Moreover, reduction in ice and snow surface albedo should have enhanced melt rates and negative surface mass balance. The ice caps in this study showed significantly different rates of surface elevation change, which was probably affected by spatially varying precipitation rates as well as ice cap surface albedo, but this was not fully interpreted in this study.

Satellite images were analyzed by Sakakibara and Sugiyama (2018) to measure the frontal positions and ice

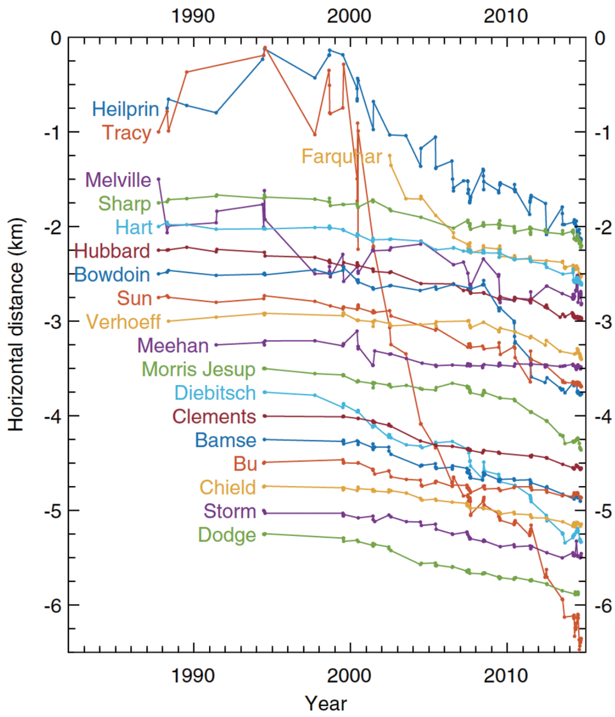

Fig. 7. 3. 9 Cumulative frontal displacements of the studied glaciers from the 1980s to 2014. Upward change in the ordinate represents glacier advance (Sakakibara and Sugiyama, 2018).

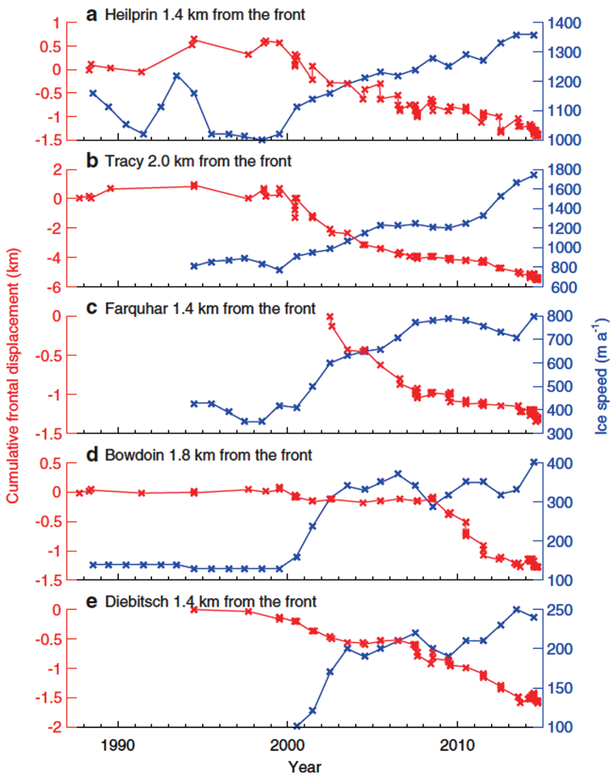

Fig. 7. 3. 10 (a) Cumulative frontal displacement (red) and annual ice speed of Heilprin, (b) Tracy, (c) Farquhar, (d) Bowdoin and (e) Diebitsch Glaciers. The speed was measured near the front (distance approximately equal to a half glacier width) along the glacier centerline (Sakakibara and Sugiyama, 2018).

speeds of 19 marine- terminating outlet glaciers along the coast of Prudhoe Land, northwestern Greenland from 1987 to 2014. To measure glacier front positions and ice flow speed, they used satellite images of the Landsat 8 Operational Land Imager (OLI) (level 1 T, with 15/30 m resolutions, 2013/14), the Landsat 7 Enhanced Thematic Mapper Plus (ETM+) (level 1T, with 15/30 m resolutions, 1999–2014), and the Landsat 4 and 5 Thematic Mapper (TM) (level 1T, with 30 m resolution, 1987–98) distributed by the US Geological Survey. All the studied glaciers retreated over the study period at a rate of between 12 and 200 m a^{-1}, with a median (mean) retreat rate of 30 (40) m a^{-1} (Fig. 7.3.9). The glacier retreat began in the year ~2000, which coincided with an increase in summer mean air temperature from 1.4 to 5.5°C between 1996 and 2000 in this region. Tracy Glacier retreated most rapidly during the study period (Fig. 7.3.9). The glacier advanced by 0.7 km between 1987 and 1999, and then retreated by 4.8 km from 1999 to 2007. The retreat rate slightly decreased after 2007, but it increased again in 2011 and the glacier retreated by 1.0 km from 2011 to 2014. The total retreat distance from 1999 to 2014 was 5.7 km (Fig. 7.3.9). Ice speed near the front of the studied glaciers ranged between 10 and 1740 m a^{-1} in 2014, and many of them accelerated in the early 2000s. In general, the faster retreat was observed at the glaciers that experienced greater acceleration, as represented by Tracy Glacier, which experienced a retreat of 200 m a^{-1} and a velocity increase of 930 m a^{-1} during the study period. A possible interpretation of this observation was that flow acceleration induced dynamic thinning near the termini, resulting in enhanced calving and rapid retreat of the studied glaciers. It was hypothesized that atmospheric warming conditions in the late 1990s triggered glacier retreat in northwestern Greenland since 2000.

Fig. 7.3.10 compares the timing of frontal retreat with the flow acceleration of selected glaciers. Tracy Glacier accelerated twice in 1999–2005 (from 770 to 1230 m a^{-1} at 2.0 km from the most retreated front) and in 2010–14 (from 1250 to 1740 m a^{-1}) (Fig. 7.3.10b). The onset of the first speedup coincided with the disintegration of the glacier tongue shared with Farquhar Glacier, which occurred in the summer of 2001 (Fig. 3.4.10c). This disintegration affected ice speed of Farquhar Glacier as well. This interpretation assumed the frontal retreat as the triggering mechanism of the flow acceleration. The second proposed mechanism of flow acceleration was basal ice motion enhanced by increased meltwater input to the glacier bed. These data also suggested that glacier bed topography was important for understanding the spatial extent of flow acceleration. Flow acceleration of these glaciers was greater near the front, thus it enhanced stretching flow regimes along the glaciers and induced dynamic thinning. The termini of Heilprin, Tracy, Farquhar and Bowdoin Glaciers were close to the hydrostatic equilibrium condition during the retreat, suggesting that thinning of the glaciers resulted in ice flotation and rapid retreat. It was hypothesized that the general retreat trend in Prudhoe Land after 2000 was triggered by atmospheric warming, with five glaciers retreating more rapidly than the others under the influence of dynamic thinning induced by flow acceleration. Because it affects the spatial extent of flow acceleration as well as the glacier front stability, ocean and glacier bed geometry is an important controlling factor of future change in outlet glaciers in Greenland.

Mechanism of calving glacier

To better understand recent rapid recession of marine-terminating glaciers in Greenland, Sugiyama et al. (2015) performed satellite and field observations near the calving front of Bowdoin Glacier, a 3 km wide outlet glacier in northwestern Greenland. Former observations suggested that ice mass loss was spreading from the south to the northwest, so collecting data in this region was of crucial importance.

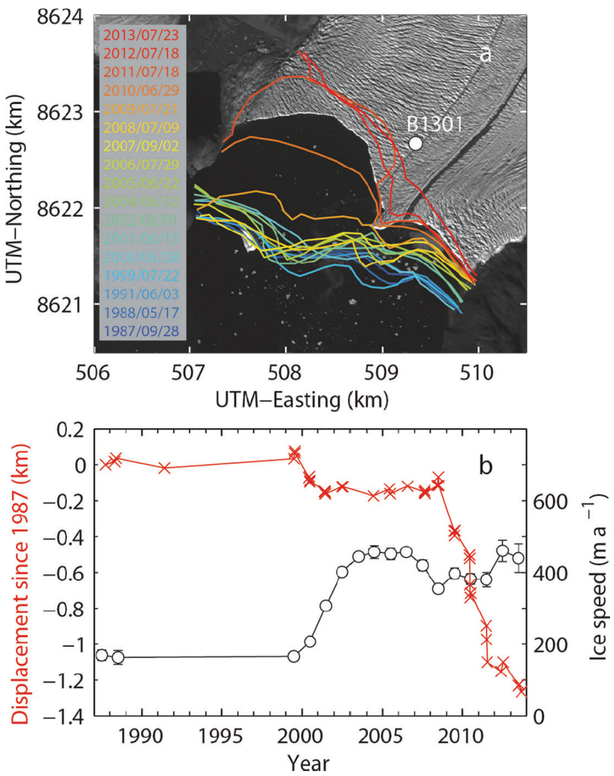

Fig. 7. 3. 11 (a) Mean displacement of the Bowdoin Glacier front position relative to 28 September 1987 (crosses), negative change in the ordinate represents glacier retreat, and annual mean ice speed at B1301 (empty circles). (b) Annual PDD (empty circles) at Thule Air Base, July and August mean SST at 77–78°N, 66–72°W (triangles) and sea- ice opening date in Bowdoin Fjord (filled circles). The sea-ice opening date is defined as the midpoint of the transition from 100% to 0% sea-ice cover, indicated by the vertical ranges associated with the data points (Sugiyama et al., 2015).

To investigate the recent frontal variations of Bowdoin Glacier, they analyzed 44 satellite images acquired in May–September between 1987 and 2013. These images were acquired by the Landsat 5 Thematic Mapper (TM) sensor, the Landsat 7 Enhanced Thematic Mapper Plus (ETM+) sensor and Landsat 8 Operational Land Imager (OLI) and were distributed by the United States Geological Survey (http://landsat.usgs.gov/). Satellite data revealed a clear transition to a rapidly retreating phase in 2008 from a relatively stable glacier condition that lasted for >20 years (Fig. 7.3.11). The terminus position had been fairly stable from 1987 to 2008, except for a 230 m retreat from 1999 to 2001. Rapid retreat then began between July 2008 and June 2009. The retreat rate decreased in 2011, but increased again in 2012. The mean retreat distance from July 2008 to September 2013 was 1.15 km (0.22 km a^{-1}).

Ice radar measurements showed that the glacier front was grounded, but very close to the floating condition. Ice thickness gradually increased up-glacier and reached 400 ±10 m at 5.3 km from the terminus. The transverse cross sections show typical glacier valley shapes, with a relatively flat bed in the glacier center and steeply inclined side-walls (Fig. 7.3.12b–d). The bed geometries were asymmetric along profiles T2 and T3, indicating the valley was deeper in the western half of the glacier (Fig. 7.3.12c and d). The radar measurements revealed that the glacier ice was deeply submerged below sea level (Fig. 7.3.12). Along the central flowline, ice below sea level accounted for 60–90% of the full ice thickness (Fig. 7.3.12a). Sea level at the glacier front was nearly equal to the ice flotation level, suggesting that the glacier terminus was grounded (Fig. 7.3.12a and b).

The lack of tidal vertical ice motion also indicated a grounded condition. Nevertheless, sea level was very close to the flotation level, suggesting that calving triggered by ice flotation regulated ice front position. This hypothesis was consistent with the previously proposed idea that the front position was controlled by the ice

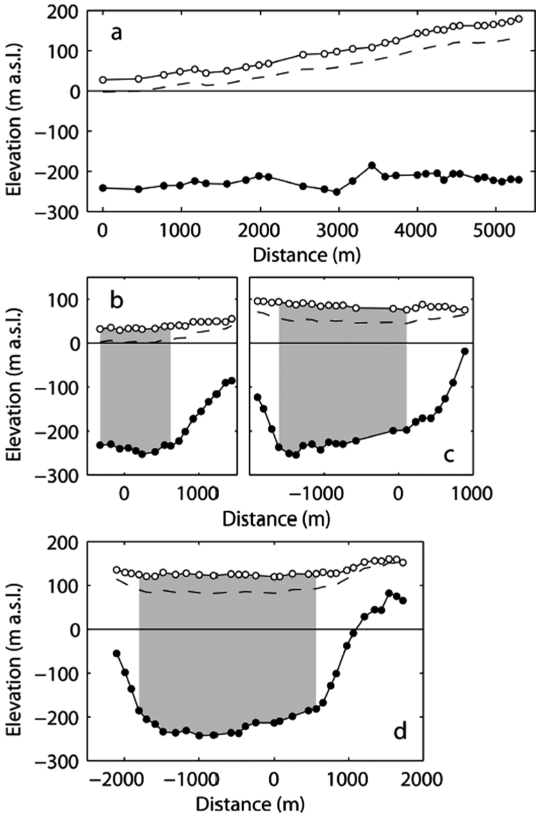

Fig. 7. 3. 12 Ice surface and bed elevations along the ice radar profiles, (a) profile L, (b) profile T1, (c) profile T2 and (d) profile T3. The dashed lines are the ice flotation levels computed with ice and sea-water densities of 910 and 1025 kgm^{-3}. The shaded regions are used to compute the fraction of ice thickness below sea level (Sugiyama et al., 2015).

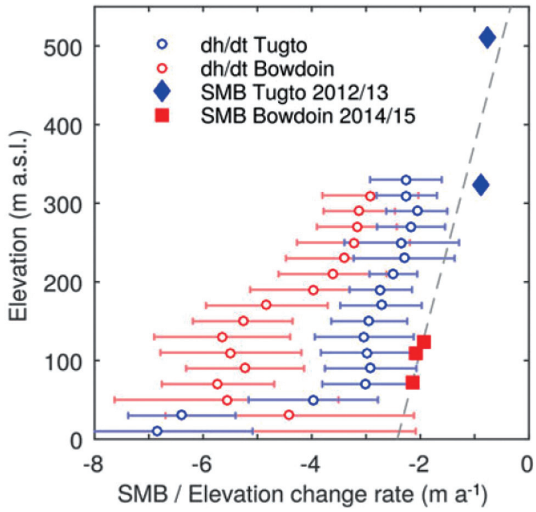

Fig. 7. 3. 13 Altitudinal distribution of surface mass balance (SMB) for Tugto Glacier in 2012/13 (blue diamonds) and Bowdoin Glacier in 2014/15 (red squares). Red and blue circles are mean rates of surface elevation change (dh/dt) of Bowdoin and Tugto Glaciers for 2007–10 for 20 m bins. The error bars indicate the standard deviations within the bins. Dashed line is the linear regression of SMB data on Tugto and Bowdoin Glaciers (Tsutaki et al., 2016).

thickness above flotation and rapid retreat of a calving glacier was initiated by thinning of ice (Van der Veen, 1996). Near the calving front, ice progressively thinned as it flew down-glacier under the influences of stretching ice flow and surface melting. Presumably, calving occurred when ice became thinner than the threshold and sea level reached the flotation level. These results, in combination with the results of ocean depth soundings, suggested bed geometry in front of the glacier was the primary control on the rate and pattern of recent rapid retreat.

Presumably, glacier thinning due to atmospheric and/or ocean warming triggered the initial retreat. In situ measurements showed complex short-term ice speed variations, which were correlated with air temperature, precipitation and ocean tides. Ice speed quickly responded to temperature rise and a heavy rain event, indicating rapid drainage of surface water to the bed. Semi-diurnal speed peaks coincided with low tides, suggesting the major role of the hydrostatic pressure acting on the calving face in the force balance. These observations demonstrate that the dynamics of Bowdoin Glacier are sensitive to small perturbations occurring near the calving front.

To quantify recent thinning of marine-terminating outlet glaciers (tidewater glaciers) in northwestern Greenland, Tsutaki et al. (2016) carried out field and satellite observations near the terminus of Bowdoin Glacier. Satellite images were used for the photogrammetric analysis. Panchromatic Remote-sensing Instrument for Stereo Mapping (PRISM) images from the Advanced Land Observing Satellite (ALOS) have a spatial resolution of 2.5 m, which is sufficient to measure several meters of glacial elevation change. These data were used to compute the change in surface elevation from 2007 to 2013 and this rate of thinning was then compared with that of the adjacent land-terminating Tugto Glacier, as shown in Fig. 7.3.13. Comparing DEMs of 2007 and 2010 shows that Bowdoin Glacier is thinning more rapidly (4.1±0.3 m a^{-1}) than Tugto Glacier (2.8±0.3 m a^{-1}). The thinning rate of Bowdoin Glacier was 1.5 times greater than that of land-terminating Tugto Glacier. Because Bowdoin and Tugto Glaciers are only ~3 km apart and at a similar altitude range, it would be expected that the surface melt induced thinning to be similar. Moreover, the negative SMB observed in this study accounts for only <40% of the surface elevation change on Bowdoin Glacier for 2007–10. This implies that the rapid thinning of Bowdoin Glacier is affected by ice dynamics. To quantify the con-

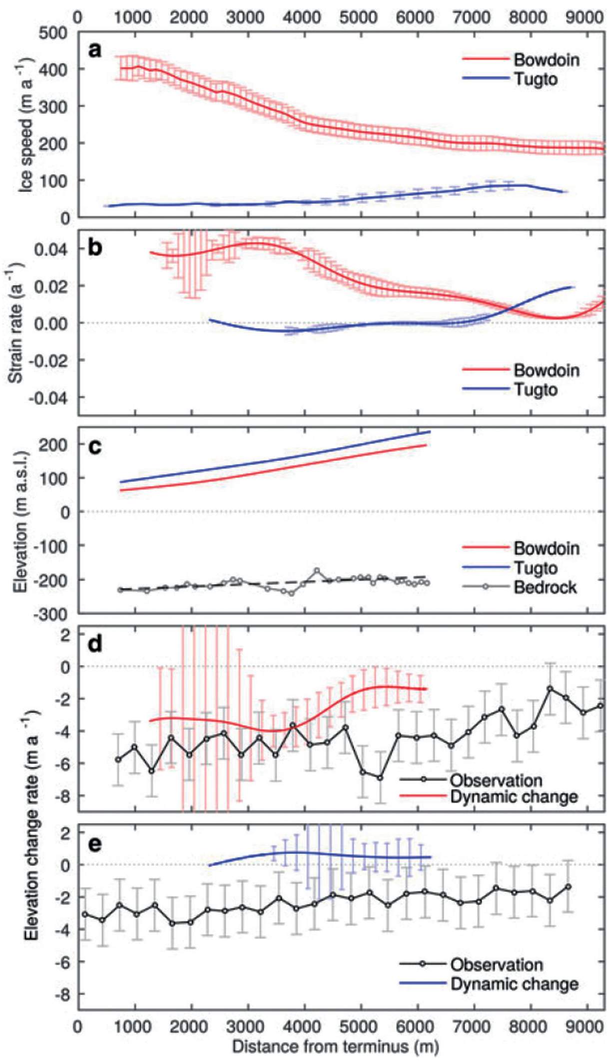

Fig. 7. 3. 14 (a) Surface ice speed and (b) longitudinal strain rate averaged over 2007–13 along the flowlines on Bowdoin and Tugto Glaciers. The strain rate was filtered with a local regression smoothing routine with a bandwidth of 700 m (Tsutaki et al., 2016).

tribution of ice dynamics to the observed thinning, the ice flow speed of Bowdoin and Tugto Glaciers were analyzed.

Fig. 7.3.14a shows the mean flow speed for 2007–13 along the flowline of Bowdoin and Tugto Glaciers. The ice speed of Bowdoin Glacier increased towards the glacier front, reaching 457 m a^{-1} near the calving front, indicating a stretching ice flow regime in the region. Within ~3500 m of the front of Bowdoin Glacier, crevasses were formed perpendicular to the ice flow direction as observed in satellite images. Formation of the transverse crevasses was an indication of a longitudinal stretching ice flow regime, which was typically observed near the front of calving glaciers. On the other hand, a decrease in speed toward the terminus of Tugto Glacier indicated a compressive flow regime. To examine the influence of these contrasting flow regimes of marine- and land-terminating glaciers on ice thinning, they calculated longitudinal strain rate along the flowline of Bowdoin and Tugto Glaciers (Fig. 7.3.14b). At Bowdoin Glacier, the strain rate increased down-glacier and reaches ~0.043 a^{-1} ~4000 m from the terminus. It is likely that this dynamically-controlled thinning has been enhanced by the acceleration of the glacier since 2000. The measurements indicated that ice dynamics indeed play a predominant role in the rapid thinning of Bowdoin Glacier.

From the ice speed measurements carried out on Bowdoin Glacier by Sugiyama et al. (2015), short term speed variations were found, correlating with air temperature and precipitation on the synoptic time scale, and with the semi-diurnal ocean tides. These observations led to the assumption that the glacier flow is sensitive to (1) water input at the surface rapidly drained to the bed, resulting in basal lubrication, and (2) changes in the force balance at the calving front. In order to simulate these processes, Seddik et al. (2019) set up two series of numerical experiments, in which the sensitivity of the glacier flow was tested to increased basal lubrication (reduced drag) as well as varying sea level in the range of the tidal amplitude. It was found that the tested range of reduced basal drag (10–40%) approximately covers the strength of the observed episodic speed-ups at the site. The simulated response of the glacier flow to ocean tides is most pronounced near the calving front and decays to almost zero a few kilometers upstream. It was also found that, in agreement with the observations, the tidal forcing and the surface speed are in anti-phase: High tide corresponds to low speed, and low tide corresponds to high speed. However, the mean speed was underpredicted by ~ 20%, and, more severely, the semi-diurnal speed amplitude was underpredicted by a factor ~ 3. This study investigated only the present dynamics of Bowdoin Glacier by means of diagnostic simulations. Further modeling work would be desirable to improve the understanding of the changes of the glacier in the recent past (Tsutaki et al., 2016) and, ultimately, to predict the future evolution of the glacier under warming scenarios for the atmosphere and the ocean.

Cryoseismology

Glacier microseismicity is a promising tool to study glacier dynamics. However, physical processes connecting seismic signals and ice dynamics are not clearly understood at present. Particularly, the relationship between tide-modulated seismicity and dynamics of calving glaciers remains elusive. Here, Podolskiy et al. (2016) analyzed records from an on-ice seismometer placed 250 m from the calving front of Bowdoin Glacier, Greenland. Using high-frequency glacier flow speed measurements, they showed that the microseismic activity was related to strain rate variations. The seismic activity correlated with longitudinal stretching measured at the glacier surface. Both higher melt rates and falling tides accelerated glacier motion and increased longitudinal stretching. Long-term microseismic monitoring could therefore provide insights on how a calving glacier's force balance and flow regime react to changes at the ice-ocean interface.

Kanao et al. (2012) also discussed the relation of Greenland Ice Sheet dynamics and glacial earthquake activities as a Cryoseismology, and contributed to the Greenland Ice Monitoring Network (GLISN).

Glacier change affecting ocean

Glacial meltwater discharge from the Greenland ice sheet and ice caps forms high turbidity water in the proglacial ocean off the Greenland coast. Although the timing and magnitude of high turbidity water export affect the coastal marine environment, for example, through impacts on biological productivity, little is known about the characteristics of this high turbidity water. Ohashi et al. (2016) reported on the spatial and temporal variations in high turbidity water off the Thule region in northwestern Greenland, based on remote sensing reflectance data at a wavelength of 555 nm (Rrs555). Rrs555 data used for this study were obtained from the NASA Moderate Resolution Imaging Spectroradiometer (MODIS) on the Aqua multispectral platform. They used the level three data with a spatial resolution of about 0.0417° and temporal resolution of eight days. The period of analysis was from July to August (the period corresponding to open water in summer) during 2002–2014. These data products were downloaded from NASA's Ocean ColorWeb (http://oceancolor.gsfc.nasa.gov). The high turbidity area, identified on the basis of high reflectivity (Rrs555 >= 0.0070 sr^{-1}), was generally distributed near the coast, where many outlet glaciers terminated in the ocean and on land (Fig. 7.3.15). Particularly in Wolstenholme Fjord, Rrs555 values were notably high (0.007–0.01 sr^{-1}) near the coast, but were relatively low (less than 0.004 sr^{-1}) in the offshore region away from the ice sheet.

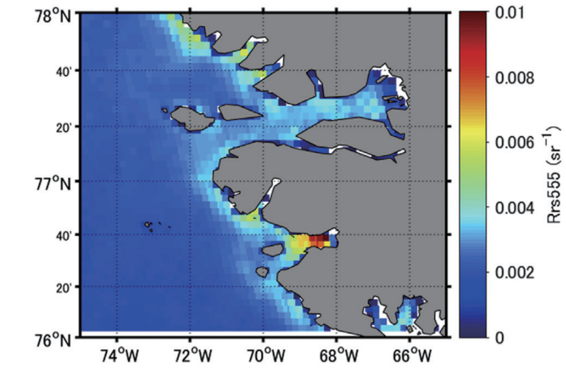

Fig. 7. 3. 15 Rrs555 values averaged from 2002 to 2014 (Ohashi et al., 2016).

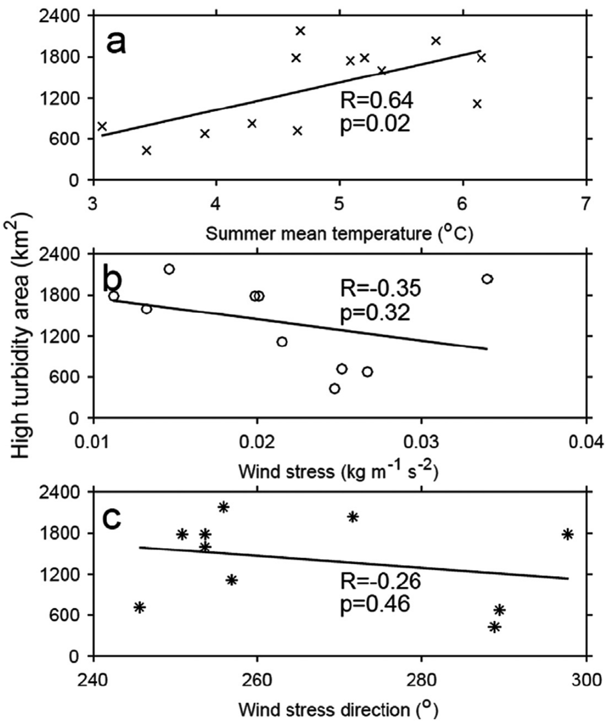

Fig. 7. 3. 16 Scatter plots of annual maximum extent of the high turbidity area and (a) summer mean temperature, (b) wind stress, and (c) wind stress direction from 1 July to the timing of annual maximum extent. Solid lines show linear regression of the data (Ohashi et al., 2016).

The extent of the high turbidity area exhibited substantial seasonal and interannual variability, and its annual maximum extent was significantly correlated with summer air temperature (Fig. 7.3.16). This positive correlation suggests that the amount of turbid glacial meltwater input increased because of increasing amount of surface melting. On the other hand, no clear correlation was observed between the turbid area and the strength/ direction of wind stress ($|R| < 0.4$, $p > 0.3$) (Fig. 7.3.16b and c). There was no significant correlation with zonal or meridional components of wind stress. These results suggested that sediment transport resulting from wind-induced upwelling had only minor influence on high turbidity water near the ocean surface. To summarize, the source of the turbid water observed off the Thule region was most likely the discharge of glacial meltwater, rather than re-suspension of sediments. Assuming a linear relationship between the high turbidity area and summer temperature, annual maximum extent increased under the influence of increasing glacial meltwater discharge, as could be inferred from present and predicted future warming trends.

Ice sheet modeling

In the Fourth Assessment Report (AR4) from the Intergovernmental Panel on Climate Change (IPCC), sea-level projections for the year 2100 ranged from 0.18 to 0.59 m, but these values excluded 'future rapid dynamical changes in ice flow' (IPCC, 2007). The additional caveat that these projections do not include 'the full effects of changes in ice-sheet flow, therefore the upper values of the ranges are not to be considered upper bounds for sea level rise' further weakened the utility of the projected ranges to drive policy decisions related to climate change. This situation resulted from the fact that no ice-sheet model could reproduce recent observed rapid changes in ice-sheet elevation and velocity, so there was no means to include the possible future evolution of these changes in a deterministic way. The IPCC AR4 conclusions regarding the difficulties in credibly projecting future sea level had focused the glaciological community's efforts to understand the cause of the observed changes in a deterministic way so that the causal processes could be included in ice-sheet numerical models.

One strategy to deal with this situation led to the project SeaRISE (Sea-level Response to Ice Sheet Evolution). Ten ice-sheet models were used to study sensitivity of the Greenland and Antarctic ice sheets to prescribed changes of surface mass balance, sub-ice-shelf melting and basal sliding (Bindschadler et al., 2013). Results exhibited a large range in projected contributions to sea-level change. In most cases, the ice volume above flotation lost was linearly dependent on the strength of the forcing. Combinations of forcings could be closely approximated by linearly summing the contributions from single forcing experiments, suggesting that nonlinear feedbacks were modest. The models indicated that Greenland is more sensitive than Antarctica to likely atmospheric changes in temperature and precipitation, while Antarctica is more sensitive to increased ice-shelf basal melting. An experiment approximating the Intergovernmental Panel on Climate Change's RCP8.5 scenario produced additional first-century contributions to sea level of 22.3 and 8.1 cm from Greenland and Antarctica, respectively, with a range among models of 62 and 14 cm, respectively. By 200 years, projections increased to 53.2 and 26.7 cm, respectively, with ranges of 79 and 43 cm. Linear interpolation of the sensitivity results closely approximated these projections, revealing the relative contributions of the individual forcings on the combined volume change and suggesting that total ice-sheet response to complicated forcings over 200 years could be linearized.

The SeaRISE effort explored the sensitivity of the current generation of ice sheet models to external forcing to gain insight into the potential future contribution to sea level from the Greenland and Antarctic ice sheets. All participating models simulated the ice sheet response to three types of external forcings: a change in oceanic condition, a warmer atmospheric environment, and enhanced basal lubrication. Here, Nowicki et al. (2013) presented an analysis of the spatial response of the Greenland ice sheet, and explored the impact of model physics and spin-up on the projections. Although the modeled responses were not always homogeneous, consistent spatial trends emerged from the ensemble analysis, indicating distinct vulnerabilities of the Greenland ice sheet. There were clear response patterns associated with each forcing, and a similar mass loss at the full ice sheet scale resulted in different mass losses at the regional scale, as well as distinct thickness changes over the ice sheet. All forcings led to an increased mass loss for the coming centuries, with increased basal lubrication and warmer ocean conditions affecting mainly outlet glaciers, while the impacts of atmospheric forcings affected the whole ice sheet.

Saito, F. et al. (2016) revisited the future surface climate experiments on the Greenland ice sheet proposed by the SeaRISE study (Bindschadler et al., 2013). The projections of the different SeaRISE participants showed dispersion, which has not been examined in detail to date. A series of sensitivity experiments were conducted and analyzed using the ice-sheet model for integrated Earth-system studies (IcIES) by replacing one or more formulations of the model parameters with those adopted in other model(s). The results showed that large potential sources of the dispersion among the projections of the different SeaRISE participants were differences in the initialization methods and in the surface mass balance methods, and both aspects had almost equal impact on the results. The treatment of ice-sheet margins in the simulation had a secondary impact on the dispersion. We concluded that spinning up the model using fixed topography through the spin-up period while the temperature was allowed to evolve according to the surface temperature history was the preferred representation, at least for the experiment configuration examined in the present paper. A benchmark model experimental setup that most of the numerical models could perform was proposed for future intercomparison projects, in order to evaluate the uncertainties relating to pure ice-sheet model flow characteristics.

Greve and Herzfeld (2013) applied the dynamic/thermodynamic shallow-ice model SICOPOLIS to the Greenland ice sheet. Paleoclimatic spin-ups from 125 ka BP until today, as well as future-climate experiments 500 years into the future, were carried out with three different grid spacings, namely 20, 10 and 5 km. The scenarios were a subset of those specified by the SeaRISE community effort. The bed topography included improved troughs for Jakobshavn Isbræ, Helheim, Kangerdlugssuaq and Petermann glaciers, processed by an algorithm that preserved shape, orientation and continuity of the troughs on the 5 km scale. Comparison of simulated and observed present-day surface velocities showed that these ice streams and outlet glaciers were resolved with different accuracies, ranging from poor (20 km grid) to reasonably good (5 km grid). In the future-climate experiments, the simulated absolute ice volumes depended significantly on the resolution, while the sensitivities (ice volumes relative to the constant-climate control run) varied only by a few centimeters of sea-level equivalent.

Observations of Mountain Glaciers

Mountain glaciers are small in volume compared to the Greenland ice sheet; therefore or however, they show rapid response to climate change compared to ice sheets and known as sensitive indicators of climate change. The glacial and mountain environments of the Arctic are changing drastically due to the recent intense warming; yet the Siberian glaciated region is one of the least studied areas in the whole Arctic. Shirakawa et al. (2016) outlined the meteorological and glaciological observations of Glcier No. 31 in the Suntar-Khayata Range, east Siberia, during 2012 and 2014 (Fig. 7.3.17). This region, located between 62° to 63°N and 140° to 142°E, forms a watershed between the Arctic Ocean and the Sea of Okhotsk. In the IGY (International Geophysical Year, 1957–58) period, the Soviet Union set up a weather station in Suntar-Khayata mountains, where observations continued for several winters (Koreisha, 1963). Some of the findings from the GRENE Arctic Project by Takeuchi et al. (2015) were already mentioned in Chapter 3. The

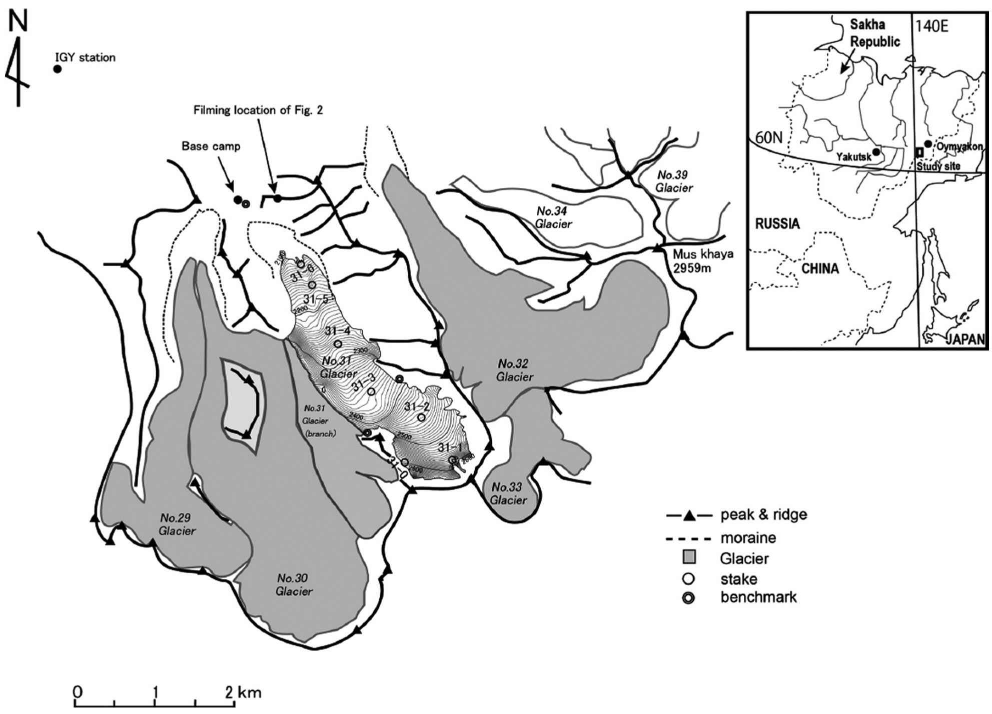

Fig. 7. 3. 17 Map showing the locations of observation sites of the GRENE Project in the Suntar-Khayata Range. On Glacier No. 31, the contour interval is 5 m. Open circles indicate glaciological observation sites in 2012, 2013 and 2014 (Shirakawa et al., 2016).

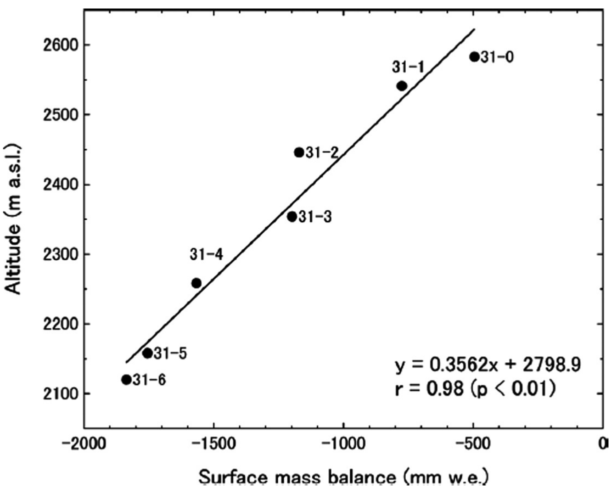

Fig. 7. 3. 18 Change with altitude of the surface mass balance of Glacier No. 31 from August 24, 2012 to August 16, 2013 (Shirakawa et al., 2016).

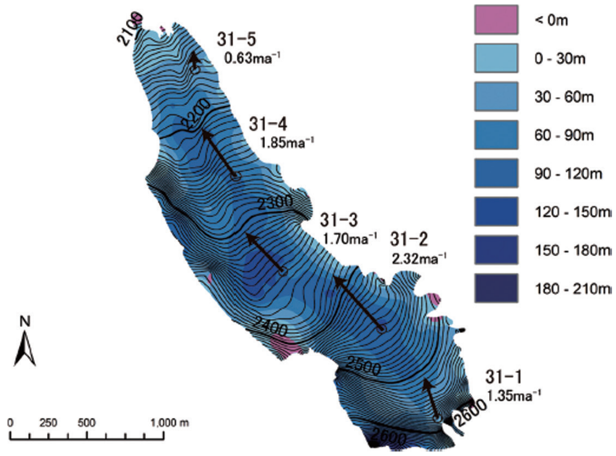

Fig. 7. 3. 19 Contour map of Glacier No. 31 derived from DEM data from August 2013. The arrow indicates the surface flow velocity from August 24, 2012 to August 16, 2013. The spatial distribution of ice thickness of Glacier No. 31 is also shown, measured by ice radar in August 2013 (Shirakawa et al., 2016).

mean air temperature between July 2012 and August 2013 was −13.9°C at site 31–2 (2240 m a.s.l.; Fig. 7.3.17) and the minimum temperature was −46.0°C. The air temperature on the glacier from November to April was approximately 10°C higher than that at Oymyakon village, where the lowest temperature in the northern hemisphere was recorded, suggesting a temperature inversion, which typically occurs during winter in this region. The snow depth records show that the snow increased at the beginning and end of winter, with almost no change from the beginning of October until the end of April. The maximum snow depth from the previous summer was 158 cm at site 31–2 on May 28, 2013.

The average annual surface mass balance for the 6 sites was −1256 mm water equivalent during the period from August 2012 to August 2013, indicating that ablation proceeded rapidly in all areas of the glacier. In the IGY period, there was an area of ice accumulation and an equilibrium-line altitude in the vicinity of 2350 m a.s.l. (Koreisha, 1963). However, in this study, all areas of the glacier were ablation areas. As shown in Fig. 7.3.18, there was a high correlation between the elevation and the mass balance of each site. From the regression equation obtained, the equilibrium-line altitude of this glacier was estimated to be 2799 m, significantly higher than in the IGY period. This result indicated that ablation was proceeding in all areas of the glacier.

The surface flow velocity in 2013/2014 was 1.57 m a^{-1} at the approximate midpoint of the glacier (Fig. 7.3.19), and was much slower than that measured during the IGY period (−4.5 m a^{-1}). The length and areal extent of the glacier were 3.85 km and 3.2 km^2 in 1958/59 and 3.38 km and 2.27 km^2 in 2012/13, respectively, showing a slight decrease over the last 54 years.

7. 4. Effect on ocean circulation

The Labrador Sea is one of the most prominent regions in the World Ocean where open ocean convection takes place. The open ocean convection reaches 1000–2300 m depth and forms Labrador Sea Water (LSW). Many studies have suggested the LSW influences the global climate, as it is one of the source waters for the North Atlantic Deep Water (NADW) and thus affects the Atlantic meridional overturning circulation. The winter time deep convection is preconditioned by weak stratification in the Labrador Current (LC) and the West Greenland Current (WGC). The smaller scale (~100–200 km) localized cyclonic circulation, which exposes water to wintertime heat loss for a longer period of time, also preconditions the deep convection in the western Labrador Sea.

The large scale cyclonic boundary current system (WGC and LC) transports buoyancy into the Labrador Sea. The Irminger Water (IW), which originates in the Irminger Sea, is relatively warm and salty and transported by WGC and LC in the subsurface along the continental slope. On the other hand, cold/fresh water, which is originated in the Greenland and Arctic Seas, is transported by WGC along the vicinity of the Greenland coast in the surface layer. This layered structure is also seen in the central Labrador Sea and formed by the eddy-induced lateral transport from the shelf region. Chanut et al.

(2008) classified the eddies into convective eddies (CEs), boundary current eddies (BCEs) and Irminger Rings (IRs). The CEs are generated by baroclinic instability of the rim current encompassing the convection area and more rapidly (less than two months) restratify the homogenized water columns than air-sea flux (~half year) does in the shallow layer.

The mesoscale eddies on the deep convection in the Labrador Sea are examined by Kawasaki and Hasumi (2014) using a realistically configured eddy-resolving ice-ocean model. The ice-ocean general circulation model employed in the study is CCO version 4 (Hasumi, 2015). The model domain is global. The model is formulated on the general curvilinear horizontal coordinates (see Fig. 5.4.4). Its poles are placed on the Labrador Peninsula and Greenland, and the horizontal resolution is eddy resolving (4–5 km) in the Labrador Sea, eddy permitting around the Cape Hatteras, Irminger and Greenland Seas (10–50 km), and coarse (> 50 km) in other regions. The sea surface heat, freshwater and momentum fluxes are calculated using a daily climatology of surface air properties based on the ECMWF reanalysis.

The cyclonic circulation including the WGC and LC, which are part of the North Atlantic subpolar gyre, is qualitatively well reproduced in the Labrador Sea. The three types of eddies (IR, BCE, CE) proposed by Chanut et al. (2008) are also well represented in the model.

In order to investigate the role of eddies in the deep convection, the model's buoyancy budget is analyzed here. Since the transported buoyancy inhibits the deep convection in winter and restratifies the homogenized water coloumns in summer, the year-round buoyancy transport should be analyzed. Fig. 7.4.1 shows the 5-year mean heat budget integrated vertically from the sea surface to the bottom. Heat is lost over the whole Labrador Sea through the sea surface (Fig. 7.4.1a). This is essentially due to the sea surface cooling in winter. In the boundary current region, heat is gained by the mean current (the WGC) and lost by eddies (Fig. 7.4.1b and c). On the other hand, the interior Labrador Sea gains heat by mesoscale eddies (Fig. 7.4.1c). The small residual (Fig. 7.4.1d) indicates that the model is well thermally equilibrated during the analyzed period.

The fresh water content (FW) is defined here as

$$\mathrm{FW} = \int (S_{\mathrm{ref}} - S)/S_{\mathrm{ref}}\, d\mathrm{V}, \qquad (7.4.1)$$

where V indicates the volume under consideration, S is salinity and S_{ref} is the reference salinity. The reference salinity is set to 34.8 g kg^{-1}, which is the average in the Labrador Sea. The budget of the vertically integrated fresh water content is shown in Fig. 7.4.2. Because of the melting of sea ice in early spring, the net sea surface freshwater flux is downward around the WGC and LC

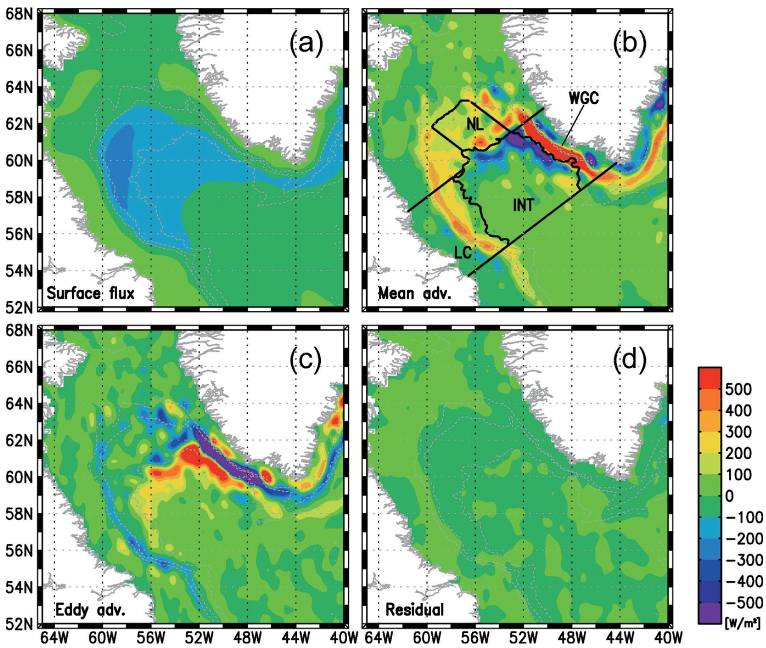

Fig. 7. 4. 1 Components in 5-year mean vertically integrated heat budget. (a) Sea surface flux, (b) mean advection, (c) eddy, and (d) residual. The positive and negative values mean the local heat gain and loss, respectively. The four boxes (WGC: West Greenland Current, NL: North Labrador Sea, INT: Labrador Sea interior, and LC: Labrador Current) are defined for quantitative analysis (Kawasaki and Hasumi, 2014).

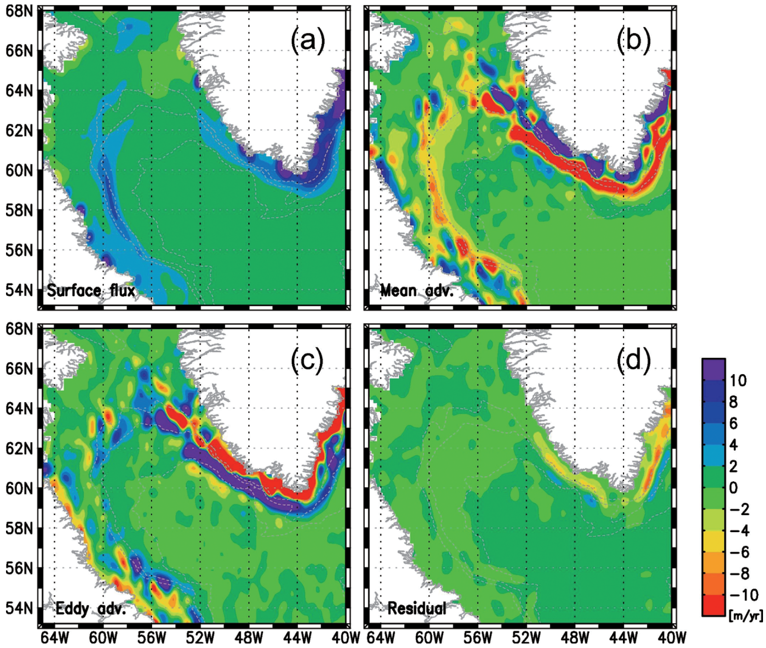

Fig. 7. 4. 2 Same as in Fig. 7. 4. 1 but for freshwater budget (Kawasaki and Hasumi, 2014).

(Fig. 7.4.2a). Several patches of upward freshwater flux along the coast are due to the freezing at coastal polynyas. The large downward sea surface freshwater fluxes along the coasts of Greenland and the Labrador Peninsula correspond to river runoff. Since the surface fresh water flux caused by sea ice does not extend to the interior Labrador Sea, the role of freshwater transport in controlling the deep convection is not affected by the biased distribution of sea ice along the western coast of Greenland (Fig. 7.4.2a). The WGC transports low salinity water on the west Greenland shelf, and high salinity water (IW) from the Irminger Sea on the continental slope (Fig. 7.4.2b). Mesoscale eddies transport high salinity water from the WGC toward the coast (Fig. 7.4.2c). The eddy-induced transfer of high of low salinity water does not extend to the interior Labrador Sea when vertically integrated over the whole depth, since the transport of fresh water in the surface layer and that of saltier water in the subsurface layer cancel each other (Fig. 7.4.2c). The small residual (Fig. 7.4.2d) means that freshwater content is well equilibrated during the analyzed period in the Labrador Sea. The heat and freshwater budgets in four regions (the boxes labeled as WGC, NL, INT and LC in Fig. 7.4.1) are calculated. In the WGC (West Greenland Current) box, the WGC imports seawater from the Irminger Sea. In the NL (North Labrador) box, the WGC and large eddy kinetic energy (EKE), which indicates active IRs, exist. The INT (interior) box corresponds to the area whose bottom is deeper than 3000 m in the central Labrador Sea. The LC (Labrador Current) box is the western boundary of the Labrador Sea, where EKE is not significantly large (less than 0.02 $m^2\ s^{-2}$) except for the noise accompanied by sea ice formation or melting near the Labrador coast

Buoyancy relative to reference state B, is decomposed into thermal and haline parts, B_q and B_S, respectively. In the buoyancy budget of the whole water column, the total advection (mean eddy) provides buoyancy by heat in almost all regions. Even considering mean and eddy advection separately, freshwater does not contribute to the buoyancy budget in the Labrador Sea for the whole-column view. However, buoyancy budget in the near surface layer (above 120 m depth) shows the different feature. In WGC box, both heat and freshwater comparably (57 and 46 × 10^4 N s^{-1}, respectively) contribute to the buoyancy injection in the total advection (mean plus eddy) (Fig. 7.4.3a and b). In the NL and LC boxes the freshwater contribution to the buoyancy (100 and 98 × 10^4 N s^{-1}, respectively) is larger than that induced by heat (69 and 42 × 10^4 N s^{-1}, respectively). In the north Labrador Sea (NL box), the freshwater and heat by mean advection mainly causes the buoyancy gain in the surface layer (Fig. 7.4.3d and e). Quantitative comparison shows that the buoyancy injection by mean advection of freshwater (91 × 10^4 N s^{-1}) is twice as large as that by mean advection of heat (42 × 10^4 N s^{-1}). In the LC box, the surface layer buoyancy gain is mainly contributed from the eddy0induced freshwater injection (162 × 10^4 N s^{-1}).

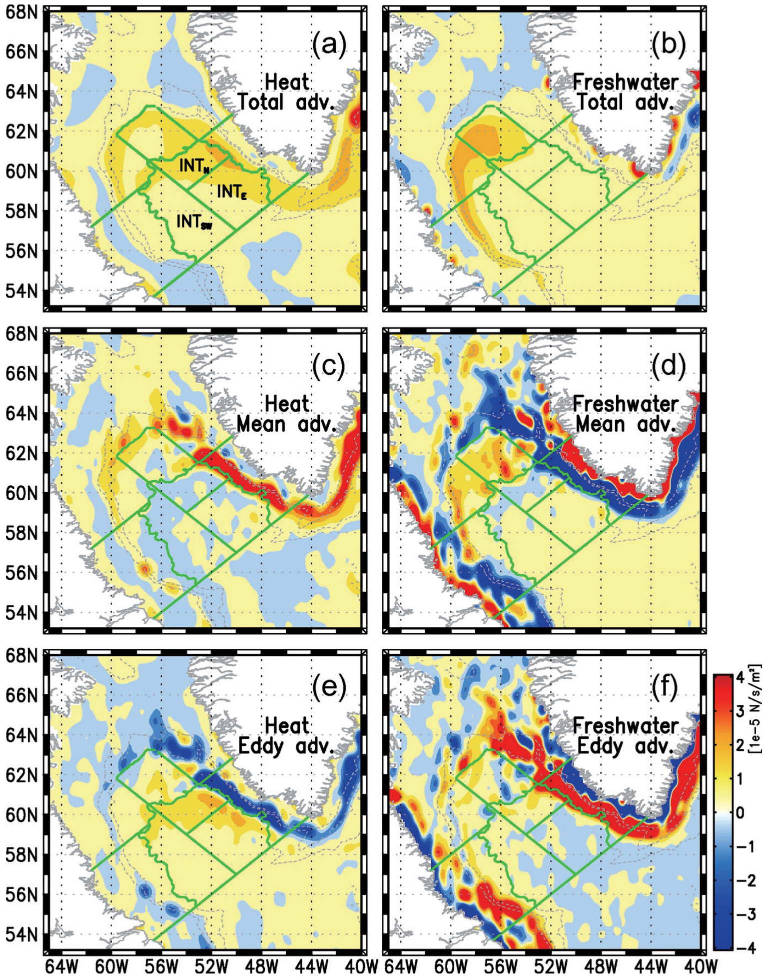

Fig. 7. 4. 3 Distribution of thermal contribution to vertically integrated gain or loss of buoyancy above 120 m depth. (a) Total of mean advection and eddy, (c) mean advection , and (e) eddy. (b), (d) and (f) are same as (a), (c) and (e), respectively, but for haline contribution. Three box (INT$_N$: northern INT, INT$_E$: eastern INT and INT$_{SW}$: southwestern INT) are defined for the qualitative analysis (Kawasaki and Hasumi, 2014).

In the INT box, the thermal buoyancy gain (199 × 104 N s^{-1}) is about three times larger than the haline buoyancy gain (73 × 104 N s^{-1}) for the total advection. However, while the eddy-induced thermal buoyancy transport spreads over the whole Labrador Sea interior, the eddy-induced haline buoyancy transport is confined to the northern Labrador Sea interior (Fig. 7.4.3e and f). The results show that the fraction of haline contribution is further significant in the northern part of the interior than that in the eastern and southwestern parts. This study directly points out that the contribution of freshwater to inhibiting the convection is important in the northern Labrador Sea for the first time.

A previous modeling study (McGeehan and Maslowski, 2011) failed to represent the low salinity water along the western coast of Greenland, and winter deep convection drastically and unrealistically developed in the northern Labrador Sea therein. Myers and Donnelly (2008) examined the roles of sea surface heat and freshwater fluxes in the interannual variability of formation of LSW, and they concluded that the buoyancy induced by freshwater is amaller than heat. Kawasaki and Hasumi (2014) studied the effect of both lateral transport and sea surface flux of heat and freshwater on the buoyancy in the central Labrador Sea, and the role of freshwater is not small than heat near the sea surface in the northern Labrador Sea. The freshwater provides in the upper 100 m of the interior Labrador Sea from March to September is ~30 cm in their result, which is half of observational estimates (Khatiwala et al., 2002). Existence of low salinity water near the sea surface would reduce oceanic heat low under cold air because strong neat surface stratification prevents heat uptake from depth and the sea surface is cooled immediately, as suggested by Geldeloos et al. (2012). Then, it is naturally expected that winter convection does not develop in the northern Labrador Sea even under the influence of the strong cold winds from the continent. If the model's underestimation of lateral freshwater flux is corrected, reproducibility of deep convection might be drastically improved.

References:

Aoki, S., Morimoto, S., Ushio, S., Ito, H., Nakazawa, T., Yamanouchi, T., Ono, N., Vinje, T., 1996. Carbon dioxide variations in the Greenland Sea. Mem. Natl Inst. Polar Res., Spec. Issue, 51, 299–306.

Arora, V. K., Matthews, H. D., 2009. Characterizing uncertainty in modeling primary terrestrial ecosystem processes. Global Biogeo. Cycles., 23, GB2016, 10.1029/2008GB 003398.

Bakker, D.C.E., Pfeil, B., Smith, K., et al., 2014. An update to the Surface Ocean CO_2atlas (SOCAT version 2). Earth Syst. Sci. Data 6, 1e22. http:// dx.doi.org/10.5194/essd-6-69-2014, 6.

Bakker, D.C.E., Pfeil, B., Smith, K., et al., 2016. A 58-year Record of High Quality Data in Version 3 of the Surface Ocean CO_2 Atlas (SOCAT) (In preparation for Earth System Science Data).

Bindschadler, R. A. and 27 others, 2013. Ice-sheet model sensitivities to environmental forcing and their use in projecting future sea level (the SeaRISE project). J. Glaciol., 59, 195–224, doi:10.3189/2013JoG12J125.

Boden, T. A., Marland, G., Andres, R. J., 2016. *Global, Regional, and National Fossil-Fuel CO_2 Emissions*, Carbon Dioxide Information Analysis Center, Oak Ridge Natl Lab., U. S. Dep. Of Energy, Oak Ridge, Tenn., doi: 10.3334/ CDIAC/00001_V2016.

Bolch, T., Sandberg Sørensen, L., Simonsen, S.B., Molg, N., Machguth, H., Rastner, P., Paul, F., 2013. Mass loss of Greenland's glaciers and ice caps 2003–2008 revealed from ICESat laser altimetry data. Geophys. Res. Lett. 40, 875–881.

Cai, W.J., Chen, L.Q., Chen, B.S., Gao, Z.Y., Lee, S.H., Chen, J.F., Pierrot, D., Sullivan, K., Wang, Y.C., Hu, X.P., Huang, W.J., Zhang, Y.H., Xu, S.Q., Murata, A., Grebmeier, J.M., Jones, E.P., Zhang, H.S., 2010. Decrease in the CO_2 uptake capacity in an ice-free Arctic Ocean Basin. Science 329, 556–559.

Chanut, J., Barnier, B., Large, W., Debreu, L., Penduff, T., Molines, J. M. and Mahilot, P., 2008. MEsoscale eddies in the Labrador Sea and their contribution to convection and restratification. J. Phys. Oceanogr., 38, 1617–1643, http:// dx-.doi.org/10.1175/2008JPO3485.1.

Dlugokencky, E. J., Bruhwiler, L., White, J. W. C., Emmons, L. K., Novelli, P. C., co-authors, 2009. Observational constraints on recent increases in the atmospheric CH_4 burden. Geophys. Res. Lett.36, L18803. DOI:10.1029/2009GL 039780.

Dlugokencky, E. J., Lang, P. M., Mund, J. W., Crotwell, A. M., Crotwell, M. J., Thoning, W., 2016. Atmospheric carbon dioxide dry air mole fractions from NOAA ESRL Carbon Cycle Cooperative Global Air Sampling Network, 1968–2015, Version: 2016-08-30. Path: ftp://aftp.cmdl.noaa.gov/ data/trace_gases/co2/flask/surface/.

Fujita, R., Morimoto, S., Umezawa, T., Ishijima, K., Patra, P. K., Worthy, D. E. J., Goto, D., Aoki, S., Nakazawa, T., 2018. Temporal variation of the mole fraction, carbon, and hydrogen isotope rations of atmospheric methane in the Hudson Bay Lowlands, Canada. J. Geophys. Res., 123, 4695–4711, https:// doi.org/10.1002/2017JD027972.

Gelderloos, R., Stranceo, F. and Katsman, C. A., 2012. Mechanism behind the temporary shutdown of deep convection in the Labrador Sea: lessons from the great salinity anomaly years 1968–71. J. Climate, 25, 6743–6755.

Goto, D., Morimoto, S., Aoki, S., Patra, P. K., Nakazawa, T., 2017a. Seasonal and short-term variations in atmospheric potential oxygen at Ny-Ålesund, Svalbard. Tellus, 69B, 1311767, http:// dx.doi.org/10.1080/16000889.2017.13117 67.

Goto, D., Morimoto, S., Aoki, S., Nakazawa, T., 2013b. A high-precision continuous measurement system for the atmospheric O2/N2 ratio at Ny-Ålesund, Svalbard and its preliminary observational results. Antarct. Rec., 57, 17–27.

Goto, D., Morimoto, S., Ishidoya, S., Ogi, A., Aoki, S., Nakazawa, T., 2013a. Development of a high precision continuous measurement system for the atmospheric O2/N2 ratio and its application at Aobayama, Sendai, Japan. J. Meteorol. Soc. Jpn, 91, 179–192.

Goto, D., Morimoto, S., Ishidoya, S., Aoki, S., Nakazawa, T., 2017b. Terrestrial biospheric and oceanic CO_2 uptakes estimated from long-term measurements of atmospheric CO_2 mole fraction, d13C and d(O2.N2) at Ny-Ålesund, Svalbard. J. Geophys. Res. Biogeosci., 122, doi: 10.1002/2017 JG003845.

Graven, H. D., 13 others, 2013. Enhanced seasonal exchange of CO_2 by northern ecosystems since 1960. Science, 341, 1085–1089.

Greve, R., Herzfeld, U. C., 2013. Resolution of ice streams and outlet glaciers in large-scale simulations of the Greenland ice sheet. Annals Glaiol., 54, 209–220.

Hasumi, H., 2015. CCSR Ocean Component Model (COCO) Version 4.0. as of January 29, 2015. Atmosphere and Ocean Research Institute, The University of Tokyo, Chiba, Japan.

Henderson-Sellers, A., McGuffie, K., Pitman, A. J., 1996. The Project for Intercomparison of Land-surface Parameterization Schemes (PILPS): 1992 to 1995. Cli. Dyn., 12, 849–859.

IPCC, 2007. Climate change 2007: the physical science basis. Contribution of Working Group I to the Fourth Assessment Report of the Intergovernmental Panel on Climate Change. Cambridge University Press, Cambridge.

IPCC, 2013. Climate change 2013: the physical science basis. In: Stocker, T.F., Qin, D., Plattner, G.K., Tignor, M., Allen, S.K., Boschung, J., Nauels, A., Xia, Y., Bex, V., Midgley, P.M. (Eds.), Contribution of Working Group I to the Fifth Assessment Report of the Intergovernmental Panel on Climate Change. Cambridge University Press, Cambridge and New York, NY, p. 1535.

IPCC, 2019: IPCC Special Report on the Ocean and Cryosphere in a Changing Climate. Chapter 3, [Meredith, M, Sommerkorn, M.], 173p.

Ichii, K., et al., 2017. New data-driven estimation of terrestrial CO_2 fluxes in Asia using a standardrdized database of eddy covariance measurements, remote sensing data, and support vector regression. J. Geophys. Res., Biogeosci., 122, 767–795, doi: 10.1002/2016JG003640.

Iida, Y., Kojima, A., Takatani, Y., Nakano, T., Midorikawa, T., Ishii, M., 2015. Trends in pCO_2 and sea-air CO_2 flux over the global open oceans for the last two decades, J. Oceanogr., 71, doi: 10.1007/s10872-01500306-4.

Ishidoya, S., Morimoto, S., Aoki, S., Taguchi, S., Goto, D., Murayama, S., Nakazawa, T., 2012. Oceanic and terrestrial biospheric CO2 uptake estimated from atmospheric potential oxygen observed at Ny-Ålesund, Svalbard, and Syowa, Antarctica. Tellus, 64B, 18924, http://dx.doi.org/ 10.3402/tellusb.v64i0.18924.

Ishidoya, S., Uchida, H., Sasano, D., Kosugi, N., Taguchi, S., Ishii, M., Morimoto, S., Tohjima, Y., Nishino, S., Murayama, S., Aoki, S., Ishijima, K., Fujita, R., Goto, D., Nakazawa, T., 2016. Ship-based observations of atmospheric potential oxygen and regional air-sea O2 flux in the northern North Pacific and the Arctic Ocean. Tellus, 68B, 22972, http://dx.doi.org/ 10.3402/tellusb.v68.29972.

Kanao, M., and 14 others, 2012. Greenland Ice Sheet Dynamics and Glacial Earthquake Activities. In Muller, J. and Koch, L. (Eds.), "Ice Sheets: Dynamics, Formation and Environmental Concerns," ISBN 978-1-61942-367-1, Hauppauge, NY, Nova Science Publishers, Inc., Chap. 4, 93–120.

Kawasaki, T. and Hasumi, T., 2014. Effect of freshwater from the West Greenland Current on the winter deep convection in the Labrador Sea. Ocean Modelling, 75, 51–64.

Keeling, R. F., Bender, M. L., Tans, P. P., 1993. What atmospheric oxygen measurements can tell us about the global carbon cycle. Global Biogeochem Cycles. 7, 37–67.

Keeling, R. F., Stephens, B. B., Najjar, R. G., Doney, S. C., Archer, D., co-authors, 1998. Seasonal variations in the atmospheric O_2/N_2 ratio in relation to the kinetics of air-sea gas exchange. Global Biogeochem Cycles. 12, 141–163.

Keeling, R. F., Manning, A. C., 2014. Studies of recent changes in atmospheric O_2 content. In: *Treatise on Geochemistry* (eds., H. Holand and K. Turekian). Vol. 5.15, Elsevier, Amsterdam, 385–404.

Khan, S.A., Wahr, J., Bevis, M., Velicogna, I., Kendrick, E., 2010. Analysing the Creep of Mountain Permafrost using High Precision Aerial Photogrammetry. Spread of ice mass loss northwest Greenland observed by GRACE and GPS. Geophys. Res. Lett. 37, L06501. http://dx.doi.org/10.1029/2010GL042460.

Khatiwala, S., Schlosser, P. and Visbeck, M., 2002. Rates and mechanisms of water mass transformation in the Labrador Sea. J. Phys. Oceanogr., 34, 32, 666–686.

Kobayashi, H., Delbart, N., Suzuki, R., Kushida, K., 2010. A satellite-based method for monitoring seasonality in the overstory leaf area index of Siberian larch forest. J. Geophys. Res. Biogeo., 115, G01002, https://doi.org/10.1029/2009JG000939

Koreisha, M. M., 1963. Present glaciation in the Suntar-Khayata Range (in Russian with English summary). Glaciologia, 11, Nauka, Moscow, 172p.

Kosugi, N., Sasano, D., Ishii, M., Nishino, S., Uchida, H., Yoshikawa-Inoue, H., 2017. Low $p\mathrm{CO}_2$ under sea-ice melt in the Canada Basin of the western Arctic Ocean. Biogeosciences, 14, 5727–5739, https://doi.org/10.5194/bg-14-5727-2017.

Le Quere, C. et al., 2016. Global carbon budget 2014. Earth Syst. Sci. Data, 8, 605–649, doi: 10.5194/essd-8-605-2016.

Machguth, H. and 31 others, including Sugiyama, S., 2016. Greenland surface mass-balance observations from the ice-sheet ablation area and local glaciers. Journal Glaciology, 62, 861–887, doi: 10.1017/jog.2016.75.

Machida, T., Matsueda, H., Sawa, Y., Nakagawa, Y., Hirotani, K., Kondo, N., Goto, K., Nakazawa, T., Ishikawa, K., Ogawa, T., 2008. Worldwidemeasurements of atmospheric CO_2 and other trace gas species using commercial airlines, J. Atmos. Oceanic Technol., 25(10), 1744–1754, doi:10.1175/2008JTECHA1082.1.

Manning, A. and Keeling, R. F., 2006. Global oceanic and land biotic carbon sinks from the Scripps atmospheric oxygen flask sampling network. Tellus, 58B, 95–119.

Matsueda, H., Inoue, H. Y., 1996. Measurements of atmospheric CO_2 and CH_4 using a commercial airliner from 1993 to 1994, Atmos. Environ., 30, 1647–1655.

McGeehan, T. and Maslowski, W., 2011. Impact of shelf-basin freshwater transport on deep convection in the wetern Labradr Sea. J. Phys. Oceanogr., 41, http://dx.doi.org/10.1175/JPO-D-11-01.1.

Miyazaki, S. et al., 2015. The GRENE-TEA model intercomparison project (GTMIP): overview and experiment protocol for Stage 1. Geosi. Model Dev., 8, 2841–2856, doi:10.5194/gmd-8-2841-2015.

Moholdt, G., Wouters, B., Gardner, A. S., 2012. Recent mass changes of glaciers in the Russian High Arctic. Geophys. Res. Lett. 39 http://dx.doi.org/10.1029/2012GL051466.

Morimoto, S., Aoki, S., Yamanouchi, T., 2001. Temporal variations of atmospheric CO_2 concentration and carbon isotope ratio in Ny-Ålesund, Svalbard. Proc. Int. Symp. "Environmental Research in the Arctic 2000", 19–21 July 1995, NIPR, Tokyo. Mem. Natl. Inst. Polar Res., Spec. Issue, 54, 71–80.

Morimoto, S., Aoki, S., Nakazawa, T., Yamanouchi, T., 2006. Temporal variations of the carbon isotopic ratio of atmospheric methane observed at Ny-Ålesund, Svalbard from 1996 to 2004. Geophys. Res. Lett. 33, L01807. DOI:10.1029/2005GL024648.

Morimoto, S., Aoki, S., Nakazawa, T., 2009. High precision measurements of carbon isotopic ratio of atmospheric methane using a continuous flow mass spectrometer. Antarctic Record 53, 1–8.

Morimoto, S., Fujita, R., Aoki, S., Goto, D., Nakazawa, T., 2017. Long-term variations of the mole fraction and carbon isotope ratio of atmos@heric methane observed at Ny-Ålesund, Svalbard from 1996 to 2013. Tellus, 69B, 1380497, https://doi.org/10.1080/16000889.2017.1380497.

Myers, P. G. and Donnelly, C., 2008. Water mass transformation and formation in the Labrador Sea. J. Climate, 21, 1622–1638.

Myneni, R. B., Hoffman, S., Knyazikhin, Y., Privette, J. L., Glassy, J., Tian, Y., Wang, Y., Song, X., Zhang, Y., Smith, G. R., Lotsch, A., 2002. Global products of vegetation leaf area and fraction absorbed PAR from year one of MODIS data. Remote Sens. Environ., 83, 214–231.

Nagai, S., Kobayashi, H., Suzuki, R., 2019. Remote sensing of vegetation. In Water-Carbon Dynamics in Eastern Siberia, Eds. T. Ohta, T. Hiyama, Y. Iijima, A. Kotani, T.C. Maximov, Springer, 231–252.

Nakaoka, S., Aoki, S., Nakazawa, T., Hashida, G., Morimoto, S., Yamanouchi, T., Yoshikawa-Inoue, H., 2006. Temporal and special variations of oceanic pCO_2 and air-sea CO_2 flux in the Greenland Sea and the Barents Sea. Tellus, 58B, 148–161.

Nakaoka, S., Telszewski, M., Nojiri, Y., Yasunaka, S., Miyazaki, C., Mukai, H., Usui, N., 2013. Estimating temporal and spatial variation of sea surface pCO_2 in the North Pacific using a self organizing map neural network technique. Biogeosciences 10, 6093–6106. http://dx.doi.org/10.5194/bg-10-6093-2013.

Nakazawa, T., Morimoto, S., Aoki, S., Tanaka, M., 1997. Temporal and spatial variations of the carbon isotopic ratio of atmospheric carbon dioxide in the western Pacific region. J. Geophys. Res. 102, 1271–1285.

Nilsson, J., Sørensen, L.S., Barletta, V.R., Forsberg, R., 2015. Mass changes in Arctic ice caps and glaciers : implications of regionalizing elevation changes. Cryosphere 9, 139–150.

Niwa, Y., Machida, T., Sawa, Y., Matsueda, H., Schuck, T. J., Brenninkmeijer, A. A. M., Imasu, R., Satoh, M., 2012. Imposing strong constraints on tropical terrestrial CO2 fluxes using passenger aircraft based measurements. J. Geophys. Res., 117, D11303, doi: 10.1029/2012JD017474.

Noguchi, K., Matsuura, Y., Sparrow, S. D., Hinzman, L. D., 2016. Fine root biomass in two black spruce stands in interior Alaska: effects of different permafrost conditions. Trees, 30, 441–449, doi: 10.1007/s00468-015-1226-z.

Nowicki, S. and 30 others, 2013. Insights into spatial sensitivities of ice mass response to environmental change from the SeaRISE ice sheet modeling project II: Greenland, J. Geophys. Res., 118, 1025–1044, doi:10.1002/jgrf.20076.

Ohashi, Y., Iida, T., Sugiyama, S., Aoki, S., 2016. Spatial and temporal variations in high turbidity surface water off the Thule region, northwestern Greenland. Polar Science, 10, 270–277, http://dx.doi.org/10.1016/j.polar.2016.07.003.

Ohta, T., Kotani, A., Iijima, Y., Maximov, T. C., Iyo, S., Hanamura, M., Kononov, A. V., Maximov, A. P., 2014. Effects of waterlogging on water and carbon dioxide fluxes and environmental variables in a Siberian larch forest, 1998–2011. Agric. Forest Meteor., 188, 64–75, http://dx.doi.org/10.1016/j.agrformet.2013.12.012.

Patra, P. K. et al., 2009. Growth rate, seasonal, synoptic abd diurnal variations in lower atmospheric methane and its budget. J. Meteorol. Soc., Jpn, 87, 635–663, doi: 10.2151/jmsj.87.635.

Pfeil, B., Olsen, A., Bakker, D.C.E., et al., 2013. A uniform, quality controlled Surface Ocean CO_2 Atlas (SOCAT). Earth Syst. Sci. Data 5, 125e143. http://dx.doi.org/ 10.5194/essd-5-125-2013.

Podolskiy, E. A., Sugiyama, S., Funk, M., Walter, F., Genco, R., Tsutaki, S., Minowa, M., Ripepe, M., 2016. Tide-modulated ice flow variations drive seismicity near the calving front of Bowdoin Glacier, Greenland. Geophys. Res. Lett., 43, 2036–2044, doi: 10.1002/2016GL067743.

Rigby, M., Prinn, R. G., Fraser, P. J., Simmonds, P. G., Langenfelds, R. L., co-authors, 2008. Renewed growth of atmospheric methane. Geophys. Res. Lett. 35, L22805. DOI: 10.1029/2008GL036037.

Saeki, T., Maksyutov, S., Sasakawa, M., Machida, T., Arshinov, M., Tans, P., Conway, T. J., Saito, M., Valsala, V., Oda, T., Andres, R. J., Belikov, D., 2013. Carbon flux estimation for Siberia by inverse modeling constrained by aircraft and tower CO_2 measurements. J. Geophys. Res., 118, 1100–1122, doi:10.1002/jgrd.50127.

Saito, F., Abe-Ouchi, A., Takahashi, K., Blatter, H., 2016. SeaRISE experiments revisited: potential sources of spread in multi-model projections of the Greenland ice sheet. The Cryosphere, 10, 43–63, doi: 10.5194/tc-10-43-2016.

Saito, J., Sugiyama, S., Tsutaki, S., Sawagaki, T., 2016. Surface elevation change on ice caps in the Qaanaaq region, nnorthwetern Greenland. Polar Science, 10, 230–248, http://dx.doi.org/10.1016/j.polar.2016.05.002.

Saito, K. et al., 2018. Energy-water budget analysis of an Arctic terrestrial models intercomparison GTMIP. Seppyo, 80, 159–174, (in Japanese with English abstract).

Sakakibara, D., Sugiyama, S., 2018. Ice front and flow speed variations of marine-terminating outlet glaciers along the coast of Prudhoe Land, northwestern Greenland. J. Glaciol., 64, 300–310, doi: 10.1017/jog.2018.20.

Sasakawa, M., Machida, T., Tsuda, N., Arshinov, N., Davydov, D., Fofonov, A., Krasnov, O., 2013. Aircraft and tower measurements of CO_2 concentration in the planetary boundary layer and the lower free troposphere over southern taiga in West Siberia: Long-term records from 2002 to 2011. J. Geophys. Res., 118, 9489–9498, doi: 10.1002/jgrd.50755.

Sawa, Y., Machida, T., Matsueda, H., 2012. Aircraft observation of the seasonal variation in the transport of CO_2 in the upper atmosphere. J. Geophys. Res., 117, D05305, doi:10.1029/2011JD016933.

Sawa, Y., Machida, T., Matsueda, H., Niwa, Y., Tsuboi, K., Murayama, S., Morimoto, S., Aoki, S., 2015. Seasonal changes of CO_2, CH_4, N_2O, and SF_6 in the upper troposphere/lower stratosphere over the Eurasian continent observed by commercial airliner. Geophys. Res. Lett., 42, 2001–2008, doi: 10.1002/2014GL062734.

Seddik, H., Greve, R., Sakakibara, D., Tsutaki, S., Minowa, M., Sugiyama, S., 2019. Response of the flow dynamics of Bowdoin Glacier, northwestern Greenland, to basal lubrication and tidal forcing. J. Glaciol., 65, 225–238, doi: 10.1017/jog.2018.106.

Sherwood, O. A., Schwietzke, S., Arling, V. A., Etiope, G., 2017. Global inventory of gas geochemistry data from fossil fuel, microbial and burning sources, version 2017. Earth System Science Data, 9(2), 639–656. https://doi.org/10.5194/essd-9-639-2017.

Shirakawa, T., Kadota, T., Federov, A., Konstantinov, P., Suzuki, T., Yabuki, H., Nakazawa, F., Tanaka, S., Miyairi, M., Fujisawa, Y., Takeuchi, N., Kusaka, R., Takahashi, S., Enomoto, H., Ohata, T., 2016. Meteorological and glaciological observations at Suntar-Khayata Glacier No. 31, east Siberia, from 2012–2014. Bull. Glaciol. Res., 34, 33–40, doi: 10.5331/bgr.16R01.

Sueyoshi, T. et al., 2016. The GRENE-TEA model intercomparison project (GTMIP) Stage 1 forcing data set. Earth Syst. Sci. Data, 8, 1–14, doi:10.5194/essd-8-1-2016.

Sugiyama, S. Sakakibara, D., Matsuno, S., Yamaguchi, S., Matoba, S., Aoki, T., 2014. Initial field observations on Qaanaaq ice cap, northwestern Greenland. Annals Glaciol., 55, 25–33, doi: 10.3189/2014AoG66A102.

Sugiyama, S., Sakakibara, D., Tsutaki, S., Maruyama, M., Sawagaki, T., 2015. Glacier dynamics near the calving front of Bowdoin Glacier, northwestern Greenland. J. Glaciol., 61, 223–232, doi: 10.3189/2015joG14J127.

Takahashi, T., Sutherland, S.C., Kozyr, A., 2015. Global Ocean Surface Water Partial Pressure of CO_2 Database: Measurements Performed during 1957–2014 (Version 2014). ORNL/CDIAC-160, NDP-088(V2014). Carbon Dioxide Information Analysis Center, Oak Ridge National Laboratory, U.S. Department of Energy, Oak Ridge, Tennessee. http://dx.doi.org/10.3334/CDIAC/OTG.NDP088(V2014).

Takata, K. et al., 2017. Reconcilation of top-down and bottom up CO2 fluxes in Siberian larch forest. Environ. Res. Lett., 12, 125012, https://doi.org/10.1088/1748-9326/aa926d.

Takeuchi, N., Fujisawa, Y., Kadota, T., Tanaka, S., Miyairi, M., Shirakawa, T., Kusaka, R., Federov, A. N., Konstantinov, P., Ohata, T., 2015. The effect of impurities on the surface melt of a glacier in the Suntar-Khayata Mountain Range, Russian Siberia. Frontiers in Earth Science, 3, 82. Doi: 10.3389/feart.2015.00082.

Tanaka-Oda, A., Tanak, K., Toriyama, J., Matsuura, Y., 2016. Variability in the growth rates and foliage $\delta^{15}N$ values of black spruce trees across a slope gradient in the Alaskan Interior. Can. J. For. Res., 46, 1483–1490, dx.doi.org/10.1139/cjfr-2015-0469.

Tei, S., Sugimoto, A., 2018. Time lag and negative responses of forest greenness and tree growth to warming over circumboreal forests. Global Change Biol. 24, 4225–4237. https://doi.org/10.1111/gcb.14135.

Tei, S., Sugimoto, A., Liang, M., Yonenobu, H., Matsuura, Y., Oosawa, A., Sato, H., Fujinuma, J., Maximov, T.C., 2017a. Radial growth and physiological response of coniferous trees to Arctic amplification. J. Geophys. Res. 122, 2786–2803. https://doi.org/10.1002/2016JG003745.

Tei, S., Sugimoto, A., Yonenobu, H., Matsuura, Y., Oosawa, A., Sato, H., Fujinuma, J., Maximov, T.C., 2017b. Tree-ring analysis and modeling approaches yield contrary response of circumboreal forest productivity to climate change. Global Change Biol., 23, 5179–5188, http://dx.doi.org/10.1111/gcb.13780.

Tei, S., Nagai, S., Sugimoto, A., 2018a. Effects of climate dataset type on tree-ring analysis: A case study for Siberian forests. Polar Science, 21, 136–145, https://doi.org/10.1016/j-polar.2018.10.008.

Tei, S., Sugimoto, A., Kotani, A., Ohta, T., Morozumi, T., Saito, S., Hashiguchi, S., Maximov, T., 2018b. Strong and stable relationships between tree-ring parametes and forest-level carbon fluxes in a Siberian larch forest. Polar Science, 21, 146–157, https://doi.org/10.1016/j-polar.2018.02.001.

Telszewski, M., Chazottes, A., Schuster, U., et al., 2009. Estimating the monthly pCO_2 distribution in the North Atlantic using a self-organizing neural network. Biogeosciences 6, 1405–1421. http://dx.doi.org/10.5194/bg-6-1405-2009.

Tohjima, Y., Minejima, C., Mukai, H., Machida, T., Yamagishi, H., co-authors, 2012. Analysis of seasonality and annual mean distribution of the atmospheric potential oxygen (APO) in the Pacific region. Glob. Biogeochem. Cycles. 26, GB4008. DOI: http://dx.doi.org/10.1029/2011GB004110.

Tsutaki, S., Sugiyama, S., Sakakibara, D., Sawagaki, T., 2016. Surface elevation changes during 2007–13 on Bowdoin and Tugto Glaciers, northwestern Greenland. J. Glaciol., 62, 1083–1092, doi: 10.1017/jog.2016.106.

Tsutaki, S., Sugiyama, S., Sakakibara, D., Aoki, T., Niwano, M., 2017a. Surface mass balance, ice velocity and near-surface ice temperature on Qaanaaq Ice Cap, northwestern Greenland, from 2012 to 2016. Annals Glacio., 58, 181–192, doi: 10.1017/aog.2017.7.

Tsutaki, S., Sugiyama, S., Sakakibara, D., 2017b. Surface elevations on Qaanaaq and Bowdoin Glaciers in northwestern Greenland as measured by a kinematic GPS survey from 2012–2016. Polar Data J., 1, 1–16. 1.00, Japan, Arctic Data archive System (ADS), 2017. https://doi.org/10.17592/001.2017060801.

Uchida, M., Muraoka, H., Nakatsubo, T., 2016. Sensitivity analysis of ecosystem CO2 exchange to climate change in High Arctic tundra using an ecological process-based model. Polar Biol., 39, 251–265, doi:10.1007/s00300-015-1777-x.

Umezawa, T., Machida, T., Aoki, S., Nakazawa, T., 2012. Contributions of natural and anthropogenic sources to atmospheric methane variations over western Siberia estimated from its carbon and hydrogen isotopes. Global Biogeochemical Cycles, 26, GB4009, doi: 10.1029/2011GB004232.

Van der Veen, C. J., 1996. Tidewater calving. J. Glaciol., 42(141), 375–385.

Wanninkhof, R., 1992. Relationship between wind speed and gas exchange over the ocean. J. Geophys. Res. 97, 7373–7382. http://dx.doi.org/10.1029/ 92JC00188.

White, J. W., Vaughn, B. H., Michel, S. E., 2015. Stable isotopic composition of atmospheric carbon dioxide (13C and 18O) from the NOAA ESRL Carbon Cycle Cooperative Global Air Sampling Network, 1990–2014, Univ. of Colo., Institute of Arctic and Alpine Research (INSTAAR), Version: 2015-10-26, Path: ftp://aftp.cmdl.noaa.gov/data/trace_gases/co2c13/flask/.

Yamanouchi, T., Aoki, S., Morimoto, S. and Wada, M., 1996. Report of atmospheric science observations at Ny-Ålesund, Svalbard. Proc. Int. Symp. "Environmental Research in the Arctic", 19–21 July 1995, NIPR, Tokyo. Mem. Natl Inst. Polar Res., Spec. Issue, 51, 153–163.

Yasunaka, S., Murata, A., Watanabe, E., Chierici, M., Fransson, A., van Heuven, S., Hoppema, M., Ishii, M., Johannessen, T., Kosugi, N., Lauvset, S. K., Mathis, J. T., Nishino, S., Omar, A. M., Olsen, A., Sasano, D., Takahashi, T., Wanninkhof, R., 2016. Mapping of the air–sea CO_2 flux in the Arctic Ocean and its adjacent seas: basin-wide distribution and seasonal to interannual variability, Polar Sci., 10, 323–334, https://doi.org/10.1016/j.polar.2016.03.006.

Yasunaka, S., Siswanto, E., Olsen, A., Hoppema, M., Watanabe, E., Fransson, A., Chieici, M., Murata, A., Lauvset S. K., Wanninkhov, R., Takahashi, T., Kosugi, N., Omar, A. M., van Heuven, S. Mathis, J. T., 2018. Arctic Ocean CO_2 uptake: an improved multiyear estimate of the air-sea CO_2 flux incorporating chlorophyll *a* concentrations. Biogeosciences, 15, 1643–1661, https://doi.org/10.5194/bg-15-1643-2018.

Zemp, M., Frey, H., G€artner-Roer, I., Nussbaumer, S.U., Hoelzle, M., Paul, F., Haeberli, W., Denzinger, F., Ahlstroem, A.P., Anderson, B., Bajracharya, S., Baroni, C., Braun, L.N., Caceres, B.E., Casassa, G., Cobos, G., Davila, L.R., Delgado Granados, H., Demuth, M.N., Espizua, L., Fischer, A., Fujita, K., Gadek, B., Ghazanfar, A., Hagen, J.O., Holmlund, P., Karimi, N., Li, Z., Pelto, M., Pitte, P., Popovnin, V.V., Portocarrero, C.A., Prinz, R., Sangewar, C.V., Severskiy, I., Sigurdsson, O., Soruco, A., Usubaliev, R., Vincent, C., 2015. Historically unprecedented global glacier decline in the early 21st century. J. Glaciol. 61 (228), 745–762. http://dx.doi.org/10.3189/2015JoG15J017.

8. Synthesis of the project

The processes we have conducted in our GRENE Arctic Project, "Rapid Change of the Arctic Climate System and its Global Influences", are as shown in the schematic of Fig. 8.1. In order to tackle these abrupt changes in the Arctic, to understand the mechanism, and to contribute to future climate change projection, we have conducted GRENE Arctic Project under 4 Strategic Research Targets (STs) as already shown in Chapters 3 to 7. Here, we have summarized outcomes and their interactions within each Targets. In order to synthesize the final goals, we had taken steps of "Pyramidal construction" to promote coordination among each research out put, and then to create research outcomes.

Synthesis of the whole strategic targets.

We have seen that each research study contributed to the respective strategic targets. However, four strategic targets themselves do not stand alone, and they have close connection each other and are closely contributing to the others. Now, we have synthesized the relation of each strategic target together with their research themes as shown in Fig. 8.1.

Among 4 strategic targets, "Arctic warming amplification (AA)", ST1 was in the center and key issue of GRENE Arctic Project. Many phenomena in the atmosphere, ocean, cryosphere and terrestrial environment have respective contributions to the AA; however, in the opposite direction, AA affects each component, that means the both directions are seen. AA (ST1) affects the global issues (ST2) and also mid-latitude weather (ST3a) or marine ecosystems and fisheries (ST3b). Sea ice retreat and possibilities of Arctic Sea Routes (ST4) also brought by AA. Thus all individual Strategic Research Targets have a systematic connection, and composed "Arctic climate system" totally.

Future direction

Outcomes contributing to four Strategic Research Targets have been greatly achieved through 7 Research Themes under the GRENE Arctic Project. However, we still have many scientific issues to be accomplished in the future.

We have laid a great emphasis on the collaborations between observation and modeling, and many efforts have been conducted to merge observations with modeling. However, these modelings were limited in process or single system, respectively, and integrating into the up-to-date global climate/ system model is still behind. It will need a long lasting study.

Arctic and mid-latitude link was one of the most studied topics in the recent; however, still many discussions are on-going, especially how to predict the link. For the short range prediction, extensive international initiative,

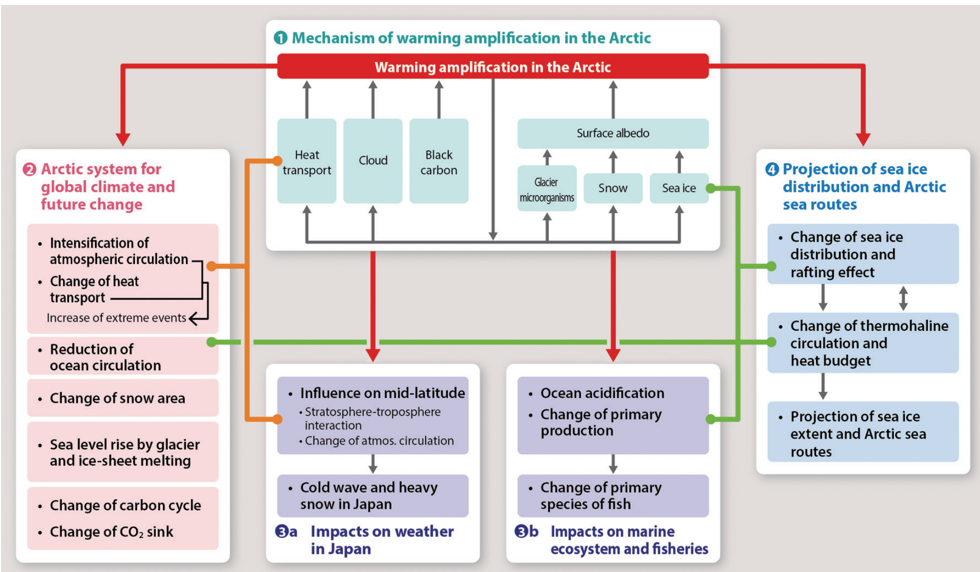

Fig. 8. 1 Schematic of the GRENE Arctic Project, showing "warming amplification in the Arctic and its global impact". The key to Arctic climate change is Arctic warming amplification (AA). AA leads to the change in sea ice extent and then to the realization of the Arctic sea routes. It also affects the global climate, such as atmospheric circulation, cryosphere, and the carbon cycle. Moreover, AA will alter marine chemical components and the living environment for plankton, and hence have impacts on the major fish species and fisheries. AA will also influence the mid-latitude weather and climate, and bring cold and heavy snow to Japan in winter

Year of Polar Prediction (YOPP), has been conducted under WMO/PPP (Polar Prediction Project), and some new insights are expected (Inoue et al., 2015, Jung et al., 2016).

Observations of ocean, sea ice and atmosphere in the broad area of Arctic Ocean are still limited. Long term effort was continued till the recent, using drifting ice stations, such as North Pole 1 (NP 1) to NP 41, by former Soviet Union and then by Russia (Frolov, 2005). However, these efforts were ceased partly due to the difficulty in the sea ice conditions. A new international project MOSAiC (Multidisciplinary drifting Observatory for the Study of Arctic Climate: 2019–2020; https://mosaic-expedition.org/) was just started to study ocean, sea ice, atmosphere, marine ecosystems, biogeochemistry and their interactions, using the frozen research vessel, *Polartern,* in the deep Arctic Ocean. It is recommended to join and contribute the project. However, since the project is just limited to one year or so, it is still needed to continue some basic observations for long term in the central Arctic Ocean, even not so comprehensive as the project. To maintain the observation system is the most important issue, and we need to develop a reliable and feasible system such as automatic drifting stations, buoys, AUVs and so on.

Many research topics still need to be studied further. One of the main issues in the atmospheric dynamics controls the weather and climate in the Arctic is the polar vortex/jet stream, and "blocking" is a key phenomenon not understood yet. Studies on clouds and aerosols (including black carbon) have been made in the broad area in the Arctic; however, they are still the largest uncertainties in the atmospheric processes even/especially in the Arctic. The extensive study of glacier and ice sheet was conducted in the Greenland ice sheet and confirmed that the melting and discharge at the ice edge are contributing to the sea level rise. However, to make a quantitative estimation of sea level rise, many more studies need to be done on the interaction between seawater and glacial front and the surface mass balance depending on the impurities and snow particles. The terrestrial system is another urgent target to be quantified. CH_4 emissions from the melting of the permafrost on the ground, under the lake and seawater, or ecosystem responses together with CO_2 exchange depending on warming are still to be clarified.

We still have many items to be tackled in the Arctic climate systems and hope the research projects to be continued, especially under strong international cooperation. After the GRENE Arctic, the next Arctic project, Arctic Challenge for Sustainability (ArCS) Project, is already ongoing, and its five year term is coming to the successful end in March 2020. After then, still, a new Arctic research project is anticipated.

Final words

We tried to synthesize and review the major outcomes of the GRENE Arctic here. However, the progress of our result is not thoroughly enough. Initially, we intended to collect the synthesis of each Strategic Targets compiled by each PIs; yet, the idea was not realized, and we, two authors, needed to tackle this work. It was so hard to handle all the vast areas of Arctic research by only two authors, and the result is so limited, not deeply enough, and covers only a limited area (papers).

Still, papers reviewed here are of a significant amount and in high scientific quality. This is showing the level of GRENE Arctic, and we are hoping international research communities would widely recognize these outcomes. Furthermore, we expect the Arctic research will progress in the future based on these outcomes brought by GRENE Arctic.

Acknowledgments

The authors are very grateful to all the members of GRENE Arctic, especially to PIs of Research Themes, Dr. Masao Fukasawa, Deputy Project Manager, and Project Steering Committee members. The project could not be accomplished without the kind effort of Prof. Yoshiyuki Fujii, the former Director-General of the National Institute of Polar Research, who kindly took the role of Acting Project Manager during a problematic health condition of Project Manager, TY. The GRENE Arctic was the project funded and supported by the Ministry of Education, Culture, Sports, Science and Technology, Japan (MEXT). The finalizing of this report was financially supported by the Arctic Environment Research Center, National Institute of Polar Research.

References

Frolov, I. E., 2005. The Arctic basin: results from Russian drifting stations. Springer, Berln, 272p.

Inoue, J., Yamazaki, A., Ono, J., Dethloff, K., Maturilli, M., Neuber, R., Edwards, P., amaguchi, H., 2015. Aditional Arctic observations improves weathe and sea-ice forecasts

for the Northern Sea Route. Sci, Rep., 5, 16868, doi:https://doi.org/10.1038/srep16868.
Jung, T. et al., 2016. Advancing polar prediction capabilities on daily to seasonal time scales. Bull. Amer. Meteorol. Soc., 97, 1631–1647, *https://doi.org/10.1175/BAMS-D-14-00246.1*

Map of GRENE Arctic Project observation activities

- Terrestrial ecosystem
- Atmosphere
- Cryosphere
- Greenhouse gas
- Marine ecosystem
- Sea Ice and ocean environment
- Snow survey lines
- Permafrost survey lines
- Airliner

Solid-lines (yellow, orange, pink, blue): Ship

National Institute of Polar Research

NiPR
National Institute of Polar Research